Functionalized Cellulose Nanomaterials for Integrated Environmental Management

by

Chunxia Tang

A thesis

presented to the University of Waterloo

in fulfilment of the

thesis requirement for the degree of

Doctor of Philosophy
in
Chemical Engineering

Waterloo, Ontario, Canada, 2021

© Chunxia Tang 2021

Examining Committee Membership

The following served on the Examining Committee for this thesis. The decision of the Examining Committee is by majority vote.

External Examiner	NAME: Yeng Ming Lam Title: Chair and Professor
Supervisor	NAME: Michael Tam Title: Professor
Internal Member	NAME: William A. Anderson Title: Professor
Internal Member	NAME: Tizazu Mekonnen Title: Assistant Professor
Internal-external Member	NAME: Juewen Liu Title: Professor

AUTHOR'S DECLARATION

I hereby declare that I am the sole author of this thesis. This is a true copy of the thesis, including any required final revisions, as accepted by my examiners.

I understand that my thesis may be made electronically available to the public.

Abstract

Bio-mass derived materials, such as cellulose nanomaterials (CNs) are naturally abundant, sustainable, and bio-degradable, and they are promising next generation materials to replace petroleum derived systems. The thesis focuses on the management of environmental pollutions caused by the discharge of emulsions and heavy metal ions in wastewater and the use of non-sustainable surfactants and toxic solvents used in conventional pesticide formulation. To achieve this goal, the general approaches adopted in this doctoral study are: 1) development of pesticide emulsion formulation using sustainable cellulose nanocrystals (CNCs) as emulsifiers, 2) development of novel organic solvent- and surfactant- free pesticide nano-dispersion using CNCs as carriers and dispersing agents, 3) development of CNs-based aerogel adsorbents for the treatment of wastewater containing heavy metal ions and emulsion droplets, 4) recovery of water pollutants as nutrients for plant growth.

Firstly, surfactant-like CNC particles were synthesized by grafting aminated polystyrene (PS-NH_2) on the end of CNC via reductive amination. The effect of reaction conditions, such as reaction time (1, 3 or 7 days), reaction temperature (room temperature or 70 ℃) and polystyrene chain length (M_n of 5000 or 10000 Da) on the modification degree were investigated. Further, the emulsification capability of the end-modified CNCs was investigated, where the modified CNCs were more effective in emulsifying toluene and hexadecane than pristine CNCs. Various parameters, such as concentration of particles, electrolytes, and polarity of solvents on the characteristics of the emulsions were investigated. Such system, bearing biocompatible and environmentally friendly characteristics, showed excellent encapsulation of a model hydrophobic compound (Nile red) without coalescence over a period of more than 4 months, which offers promise for preparing emulsion formulations for pesticide encapsulation.

Following this, an organic solvent- and surfactant-free pesticide nano-dispersion was developed using pristine CNCs as carriers and dispersing agents, eliminating the use of organic solvents in the final formulation. Such characteristic aligns with one of the key focuses of sustainable agriculture, i.e., development of environmentally friendly nano-sized pesticide formulation. CNC was used as a carrier and dispersing agent for two water-insoluble pesticides (Deltamethrin and Permethrin) to formulate aqueous pesticide formulations. The optimum loading mass ratio between pesticide and CNC was determined as 1:100 from UV-vis spectrophotometer, dynamic

light scattering (DLS), zeta potential, and transmission electron microscopy (TEM) analyses. Besides, the possible attractive force between the pesticide molecules and CNC was studied by Fourier transform infrared spectroscopy (FTIR) and Isothermal Titration Calorimetry (ITC). In addition, both laboratory and field trial tests were conducted to evaluate the pest control efficacy of the nano-dispersion, with performance better or equal to existing commercial formulations.

Functionalized cellulose nanofibrils (CNFs) based aerogels were synthesized to remove Cu (II) ions and emulsified emulsion droplets in wastewater streams. Firstly, amine-functionalized CNF was prepared by cross-linking polyethylenimine (PEI) to cellulose nanofibrils (CNF) using 3-glycidyloxypropyl trimethoxysilane (GPTMS). Robust cellulose aerogel beads (CGP, diameter of 3~4 mm) were produced by injecting crosslinked CNF dispersion into liquid nitrogen, followed by freeze drying. The effect of mass ratio between PEI and GPTMS (1:1 or 3:1) on the total amine contents, mechanical strength and morphologies of the aerogel beads were investigated. In addition, the effect of pH, ionic strength, adsorbent dosage, temperature as well as initial concentration on the adsorption performance were studied, where the maximum adsorption capacity, adsorption kinetic were examined. Small CGP beads with desirable characteristics, such as high amine content (5.74 mmol/g for CGP3 beads), large maximum Cu (II) adsorption capacity (163.40 mg/g for CGP3 beads), very fast adsorption rate (< 10 h to reach equilibrium), high shape recovery (2.00 % plastic deformation for CGP3 beads at 50% strain), robust mechanical strength (stress around 10.5 KPa at 50% strain), and possible regeneration were achieved.

As an extension from the previous study, carboxylated CNF aerogel beads were prepared for Cu (II) ions removal. A one step protocol to prepare highly carboxylated and chemically crosslinked cellulose nanofibril (CNF) aerogel beads using maleic anhydride (MA) was developed. The crosslinking was achieved by esterification reaction based on the results from Fourier transform infrared spectroscopy (FTIR) and conductometric-potentiometric titration. The carboxyl groups and ester linkages were produced simultaneously during the ring open reaction of MA, yielding a carboxylic content of up to 2.78 mmol/g. The effect of CNF concentration on the morphology and wet mechanical strength of the crosslinked aerogel beads were also investigated. Results suggested that higher CNF concentration yielded a compact network that displayed a maximum compressive stress of 2800 Pa at 60% strain. In addition, Cu (II) ions adsorption capacity of 60.92 mg/g and

84.12 mg/g was yielded for CNF-MA 1% and CNF-MA 2%, respectively. The adsorption was achieved by complexation between carboxylic and hydroxyl groups.

Furthermore, an ambient amphiphilic cellulose aerogel was prepared for both emulsified oil-in-water and water-in-oil emulsion filtration. Dicarboxylated-PEG crosslinkers of different lengths were synthesized by grafting MA on Poly (ethylene glycol) (average M_n = 600, 1500, 3350, 8000 Da) by esterification reaction. Then, ambient amphiphilic and underwater superoleophobic cellulose aerogels (CPMs) were prepared by crosslinking cellulose nanofibrils (CNF) with dicarboxylated-PEGs of different lengths. The dried aerogels showed excellent uptake capacity for various solvents possessing different polarities, and the released of the absorbed oils in water. The crosslinking efficiency decreased with increasing crosslinker length. Both crosslinking degree and network density contributed to the mechanical strength of the aerogel. Such amphiphilic aerogels were effective for both oil-in-water and water-in-oil emulsion separation. The permeation flux and separation efficiency for oil-in-water emulsions are controlled by a combination effect of size sieving and electrostatic interaction between oil droplets and the negatively charged aerogel. The aerogel also demonstrated excellent separation performance (>92%) for cellulose nanocrystal stabilized oil-in-water Pickering emulsions. For water-in-oil emulsions, the viscosity of oil showed a significant effect on the permeate flux. A separation efficiency over 97% was achieved for all studied water-in-oil emulsions.

Finally, the potential of CNF based aerogel as an absorbent for water and nutrient capture and release was examined. As an example, the as prepared CPM aerogel was buried in soil before planting pea seeds. Seed germination and growth rates in CPM aerogel containing soils was compared with normal soil. After harvesting, the fresh weight, average shoot/ root length and diameter of seedlings from each pot were compared. The results suggest that the functionalized aerogels were effective for promoting seed germination and seeding growth.

In summary, the thesis contributes to the development of CNs from two perspectives: 1) development of new and novel sustainable systems and advancing new fundamental understanding on the properties of these systems and 2) expanding their applications to other fields, such as agricultural (not often reported) and wastewater treatment. The specific applications being demonstrated are novel pesticide formulations preparation, aerogel beads for heavy metal ions

removal, superwetting cellulose aerogel for oily wastewater purification, and aerogel for promoting plant growth.

Acknowledgements

Firstly, I would like to thank my supervisor, Professor Michael Tam, for offering me the Ph.D position. Specially, I am appreciative of his guidance, encouragement, and persistent help during my four years PhD study, without which this thesis would not have been possible. Beyond this, I have learnt how to conduct good research, balance life and work, and communication.

I would also like to thank my committee members Prof. William Anderson, Prof. Tizazu Mekonnen and Prof. Juewen Liu for their insightful suggestions, comments and instructions on my PhD research and study. Special thanks to my external examiner Professor Yeng Ming Lam, for her valuable suggestions and help to improve the quality of this thesis. Also, I would like to thank Prof. Juewen Liu, Professor Boxin Zhao and Professor Vivek Maheshwari for allowing me to use their labs and equipment.

In addition, I would like to acknowledge all the friendly group members I have met in Dr. Tam's group, for their kind support, encouragement, and valuable discussion. Particularly, I am grateful for several of my best friends at Waterloo, who have continuously encouraged and supported me when I was in difficulties and under stress. All the time spent with them are precious memories in my life.

Sincere thanks to my lovely parents for their great love, unconditional understandings and supports.

Lastly, I am also very grateful for every effort I have made to transform myself a better person!

Table of Content

Table of Figures

Table of Tables

Chapter 1 Introduction

1.1 Problem statement

With the increasing population, agricultural production of food must significantly increase to meet the demand for food for nutrition. In the past decades, increasing the application of pesticides, fertilizers, water, and other resources is a very straightforward approach to enhance crop yield.[1] As most pesticide active ingredients (AI) are insoluble in water, auxiliary ingredients, such as carriers, solvents, surfactants, are required to prepare suitable formulations to facilitate their applications in the field.[2–6] For example, emulsifiable concentrate (EC), a type of commercial pesticide formulations, is prepared by mixing toxic organic solvents containing AI with surfactants to improve the water dispersity of the AI.[7] However, the inefficiencies of agrochemical formulations has led to the overuse of pesticides, surfactants, solvents, fertilizers and water, which causes environmental pollutions. According to a report, 187 million metric tons of fertilizer, four million tonnes of pesticides, 2.7 trillion cubic meters of water (about 70% of all freshwater consumptive use globally) are required to produce three billion metric tons of crops per year.[8]

As a consequence of agrochemical loss through leaching, water and soil pollution has become an environmental issue and concern.[9] To reduce environmental pollutions caused by agrochemicals loss through leaching, advanced delivery systems based on polymer capsules, spheres, micelles, emulsions, suspensions, and carriers were developed in the past decades. The goal is achieved by improving nutrient delivery efficiency to enhance crop production yield.[7] However, most of these systems use synthetic and non-degradable polymers which further contribute to the environmental problems. According to the description of "sustainable agriculture" by the Food and Agriculture Organization of the United Nations, land, water, and ecosystems must be sustainably managed while ensuring crop yield. Compared to conventional agrochemical formulations for plants, sustainable agriculture requires bio-degradable and bio-compatible materials for designing efficient agrochemical delivery systems or water retention systems without comprising crop yield.[10]

The discharge of wastewater containing emulsions droplets, dyes, pharmaceuticals, metal ions, fertilizers, pesticides, and oil spills is another major source of water pollution for decades. Methods including sorption, membrane filtration, chemical precipitation, coagulation-flocculation, and catalytic degradation are widely adopted to remove pollutants from wastewater. Notably, the

removal of emulsions from oily wastewater is a global challenge, especially for surfactants stabilized emulsions due to their good stabilities resulting from their micro- or nano- droplet sizes.[11] Traditional methods, such as centrifugation, oil skimming, and floatation for oil/water mixture separation are not applicable for separating these emulsions.[12] Activated carbon and petroleum based polymers with a large carbon footprint are commercially used to treat wastewater. From a sustainable perspective, natural materials are more desirable to design effective systems for water treatment.

Biomass materials, such as wheat straw, wood and sugar bagasse are natural resources that are being considered for these applications. The utilization of large volume of agricultural wastes is an environmentally and economically friendly approach to minimize soil contamination. As these materials mainly consist of cellulose, hemicellulose, lignin, pectin etc, they can be converted to high value products like cellulose nanomaterials, bio- polyols, bio-oil, and biochar.[13,14] Furthermore, these products are starting materials to design systems for agricultural and water treatment applications, for example, agrochemical delivery, water retention, pesticide/ fertilizer/ metal ions removal, oil absorbents, etc. Such close loop strategy greatly reduces the environmental pollution caused by agricultural activities, which supports the sustainable agriculture concept.

As the largest component of the biomass, cellulose is a promising material to replace non-degradable polymers in developing many advanced delivery and pollutants removal systems. Cellulose is a high molecular weight polysaccharide composed of anhydro-glucose units, where the repeating segments are connected *via* the β-1, 4-glycosidic linkages. To extract cellulose fibers from biomass, it is necessary to remove hemicellulose, lignin, and other components from the raw materials. Under chemical, mechanical, or enzymatic treatment, cellulosic fibers can be further broken down to cellulose nanomaterials (CNs), such as cellulose nanofibrils (CNFs) and cellulose nanocrystals (CNCs). The detailed isolation procedure of CNs from biomass wastes have been reviewed by Rajinipriya et al.[15] García et al.[16] and Mishra et al.[17] As nanoscale materials, CNs possess many beneficial characteristics, such as large surface area, high aspect ratio, excellent water stability in addition to sustainability and hydrophilicity.

In addition, surface modification methods on CNs have been widely reported due to its abundant surface hydroxyl groups. There are several comprehensive review papers discussing the background information on the structure, physical property, classification, preparation, and

modification of cellulose.[18–20] These techniques provide solid support for researchers to construct various functional systems for multiple applications.

1.2 Research objectives

The scope of this research is to reduce environmental pollution caused by conventional pesticide formulations and wastewater discharge. The objective is achieved via four approaches: 1) development of pesticide emulsion formulation using sustainable cellulose nanocrystals (CNCs) as emulsifiers, 2) development of novel organic solvent- and surfactants- free pesticide nano-dispersion using CNCs as carriers and dispersing agents, 3) development of CN based aerogel adsorbents for treating wastewater containing heavy metal ions and emulsion droplets, 4) recovery of water pollutants as nutrients for plant growth. A detailed literature review is described in Chapter 2, where only a few reports on the use of cellulose nanomaterials to prepare pesticide formulations were evident compared to their applications in water treatment, oil recovery, nanocomposites, biomedical, etc. For pollutants removal, porous aerogel possessed significant advantages over single cellulose nanofibers in terms of the performance. Besides, there are very few studies on the application of cellulose aerogel for emulsified oil droplets removal.

Based on the literature survey, the following hypothesis and research goals are formulated:

Research hypothesis:

(1) Cellulose nanocrystals can be used to encapsulate water-insoluble active pesticide compounds;
(2) Pesticide nano-dispersion with good water dispersity can be prepared using cellulose nanocrystal as the carrier;
(3) Cellulose aerogel beads possess faster pollutants adsorption rate than monolithic cellulose aerogel;
(4) The recovered water pollutants can be used as nutrients for promoting plant growth;
(5) Super amphiphilic cellulose aerogel can be synthesized for both oil-in-water and water-in-oil emulsions separation.

Research objectives:

(1) Synthesis and characterization of amphiphilic cellulose nanocrystals by grafting aminated polystyrene on its reducing end via reductive amination reaction. Its capacity as an

emulsifier to stabilize oil-in-water emulsions for the encapsulation of a model hydrophobic compound, i.e. Nile red was evaluated.

(2) Preparation of organic solvent- and surfactant-free pesticide nano-dispersion using cellulose nanocrystals as carriers, where the preparation conditions and pest control efficiency will be evaluated.

(3) Synthesis and characterization of aminated and carboxylated cellulose aerogel beads for heavy metal ions removal. The adsorption performance of aerogel monolith and beads will be compared.

(4) Synthesis of ambient amphiphilic and underwater super-oleophobic for oil-spill recovery as well as emulsion droplets separation.

(5) Explore the potential of functionalized cellulose aerogel as a platform for water and nutrient capture and delivery to promote plant growth.

1.3 Thesis outline

The thesis comprises 8 chapters. Chapter 1 introduces the environmental pollutions caused by conventional pesticide formulation and wastewater discharge. It also introduces the research objectives and outline of the thesis. Chapter 2 consists of a detailed literature review covering the background information of commercial pesticide formulation, cellulose nanomaterials (CNs) preparation and property, CNs as Pickering emulsifiers, CNs as drug carriers, and the application of CNs in crop protection as well as in water treatment. The results from all the research work conducted in this doctoral research are reported in the manuscript format and they are described in Chapter 3 through Chapter 7. Specifically, Chapter 3 reports on the synthesis of an amphiphilic cellulose nanocrystals through reductive amination reaction at its reducing end, and its capacity as a Pickering emulsifier for hydrophobic pesticide encapsulation was investigated. Chapter 4 provides a scalable and novel solution to prepare organic solvent- and surfactant-free pesticide nano-dispersion using cellulose nanocrystals as carriers. Its pest control efficiency was evaluated in both laboratory and field trial experiments. Chapter 5 to Chapter 7 focuses on the pollutant removal from wastewater using aerogels prepared using cellulose nanofibrils (CNFs). Chapter 5 and Chapter 6 report on the synthesis of aminated and carboxylated cellulose aerogels for the capture of heavy metal ions (such as Cu^{2+}) respectively. Chapter 7 describes and discusses an ambient amphiphilic and underwater super- oleophobic carboxylated cellulose aerogel for oily wastewater treatment including spilled oil recovery and emulsified oil droplet removal, and for

emulsified water droplet removal from oil. In addition, the potential of the aerogel as water and nutrient capture and delivery platform for promoting plant growth was explored. Lastly, Chapter 8 summarizes the major conclusions and contributions of this research work along with the recommendations for future studies.

Chapter 2* Literature review

2.1 Commercial pesticide formulations

As most of the pesticide active ingredients (AI) are insoluble in water, auxiliary ingredients, such as solvents, surface active compounds, and stabilizers are used to prepare the pesticide formulation. Commercial pesticide formulations typically consist of: emulsifiable concentrates (EC), suspension concentrates (SC), soluble concentrates (SL), capsule suspension (CS), wettable powders (WP), water-dispersible granules (WG), granules (GR), tablets (TA), etc. The specific format is determined by the property of AI, for example, its solubility in organic solvents and its toxicity to non-target organisms. Each formulation has its advantages and disadvantages, and the general components, characteristics, and preparation process of the most widely used formulations such as EC, SC, WP and WG are reviewed.

Emulsifiable concentrates (EC)

EC is a concentrated oil-in-water emulsions consisting of an organic solvent (e.g., toluene and xylene) with the solubilized AI and large amounts of surfactants (e.g., alkylphenol ethoxylates). The solvent type determines the odor, viscosity, flammability and potential phytotoxicity of the formulation. Upon dilution, EC forms oil-in-water emulsions, where creaming and oil droplets coalescence are commonly observed during application. Due to the presence of toxic solvents, ECs may be more phytotoxic to plants than other types of formulations, especially for active ingredients that are intended to remain on the leaf surface and not to penetrate plant tissues.

Suspension concentrates (SC)

A SC formulation usually contains milled AI particles suspended in water with the aid of suspension agents to prevent the AI particles from settling. To increase the water dispersity of AI particles, wetting agents are required as most AIs are hydrophobic. The SC formulation generally possesses high viscosity to prevent phase separation. Upon dilution in water, AI particles tend to settle in the tank bottom due to the reduced concentration of suspension agents and their micro-size. Therefore, it is critical that agitation be maintained on dilution. Depending on the formulation, the solids can be difficult to resuspend once they have settled.

Wettable powders (WP)

* This chapter is adapted from a manuscript in preparation for a review paper.

WP is a powder pesticide formulation comprising of milled AIs, usually with a carrier, inert fillers, and other additives. As WPs are dry powders, they can be dusty and require proper protection. Upon dispersing in water, WPs form a suspension similar to SC, thus agitation should be maintained during dilution.

Water-dispersible granules (WG)

Water-dispersible granules (WGs) are also dry formulations that are similar with WPs except they consist of larger AI particles and are typically much less dusty. Prior to the application, they are required to be dispersed in water to form a suspension consisting of solid particles. Similarly, adequate agitation must be maintained to prevent the settling of the solids.

2.2 Cellulose nanomaterials preparation and property

2.2.1 Cellulose nanomaterials preparation

Cellulose is a high molecular weight linear polysaccharide containing β-D-glucopyranose units, where the repeating segments are connected via the β-1, 4-glycosidic linkages. Cellulose is an abundant material widely found in wood, plants, tunicates, algae, and bacteria. It is a promising material due to its abundance, biodegradability, and low cost. Cellulose fibers are comprised of alternating tightly packed crystalline regions and loosely packed amorphous regions as shown in Figure 2.1 (A). Such characteristic provides the scientific basis for researchers to prepare CNs. Under chemical, mechanical, or enzymatic treatment, the loosely packed amorphous domains can be partially or completely removed, producing CNFs or CNCs, respectively. As proposed by the Technical Association of the Pulp and Paper Industry (TAPPI), US Department of Agriculture, US Forest Service and various Canadian entities, the classification of CNs can be divided into two groups, namely cellulose nanocrystals (CNCs) and cellulose nanofibrils (CNFs).

The detailed isolation procedure of CNs from biomass have been reviewed by Rajinipriya et al.,[15] García et al.,[16] Mishra et al.,[17] and Moon et al..[21] Generally, CNCs are produced via acid hydrolysis of the cellulose fibers, while CNFs are prepared solely by mechanical disintegration treatment or combined with chemical treatment as shown in Figure 2.1 (B). Using mineral acids, such as sulfuric, hydrochloric, or phosphoric acids treatment, the amorphous regions in the cellulose fibers are disintegrated, leaving behind the crystalline domains, which is generally referred to as CNCs. In recent 5 years, organic weak acids, such as citric acid, maleic acid, oxalic acid, were also reported for the preparation of CNCs. CNCs extracted from plants possess lateral dimensions of 5-10 nm, lengths ranging from 60- 250 nm and thickness of around a few nanometers depending

on the sources. For example, CNCs extracted from cotton possessed a length of 195 ± 35 nm, width of 22 ± 3 nm, and thickness of 6 ± 0.2 nm.[22] In addition, negatively charged ester groups are decorated on CNCs after hydrolysis, which induce electrostatic repulsion between CNC particles, resulting in an excellent colloidal stability. On the other hand, mechanical shearing, such as refining, grinding, microfluidization, intense ultrasonication, high-pressure homogenization and chemical treatment (TEMPO oxidation and acid hydrolysis) are used to prepare CNFs. CNFs contain some amorphous domains, and their dimension differ widely depending on the methodology and treatment process. For example, Zimmermann et al. reported the use of a microfluidizer (Microfluidics Inc., USA) for CNF production. Sulphite pulp suspensions were first treated by an ultra-turrax (FA IKA) at 24,000 rpm for 8 h, and then subjected to microfluidization at a pressure of 1000 bar for 60 min. Finally, CNFs with a diameter of 20-100 nm and length of several tens of micrometers were obtained.[23] In another study, Isogai et al. prepared CNFs from native wood celluloses through TEMPO oxidation, yielding individual nanofibers with a width of 3-4 nm and length of several microns.[24] Typically, CNF have a diameter of 5-50 nm and a length of few micrometers.[25]

2.2.2 Properties of cellulose nanomaterials

In addition to sustainability and biodegradability, CNs also possess favorable physical and chemical properties. As nanoscale materials, CNs exhibit superhydrophilicity, large surface area, high aspect ratio, excellent colloidal stability (refers to CNCs), and high modulus. Besides, various modifications can be performed on CNs due to the abundance of surface hydroxyl groups. Moon et al. summarized the commonly used approaches for the surface modification of CNs. These strategies can be categorized into 3 distinct groups: (1) decoration of functional moieties on CNs during their preparation process as shown in Figure 2.1 (C), (2) physically adsorb modifying agents onto the surface of CNs as shown in Figure 2.1 (D), and (3) chemically grafting reagents to the surface of CNs as highlighted in Figure 2.1 (E).[26] These advantages can be used for the design of systems for many different applications, and this topic will be discussed in section 2.3 to section 2.7.

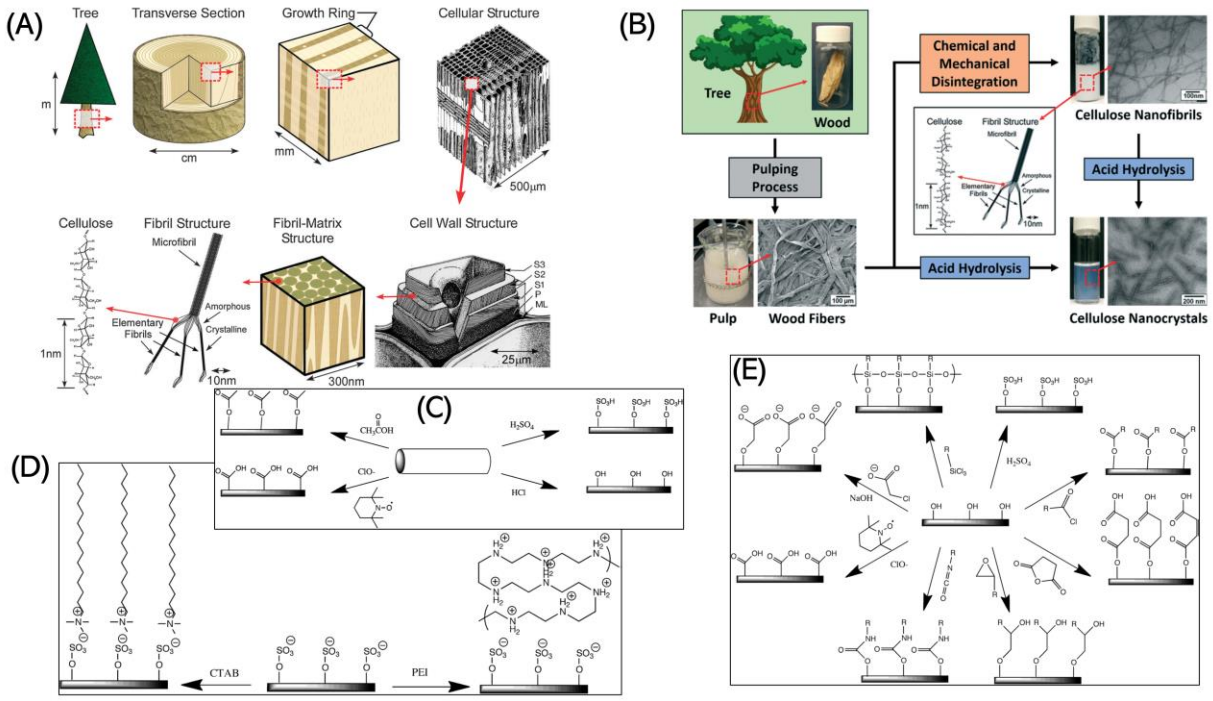

Figure 2.1 (A) Schematic of the tree hierarchical structure.[27] (B) Schematic diagram showing the process of extracting CNs from trees along with micrographs of wood fibers during the various stages of the extraction process.[28] Surface modification on CNs by the extraction method (C), by physical adsorption (D), and by chemically grafting (E).[26]

In addition to surface functionalization, there are several reports on the end-modification of CNCs in the recent 10 years. The phenomenon that the hemiacetal ring form of glucose is in equilibrium with an open-chain aldehyde form as shown in Figure 2.2 (A), so called mutarotation, was discovered at the beginning of the 20th century.[29] Although such characteristic has been known for decades, the end-modification on CNCs that utilizes the reducing end (reactive aldehyde group) have only emerged recently, because of analytical challenges associated with the low concentration of the modified groups. It is known that the cellulose chains of native cellulose are aligned in parallel, thus the reducing end groups in CNs are at the same terminal. To date, reducing end modification is mainly performed on CNCs for interface stabilization, fluorescent labelling, composite reinforcement, and self-assembly regulation as seen in Figure 2.2 (B).[30] The most commonly used approaches for the modification of the aldehyde end-group are summarized in several studies. These methods can be classified into 4 types: (1) hydrazine, hydroxylamine, and thiosemicarbazide ligation,[31] (2) reductive amination,[32] (3) Pinnick oxidation or followed by

amidation,[33,34] and (4) Knoevenagel condensation.[35] The corresponding chemical reaction scheme is shown in Figure 2.2 (C).

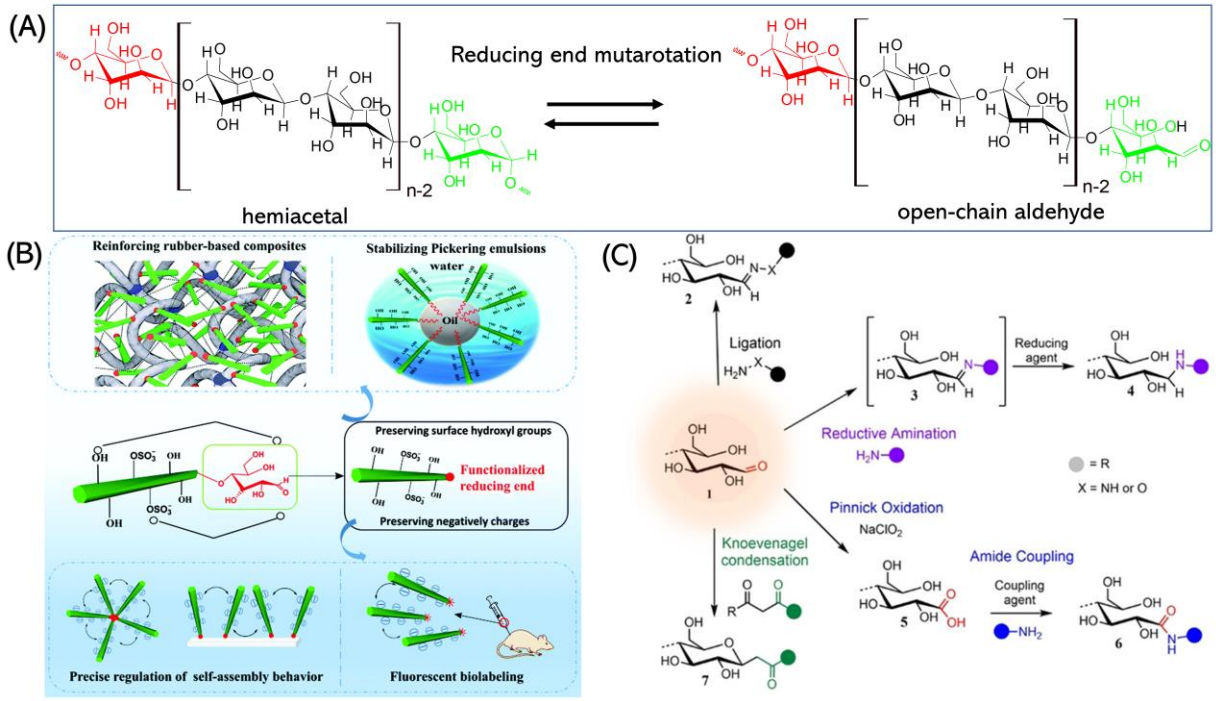

Figure 2.2 (A) Open chain mutarotation phenomenon of cellulose chain, (B) several reported applications of reducing end-modified CNCs,[30] (C) most commonly used approaches toward modifying reducing aldehyde group on CNCs.[29]

2.3 Cellulose nanocrystals as Pickering emulsifiers

Emulsions are widely used in cosmetic, food, and agriculture industries. Generally, surfactants are necessary to reduce the oil and water interfacial tension for preparing emulsions. Since the first report on Pickering emulsion by Pickering in 1907, micro- or nanoparticles have been widely used as "Pickering emulsion" stabilizers. With the rapid development of materials science, more and more types of solid particles beyond silica nanoparticles were developed as stabilizers. Also, additional modifications can be performed on solid particles to impart multi-functions compared to surfactants. Moreover, Pickering emulsions possess superior stability and low toxicity compared to classical emulsions.[36]

To yield a stable Pickering emulsion, the key factor is to prepare solid particles with wettability towards both oil and water. Under partial wetting conditions, the contact angle of the air or oil/

water interface with the solid (termed θ) as shown in Figure 2.3 (A) determines the type of emulsion for a given solid particle. For hydrophilic particles with 20° < θ < 90°, the major part of the particle would immerse in the aqueous phase, inducing the formation of an oil-in-water (o/w) emulsion. On the other hand, hydrophobic particles with 160°> θ > 90° would produce water-in-oil (w/o) emulsions. Theoretically, particles with an angle of 90° at the oil-water interface possess the maximum desorption energy according to Eq. (2.1),

$$E = \pi r^2 \gamma_{ow} (1 \pm cos\theta)^2 \qquad (2.1)$$

where γ_{ow} is the interfacial tension between oil and water; r is the radius of solid particle; θ is the the contact angle of the interface with the solid (measured through the aqueous phase).

From the equation, we conclude that the particle radius has a critical effect on the adsorption energy, i.e., larger particles possess higher adsorption energy. As an example, the adsorption energy of 10 nm spherical silica nanoparticles at the toluene-water interface (γ_{ow} = 36 mN·m^{-1}) with a contact angle of 90° is 2750 kT, which is multiple orders of magnitude larger than thermal energy kT (4×10^{-21} J at 293 K). In contrast, surfactant molecules usually have a radius less than 0.5 nm, which results in an adsorption energy of several kT. Thus, the adsorption of solid particles on the interface is considered irreversible, while surfactants could adsorb and desorb at a relatively short time scale.[37] In recent years, particles with different shapes such as fibers, cubes, rods were also used as Pickering stabilizers. Compared with spheres, fibers and rods possess high aspect ratio, which could connect to each other and form a stable coverage on emulsion droplet at a higher concentration. The phenomenon was observed by Kalashnikova et al. who prepared cellulose nanorods with aspect ratios between 13:1 and 160:1.[38]

Cellulose nanomaterials (CNs) exhibit inherent advantages as Pickering emulsion stabilizers due to its bio-renewability, bio-degradability, high aspect ratio and ease of functionalization. Moreover, it is also reported by Kalashnikova et al. that CNC possesses hydrophilic planes ((010)β/(110)α and (1–10)β/(100)α), and hydrophobic edge plane ((200)β/(220)α).[39] The hydrophobic face could oriented to the oil phase while the hydrophilic faces stayed in the water phase as shown in Figure 2.3 (B). Pristine CNC extracted from bacterial cellulose and cotton cellulose with surface charges less than 0.03 e/nm^2 could stabilize hexadecane in water emulsions as seen from Figure 2.3 (C). These adsorbed CNCs functioned as physical barriers, preventing the coalescence of the droplets. It was reported that the surface charge played a critical role in emulsion preparation. Strong repulsion between CNC particles were generated when its surface charge density exceeded 0.03

e/nm^2. To reduce the surface charged density, they prepared de-sulfated CNCs by treating sulfated CNCs with 2.5 N HCl. The surface charge decreased from 0.16 e/nm^2 to 0 e/nm^2 after treatment. The orientation of CNCs at the oil/water interface was confirmed using Small Angle Neutron Scattering (SANS) technique, and the emulsifier thickness was determined from the signal intensity contrast as shown in Figure 2.3 (D). SANS results revealed that the CNCs adsorbed on the oil droplet possessed a thickness of 7 nm, which corresponded to the lateral cross section dimension of the CNC measured oriented to the (200) plane, while the thickness perpendicular to (1-10) and (110) were around 4-6 nm. Besides, the thickness maintained at 7 nm regardless of the CNC concentration, suggesting that the monolayer of the sulfated CNCs were packed on the surface of the oil droplet, while the excess CNCs remained in the water phase. Finally, hexadecane in water emulsion with an average droplet size of around 3 μm was obtained, and the corresponding surface coverage by the CNCs was 85%.[40]

As limited by the surface charge, hydrophilicity, and insufficient wettability in the oil phase, pristine CNCs have limited emulsification capacity for many types of solvents, especially for polar solvents such as toluene. It is known that interfacial tension decreases with increasing oil polarity, becoming negligible when the oil and water is completely miscible. From Eq. (2.1), one can predict that the adsorption energy decreases with increasing oil polarity. Thus, the introduction of hydrophobic domains on the surface of CNCs is an effective strategy to drive the solid particles towards the oil phase to increase its contact angle with the interface, which enhances the adsorption energy to form stable oil-in-water emulsions. Recently, hydrophobic modifications of CNCs have been developed for stable Pickering emulsions preparation. For example, Le et al. grafted octenyl succinic anhydride on CNCs via esterification, and the static water contact angle of CNCs increased from 56.0° to 80.2° after hydrophobic modification, which allowed the modified CNCs to be partially wetted by both phases for food-grade oil tripropionin and tributyrin stabilization.[41] In another study, Hiranphinyophat et al. decorated a bio-compatible and bio-degradable thermo-responsive polymer poly[2-isopropoxy-2-oxo-1,3,2-dioxaphospholane] (PIPP) on CNCs via ring-opening polymerization of cyclic phosphoester monomers 2-isopropoxy-2-oxo-1,3,2-dioxaphospholane (IPP). The obtained CNC-g-PIPP functioned as an effective emulsifier at 4 °C for the preparation of heptane-in-water emulsions, while the phase separation was observed when the temperature exceeded its low critical solution temperature (45°C).[42] Other methods, such as

acetylation, carboxymethylation, surfactant coating, ATRP polymer grafting were also widely adopted to prepare hydrophobically modified CNCs.

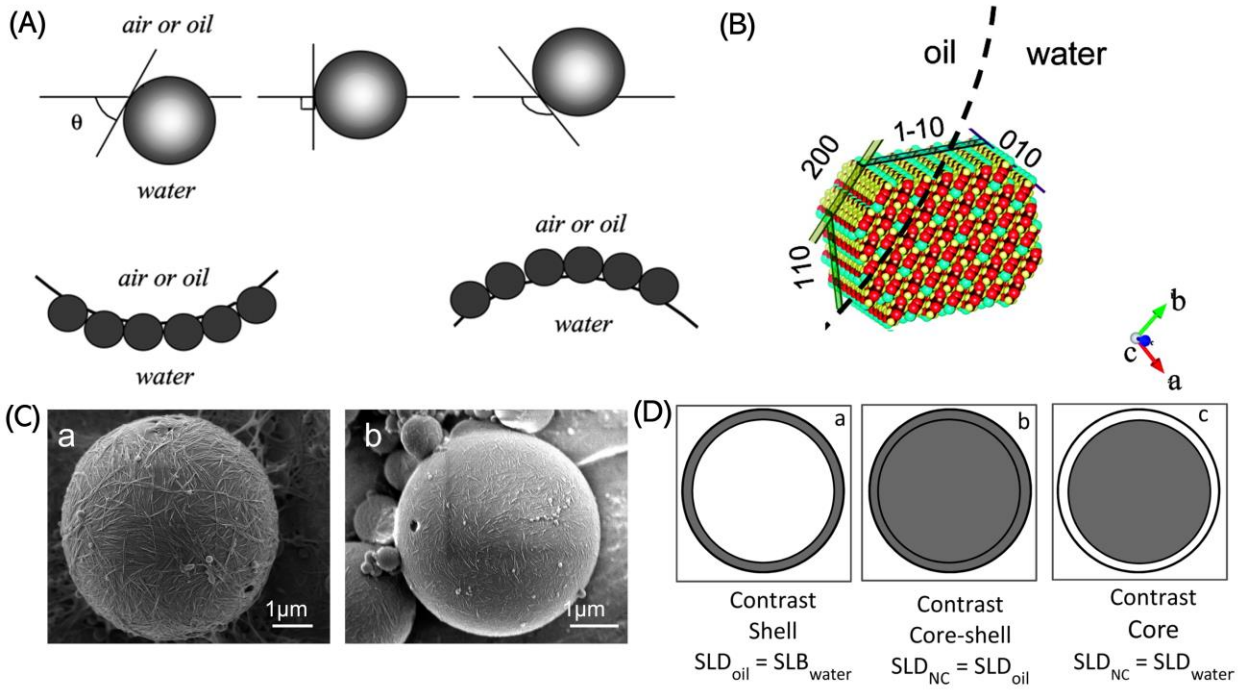

Figure 2.3 (A) Schematic illustration of contact angle at the air/oil interface with solid particles (measured through water phase) less than 90° (left), equal to 90° (middle), and greater than 90° (right), and the corresponding emulsions formed.[37] (B) Schematic illustration of the orientation of cellulose nanocrystals at the oil/water interface with the hydrophobic edge (200) towards at the oil phase.[39] (C) SEM images of polymerized styrene/water emulsions stabilized by (a) bacterial cellulose nanocrystals (BCN) and (b) cotton cellulose nanocrystals (CCN).[39] (D) A concept demonstration of the CNC layer thickness measurement by SANS.[40]

2.4 Cellulose nanocrystals as carriers

As introduced earlier, CNCs possessed bio-compatibility, low toxicity, high surface area, and excellent colloidal properties. Its use as carriers for drugs, dyes and inorganic particles were reported in recent years.[43–46] The carriers can be a hydrogel, a complex particle formed by CNC and other polymers, a film, a membrane, or CNC itself. Here, we summarize the recent key progress of using CNCs solely to conjugate/load organic compounds in dispersion form. In 2011, Jackson et al. first reported the use of CNCs as a drug delivery excipient. These CNCs bound large quantities of water-soluble, ionizable drugs tetratcycline and doxorubicin by opposite charge

interaction, achieving around 20 wt% drug loading capacity (0.5 mg tetratcycline on 2 mg CNCs). For loading hydrophobic anticancer drugs, such as docetaxel, paclitaxel, and etoposide, cetyl trimethylammonium bromide (CTAB) was used to decorate hydrophobic domains on CNCs. Around 200 μg hydrophobic drug were bound on 2 mg CNCs *via* hydrophobic interaction.[47] Hydroquinone is a hydrophilic drugs that could inhibit the production of melanin and eliminate the discolorations of skin. Taheri et al. introduced cellulose nanocrystals as suitable carriers for the delivery to skin. A maximum 79.32% binding efficiency was obtained when 1.1 mg hydroquinone was added to 2 mg of cellulose nanocrystals.[48] In 2017, a detailed study on CNCs as carriers for water-soluble drug was reported by Wijaya et al., who extracted CNCs from passionfruit peels through sulfuric acid hydrolysis to conduct the binding experiments. Its adsorption for tetracycline, a pH-dependent amphoteric antibiotic, was investigated at 30 ℃ in various pH conditions (3, 4, 5, 6, and 7). A maximum adsorption capacity of 129.5 mg/g was achieved at pH 3. It's known that the tetracycline molecules exist as cations at pH < 3.3, as zwitterions at pH between 3.3-7.7, and as anions at pH > 7.7. In addition, hydrophobic interaction between the CNCs and tetracycline increased with decreasing pH, which also contributed to the adsorption capacity.[44]

The loading capacity of CTAB modified CNCs for water-insoluble drugs was investigated by Qing et al., who coated a cationic surfactant cetyltrimethylammonium bromide (CTMAB) onto spherical CNCs via electrostatic interaction. Adsorption isothermal studies indicated that the adsorption of CTMAB on CNCs followed the Freundlich model, which suggested a multi-molecular layer adsorption. Kinetics study revealed that the adsorption followed the pseudo-second-order kinetics process. The CTMAB coated CNCs possessed a stable and good dispersion in water, which were further used as carriers for two water-insoluble anticancer drug luteolin (LUT) and luteoloside (LUS). Moreover, the drug loading and release performance of CTMAB-coated NCC were studied using as model drugs. The hydrophobic CTMAB could bind hydrophobic drugs and resulted in a loading capacity of 12.9 ± 1.5 and 56.9 ± 0.9 mg/g for LUT and LUS, respectively. In addition, the authors also attributed the drug loading capability to the possible electrostatic attraction between positive CTMAB and negative charged drug particles. Both LUT and LUS showed a sustained release manner at 37℃ in PBS buffer solution over one day observation.[49]

The performance of pristine CNCs for loading hydrophobic compound was investigated by Sun et al. and Tang et al. in 2014 and 2017, respectively. A hydrophobic spirooxazine (SO)-based dye

was loaded to CNCs prepared by sulfuric acid hydrolysis. Nano scaled SO dyes were uniformly distributed on CNCs as shown in Figure 2.4 (A), which significantly improved the photochromic efficiency of SO. However, the loading capacity and adsorption mechanism of CNC for hydrophobic SO dyes were not examined.[45] In the study reported by Tang et al., pristine CNCs prepared by sulfuric acid hydrolysis was used as carriers for dispersing a hydrophobic antioxidant, 20 (R)-ginsenoside Rg3, to improve its free radical scavenging property. Similarly, the surface charge of 20 (R)-ginsenoside Rg3, the loading capacity of CNCs and adsorption mechanism were also not discussed.[50] Nevertheless, their researches have demonstrated that pristine CNCs without surface modification could be an effective carrier for loading and dispersing water insoluble compounds to improve their water dispersity and solubility. These findings provide insights for the administration of drugs with low water solubility. It has been previously reported that compounds, such as CTAB and PEI possess cytotoxicity that could led to adverse effects on cell survival, viability, and proliferation. In contrast, CNCs itself exhibited very low cytotoxicity, which is very promising as drug vehicles. [43,51,52]

2.5 Cellulose nanomaterials for pesticide encapsulation

With the advancement of nanotechnology, nanomaterials have been incorporated in many systems due to their size, high surface area, as well as attractive mechanical properties.[53] Nanomaterials are widely used to design systems for drug delivery, which can also be used for pesticide delivery.[54] As discussed earlier, CNs are extracted from bio-mass based materials, they are sustainable, renewable, and bio-degradable. They are very promising materials for the fabrication of pesticide delivery systems to reduce the carbon footprint. Encapsulation technology is very effective to reduce AI loss, improve handling safety, prevent AI degradation, and control AI delivery.[55] This section summarizes systems prepared using CNs for pesticide encapsulation. Based on the nomenclature, the systems can be classified into hydrogels, emulsions, capsules, dispersions, and other types of systems.

2.5.1 Cellulose nanomaterial-based hydrogels for pesticide encapsulation

Hydrogels possess highly porous structure that allows the loading of compounds into the matrix. Therefore, it is very promising to load pesticides, which could be released from the matrix at a rate that is dependent on the diffusion coefficient upon swelling. For example, Nörnberg et al. incorporated 5 wt% cellulose microfiber into alginate solution, and the mixture was further crosslinked with $CaCl_2$ to prepared hydrogel beads.[56] The addition of CMF increased the herbicide

imazethapyr (IMZ) encapsulation efficiency (>85%) by reducing the crosslinking density within the beads network, which generated more vacant spaces for loading IMZ molecules. Release experiments in water showed that the beads could prolong the herbicide release by up to 30 days.

Bacterial cellulose (BC) is produced by bacterial species, and it exhibits high water holding capacity, and gel-like character. BC has similar chemical composition to the plant cellulose, and it possesses higher purity, crystallinity, and water absorbance. Alonso-Díaz et al. anchored Ag NPs in bacterial cellulose by in-situ thermal reduction under microwave irradiation to construct a slow release of silver nanoparticles hydrogel patch (BC-AgNPs) for pathogens control.[57] The hydrogel texture exhibited excellent adherence to *N. benthamiana* leaves as shown in Figure 2.4 (B), reducing nanoparticles loss and roll-off. The authors also assessed the *in vitro* antibacterial and antifungal properties of the hydrogel patch against the bacteria *Escherichia coli* and two agro-economically relevant pathogens: the bacterium *Pseudomonas syringae* and the fungus *Botrytis cinereal* (a causal agent of gray mold disease). Results showed that the BC-AgNPs exhibited positive inhibitory effect towards *Escherichia coli* and inhibited *Botrytis cinereal* colonization and spore production. Besides, the authors also studied the *in vivo* inhibition of the BC-AgNPs in *Nicotiana benthamiana* and tomato leaves infected by *P. syringae*. The positive inhibitory properties were proven by quantitative gene expression profiling of various plant defense marker genes (Pathogenesis-related a1, Homebox 1 and Harpin-induced gene) and reduced production of reactive oxygen species (H_2O_2).

2.5.2 Cellulose nanomaterial-based emulsions for pesticide encapsulation

As introduced in Section 2.1, the production of EC involves organic solvents and synthetic surfactants, which generate adverse effects to the environment and non- target organisms. In recent years, many studies have demonstrated that Pickering emulsions (emulsions stabilized by solid particles) possessed better thermal stability and required less emulsifier compared to surfactants stabilized emulsions due to their irreversibly adsorption at the oil/water interface.[58,59] Cellulose nanomaterials have been widely used as Pickering emulsion stabilizers in food and oil recovery industry, showing good promise to replace traditional surfactants in agrochemical formulations.

Essential oil (EO) is plant-derived compound that display a broad-spectrum biological activity such as anti-repellency, anti-germination, fungicidal, antibacterial, etc. EO mainly consist of terpenes, terpenoids, and rarely nitrogen- and sulphur-containing compounds. In agriculture, EO has been used as pest repellent and anti-bacterial agents.[58] Its mode of action is through passing

the cell wall and penetrating between the fatty acid chains of the lipid bilayer, making the cell membrane more permeable. Eventually, it can cause cytoplasm leakage, cell lysis and cell death, thus inhibiting the sporulation and germination of spoilage fungi. On the other hand, some studies shown that EO can play a role in plant defense mechanisms by production of secondary metabolites such as alkaloids, benzoxazinoids, phenolics, and terpenoids for self- protection. Some typical examples of EO are cinnamon, citronella, lemon grass, garlic, thyme, eugenol, and turpentine. Compared to synthetic agrochemicals, EOs can reduce the environmental risk and are exempted from registration along with extensive toxicological and environmental tests. However, EO is volatile, which is not favorable for long term storage. Therefore, techniques such as encapsulation are required to formulate stable EO based products.[60]

Shin et al. encapsulated thyme white essential oil, which composed of p-cymene (38.14%), thymol (35.82%), limonene (7.93%), pinene (7.22%), and linalool (3.57%) using sulfate CNC (degree of sulfate substitution was 0.40) as emulsifier.[61] The successful EO encapsulation was evident by confocal microscopic images as shown in Figure 2.4 (C).The droplet size decreased with increasing CNC content, which in turn enhanced emulsion stability as demonstrated by the turbidity and rheological tests. Also, the antimicrobial activity against *Escherichia coli* and *Staphylococcus aureus* of the emulsion were investigated. The Pickering emulsion exhibited positive results with a lower minimal inhibitory concentration (MIC) and minimum bactericidal concentration (MBC) values when compared to the pure EO counterpart. As seen from Figure 2.4(D), the emulsion possessed faster and longer bactericidal activity than pure EO due to the increased permeability towards bacterial as well as the densely absorbed CNC shell that reduced the volatility of EO. At last, the emulsion shown larvicidal activity against Asian tiger mosquito *Aedes albopictus.*

In another study, Mikulcová et al. conducted a more detailed study using nanocellulose (CNC and MFC) as emulsifier for three types of antimicrobial EO (cinnamaldehyde, eugenol and limonene) encapsulation.[62] The effects of nanocellulose type, EO type and content on the emulsion antibacterial activity were investigated. In terms of emulsion droplet size, 0.5 wt% CNC could yield smaller droplet size (14-34 μm) compared to 0.5 wt% MFC (27-51 μm). This is because the shorter length CNC could accommodate a higher curvature and form a dense layer on the droplet surface, while longer length MFC lack such flexibility. Oil polarity is another factor affecting the droplet size, where oil with lower polarity yielded smaller droplet size. Thus, smaller droplet sizes

were observed in limonene and cinnamaldehyde emulsions. The antibacterial activity was mainly governed by oil type, and they followed the order cinnamaldehyde > eugenol > limonene. Cellulose type only played a minor effect on the antibacterial activity when higher oil content was used. At lower oil content, MFC stabilized emulsions displayed slightly better inhabitancy, however, the authors did not give a clear explanation for such phenomenon. Besides, the emulsions displayed stronger inhibition efficiency on Gram positive bacteria than Gram negative species. The CNC and MFC stabilized emulsions exhibited good storage stability of 8 weeks and they could be effective in protecting the EO from oxidation and volatilization.

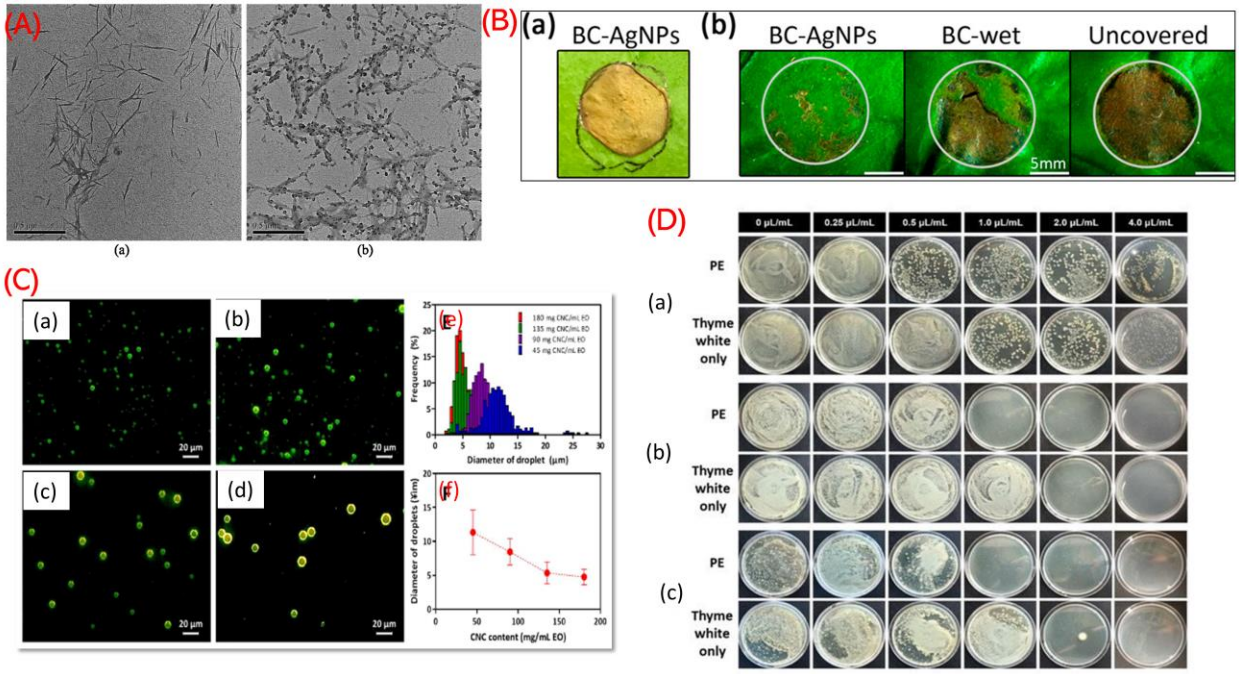

Figure 2.4 (A) TEM images of CNCs before (a) and after loading SO dyes (b).[45](B) Antibacterial and antifungal activity of BC-AgNPs in N. benthamiana against P. syringae. (a) BC-AgNPs adhered to a N. benthamiana leaf. (b) Three-week-old N. benthamiana plants were infiltrated with P. syringae (DC3000) at an O.D.600 of 0.0008. After infiltration, infected areas were covered with different treatments: BC-AgNPs, BC, or left uncovered. [57] (C) Size distribution of CNC/EO PE prepared at the different contents of CNCs.[61] (D) Antimicrobial activity of CNC/EO PEs and thyme white only against E. coli, The extracts were diluted 1000 times and spread on an agar plate after the storage for (A) 0 d, (B) 10 d, and (C) 25 d. [61]

2.5.3 Cellulose nanomaterial-based capsules for pesticide encapsulation

Designing of microcapsule for AI encapsulation is highly desirable as it ensures safer handling, reduces AI leaching and early degradation. Pickering emulsion can be used as template to prepare microcapsule. For example, Tang et al. developed polydopamine (PDA) microcapsule templated by cinnamoyl chloride modified cellulose nanocrystals stabilized W/O Pickering emulsion for essential oil (turpentine) and herbicide (2,4-D) encapsulation.[63] This technique eliminated the template etching process and the use of synthetic surfactant and achieved a 2,4-D encapsulation efficiency of 74.9% when 1200 mg dopamine was used. The PDA microcapsule exhibited sustained release of the herbicide and showed potential leaf affinity as well as UV resistance due to the adhesive PDA shell and UV absorption capacity of cinnamoyl moiety. In another study, Kadam et al. modified CNF by stearic acid to prepare surfactant free W/O and O/O emulsions, which functioned as templates to prepare polyurethane microcapsules through interfacial polycondensation.[64] The hydrophobicity of the modified CNF was demonstrated by its water contact angle of 112.2°. Such hydrophobic CNF could be well dispersed in paraffin oil as the continuous phase. Then, the dispersed phase containing a water sensitive insect repellant agent N, N-diethyl-3-methylbenzamide (DEET) and monomer toluene- 2, 4-diisocyanate (TDI) was added to the continuous phase under vigorous stirring to produce emulsions. Afterwards, ethylene glycol (EG) was added to the mixture to conduct the interfacial polycondensation with TDI. The presence of CNF in the microcapsule wall greatly decreased DEET release rate due to its barrier effect.

2.5.4 Cellulose nanomaterial-based dispersions for pesticide loading

Compared to microscale emulsions and capsules, pesticide formulation in nanoscale can greatly facilitate its bioavailability (especially for poorly water-soluble pesticides) due to the enhanced surface area and better leaf affinity. Nano-suspension or nano-dispersion is an important type of nano- formulations. Different from emulsifiable concentrate (EC), nano-dispersion has no organic solvents in the final product, which can reduce environmental risk and enhance safety to end users and non- targeted organisms. Also, unlike suspension concentrate (SC), whose AI particles are generally produced by top-down approach, nano-dispersion usually produce AI nanoparticles by bottom-up approach. SC also requires mixing surfactants to stabilize the AI NPs, while the AI NPs in nano-dispersion were often loaded onto the nano-carriers. NPs, such as silica, metal, metal oxides, lipids, carbon, and polymeric nanoparticles are some common nano-carriers for agrochemicals.

In recent years, CNCs display advantages as drug carriers in food, cosmetic, biomedical and nutraceutical applications. However, the exploration of CNCs as agrochemical carriers was less reported. CNC can be a very competitive candidate to formulate water-based pesticide nano-dispersions considering its excellent colloidal stability due to its high negative surface charge and nano dimension. Another advantage of CNC is its rod-shape particle. In general, CNC has an average length of around 200 nm and width of 10 nm, hence it possesses a moderate to large aspect ratio. The rod-like morphology will prevent the rolling off from leaves, thereby offering good foliar retention properties. It is widely accepted that the size of the pesticide particle significantly affects its bioavailability and efficacy. CNC as carrier for pesticide and a length of around 200 nm, imparts significant advantage compared to the micro-/bulk pesticide particles. For example, Elabasy et al. loaded a water-soluble pesticide thiamethoxam (TMX) on CNC by emulsion solvent evaporation method as shown in Figure 2.5.[65] Briefly, TMX and CNC were mixed with methylene chloride as the organic phase, then dropped to the water phase containing PVA under stirring to form O/W emulsions. The mixture was subjected to solvent evaporation to produce TMX loaded CNC nanosuspension. TGA results and UV analysis revealed that the loading efficiency and entrapment efficiency of TMX was 18.7% and 83.7 ± 1.8%, respectively. The release study of TMX from CNC indicated a sustained release behavior, achieving 12.73% in 72 h. The slow-release rate was due to the hydrogen bond interaction between CNC and TMX. The bioassay test against *Phenacoccus solenopsis* was conducted by a leaf dipping method. Leaves were dipped in the nano-formulation or control formulations containing different concentrations of TMX, and 10 *P. solenopsis* second-instar nymphs were transferred to the dried leaves. The TMX loaded CNC nano- formulation exhibited lower LC50 than the technical and commercial formulation due to the smaller particle size and larger surface area.

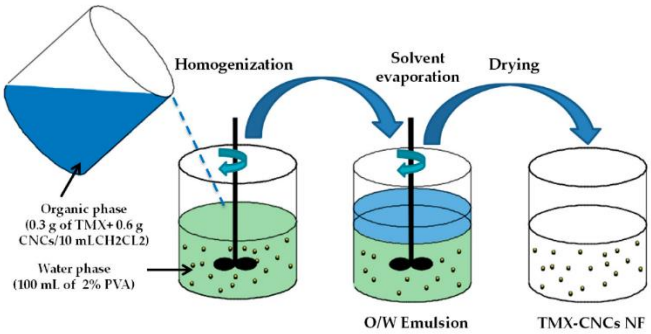

Figure 2.5 Schematic description of the preparation of the thiamethoxam (TMX)-loaded cellulose nanocrystals (CNCs).[65]

In another study, hexadecyl trimethyl ammonium bromide (CTAB), an efficient anti-microbial surfactant, was coated on CNC *via* electrostatic interaction for oomycete control.[66] Atomic force microscope (AFM) analysis indicated that the diameter of CNC increased from 21.6 ±1.8 nm to 32.5 ±1.6 nm after being coated with CTAB. Besides, a change of zeta potential from -39.4 mV to +7.7 mV was observed after the coating with CTAB because of the quaternary ammonium head groups. The antimicrobial activity was achieved through the adsorption of quaternary ammonium moiety of CTAB onto the cell surface, which enabled its hydrophobic long chain to interact with the phospholipid bilayer of the cell membrane. Such interaction could destroy the self-assembled structure of the pathogeny cell membrane, leading to cell death. Enhanced anti-oomycete efficiency was observed by increasing CTAB@CNC concentration or CTAB coating density. The particle could also prevent infestation when applied on the leaves of pepper achieving a disease index as low as zero when CTAB density was greater than 3.96×10^{-2} nmol/cm^2.

2.5.5 Other cellulose nanomaterial-based systems for pesticide encapsulation

To prepare an anti-UV membrane for controlled biopesticide potenone and chlorogenic acid release, microcrystalline cellulose was dissolved in N, N-dimethylacetamide (DMAc)/ LiCl mixture to yield a homogenous cellulose solution. An isocyanate crosslinker synthesized by toluene di-isocyanate (TDI) and an excellent UV absorber 4,4'-dihydroxy benzophenone (DHBP) was added to the cellulose solution to produce mechanically robust, hydrophobic and anti-UV cellulose membrane.[67]

Patil et al. mixed CNF derived from sugarcane bagasse in starch with urea-formaldehyde granules to encapsulate a well-known mosquito repellent agent dimethyl phthalate (DMP).[68] The CNF-reinforced starch granules displayed much higher water uptake capacity than granules without CNF, which was attributed to the increased hydrophilicity after the addition of CNF. It is worthy to note that the incorporation of CNF could reduce initial burst release of DMP, which enhance the overall release amount. The authors indicated that the addition of CNF could reduce the network porosity, thus inhibiting the initial release. On the other hand, the overall increase of the DMP release in CNF incorporated granule was due to water induced swelling.

The barrier effect of CNF to reduce the pesticide release rate was also reported by Mattos et al., who blended CNF with nano-SiO_2 isolated from *Equisetum arvense* (horsetail) for tebuconazole loading.[69] The added CNF was able to trap the silica nanoparticles in a compact structure. Moreover, CNF possessed affinity towards tebuconazole due to the hydrophobic interaction

between the non-polar moieties from tebuconazole and hydrophobic backbone of CNF. A short-term slow-release rate was achieved by the dual effects of CNF.

2.6 Cellulose nanomaterials for aerogels preparation

Since the first report of silica aerogel by Kistler in 1931 using super-critical drying method, many types of aerogels have been synthesized from the advancement of material science and drying techniques. In the beginning, the terminology "aerogel" was reserved for porous materials prepared by supercritical drying, while porous materials obtained by ambient evaporation and freeze-drying were referred to as xerogels and cryogels, respectively. However, the definition of aerogel has shifted from drying method to pore size in recent years. At present, any lightweight, sol- gel derived porous materials with predominantly mesoporous (pore size between 2 and 50 nm) pores are considered as an aerogel. Recently, sol-gel derived porous materials that possess macroporous (>50 nm) pores were also called as aerogels, which are also appropriately labelled as foams or sponges.[70] Therefore, we adopt "aerogel" to describe porous materials that are sol-gel derived and possess predominantly mesoporous or macroporous structure throughout the thesis.

Aerogels have attracted significant interest due to their unique characteristics, such as high porosity, low density, large surface area and low thermal conductivity. They have demonstrated excellent advantages as absorbents, heat insulators, scaffolds, and sensors. Currently, research activities on aerogel synthesis are motivated by using sustainable precursors rather than traditional polymer derived from petroleum products. As the most abundant and sustainable bio-synthesized material, cellulose fibers have attracted intense interests for aerogel preparation. In addition, aerogels prepared by cellulose fibers exhibit better mechanical property than silica based inorganic aerogels. [71] CNs expose more hydroxyl groups and larger surface area than raw cellulose fibers, and they are very promising for designing functionalized aerogels through surface modification. In the following sections, the advances in the preparation process, drying methods, commonly used pore forming templates, and aerogel beads preparation based on cellulose nanomaterials are reviewed.

2.6.1 General preparation process

In general, the preparation of CNs aerogel involves three steps: 1) preparation of CN dispersion; 2) gelation of CN by physical or chemical crosslinking, 3) drying of wet gels. In some situations, only step 1) and 3) were performed to produce pristine CN aerogels, which were subjected for post-modification treatment to obtain robust and functionalized aerogels. Physical crosslinking

induced gelation includes hydrogel bonding interaction, ionic/electrostatic interaction, reversible bonding, and self-assembly, while chemical crosslinking formed irreversible covalent bonds between the cellulose chains. For example, Zheng et al. prepared a hybrid physically crosslinked CNF/PVA aerogel by freeze drying, followed by treatment with methyltrichlorosilane *via* a thermal chemical vapor deposition process.[72] Lewis et al. adopted a freeze-thaw method to induce the gelation of CNCs by physical aggregation as shown in Figure 2.6 (A),[73] Dong et al. reported the ionic gelation of carboxylated CNF by divalent or trivalent cations (Ca^{2+}, Zn^{2+}, Cu^{2+}, Al^{3+}, and Fe^{3+}) (Figure 2.6 (B)),[74] Li et al. prepared chemically crosslinked CNF gel network by crosslinking of PEI on CNF with GPTMS as crosslinkers (Figure 2.6 (C)).[75] A drying process is required to displace the liquid with gas to maintain porous network after gelation. The dried product is referred to as aerogel.

2.6.2 Drying methods

2.6.2.1 Ambient drying

During the drying process, the evaporation of the solvent at the gas-liquid interface transmitted to the pore walls can generate capillary pressure, which is caused by the liquid surface tension at the liquid-solid interface that is sufficient to induce structural collapse.[76] As illustrated in (a) of Figure 2.6 (C), the resultant forces on the pore walls in the horizontal direction are not balanced, which ultimately lead to the collapse of the pores. The capillary pressure can be expressed by the Young-Laplace formular in Eq. (2.2)

$$P = -\frac{2\gamma \cos\theta}{r} \qquad (2.2)$$

where γ is the surface tension of the solvent in the gel, θ is the contact angle between the solvent and the pore wall, r is the radius of the pore.

To reduce the capillary pressure, four strategies are adopted for ambient drying based on Eq. (2.2): i) replace water in the wet gels with solvents of low surface tension, ii) increase the pore size to reduce θ, iii) regulate the uniformity of the pores, and iv) increase the pore mechanical strength by crosslinking reaction. For example, Toivonen et al. adopted a solvent exchange process for vacuum filtrated CNF gel to prepare CNF aerogel as shown in Figure 2.6 (D). Water was exchanged with 2-propanol and further to octane, followed by ambient drying, and no lateral shrinkage was observed upon drying from octane.[77] In another work by Li et al., acetone was used to replace water in the wet CNF gel during Soxhlet extraction to decrease the capillary pressure within the

pores, and subjected to ambient drying. The obtained aerogels possessed excellent flexibility and a much higher (4.3 times) specific surface area than that obtained from freeze-drying.[75] However, ambient drying cannot completely prevent the collapse and cracking of the pore structure due to the presence of surface tension of air-solvent interface. In addition, the integrity and porosity of the aerogel is highly dependent on the replaced solvent as well as the replacement time.

2.6.2.2 Supercritical drying

Supercritical drying method is performed under high pressure and temperature conditions based on the supercritical fluid (e.g., carbon dioxide, alcohol, and acetone) principle. Carbon dioxide is commonly used in supercritical drying methods because of its accessible critical temperature and pressure (304 K, 7.4 MPa) and the advantages of low cost and high safety. Gas-liquid conversion occurred under the critical conditions, where no liquid surface tension existed during the solvent replacement. The benefits of using this method are that it can avoid damage to the three-dimensional network structure caused by capillary pressure inside the pores. The produced aerogel has a low shrinkage rate, which allows the production of aerogel materials with a more uniform structure. For example, Sakai et al. prepared CNF aerogel using CO_2 supercritical drying and compared with freeze drying.[78] They concluded that aerogels from supercritical drying possessed much higher surface area (160 m^2/g) than freeze dried aerogels (30 m^2/g), which agrees with the conclusion from Darpentigny et al. [79] However, supercritical drying is not extensively used, mainly because of the high cost of the equipment for extreme conditions (temperature and vacuum) and complexity of the process. Besides, the process can be solvent- and time-consuming.

2.6.2.3 Freeze drying

Compared to supercritical drying and ambient drying methods, freeze-drying is the most common method to make lightweight porous CN aerogels from the wet gels according to a literature survey shown in Figure 2.7 (A). During the freeze-drying process, the gel is first frozen at a temperature below the freezing point of the liquid medium (usually water). Then, the solid ice crystals are eliminated by sublimation under low pressures, leaving pores in the network. This process avoids contact with the gas-liquid phases, thus preventing the capillary pressure formed during the drying process. Freeze-drying is a simple, efficient, and environment-friendly method, and the resulted aerogel has a lower rate of shrinkage and excellent porosity.

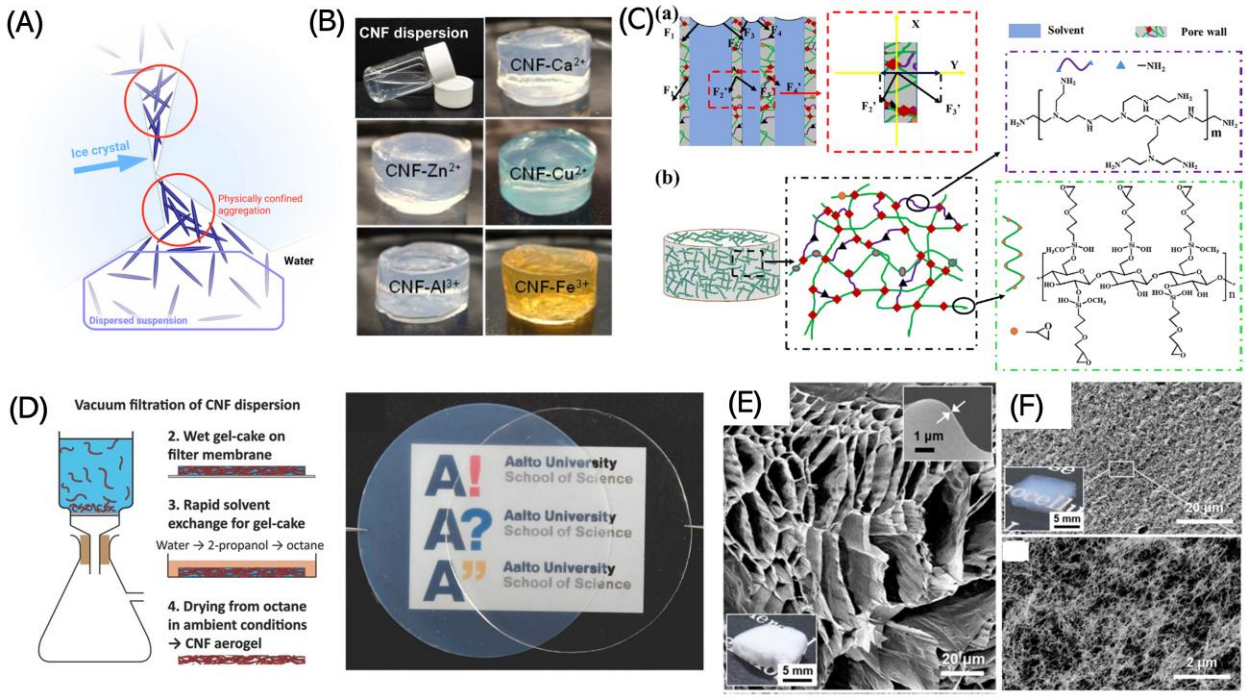

Figure 2.6 (A) gelation caused by physically aggregation of CNCs.[73] (B) Free-standing gels formed ionic gelation between metal salt and carboxylated CNF dispersions.[74] (C) (a) Capillary pressure analysis of pore walls of porous materials during the drying process and (b) schematics of the cross-linked networks.[75] (D) Schematic illustration of the preparation process of CNF aerogel membranes and its photograph of CNF aerogel membrane (left) and compacted film (right).[77] (E) CNF aerogel prepared from freeze drying method and (F) supercritical drying method and their SEM images.[78]

2.6.3 Pore forming templates

To create a porous structure, a template is required during the gel formation process. The template is either removed during the drying process or removed by post-treatment process, leaving the cavities in the network. These templates can be categorized as ice crystals, emulsions, air bubbles and solid particles. Among them, ice crystals are most commonly used templates during the aerogel preparation.

2.6.3.1 Ice crystal template

Factors such as cooling rate induced by the freezing temperature and temperature gradient play significant roles in the pore morphology due to the ice crystals growth behavior.[79] Jiang et al. investigated the freezing temperature on the resultant pore size and morphology of the CNF

aerogel. CNF suspensions were frozen for approximately 2 h in a freezer (-20 °C) or frozen in liquid nitrogen (-196 °C) for 5 min, followed by freeze drying.[81] Much smaller nuclei were formed at -196 °C due to the faster cooling rate, while larger ice crystals were formed at -20 °C. Consequently, smaller pores were observed in the rapid frozen CNF aerogel after drying. In addition, the morphology of the pore walls displayed significant difference due to the different rate of ice formation. Seen from Figure 2.7 (B), more ordered and smoother structures were observed in the slower frozen aerogel, while more dispersed and less ordered thinner walls were formed in rapid frozen CNF aerogels as shown in Figure 2.7 (C).

However, aerogels produced by these homogenous freezing conditions possessed randomly distributed pores, which prevents the aerogel from achieving a directional light propagation, heat and mass transfer, electrical conductivity, and water transportations. The growth direction of ice crystals can be controlled by manipulating the temperature gradient. To date, unidirectional freezing and bi-directional freezing has been reported for highly ordered porous aerogel preparation. The difference between them is that one direction and two directions temperature gradient were applied to the gel during the freezing process. A bottom-up temperature gradient is applied for unidirectional freeze drying (Figure 2.7 (D, a)), inducing the ice crystals growth along this direction.[82] Generally, honeycomb-like pores along the transverse direction and parallel channels along the longitudinal direction are produced in unidirectional freezing (Figure 2.7 (D, b)), which was also demonstrated by Pan et al.[83] The authors prepared CNF monolith by unidirectional freeze drying, producing parallel micro-honeycomb structure in the network. Such structure could only allow laser light to penetrate through the aligned channels, while was blocked in the transverse direction as shown in Figure 2.7 (D, c). Similar to homogenous freezing, an inverse relation between pore size and cooling rate is also applicable for directional freezing. Seen from Figure 2.7 (D, e and f), the aerogel exhibited a smaller pore size when a higher cooling rate was applied.

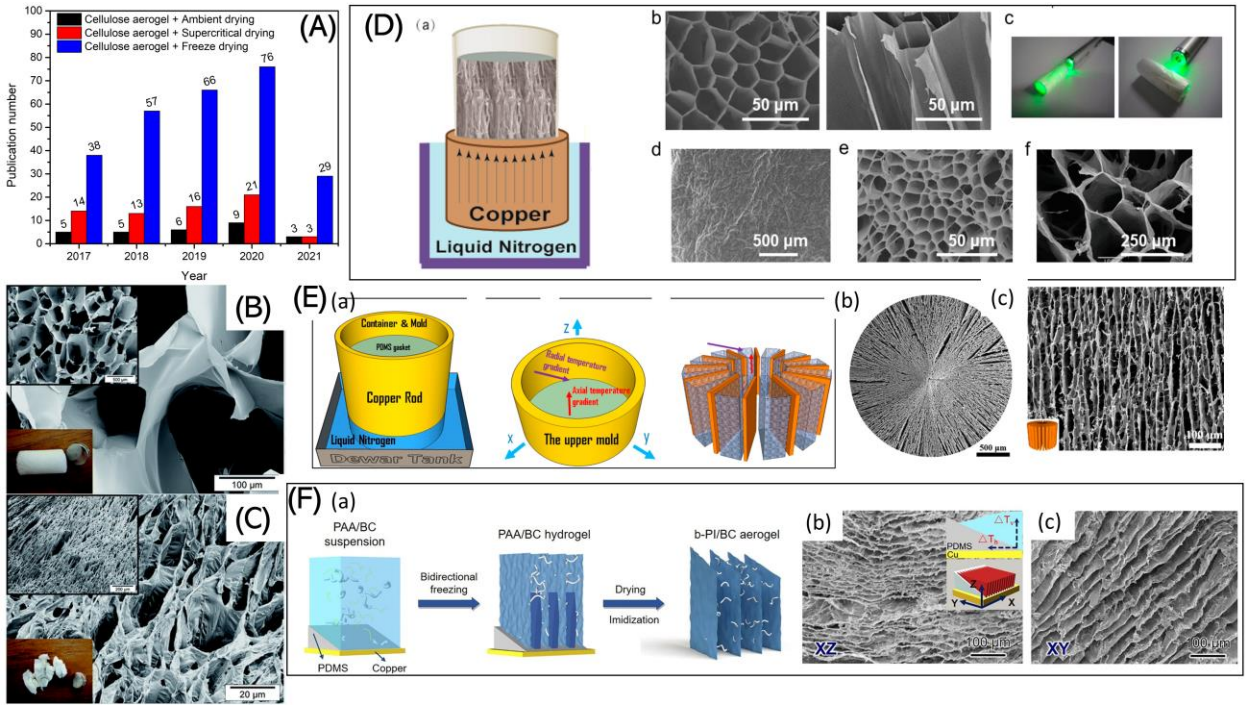

Figure 2.7 (A) A literature survey by web of science database with a topic of "cellulose aerogel" and "ambient drying", or and "supercritical drying", or and "freeze drying" in the past 5 years. SEM image of CNF aerogel obtained after frozen in freezer (-20 °C) (B) and obtained after frozen in liquid nitrogen (-196 °C) (C).[81] (D) (a) an illustration a setup for unidirectional freezing,[82] (b) SEM images of the cross section of the transverse and longitudinal direction of CNF aerogel produced by unidirectional freezing, (c) Laser penetration tests on the aerogel, (d) highly magnified SEM image of the aerogel wall, (e, f) SEM images of the cross-sections of aerogels produced with a cooling rate of 50 cm/h and 2.5 cm/h into liquid nitrogen, respectively.[83] (E) (a) an illustration a setup for bidirectional freezing, (b) SEM images of the cross section of the transverse and (c) longitudinal direction of graphene oxide aerogel produced by bidirectional freezing.[84] (F) (a) an illustration the setup for bidirectional freezing developed by Wang et al. (b) and (c) SEM images of the cross sections of the X-Z and X-Y planes of b-PI/BC aerogel prepared by bidirectional freezing.[85]

A radial and centrosymmetric porous structure was obtained when a bi-directional freezing was used as shown in Figure 2.7 (E, a). As copper rod has good thermal conductivity, the dispersion loaded in the setup was subjected to two temperature gradients, one from bottom-up along the copper rod and the other in the radial direction. Wang et al. produced graphene oxide with highly

ordered vertical and radially aligned structure using this method, which was demonstrated by the SEM images shown in Figure 2.7 (E, b and c).[84] However, similar morphology has not been reported on CN based aerogels. A different bidirectional freezing technique was developed by Zhang et al. (Figure 2.7 (F, a)), where a PDMS wedge with a slope angle of around 20° sitting on a copper plate was used as the bottom.[85] An upward temperature gradient perpendicular to the copper plate and a temperature gradient parallel to the diagonal of wedge were generated. Bi-directional anisotropic polyimide/bacterial cellulose (b-PI/BC) aerogels with well-aligned lamellar structure were obtained by this technique. The SEM images from the X-Z and X-Y cross section b-PI/BC aerogel demonstrated the excellent and uniform lamellar structure (Figure 2.7 (F, b and c)). Significant distinct thermal insulation behaviors were observed in the radial direction (perpendicular to the lamella) and in the axial direction (parallel to the lamella). Ultra-low thermal conductivity of 23 mW m^{-1} K^{-1} in the radial direction was observed, which was nearly twice times lower than the axial direction (44 mW m^{-1} K^{-1}). The anisotropy structure shows promise for heat management in thermal insulation applications.

2.6.3.2 Emulsion template

As described earlier, CNs are excellent Pickering emulsifiers for emulsion preparation. Oil droplets are trapped by CNs with higher aspect ratio (e.g., CNF) after emulsification, producing a stable network. Jiménez-Saelices et al. used CNF stabilized emulsion droplets as templates to prepare CNF aerogel for thermal insulation applications as illustrated in Figure 2.8 (A).[86] Hexadecane oil was selected as the oil phase due to its high crystallization temperature (18 °C). Stable and gel-like oil-in-water emulsions was produced using an oil/aqueous phase volume ratio of 20/80 and CNF concentration from 10 to 30 g/L. After freeze drying, highly porous aerogels with BET surface area between 65 and 13 m^2/g were produced. The authors described a hierarchical pore morphology according to the SEM image: alveolar larger macropores from ice crystals sublimation, spherical macropores from emulsion template, and mesoporous pores at the pore walls formed by entangled CNF fibers. Except for the high porosity, the aerogels also possess high compression moduli of 1.5 MPa and low thermal conductivity of 0.018 W/(m·K).

In another study, Li et al. prepared various CNF/polymer composite aerogels by dissolving different polymers (polylactic acid, polycarbonate, polystyrene, polymethyl methacrylate) in 1,2-dichloroethane (DCE), followed by emulsification and freeze drying (see Figure 2.8 (B)).[87] It was found that stable and gel-like emulsions were obtained for all types of polymers at a water to oil

volume ratio of 4:1, CNF concentration of 0.4 % in the water phase, and polymer concentration of 2 % in the oil phase. Polymers were adhered to the lamellar structure of the CNF after ice crystals sublimation, producing strong pore walls consisting of CNF/ polymer composite. Based on the results, the authors further added a fluorophore, 1,4-dihydroxyanthraquinone (1,4-DHAQ), in the oil phase during CNF/PLA composite aerogel preparation. Water insoluble 1,4-DHAQ was uniformly distributed in the aerogel network using this method. The 1,4-DHAQ loaded CNF/PLA composite aerogel exhibited an extremely low detection concentration of 10^{-8} mol/L, which is very promising as a novel solid-state fluorescence probe for Cu^{2+} detection.

2.6.3.3 Air bubble template

Similar to Pickering emulsion, CNs are also effective in stabilizing the air-liquid interface to produce air bubbles. Cervin et al. coated octylamine on carboxyl methylated CNF at pH 9 to increase CNF hydrophobicity, the modified CNFs were further used as emulsifiers to prepare stable air bubbles.[88] The mixture was stirred using an Ultra Turrax mixer for 10 min at 8000 rpm and for another 10 min at 13500 rpm. After stirring with a stainless-steel milk beater, CNF stabilized air bubbles was generated as seen in Figure 2.8 (C). Excessive water in the foam was drained with a funnel, and the resulting wet cake was dried at 60 ℃ to yield the aerogel. It was found that stable foam and good mechanical strength aerogel was obtained when 1% modified CNF was used. The aerogel possessed a porosity of 98% and an average pore diameter of 500 μm as shown in Figure 2.8 (D). However, the wet foam was dried in a humid environment by placing on top of a water-filled porous ceramic frit to reduce drying rate. Such process took 2 days for drying the wet foam, which is not efficient.

The mechanisms behind wet foam stability and CNF emulsifier property were clarified by Cervin et al. in another study.[89] It was found that octylamine modified carboxylated CNF possessed lower surface energy than unmodified CNF, which contributed to reducing the interfacial tension between air and water, thereby producing stable foam. The aspect ratio of the emulsifier has a significant effect on the foam stability. A more stable foam was generated when CNF was used as emulsifier compared to CNC. Based on these findings, Cervin et al. further prepared a water-durable and wet-resilient foam using octylamine modified periodate oxidized CNFs as emulsifiers.[90] The aldehyde groups could react with neighboring hydroxyl groups, forming hemiacetal groups and crosslinked CNF networks after drying. The resulting foams could uptake

water up to 34 times their own weight with water release and reabsorption upon compression as seen in Figure 2.8 (E).

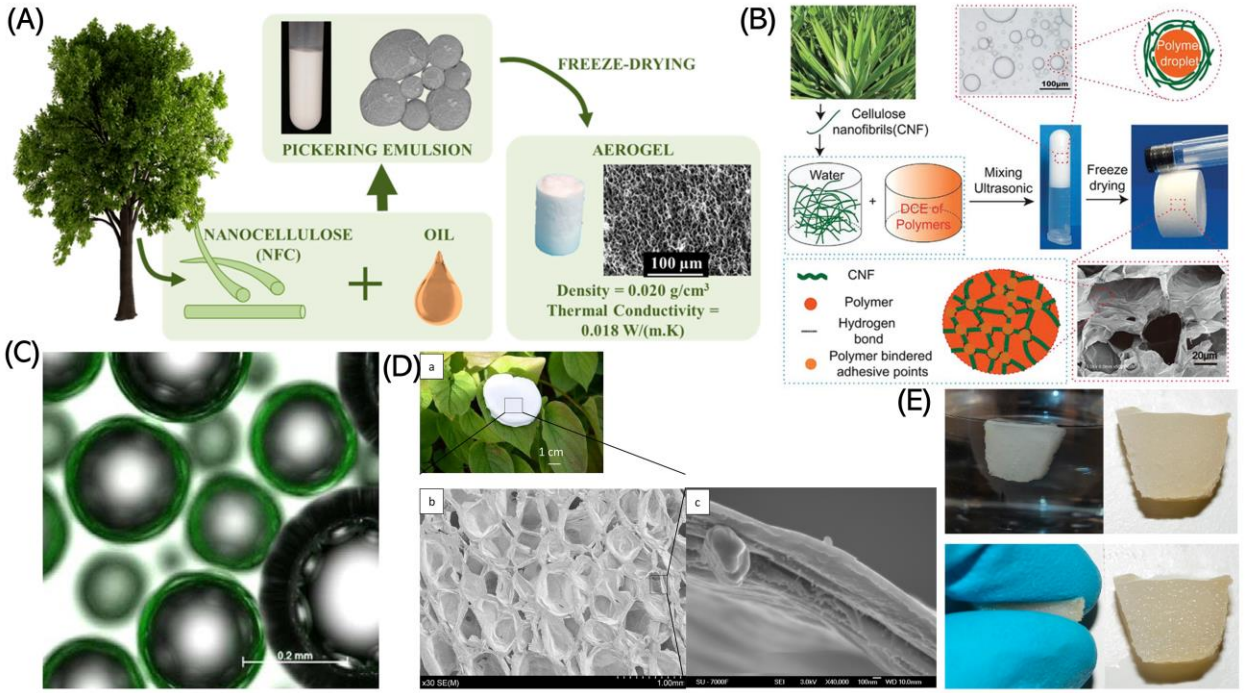

Figure 2.8 (A) Illustration of CNF stabilized hexadecane in water emulsion droplets as templates to prepare CNF aerogel for thermal insulation applications.[86] (B) Illustration of Pickering emulsions as templates to prepare CNF/ Polymer composite aerogels.[87] (C) Confocal microscopy image of air bubbles stabilized by fluorescently labeled octylamine-coated CNF.[88] (D) A photograph of porous CNF foam prepared by air bubble templates and its corresponding SEM images.[90] (E) A demonstration of water absorption capacity of crosslinked CNF foam prepared by air bubble templates.[90]

2.6.3.4 Solid particle template

Solid particles, such as $CaCO_3$, polystyrene beads, and sodium bicarbonate are widely used as hard templates to fabricate capsules and porous materials. Li et al. used nanosized $CaCO_3$ particle as pore forming agent to prepare porous cellulose aerogel beads. Nanosized $CaCO_3$ particles were added to dissolved cellulose solution and microfibrillated cellulose mixture, followed by dropwise addition of HCl to generate beads *via* precipitation. CO_2 bubbles were released during the process to generate pores inside the network. The resulting hydrogel beads were soaked in acetone for 24 h, and dried in the vacuum oven to yield cellulose aerogel beads. The method effectively enhanced

the porosity of the aerogel beads, leading to a high adsorption capacity (303 mg/g) toward to methylene blue dye.[91]

2.6.4 Cellulose nanomaterial-based aerogel beads preparation

Due to the convenient preparation process, aerogel monoliths were often studied in many applications. In recent years, aerogel beads have received more attention because of their larger surface area, shorter drying duration, and potential for large scale production when compared with aerogel monoliths. Aerogel beads are very promising as carriers for drug delivery, absorbents/ filters for pollutants removal, and flame retardants for thermal insulation applications. In this section, the production methods and applications of aerogel beads based on CNs will be reviewed.

2.6.4.1 Spraying and atomizing

Atomization is a process that disintegrates a liquid stream with compressed air, leading to the formation of poly- or monodispersed droplets. These droplets were usually injected in a "low temperature sink" or a non-solvent medium, followed by droplets collection and drying to obtain aerogel beads. Cai et al. adopted such method to prepare crosslinked CNF aerogel beads as cell culture scaffold. CNF with a diameter below 50 nm was prepared as the starting material. CNF dispersion was mixed with a crosslinker Kymene (polyamide-epichlorohydrin resin), which was poured into the steel feed tank of the atomization equipment, followed by spraying into liquid nitrogen as the freeze-drying process as illustrated in the schematic shown in Figure 2.9 (A). Crosslinked aerogel beads were achieved by curing the dried aerogels at 120 °C for 3 h. The diameter of CNF aerogel beads was distributed between 60-120 μm, which increased inversely with CNF concentration. Besides, the aerogel beads possessed a low bulk density of as low as 1.8 mg/cm^3, and pore size ranged from nano- to macroscale with an excellent water uptake capacity of 100 g/g, which is very promising as a scaffold for cell culture.[92]

2.6.4.2 Precipitation

It's known that cellulose fibers can be dissolved in solvents such as ionic liquid and NaOH/ urea/ water mixture (7 wt % NaOH,12 wt % urea and 81 wt% water), yielding homogeneous cellulose solutions. Under acid condition, cellulose dissolved in NaOH/ urea/water solution will precipitate due to its reduced solubility. Based on the mechanism, cellulose beads are produced by dropping cellulose solution in a coagulation bath. For example, Blachechen et al. dissolved carboxylic cellulose fibers in NaOH/ urea/ water mixture, which was injected into 2M HCl via a syringe. It was found that spherical hydrogel beads with an average diameter of 3 mm were produced when

the distance from syringe tip to bath was controlled between 2.5-3.5 cm. Aerogel beads were obtained after freeze drying.[93] Similarly, Guo et al. prepared polyethylenimine-functionalized cellulose aerogel beads for efficient removal of chromium (VI) and Li et al. prepared carboxylic functionalized cellulose aerogel beads for methylene blue removal using the syringe injection and coagulation method.[91,94]

2.6.4.3 Emulsification

Emulsions are spherical droplets that are commonly prepared by mixing two immiscible liquids in the presence of stabilizers. By injecting dissolved cellulose solution or CN dispersion in an immiscible oil phase, spherical cellulose droplets in oil phase were generated after the emulsification process. As illustrated in Figure 2.9 (C), Levin et al. prepared crosslinked CNC aerogel beads using a T-junction microfluidic fabrication device, which is promising for a larger scale production. Aldehyde functionalized CNCs and hydrazide functionalized CNCs were mixed to form the water phase, which was dispersed in food-grade soybean oil containing food-grade emulsifier polyglycerol polyricinoleate (PGPR). Uniform spherical CNC droplets stabilized by PGPR were produced, followed by evaporation at 40 ℃ for 72 h. During the process, hydrazone bonds were formed between aldehyde and hydrazide groups between neighbouring CNC particles. The dried CNC aerogel beads possessed ultra-porous with an average size of 110 ± 50 μm as evident from the SEM images.[95] In contrast to Levin et al., Druel et al. prepared cellulose aerogel beads using a emulsion-coagulation method as shown in Figure 2.9 (D). Homogenous cellulose solution was obtained by dissolving microcrystalline cellulose in NaOH/ urea mixture. Emulsion prepared by cellulose solution and paraffin oil and emulsion prepared by cellulose in a non-solvent (acetic acid (8.6 M)) and paraffin oil were mixed to induce coagulation. The gelation was achieved by the slow diffusion of acetic acid from its emulsified droplet to cellulose solution droplet since acetic acid is partly soluble in paraffin oil. The resulting cellulose microgels were subjected to supercritical drying to produce cellulose aerogel beads. Results showed that the aerogel beads possessed an average diameter of 21 μm with a high surface area around 355 m^2/g.[96]

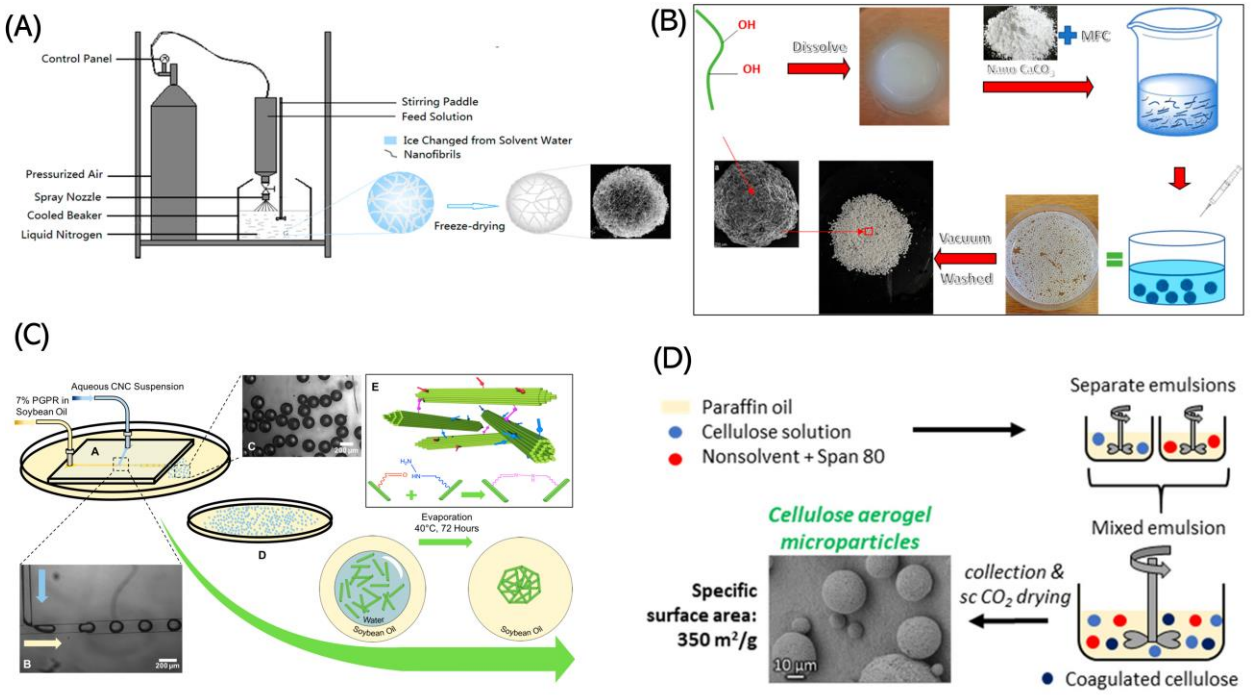

Figure 2.9 (A) Schematic illustration of Kymene crosslinked CNF aerogel beads prepared by a spraying- atomizing- freeze drying process.[92] (B) Schematic illustration of cellulose aerogel beads prepared by non- solvent precipitation method.[90] (C) Schematic illustration of crosslinked CNC aerogel beads prepared by microfluidic emulsification process.[95] (D) Schematic illustration of cellulose aerogel beads prepared by emulsification- coagulation process.[96]

2.7 Cellulose nanomaterial-based aerogels for water treatment

Due to the bio-degradable, sustainable, large surface area, highly porous and easy to modify properties, CN-based aerogels are popular in water treatment applications. They were reported for dye adsorption, metal ions adsorption, agrochemicals adsorption, pharmaceutical residues, spilled oil absorption, and emulsion droplets separation. In the recent 5 years, there are several comprehensive reviews summarizing the application of CNs in water treatment applications, including 1D CN fibrils, 2D CN membranes, and 3D CN hydrogel/ aerogels. Herein, a detailed summary regarding the scope of each review is provided.

In 2015, Carpenter et al. summarized the processing and property of CNs and compared them with carbon nanotubes. The review also covered the application of 1D CN fibrils as adsorbents for heavy metal ions removal, CNs as reinforcing materials to fabricate 2D membranes for wastewater filtration, CNs as scaffolds to prepare superhydrophobic 3D aerogels for oil/ organic solvents

absorption.[97] In 2017, Liu et al. reviewed CN-based 3D aerogels as oil absorbent for oil spill cleanup application.[98] In 2018, Abouzeid et al. provided an overview of surface modification strategies of CNs and the hydrogels, aerogels, membranes absorbents for dyes, heavy metal ions, and organic pollutants removal. Notably, they only summarized the application of CN-based aerogels as oil absorbents.[99] In the same year, Mohammed et al. published a critical review of CNs in water treatment applications. In addition to the preparation process, property, surface modification, the review also included CNs based flocculants, absorbents, membranes, catalysts for water treatment. In terms of CN-based aerogels, the authors reviewed its application for oil absorption, dye adsorption, and heavy metal ions adsorption.[100] In the paper by Choudhury et al., the recent advances of CN-based aerogels for oil absorption were also reviewed.[101] The application of CN-based membranes for water treatment were reviewed by Mautner et al. in 2020.[102] In 2021, Chen et al. summarized the preparation and modification of CN-based aerogel and discussed their application in adsorption, separation, energy storage, thermal insulation, electromagnetic interference shielding, and biomedical applications.[103]

In summary, CN-based aerogels exhibit more advantages over 1D CN fibrils regarding the recoverable property after adsorption, avoiding secondary contamination. A comprehensive review on the recent advances of CN-based aerogel for oily wastewater (emulsion droplets) is lacking. Specifically, the recovery of pesticide/ fertilizer from wastewater using CN-adsorbent has not been reported. Based on the function of CN-based aerogels, they are categorized as adsorbents and filters. In the followings, CN-based aerogel adsorbents for dyes, heavy metal ions, pesticide and fertilizers, and spilled oils removal was firstly reviewed. Then, CN-based superwetting filters for oil/water mixtures and emulsions separation was summarized.

2.7.1 Cellulose nanomaterial-based aerogels as adsorbents

Parameters, such as pH, temperature, ionic strength, and adsorbent dosage are generally investigated to optimize the adsorption conditions, and the maximum adsorption capacity, adsorption rate, and recovery property are key references used to evaluate the performance. The adsorption capacity of the adsorbent is typically determined by the batch adsorption protocol. A known amount of adsorbent is mixed with the pollutant solution at controlled concentrations and volume. The concentration of pollutants at equilibrium was measured, and the adsorption capacity q_e (mg/g) is calculated using Eq. (2.3):

$$q_e = \frac{(C_0 - C_e)}{m} V \quad (2.3)$$

where C_0 (mg/L) and C_e (mg/L) are the initial and equilibrium concentrations, respectively; V(L) represents the solution volume of pollutants and m (g) represents the mass of the aerogel adsorbent.

The adsorption isothermal is determined from the batch adsorption experiment, where a fixed amount of absorbent is added to a fixed volume of the pollutant of varying concentrations at a given temperature. The adsorption behavior is described by Langmuir isotherm model as expressed in its non-linear and linearized forms as shown in Eq. (2.4) and (2.5) respectively.

$$q_e = \frac{q_m K_L C_e}{1 + K_L C_e} \quad (2.4)$$

Or its linearized form

$$\frac{C_e}{q_e} = \frac{C_e}{q_m} + \frac{1}{K_L q_m} \quad (2.5)$$

where q_m (mg/g) is the maximum adsorption capacity of the absorbent, and K_L (L/mg) is the binding constant that describes the affinity between the pollutant and adsorbent. The Langmuir isothermal model assumes that a monolayer adsorption occurs on adsorption sites, which are identical and homogenously distributed on the adsorbents. For heterogenous, non-identical distributed sites and multi-layer adsorption, Freundlich isotherm model is more suitable model to describe the adsorption behavior. This model is developed from empirical assumptions, as illustrated in its non-linear and linear forms shown in Eq. (2.6) and Eq. (2.7) respectively.

$$q_e = K_F C_e^n \quad (2.6)$$

$$ln q_e = ln K_F + n ln C_e \quad (2.7)$$

where K_F is a constant, and n represents the empirical parameter describing the magnitude of the adsorption driving force or the surface heterogeneity. Generally, the adsorption process is linear (n = 1), favorable (0 < n < 1), and unfavorable (n > 1).

During the adsorption process, the adsorption capacity (q_t) versus contact time (t) is examined graphically. The adsorption kinetics and mechanisms of adsorption can be examined using different kinetics models. For physical adsorption, pseudo first-order model is used, while pseudo second-order model is used when chemical adsorption dominates the process. Pseudo first-order

kinetic model in its non-linear form (Eq. (2.8)) and linear form (Eq. (2.9)), pseudo-second order kinetic model in its non- linear form (Eq. (2.10)) and linear form (Eq. (2.11)), and intra-particle diffusion model (Eq. (2.12)) are shown below:

$$q_t = q_e(1 - e^{-k_1 t}) \quad (2.8)$$

$$\ln(q_e - q_t) = lnq_e - k_1 t \quad (2.9)$$

$$q_t = \frac{q_e^2 k_2 t}{1 + k_2 q_e t} \quad (2.10)$$

$$\frac{t}{q_t} = \frac{1}{(k_2 q_e^2)} + \frac{t}{q_e} \quad (2.11)$$

$$q_t = K_{id} t^{0.5} + C \quad (2.12)$$

where q_t (mg/g) is the adsorption capacity at time t, and k_1 and k_2 are the rate constants for the pseudo-first order adsorption and pseudo-second order adsorption kinetic models, respectively. K_{id} is the rate constant (g mg^{-1} min^{-1}) of intra-particle diffusion kinetics.

2.7.1.1 Dye adsorption

Organic dyes, such as acid red G (ARG), methylene blue (MB), methylene orange (MO), malachite green (MG), and rhodamine B (RhB) are widely used in textile, food, paper, drug, and leather industries. Most of them are toxic, nonbiodegradable and carcinogenic, which threaten water quality, ecological balance, and human being health when discharged into the water stream. Therefore, methods like membrane filtration, flocculation, degradation, and adsorption are used to efficiently remove these organic pollutants from wastewater. Among them, adsorption method has been considered as an economic method due to its simplicity and efficiency.

Diverse functionalized CN-based aerogels were designed for targeting the removal of dyes depending on their properties. The adsorption can be achieved by pore diffusion, electrostatic interaction, and π-π stacking interaction. Jiang et al. prepared carboxylated CNF hydrogel by assembling TEMPO oxidized CNFs *via* freezing-thaw method, followed by solvent exchange with tert-butanol and freeze drying to obtain a honeycomb cellular structured carboxylated aerogel. CNF aerogel with a surface area of 193 m^2/g and surface charge of 1.29 mmol/g was used for the removal of cationic malachite green dyes. A maximum adsorption capacity of 212.7 mg/g was achieved at an optimal condition mainly through electrostatic interaction.[104]

For anionic dyes such as methyl orange, cationic CNF aerogel was prepared by Zhang et al., who introduced aldehyde groups on CNFs via periodate oxidation, followed by the freeze-induced chemical crosslinking *via* the formation of hemiacetal bonds between aldehyde and hydroxyl groups. To produce a cationic CNF aerogel, polyethyleneimine (PEI) was grafted to the cryogel *via* reduction amination reaction. The maximum adsorption capacity of 500 mg/g was achieved at a pH of 4.5 that was attributed to the strong interaction between protonated amino groups and negatively charged MO. It is known that both acidic and basic forms of MO coexisted at pH between 4.5 to 2.5, thus enhancing the electrostatic repulsion between MO molecule and the aerogel. However, the protonation degree of amino groups decreased as the pHs were increased from 4.5 to 11, thereby causing a reduction in the adsorption capacity. The aerogel also possessed excellent mechanical strength, where a stress of 304.5 kPa was achieved at 80% strain.[105]

Lyu et al. prepared a carboxylated and polyaniline (PANI) functionalized CNF aerogel for both Acid Red G (ARG, anionic dye) and Methyl Blue (MB, cationic dye) removal. A maximum adsorption capacity of 600.7 and 1369.6 mg/g was achieved for ARG and MB respectively. The adsorption of ARG on aerogel was mainly through the electrostatic interaction with protonated amine groups on PANI, while the adsorption of MB was achieved by π-π stacking interaction with aromatic rings of PANI and electrostatic interaction with the carboxyl groups on the CNF.[106] To achieve multi-types of pollutant adsorption performance, Wang et al. loaded one type of MOF, i.e., UiO-66, on the CNF aerogel. MOFs have received much attention for pollutants removal due to their large surface area and high porosity. Cubic shaped UiO-66 nanoparticles with a size of about 500 nm were loaded to CNF aerogel network through hydrogen bonding between hydroxyl groups on CNF and oxygen-containing groups on UiO-66 particles. The obtained composite aerogel possessed high adsorption ability towards both anionic methyl orange (71.7 mg/g) and cationic methylene blue (51.8 mg/g), which was attributed to the π-π stacking interaction between UiO-66 and dye molecules.[107] A similar concept was adopted by Zhao et al., who prepared porous aromatic frameworks (PAFs) loaded CNF aerogel composite for the removal of bisphenol A through π-π stacking interaction.[108]

2.7.1.2 Heavy metal ions adsorption

Heavy metal ions (e.g., Pb (II), Cu (II), Cr (VI), Hg (II)) are serious water pollutants that threaten human health due to their high toxicity, non-degradability, and bio-accumulation characteristics. Similar with dyes removal, recent studies have shown that CNs based aerogels could effectively

remove heavy metal ions from wastewater. Thiol moieties exhibited strong affinity for Hg (II) ions as shown by Geng et al. who grafted 3-mercaptopropyltrimethoxysilane (MPT) on TEMPO-oxidized CNF fibers to decorate thiol groups on the aerogels (Figure 2.10 (A)). MPT not only functioned as modification agent, it was also a crosslinking agent to prepare CNF aerogel. The as prepared aerogel possessed both carboxyl and thiol groups, allowing a high adsorption capacity for Hg (II) ions of approximately 718.5 mg/g. In addition, the modified aerogel could effectively and selectively remove more than 92 % Hg (II) ions over a wide range of 0.01- 85 mg/L.[109]

Polyethyleneimine (PEI) is a widely used functional agent for multiple heavy metal ions removal in water treatment applications due to its positive and excellent chelating properties. For example, Li et al. prepared physically crosslinked aerogel through the charge interaction between PEI and carboxylated CNF. The aerogel was effective for the removal of Cu (II) and Pb (II) ions, resulting in a maximum adsorption capacity of 175.44 mg/g and 357.44 mg/g, respectively, which was determined from the Langmuir isothermal model.[110] Hong et al. prepared amine functionalized CNF aerogel by grafting PEI on CNF with glutaraldehyde as crosslinker. The synthesized PEI@CNF aerogel exhibited outstanding ion selectivity and excellent Cu (II) adsorption capacity of 135.1 mg/g. A continuous treatment of wastewater containing low concentration of Cu (II) (20 mg/L) was realized by loading the synthesized aerogel into the column.[111] Notably, Mo et al. reported a PEI-functionalized TEMPO- oxidized CNF aerogel adsorbent that possessed the highest Cu (II) ion adsorption capacity of 485.44 mg/g among all reported cellulose-based adsorbents.[112]

In addition to PEI, other types of compounds that contain amino groups were also reported for heavy metal ions removal. Li et al. prepared an oriented microchannel structured chitosan (CS)/ CNF composite aerogel *via* directional freeze-drying method. Such structure reduced the metal ions diffusion length that yielded a rapid adsorption equilibrium within 10 min. The aerogel possessed excellent adsorption capacity for Pb (II) (248.5 mg/g) due to the amine groups from chitosan.[113]

Among heavy metal ions, Cr (VI) is more complex than others as it existed in different forms, such as H_2CrO_4, $HCrO_4^-$, CrO_4^{2-}, and $Cr_2O_7^{2-}$ depending on the pH and concentration. It was reported that amine and quaternary ammonium groups were effective for Cr (VI) removal. For example, both He et al. and Liang et al. developed quaternary ammonium functionalized CNF aerogel for Cr (VI) removal. According to He et al., a maximum adsorption capacity was achieved at pH 3.0 since $HCrO_4^-$ was the dominant specie under this condition. Further increase in the pH produced

CrO_4^{2-}, and $Cr_2O_7^{2-}$, which required two Cl^- ions for exchanging of one Cr (VI) ion, thus reducing the aerogel adsorption performance.[114] Similar conclusion was also obtained by Liang et al.[115] In another study, Zhao et al. reported a dendrimer poly(amidoamine)-grafted CNF aerogel that possessed the highest Cr (VI) adsorption capacity of 377.36 mg/g. It has abundant amine groups and amide groups with strong affinity for Cr (VI) species.[116] Other types of aerogels, such as UiO-66 particles loaded CNF aerogel was reported for Pb^{2+} and Cu^{2+} removal,[117] and carboxylated CNF aerogel was reported for Pb^{2+}, Cu^{2+}, Zn^{2+} and Ni^{2+} ions removal.[118]

2.7.1.3 Pesticide and fertilizer adsorption

Water and soil pollutions associated with the improper use of pesticide formulations and leaching of fertilizers have been one of the major challenges in environmental management. Except for the development of novel smart agrochemical formulations to reduce the total pesticide input, techniques used to remove such containments from environment are urgently needed. Various methods, such as photocatalysis, biodegradation, electrochemical oxidation and adsorption for pesticide removal are being explored. Porous silica, activated carbon, metal oxide particles, and porous polymers have been widely used for pesticides adsorption and removal. N and P as essential nutrients for plant growth, are prone to leaching due to the high-water solubility and poor soil retention capability, which further induce water eutrophication. The Environmental Protection Agency (EPA) limit the acceptable phosphorus discharge to less than 0.1 mg/L. The recovery of nutrients from wastewater could reduce water pollution as well as preserve the limited P rock resource.

Remediation methods, such as chemical precipitation, reverse osmosis, coagulation-flocculation, and adsorption have been applied to remove NH_4^+ and $H_2PO_4^-$. Design of such systems for containment removal based on cellulose materials have been widely reported. By surface functionalization, cellulose materials display many advantages as absorbents for heavy metals (e.g., Cu^{2+}, Pb^{2+}, Cr^{6+}, etc.) removal,[119,120] organic dyes (methylene orange, methylene blue, and Congo red, etc.), and oil spill cleanup. CNFs possess unique properties that are ideal for the fabrication of absorbents for pesticides and fertilizers adsorption due to their flexible fiber structure, large surface area, versatile modification methods, hydrophilicity, and biocompatibility.

Komal et al. synthesized CdS nanoparticles on saline modified CNFs derived from sugarcane bagasse via a solvothermal route.[121] Cd^{2+} ions were adsorbed on the surface of SCNF through metal coordination interaction with oxygen containing groups on the SCNF. DMSO was used as

the solvent as well as S elemental source in the hydrothermal synthesis of CdS. As temperature was increased, the S=O bond of DMSO became weaker liberating the S^{2-} ions that coordinated with the absorbed Cd^{2+} ions. Thus, SCNF provided sites for the nucleation of CdS nanoparticles that minimized the particle agglomeration. The adsorption of the nanocomposites towards an organophosphate pesticide Chlorpyrifos (CPF) was investigated. Adsorption conditions such as pH, absorbent dosage and SCNF content were investigated, where the maximum adsorption capacity (86.95 mg/g) was achieved at pH of 3, absorbent dosage at 1 g/L, and SCNF content of 10 wt%. The adsorption was achieved by: (1) the charge interaction between the organophosphate anion and the protonated nanocomposites at lower pH, and (2) hydrogen bonding between the O atoms of CPF and protons of the adsorbent at lower pH.

Khalfaoui et al. functionalized cellulose fiber extracted from Juncus acutus L. plant (Smar) by an amine containing compound diethylenetriamine (DET) for linuron adsorption.[122] The authors found that enhanced linuron adsorption capacity could be achieved when Cu^{2+} was used as a bridge between the pesticide and amine functionalized cellulose fiber. After further coordination with Cu^{2+}, the DET grafted cellulose fiber displayed stronger interaction towards linuron (64.8 mg/g at 20 °C) due to the metal coordination bonding with the amine groups.

Adsorption of fertilizer ions through charge interaction is widely adopted due to the ease of operation. Shang et al. fabricated cationic cellulose with quaternary ammonium groups for phosphate ions adsorption by grafting of epichlorohydrin, ethane diamine, and trimethylamine.[123] It was found that the presence of competing ions can greatly affect the adsorption performance. Compared to Cl^- and NO_3^-, the coexistence of SO_4^{2-} with higher ionic strength could significantly reduce adsorption capacity. After phosphate adsorption, the potential of the composites for use as a slow-release fertilizer in soil was evaluated, and 27.5 % loaded phosphate was released in 4 days, which was much slower than the release in aqueous solution.

In another study, Wang et al. dissolved cellulose extracted from wheat straw in NaOH/Urea mixture and further decorated quaternary ammonium groups and carboxyl groups by grafting 3-chloro-2-hydroxypropyl trimethylammonium chloride (CTA) and chloroacetic acid (CA) to produce amphoteric straw cellulose (ASC).[124] The ASC displayed rapid adsorption rate for both NH_4^+ and $H_2PO_4^-$ due to the dual functional groups. Adsorption conditions, such as pH, temperature, absorbent dosage, and ionic strength were thoroughly studied, and an equilibrium adsorption capacity for NH_4^+ and $H_2PO_4^-$ was 68.4 mg/g and 38.6 mg/g respectively. The nutrients

laden ASC exhibited pH-responsive slow release and water retention properties, which could reduce water pollution/ consumption and promote crop growth.

Martin et al. used cellulose as a template to fabricate porous pellets for the removal and recovery of phosphate.[9] Water insoluble magnesium carbonate was blended with cellulose (of varying weight ratios 0, 5, 10, 15, 20 %) to synthesize the pellets, which were then calcined at 300 ℃ to yield internal porous absorbents. Magnesium (Mg) elements in the composites functioned as binder for the phosphates. BET tests on the pellets revealed a maximum area of 43.1 m^2/g when 15 % cellulose was used. Unstable porous structure with reduced surface area was observed when 20 % cellulose was incorporated. The phosphate adsorption capacity of the pellets was investigated, and the concentration of phosphate was determined by using a UV-Vis spectrophotometer (DR 2700, HACH) via the US EPA PhosVer 3® (Ascorbic Acid) method at 880 nm. Isothermal study showed an average adsorption capacity of 96.4 mg/ g was yielded when 15 % cellulose was used.

2.7.1.4 Oil absorption

Frequent oil spills during marine transportation and organic solvent leakage have been persistent sources of water pollution. Owing to the low density, spilled oils/organic solvents usually float on the top of water. Aerogel is a promising absorbent to remove oil spills due to its light, porous, flexible, and recoverable properties. CN-based aerogels have attracted great interests because they can be produced from natural and abundant raw materials. To allow the aerogels to float on water to selectively uptake oils, superhydrophobic modification of the cellulose-based aerogels is required to reduce their bulk absorption towards water. As discussed early, the application of CN-based aerogel for oil absorption has been reviewed in the past 5 years, thus only several representative works will be highlighted here.

Chemical vapor deposition (CVD), esterification, and fluorination methods were commonly used to fabricate a superhydrophobic surface. Zheng et al. prepared glutaraldehyde crosslinked PVA/CNF aerogel by freeze drying, which was treated with methyltrichlorosilane via a simple thermal chemical vapor deposition process. The resulted aerogel possessed superhydrophobic (water contact angle 150.3 ± 1.2°), superoleophilic, low density, and high porosity properties, allowing the aerogel to float on water for various types of oil spill adsorption. It could uptake oil weights ranging from 44 to 96 times compared to its dry weight depending on the oil density.[72] Similarly, Rafieian et al. prepared CNF aerogels from CNF dispersion of varying concentrations through freeze drying, and they were further modified via chemical vapor deposition (CVD) of

hexadecyltrimethoxylan (HDTMS). The resulting hydrophobic aerogels possessed water contact angles ranging from 121° to 139°, which were effective to remove oil and organic pollutants from water.[125] In another study by Zhou et al., a composite aerogel with highly ordered anisotropic lamellar microstructure was prepared by directional freeze-drying of graphene/polyvinyl alcohol/CNF mixture. The freeze-dried composite aerogel was further treated by carbonization processes to yield compressive and superhydrophobic properties (water contact angle of 138°). Such aerogel showed excellent oils and organic solvents absorption capacity of up to 155-288 times its own weight due to its parallel lamellar porous structure. In addition, the aerogel was reusable by a convenient extrusion process due to its elastic property.[126]

2.7.2 Cellulose nanomaterial-based aerogels as filters

The discharge of oily wastewater containing emulsions and oil spills during marine transportation have been one of the major sources of water pollution for decades. Removal of emulsions from oily wastewater is a global challenge especially for surfactants stabilized emulsions due to their good stabilities and micro- or nano- droplet sizes.[11] In another aspect, water will also be a pollutant when it exists in oils particularly in fuels regardless whether they are free, soluble, or emulsified. The presence of water promotes microbial growth and corrosion that could further damage the vehicle engine system.[127,128] Therefore, the removal of emulsified oil and water droplets is of great importance for environmental management as well as oil purification industries.

Traditional methods including centrifugation, oil skimming, adsorption, and floatation for oil/water mixture separation are not applicable to separate emulsions.[12] Filtration technology is promising for oily wastewater treatment due to its high efficiency and low energy consumption. Commercial 2D membranes, such as PVDF and PTFE membranes exhibited high separation efficiency for emulsions due to their small pore size. However, they are easily fouled by contaminants due to the low porosity and short permeation channels, thus compromising the duration and separation performance. 3D porous aerogels overcome such shortcomings compared to 2D membranes because of their high porosity and longer channels. Other than porosity and thickness, proper surface wettability and pore size are two key factors for aerogel filters to achieve an excellent separation efficiency by either blocking oil or water droplets permeate through the filter.[11] Cellulose based membranes were widely reported for dyes and heavy metal ions removal, emulsion separation, air purification, and other types of particles exclusion.[102,129] In contrast, cellulose aerogel filters were only reported for oil/ water mixture, oil-in-water emulsions, water-

in-oil emulsions separation in the past decade. In the scenario of oil-in-water emulsions separation, superhydrophilic cellulose aerogel filters possess intrinsic advantages over superhydrophobic filters due to their low oil adhesion while high water affinity properties. On the other hand, superhydrophobic cellulose aerogel filters are widely adopted for oil spill cleanup and water-in-oil emulsions separation.[130]

2.7.2.1 Superhydrophilic CN-based aerogel filters

Cellulose has intrinsic superhydrophilic property due to the abundance of surface hydroxyl groups. Its interaction with water is associated with different length scales. As illustrated in Figure 2.10 (B), the interaction consists of hydration, wetting, capillarity - diffusion when the hierarchy degree of cellulose extends from supramolecular structure, 1D primary fiber, 2D fiber assemblies, and 3D bulk porous materials.[131] A large amount of water can be retained in the aerogel network, forming a water film on the surface, which prevents the adhesion of oils. In general, only a few publications describing the application of superhydrophilic cellulose aerogel for oil-in-water emulsions filtration have been reported in the last ten years. In contrast, superhydrophilic cellulose aerogel for oil/ water mixture filtration are widely reported.

A superhydrophilic and under-water superoleophobic cellulose sponge solely prepared by cellulose was first developed by Wang et al. in 2015. Generally, the sponge was prepared by dissolving of cellulose powder in $ZnCl_2$ solution, followed by a regeneration process. To fabricate a double layer cellulose sponge with different pore size, pore forming agent ($Na_2SO_4 \cdot 10H_2O$) was added in the upper layer before regeneration as illustrated in Figure 2.10 (C). The resulting cellulose sponge displayed a distinct two layers with micropores (> 3 μm) in the upper layer and nanopores (< 1 μm) in the bottom as shown in Figure 2.10 (D, a and b). Underwater oil contact angle (OCA) and underoil water contact angle (WCA) are commonly examined to investigate the wettability. As expected, the cellulose sponge possessed underwater OCAs greater than 150° and underoil WCA of nearly 0° (see Figure 2.10 (D, c)), suggesting its superhydrophilic and underwater superoleophobic characteristics. Toluene in water emulsion was prepared by mixing 4 mL toluene in 120 mL water containing 0.2 wt% Tween 80 as surfactant. The produced emulsion droplet has a size below 20 μm as seen in Figure 2.10 (D, d). Owning to the unique pore structure, the cellulose sponge could achieve an excellent oil-in-water emulsion separation efficiency over 99.94 %. A clear contrast for the emulsions before and after filtration was observed in Figure 2.10 (D, e), where the filtrate on the right side is clearly transparent. However, the filtration flux was

only about 91 L/(m^2·h) due to the nano-sized pores in the bottom layer. Notably, such configuration allowed the sponge forming a layer of water film on the upper layer and preventing the permeation of oil droplets through the bottom layer.[132]

In 2021, Yang et al. adopted the same method to prepare a superhydrophilic and underwater superoleophobic cellulose sponge. The difference is that Yang et al. prepared a partially dissolved cotton cellulose, and the final sponge possessed a hierarchical pore structure including nano-, micro-, and macro-scale pores. In addition, the sponge exhibited ultralow underwater oil adhesion force (< 2 μN) when tested with various types of oils. The superoleophobic nature of this sponge contributed to its excellent separation efficiency towards both surfactant-free and surfactant-stabilized oil-in-water emulsions. For example, a separation flux of 290 L/(m^2· h) and efficiency of 99.2% were achieved solely driven by gravity for Tween 80 stabilized n- Octane in water emulsions.[133]

In another study, a super-hydrophilic and underwater super-oleophobic polyamideamine-epichlorohydrin (PAE) crosslinked CNF aerogel filter with tunable pore structure was synthesized by He et al. The prepared aerogel filter showed an underwater oil contact angle about 155.6° ± 2.5° and nearly 0° water contact angle in air. The pore structures can be tuned by altering the CNF concentration before freeze-drying. As a result, the aerogel achieved an excellent separation efficiency for both oil/water mixture (100 %, even after 10 cycles) and surfactant-free oil/water emulsions (98.6%) solely by gravity.[134]

For oil/ water mixture separation, Sun et al. prepared a superhydrophilic and underwater superoleophobic aerogel solely by CNF. Negatively charged CNFs were prepared by sodium periodate oxidation and consecutive sodium sulfite sulfonation. A more uniform dispersion was obtained after such modification, yielding a better dispersion morphology of nanofibers in the final aerogel after freeze drying. The aerogel showed very high underwater OCA of 173.9°, 167.1°, 160.9°, 172.7° and 172.5° for five different oils, hexadecane, hexane, toluene, paraffin oil and kerosene, respectively. After pre-wetting, the aerogel could act as filters to realize five types of oil/water mixtures separation. However, the authors did not explain how the aerogel maintained its shape in water as the aerogel was formed solely by physical entanglement between CNFs. Although a compression test was conducted, the testing condition (in dry or wet state) and the unloading curve were not shown.[135]

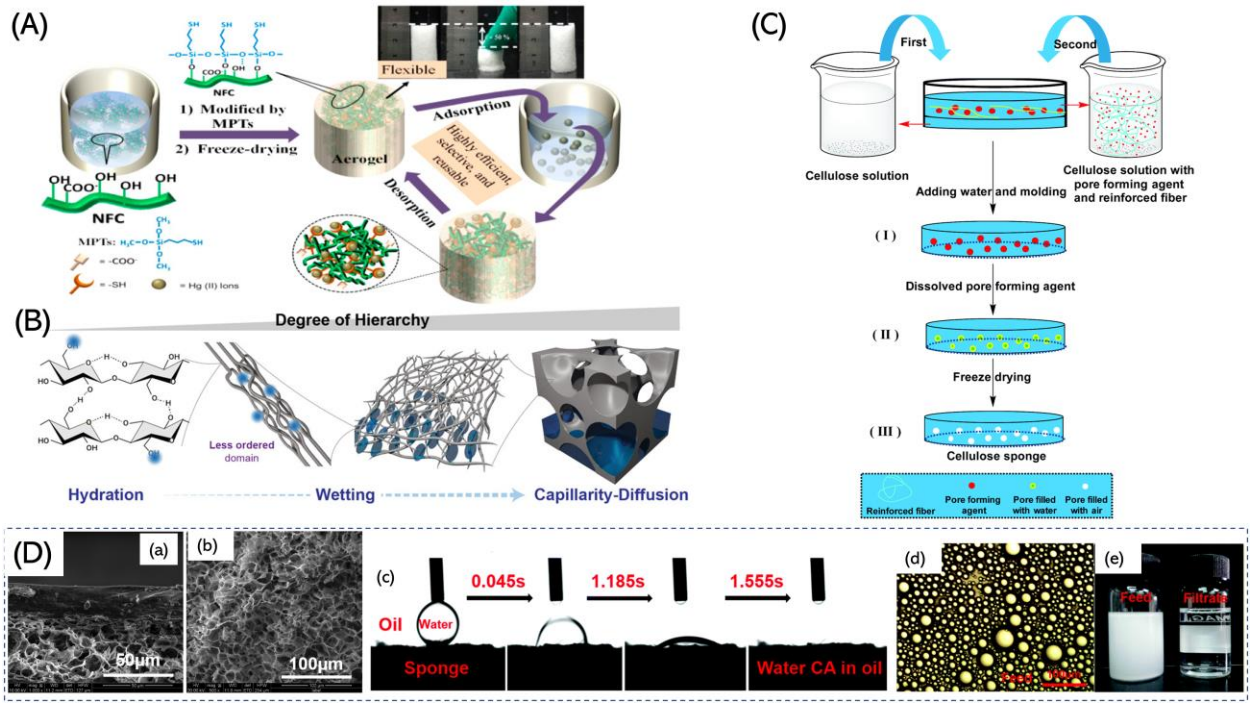

Figure 2.10 (A) Schematic illustration of the preparation process of 3-mercaptopropyltrimethoxysilane (MPT) modified CNF aerogel.[109] (B) Water interaction scale with cellulose along with its degree of hierarchy.[131] (C) Illustration of the preparation process of double layer superhydrophilic cellulose sponge.[132] (D) SEM images of double layer cellulose sponge (a) and a top view of the upper layer (b), underoil water contact angle test of a dried sponge immersed in n-hexane (c), microscope image of toluene in water emulsions stabilized by tween 80 (d), and photos of emulsions before and after filtration (e).[132]

Other superhydrophilic and underwater superoleophobic composite aerogel prepared using hydrophilic components such as graphene, chitosan, and alginate together with CNF were also reported for oil/water mixture separation. For example, Li et al. prepared an alginate/CNF composite aerogel using Ca^{2+} ions as crosslinkers. The resulted aerogel possessed numerous randomly distributed micropores with sizes of 50-200 μm. Besides, it displayed under seawater oil contact angles greater than 155° for n-hexane, kerosene, vacuum pump oil, toluene, soybean oil and crude oil. Such underwater superoleophobicity (underwater OCAs >150°) could be maintained even after being immersed in the seawater for 30 days due to the salt- tolerant property of alginate. Results showed that the composite could hold an intrusion pressure about 1.46 KPa, allowing the separation of kerosene-seawater mixture with a maximum height of 18.6 cm for kerosene.[136] In

their another study, the authors mixed chitosan with CNF to prepare a composite aerogel for oil/water mixture separation. The resulted aerogel also possessed salt-tolerant and superoleophobicity properties under seawater. Moreover, it was able to separate various kinds of oil/seawater mixtures with high efficiency (> 99%) and excellent recyclability, which is very promising for oil/water separation in marine environments.[137]

2.7.2.2 Superhydrophobic CN-based aerogel filters

Except for oil absorption, superhydrophobic CN-based aerogels could also be used as filters for water-in-oil emulsions separation. To construct a superhydrophobic surface, surface roughness and low surface energy are necessary. Zhou et al. prepared a superhydrophobic CNF aerogel by freeze drying a mixture containing methyltrimethoxysilane (MTMS) modified CNF and SiO_2 (~30 nm) nanoparticles. It is known that MTMS is a hydrophobic reagent that possesses low surface energy, while the presence of SiO_2 could increase the surface roughness. Hence, the resulted aerogel displayed a water contact angle of 168.4° in air. In addition, the aerogel possessed multi-scale pores including nano-sized pores ~6-40 nm, micro-sized pores around 8- 20 μm. Various water-in-oil emulsions with a water content of 2 wt% stabilized by 0.1 wt % span 80 were prepared to evaluate the aerogel separation performance. Water droplets in the range of 5-10 μm were observed under optical microscope before filtration. A high separation efficiency (> 99%) and high oil flux (1910 ± 60 L/(m^2·h)) was achieved solely driven by gravity. The separation was completed by size sieving and de-emulsification effects attributed to the small pore size as well as the surface super-hydrophobicity. Moreover, the aerogel could maintain stable efficiency even after 20 recovery cycles. Such advantages make the aerogel very promising for oil/ organic solvents purification.[138]

Grafting low-surface-energy long alkyl chain or fluorine functional groups to aerogel surface is a common strategy to produce a superhydrophobic surface. However, these organic reagents, especially fluoroalkylsilane, could cause serious water pollution and threat human being health in the long run. The exploration of green and efficient modifiers has never ceased. It is known that surface wettability is determined by both micromorphology structure and chemical composition. Li et al. deposited copper nanoparticles on cellulose fibers extracted from Sisal by chemical reduction of copper acetate in the presence of hydrazine hydrate. Cu nanoparticles with particle size ranging 50-200 nm were distributed on cellulose fibers as seen in Figure 2.11 (A). The resultant cellulose aerogel possessed a water contact angle around 150.3°, while an oil contact angle around 0° (Figure 2.11 (B)). The superhydrophobic and superoleophilic property allowed

the aerogel absorbed oils both lighter and heavier than water. In addition, it could separate oil/water mixtures and emulsions continuously and rapidly with a high separation efficiency (above 97%) as seen in Figure 2.11 (C).[139]

2.7.2.3 Superamphiphilic CN-based aerogel filters

To achieve a dual selectivity for emulsions separation, smart filters were also reported. In recent years, stimuli-responsive compounds, such as PDMAEMA, PNIPAM, TiO_2, ZnO, were adopted to fabricate such smart surfaces. A wettability transition was achieved when the filters were subjected to external stimuli, for example pH, temperature, gas, and light.[140] Switchable wettability can be realized by grafting responsive polymers on CN aerogels. A CO_2 responsive CNF aerogel was reported by Li et al., who grafted poly (N,N-dimethylamino-2-ethyl methacrylate) (PDMAEMA) polymer brushes on PEI modified CNF aerogel *via* surface-initiated atom-transfer radical polymerization as illustrated in Figure 2.11 (D). BJH method revealed that the resulting aerogel possessed numerous mesopores in the range of 2-10 nm and 60-120 nm. Surface wettability of the aerogel was further evaluated by water contact angle with and without CO_2 treatment. As evident from Figure 2.11 (E), the aerogel possessed a water contact angle of around 130° even after 50 s without CO_2 treatment, while it gradually decreased from 130° to 0° within 50 s after treatment with CO_2. The switchable wettability allowed the aerogel to realize oil/water mixture and their emulsions separation. By bubbling with CO_2 for 15 min, the aerogel was effective to separate water from oil-in-water emulsion, and the process could be reversed for separation of oil from water-in-oil emulsion after bubbling with N_2 for 15 min.[141]

The same group has also reported a CNF aerogel with pH-responsive wettability in 2020 for oil-water separation. CNF and cellulose acetoacetate fibers were crosslinked with amino silane (3-aminopropyl) triethoxysilane (APTES) to form a strong porous cellulosic network. By controlling the amount of APTES, some acetoacetyl moieties were allowed to react with alkylamines via reversible Schiff base reaction. Three types of alkylamines of different of alkyl chain lengths, i.e., hexylamine (HA), dodecylamine (DCA) and octadecylamine (ODA), were grafted on the crosslinked aerogel to yield hydrophobic aerogels. Water contact angle of the aerogel increased from 129 ± 2°, 135 ± 2°, 146 ± 2° with increasing of alkyl chains length. The aerogels became superhydrophilic by the removal of alkylamines when treated with HCl. Therefore, it could achieve excellent separation efficiency for both water-in-oil (99.2%) and oil-in-water emulsions (99.5%) by attaching and de- attaching alkylamines, respectively.[142]

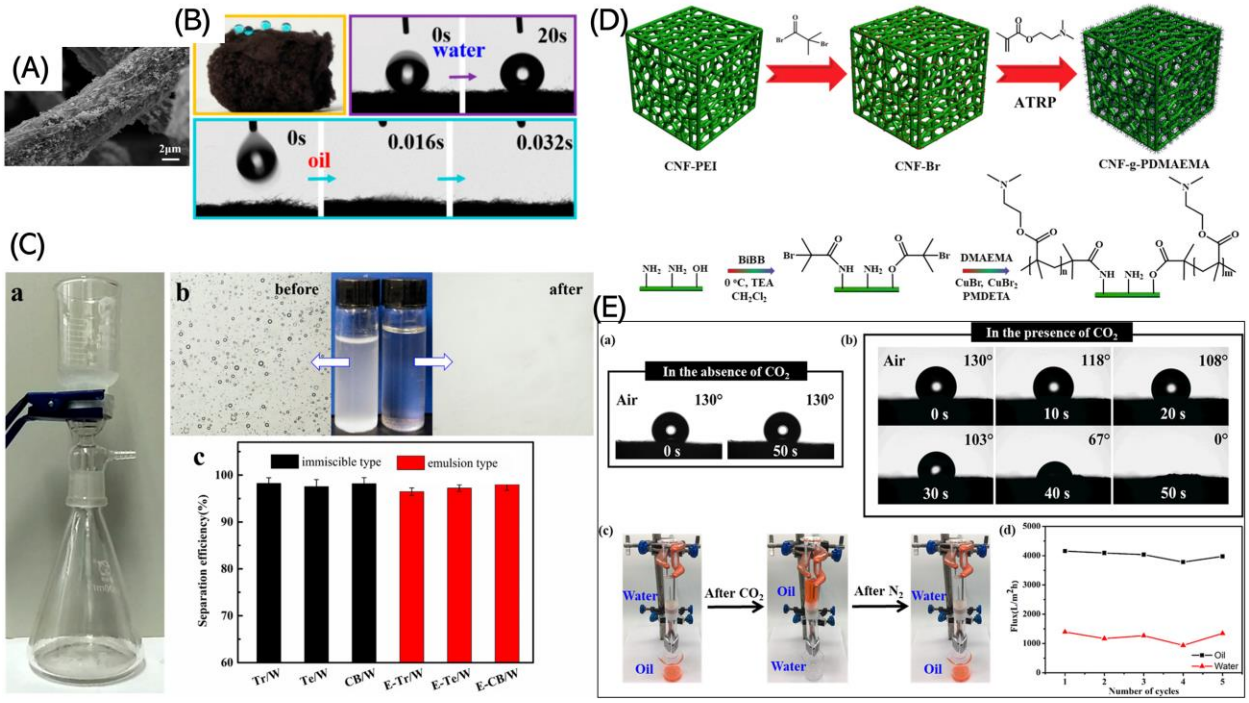

Figure 2.11 (A) SEM image of Cu nanoparticles coated cellulose fiber. (B) Water and oil contact angles of the Cu nanoparticle modified cellulose aerogel in air. (C) Set up for water-in-oil emulsion separation (a), optical microscope images of the water-in-oil emulsions before and after filtration (b), and a summary of oil/water mixture and water-in-oil emulsions efficiencies (c).[139] (D) Schematic illustration of the synthesis process of PDMAEMA grafted CNF aerogel. (E) Water contact angle of the aerogel in air without CO_2 treatment (a), with CO_2 treatment (b), photograph of its CO_2 responsive oil/water mixture separation performance (c), and fluxes of oil/ water mixture separation in the absence and presence of CO_2 (d).[141]

2.8 Summary

In this chapter, commonly used commercial pesticide formulations and their corresponding preparation, components, and characteristics were firstly reviewed. Then, the preparation, property, surface, and end modification methods of cellulose nanomaterials were reviewed. In the rest of this chapter, CN-based applications were reviewed. Due to the large surface area, high aspect ratio, amphiphilic, and sustainable properties, CNs are effective as Pickering emulsion emulsifiers. The emulsion stabilization mechanism of CNC was discussed and compared with that stabilized by surfactants. Factors such as shape, aspect ratio, surface charge, wettability, and oil polarity on

emulsion stability were also discussed. In addition, CNCs are effective carriers for organic compounds such as drugs and dyes. Pesticide delivery systems based on CNs such as hydrogel, emulsions, capsules, dispersions, and other systems were also reviewed. CNs can also be used as skeletons for aerogel preparation for multiple applications. The general preparation process, drying methods, pore forming templates and methods for aerogel beads preparation were reviewed. Lastly, CNs based aerogels as absorbent for heavy metal ions, dyes, pesticides & fertilizers, and oils adsorption were summarized. CNs based aerogels as filters for oil/water mixtures and emulsions separation were also introduced.

Through the literature review, it is found that CNs are excellent natural materials for pesticide delivery and pollutants removal. However, several research gaps remained between CNs and their applications in agriculture and wastewater treatment. Firstly, report on the capacity of end-modified CNC as Pickering emulsifier has not observed. Consequently, its capacity for hydrophobic compounds encapsulation is unknown. Besides, the loading capacity of pristine CNC for hydrophobic compounds and the corresponding driving force have not been reported. For CN-based aerogel beads, a method that can precisely measure the mechanical strength is lacking. Furthermore, the pollutant adsorption performance between the aerogel bead and aerogel monolith has not studied. Lastly, there are very few studies on the application of CN-based aerogel for emulsified oil droplets removal. The goal of this doctoral research is to narrow the gaps and to expand the application of CNs.

Chapter 3* Amphiphilic Cellulose Nanocrystals for Enhanced Pickering Emulsion Stabilization

Sulfated cellulose nanocrystals (CNC) with high surface charge density are inadequate for stabilizing oil-water emulsions, which limits their applications as interfacial stabilizers. We performed end-group modification by introducing hydrophobic chains (polystyrene) to CNC. Results showed that the modified CNC are more effective in emulsifying toluene and hexadecane than pristine CNC. Various parameters were investigated, such as concentration of particles, electrolytes and polarity of solvents on the characteristics of the emulsions. This study provides strategies for the modification of cellulose nanocrystals to yield amphiphilic nanoparticles that enhance the stability of emulsions. Such systems, bearing biocompatible and environmentally friendly characteristics, are attractive for use in a wide range of industries spanning food, biomedicine, pharmaceuticals, cosmetics, petroleum etc.

Graphical Abstract

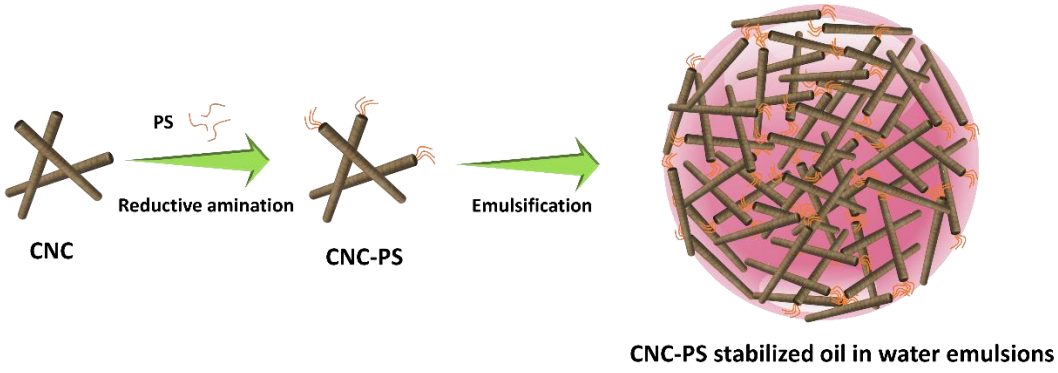

* This chapter is adapted from a paper "Tang, C.; Spinney, S.; Shi, Z.; Tang, J.; Peng, B.; Luo, J.; Tam, K. C. Amphiphilic Cellulose Nanocrystals for Enhanced Pickering Emulsion Stabilization. Langmuir 2018, 34 (43), 12897-12905."

3.1 Introduction

Emulsions stabilized by solid particles, known as Pickering emulsions, have attracted increasing attention as alternatives to surfactant stabilized emulsions.[143–145] They require less emulsifier, benefit from increased stability, and possess other advantages when compared to emulsions stabilized by surfactants.[146–150] Pickering emulsions perform better over classical emulsions because the solid particles are irreversibly adsorbed onto the oil-water interface, and subsequently form an effective electro-steric protective shield for the emulsified droplets.[36,151–154] While in surfactant-based emulsions, thermodynamic equilibrium is usually observed, which means that the stabilizer molecules are exchanging between oil-water interface and bulk continuous phase.[146]

Currently, there is an increasing interest in sustainable systems that are natural, green, and abundant, where the present need is achieved without compromising the resource of future generation. Thus, the production and extraction of sustainable nanoparticles for use in the formulation of Pickering emulsions have been actively pursued over the last 10 years.[155,156] Cellulose nanocrystal (CNC), derived via the acid hydrolysis of biomass, are one type of nanoparticles that have received increasing attention.[145,151–153,157–159] Due to their renewable and "green" characteristics[160–162], and functional groups on their surface that can be readily modified[163,164], new systems have been developed. Hence, this sustainable material has been used in a wide range of applications, such as catalyst and drug carrier[165,166], composite nanofiller[167], as well as Pickering emulsifier.[168,169] Their capabilities to stabilize various types of emulsions, such as oil-in-water, water-in-oil, water-in-water and complex emulsions have been reported.[155,159,170,171] All these studies have shown that surfactant-free emulsions for pharmaceutical, food, and cosmetic applications can be formulated using nanomaterials from nature.[172]

As a result of the anhydrous glucose units, CNC possesses abundant functional moieties, such as aldehyde and hydroxyl groups, which can be modified, enabling the control over their physical or chemical properties.[173,174] Anisotropy in the modified CNC can be enhanced by taking advantage of decorated aldehyde groups at the end of the CNC nanorods, allowing for the selective modification of the reducing ends of CNC. Although such study has not been widely reported, several groups have taken advantage of the reactive reducing ends to prepare functional cellulose nanocrystal with special characteristics.[32,175–177] Lokanathan et al. introduced thiol groups at the reducing aldehyde ends of cellulose nanocrystals using either a one-step method via direct

reductive amination or a two-step procedure consisting of oxidation and carbodiimide-mediated reaction.[32] Very recently, Zoppe et al. reported on a 3-step process to introduce initiators at the reducing end of cellulose nanocrystals, where the end-group can be used to initiate a controlled radical polymerization reaction.[177] However, such modification protocol is complicated and some degree of functionalization occurred along the principal CNC axis (surface), which is unavoidable. Acid hydrolysis by sulfuric acid is one of the common methods to produce negatively charged CNC. However, sulfated CNC is not effective in stabilizing oil droplets due to the strong repulsion between the nanoparticles that inhibit their adsorption at the oil-water interface.[156,178] Surface modifications of the CNC are commonly performed to improve the stability of the emulsions, and most of these studies focused on the surface hydroxyl group modifications.[154,168,169,179,180] However, a possible modification of CNC can be conducted at the reducing end to prepare amphiphilic nanoparticles or surfactant-like particle, where such modification is rare. In this work, we seek to prepare an amphiphilic nanoparticle, which is akin to the concept of a "particle surfactant". With a hydrophilic CNC surface and a hydrophobic end group, the amphiphilic character of the modified CNC will improve the wetting characteristics that promotes the partitioning of the nanoparticle to the oil-water interface, thereby enhancing the emulsion stability. This approach consists of a one-step modification protocol, is simple and straight forward, where amine terminated polystyrene as a model compound is grafted to the reducing end of sulfated CNC via the Schiff base reaction. Additionally, the imine linkage could be further reduced to amine groups by the addition of reducing agents (Scheme 3.1). Different reaction conditions and parameters, such as concentration of particles, electrolytes and polarity of solvents on the properties of the emulsions were examined. This study provides some perspectives on the modification of CNC, which could be utilized to prepare alternative amphiphilic nanoparticles to improve the stability of emulsions.

3.2 Materials

Sulfated cellulose nanocrystals were kindly provided by Celluforce Inc. Amine terminated polystyrene (average M_n = 5000 Da, PDI<1.2; average M_n = 10000 Da, PDI<1.3), N, N-dimetheyl formamide (DMF, anhydrous 99.8%), tetrahydrofuran (THF, anhydrous 99.9%), sodium cyanoborohydride (reagent grade, 95%), hydroxylamine hydrochloride (reagent grade, 98%), toluene (anhydrous 99.8%), hexadecane (anhydrous 99%), potassium bromide (KBr), sodium chloride (NaCl), and Nile red were purchased from Sigma Aldrich unless specified otherwise. All

chemicals were used without additional purification, unless stated otherwise. Milli-Q water (resistivity of 18.2 MΩ.cm) was used to prepare the aqueous dispersions.

3.3 Methods

3.3.1 Selective grafting of polystyrene onto CNC via reductive amination

0.5 g of cellulose nanocrystals were dispersed in 50 ml of N, N-dimethyl formamide (DMF) in a 250 mL reaction flask. The dispersion was sonication for 10 mins to obtain a well-dispersed CNC dispersion. 50 mg of amine terminated polystyrene (M_n of 5000 or 10000 Da) was added to the mixture, and the dispersion was stirred at 600 revolutions per minute. 5 mg of sodium cyanoborohydride was weighed into another vial and dissolved in 5 mL of DMF. The solution of sodium cyanoborohydride was then transferred to the original reaction flask, and degassed with N_2 under constant stirring for 20 minutes. After degassing, the dispersion was allowed to stir for certain time (refer to discussion section) at room temperature (r.t.) or 70 ^oC. The reaction mixture was then recovered via centrifugation in tetrahydrofuran (three times) and acetone (once). The nanoparticle was re-dispersed in water and dialyzed (M_w cut-off of 12000 Da) against Millipore water for 3 days with constant change of water. The solution was then concentrated and freeze-dried for subsequent use.

3.3.2 Preparation of Pickering emulsions

All the emulsions were prepared using pristine CNC or modified CNC dispersions, where water and toluene or hexadecane were used as the aqueous and organic phase respectively. The emulsions were prepared using an ultrasonic probe (Misonix-Microscon-XL2000), unless otherwise stated. All the emulsions were produced in 1 and 2 mL of organic and aqueous phase respectively, with various concentrations of nanoparticles (based on the aqueous volume). The power setting was calibrated using DI water, achieving a 10 W power output when partially immersed in DI water. The mixtures were premixing by hand and then subjected to sonication for 1 minute.

3.3.3 Characterization of nanoparticles and emulsions

Dynamic light scattering (DLS) and ζ-potential experiments were conducted using a Malvern Zetasizer Nano series at nanoparticles concentration of 0.04 wt%. Values for zeta potential were determined from the average of 3 measurements, consisting of 12 runs per measurement. The surface tension profiles were acquired using a surface tensiometer (Data Physics DCAT 11).

Samples were prepared by dispersing the freeze-dried powders in water and homogenized to yield a homogeneous dispersion.

Fourier transform infrared spectroscopy (FTIR) spectra were obtained using a Bruker Tensor 27 spectrometer FT-IR spectrometer with a resolution of 4 cm^{-1} and a scanning number of 32 from 400 to 4000 cm^{-1}. Briefly, pellets were prepared by mixing the freeze-dried samples with KBr, grinding via mortar and pestle and the compressed into a pellet. Nuclear magnetic resonance (NMR) spectra were recorded on a Bruker Advance 500 MHz spectrometer with DMSO-d6 as solvent, where 15 mg of samples (CNC-PS or CNC) were dissolved in 1 mL DMSO-d6.

The aldehyde content on the reducing end of CNC was determined using the classical hydroxylamine hydrochloride[181] as well as the potentiometric titration techniques.[32] The two methods are described below:

In the first method, the reaction of hydroxylamine hydrochloride with the aldehyde on the nanoparticles produces an oxime, and releases an HCl equivalent for each formyl residue. The amount of HCl produced was determined from potentiometric titration, and the change in the pH values were used to determine the amounts of aldehyde groups on the nanoparticles. Typically, 1.0 g of hydroxylamine hydrochloride powder was added to 50 ml of 1 wt% CNC or CNC-PS that was kept stirring under dark for 12 hrs.

In the second method, the aldehyde groups on the reducing end of CNC were selectively oxidized to carboxyl groups as described by Arcot et al.[32] Specifically, $NaClO_2$ powder was introduced to 10 mg/mL CNC suspension to obtain a final $NaClO_2$ concentration of 250 mM. The pH of the dispersion was adjusted to 3.5 using acetic acid, and the reaction mixture was stirred for 20 h at room temperature. Then, the mixture was centrifugated and dialyzed against MQ water to remove excess reactants and side products. The resulting CNC with carboxyl functionalized ends (CNC–COOH) were subjected to potentiometric and conductometric titration using 0.005 M NaOH, and the aldehyde content on the reducing end of CNC was determined.

The emulsions were all visualized by an inverted optical microscope (Nikon Elipse Ti–S) equipped with a CCD camera (QImaging ReTIGA 2000R). A total of 10 μL of the resulting Pickering emulsion was added onto glass slides, then a single drop of water was added to dilute the emulsions and observed in a microscope. Droplet diameter was measured by image analysis using the "ImageJ" software. A total of at least 300 droplets were measured and the surface mean diameter

D (3,2) (the Sauter diameter) was reported as the average diameter. Additionally, 0.3 wt% aqueous dispersion of samples were prepared by spraying onto copper grids (200 mesh coated with copper) and allowed to dry for TEM characterizations (Philips CM10).

The surface coverage (C) was determined according to Capron et al,[182] which is defined as the ratio between the maximum surface area of CNC particles to the total surface displayed by the oil droplets:

$$C = \frac{m_p D}{6h\rho V_{oil}} \quad (3.1)$$

where m_p is the mass of CNC-PS particles in the aqueous phase; D(3,2) is the surface-mean diameter of the emulsion droplets; V_{oil} is the volume of oil (1 mL), h is the width of the CNC-PS particles (10 nm) measured by TEM; ρ is the density of the CNC-PS particles (1.6 g/cm^3) assuming that this density is similar to that of the CNC.

The stability of the Pickering emulsions was monitored by the creaming behavior and the height ratio of the creaming layer to the total height (H %) was compared. Photographs of the vials containing the emulsions were recorded using a P1 digital camera (Olympus), and the thickness of the creaming layer was measured with a digital caliper. The oil fraction in the formulated emulsions was calculated from Eq. (3.2)

$$\text{Oil fraction} = \frac{1\ \text{mL}}{3\ \text{mL} \times \text{H}\%} \times 100\ \% \quad (3.2)$$

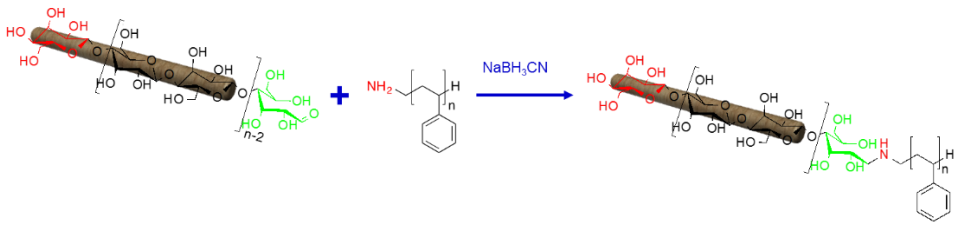

Scheme 3.1 Schematic illustration of the procedure used to selectively modify the reducing end of CNC with polystyrene (via reductive amination).

3.4 Results and Discussion

The chemical structure of cellulose suggests that two types of reactive sites could be used for covalent modification: hemiacetal group and hydroxyl groups. Cellulose nanocrystal (CNC), a product derived from cellulose fiber, could also possess the same chemical properties since the

chemical structures were retained after acid hydrolysis. For the hydroxyl groups, the hemiacetal group only exist at the reducing end of cellulose chains/molecules (See Scheme 3.1). This terminal unit is in an equilibrium state as it undergoes exchanges between the ring and open structure.[32,173,180] An aldehyde functional group could be exposed to the environment while in its open structure. Several studies have reported that further reactions with these aldehydes are typically slow, taking up to one week to achieve a good yield.[183] This is due to the low availability of the aldehyde functional groups.

3.4.1 Characterization of particles and colloidal dispersions

Polystyrene with a M_n = 5000 Da (PS-NH_2) was used as a well-defined representative polymer to conduct the reactions. In order to achieve good yield, we set the CNC to PS-NH_2 (M_n = 5000 Da) weight ratio at 10:1 and allowed the reactions to proceed at room temperature for 1, 3 and 7 days. The reaction mixture was then dialyzed with Millipore water, and a 0.2 wt% CNC dispersion was prepared for the surface tension measurements. Figure 3.1(A) shows that the surface tension of 0.2 wt% nanoparticle dispersion decreased from 72 to around 69 mN/m when the reaction time was increased. When compared to pristine CNC dispersions, the reduction in the surface tension is attributed to the hydrophobic polystyrene on the nanoparticles. Similar phenomena was observed when amphiphilic polymers were grafted onto CNC surface.[168,169,184] As negligible change was observed on the surface properties when the reaction time was extended from 3 to 7 days, we then conducted all subsequent modification by setting the reaction time to 3 days. For quantifying the aldehyde contents on the pristine CNC as well as the CNC-PS, the classical hydroxylamine hydrochloride (CHC) and potentiometric titration (PT) methods were used.[181] The CHC method revealed an aldehyde content on the reducing end of pristine CNC to be 24.5 μmol/g, while the PT method gave a value of 31.08 μmol/g (Data shown in Figure 3.1 (B)). Similar results was obtained by Lokanathan et al., who reported that the concentration of reducing ends on pristine CNC was between 35 to 45 μmol/g.[32] As the CHC method is efficient, we utilized it to determine the amounts of PS-NH_2 grafted on the ends of CNC nanorods. It was found that after modification, the aldehyde content decreased from 24.5 to 11.4 μmol/g, confirming that the grafting to the reaction was successful.

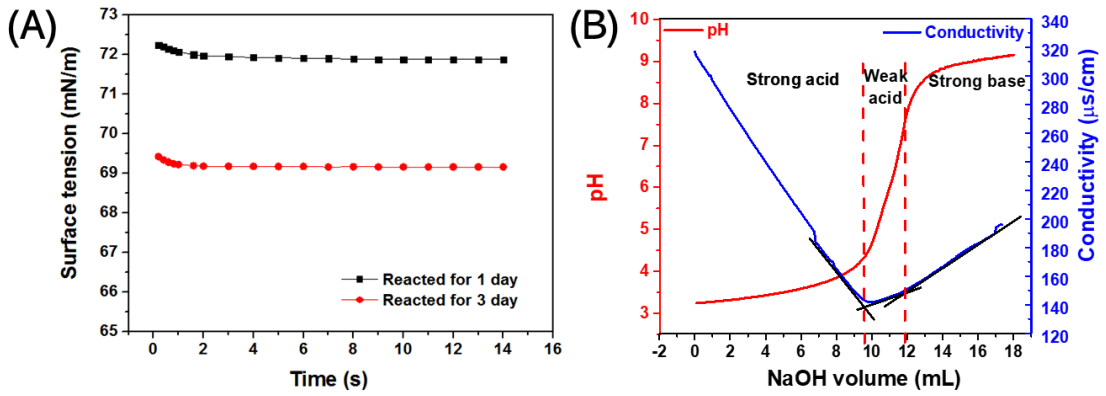

Figure 3.1 (A) Surface tension of CNC-PS reacted for 1 day (black) and 3 days (red). (B) pH and conductivity titration curves of selectively end carboxylated CNC.

Reaction temperature is another important factor that should be considered as the number of high energy collisions increased disproportionately when the temperature is increased. For this purpose, reactions were performed either at room temperature (r.t.) or at 70 ^{o}C for 3 days and the weight ratio between CNC and PS-NH_2 (M_n = 5000 Da) was kept at 10:1. The FTIR spectroscopy was used to confirm the presence of polystyrene on the cellulose nanocrystals after modifications. As discussed earlier, small amounts of aldehyde groups were accessible during the reactions and thus it would be difficult to achieve high grafting density. Figure 3.2 (A) shows the presence of several specific signals that were correlated to the structure of polystyrene. For example, the aromatic C-H stretching vibration at around 3000 cm^{-1}, the benzene ring C=C stretching at 1494 cm^{-1}, and the C-H bending at around 700 cm^{-1} were observed. The intensity of these peaks increased significantly by increasing the temperature of the reactions (e.g. from room temperature to 70 ^{o}C). The ^{1}H NMR spectrum (Data shown in Figure 3.2 (B)) was also recorded to confirm the presence of PS-NH_2 on the CNC after the reductive amination reaction temperature at 70 ^{o}C. It can be clearly observed that the chemical shifts at δ = 6.3-7.2 ppm and δ = 1.2–2.1 ppm are associated to the protons of -C_6H_5 and -CH_2-CH- on the polystyrene chains, respectively.

The colloidal properties of pristine and modified CNC nanoparticles were also studied as they provided valuable information on the physical properties of the modified CNC in aqueous solution (see Figure 3.2 (C) and Table 3.1). Although CNCs are rod-like nanoparticles, the scattering from dynamic light scattering measurements can be used to estimate the hydrodynamic diameter of the

nanoparticle.[184] Pristine CNC possessed a hydrodynamic diameter of 25.4 nm while CNC-PS (r.t.) and CNC-PS (70 ^{o}C) possessed a hydrodynamic diameter of 34.5 nm and 55.7 nm respectively. The increase in the size of the modified CNC is associated to the aggregation induced by hydrophobic interactions. Such aggregation was also evident from TEM analyses as shown in Figure 3.3. It can be evident that the size of rod-like CNC particles increased after hydrophobic modification of CNC with polystyrene. However, the aggregation was somewhat limited, and this may be due to the low grafting of the PS chain on the ends of CNC. We postulate that interesting properties may be achieved if we can tune the composition hydrophobic and hydrophilic domains of the system. The zeta potential of nanoparticle dispersions was measured, and they are summarized in Table 3.1. Pristine cellulose nanocrystals possessed a zeta potential of -47.5 mV, while the polystyrene modified CNC had a zeta potential ranging from -33.3 to -39.2 mV, depending on the reaction temperatures. When polystyrene chains were grafted on the ends of CNC, some inter-particle interactions may occur due to hydrophobic interactions, and the aggregated CNC may screen the surface charge of the CNC aggregates.

Table 3.1 A summary about the aldehyde contents, average size and zeta-potential of the nanoparticles

Nanoparticle	**Aldehyde contents (μmol/g)**	**Average Size (nm)**	**ζ-potential (mV)**
CNC	24.5	25.4	-47.5
CNC-PS r.t.	11.4	34.5	-39.2
CNC-PS 70^{o}C	6.8	55.7	-33.3

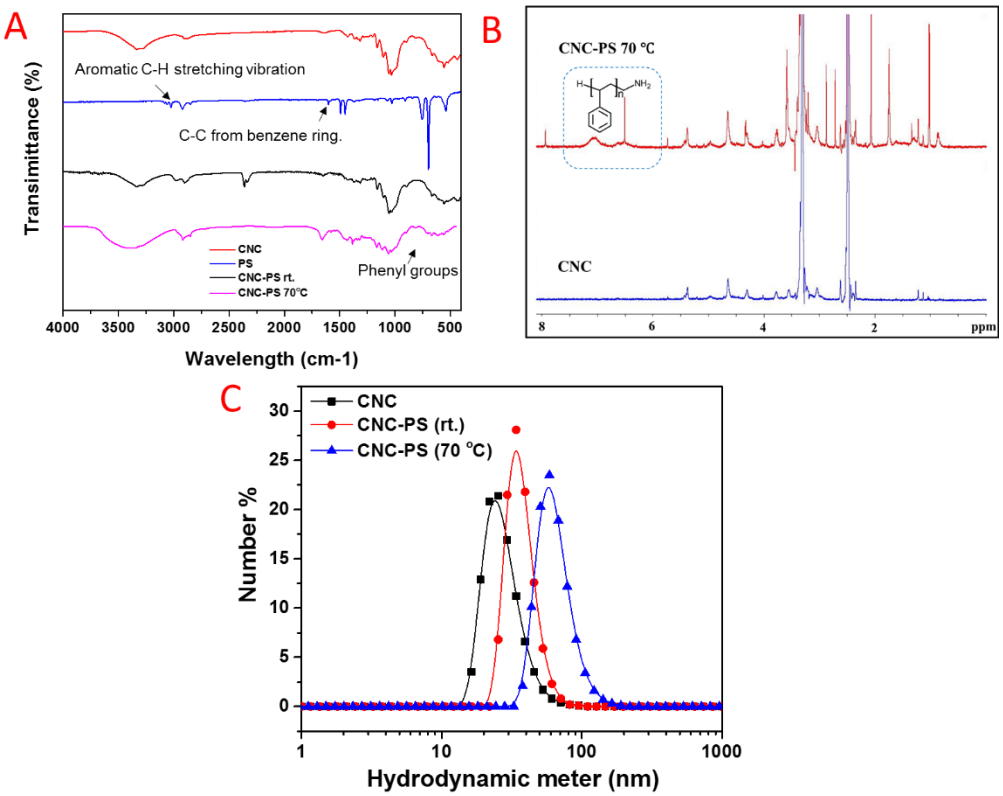

Figure 3.2 (A) FTIR spectra of sulfated cellulose nanocrystal (red), polystyrene (blue), CNC-PS from room temperature (black), CNC-PS from 70 ^{o}C (pink); (B) ^{1}H NMR spectrum of cellulose nanocrystal (blue), CNC-PS from 70 ^{o}C (red); (C) Intensity distribution of a 0.1 wt % suspension of nanoparticles (CNC, CNC-PS at r.t. and CNC-PS at 70 ^{o}C) in water measured by DLS.

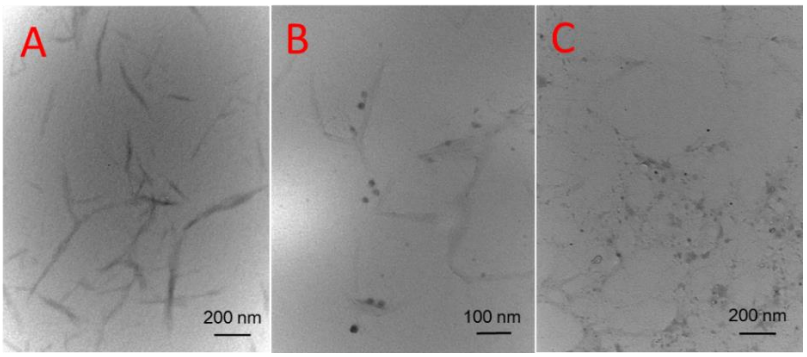

Figure 3.3 TEM images showing the morphologies of (A) pristine CNC, (B) CNC-PS from room temperature, and (C) CNC-PS from 70 ^{o}C.

3.4.2 Pickering emulsion stabilized by pristine CNC and CNC-PS

In order to investigate the capability of the various types of CNCs for the stabilization of oil/water emulsions, toluene was used as the model solvent and different concentrations of CNCs were examined. The volume of oil to water used was kept at 1 and 2 ml respectively, unless stated otherwise. As shown in Figure 3.4 (A), for all the concentrations examined (0.3, 0.5, 1.0 wt%), emulsions stabilized by pristine CNC were unstable against coalescence and total phase separation occurred immediately after sonication. All the sulfated CNC were highly negatively charged, and the highly hydrophilic character of the CNC hindered their partitioning to the oil-water interface. The strong repulsion force between the nanoparticles could induce the destabilization of emulsions as reported in the literature.[156,169] However, the toluene-in-water emulsions stabilized by CNC-PS (r.t.) were stable against coalescence for all the concentrations tested, as shown in Figure 3.4 (B) and Figure 3.4 (C). The emulsions would cream to the top of dispersed phase due to the density difference between the oil and water, however the emulsion remained stable against coalescence even after 4 months. This clearly showed the enhancement in the emulsion stability when the end modified PS-CNC was used as the emulsifier instead of CNC.

The effect of particle concentration on the characteristics of emulsions was investigated and the result is shown in Figure 3.5 (A). Toluene-in-water emulsions were stable against coalescence at high concentrations (above 0.3 wt%), while some coalescence and phase separation were evident at low CNC concentrations (below 0.3 wt%). This difference was attributed to the dosage of nanoparticles that were partition to the oil-water interface. Selective end modification imparts hydrophobic domains to the nanoparticles that promote the adsorption of the nanoparticles to the toluene-water interface. Ultimately, the average emulsion droplet size is controlled by the nanoparticles present at the oil-water interface, and the grafting of PS to CNC resulted in a reduction in the droplet size from around 25 to 14 μm (see Figure 3.6(B)). We also noted that the average emulsions droplet size remained unchanged when the nanoparticle concentration exceeded 0.5 wt%, and this is associated to the complete coverage of the oil-water interface by the modified CNC. Therefore, the surface coverage ratio is 1.4 with 0.5 wt% nanoparticles according to Eq. (3.1), which indicated that 0.5 wt% CNC-PS was sufficient to stabilize 1 mL toluene. Similar phenomenon was also observed by Capron et al. where the surface coverage ratio exceeded 100 %, where the particles exceeded the critical point.[42]

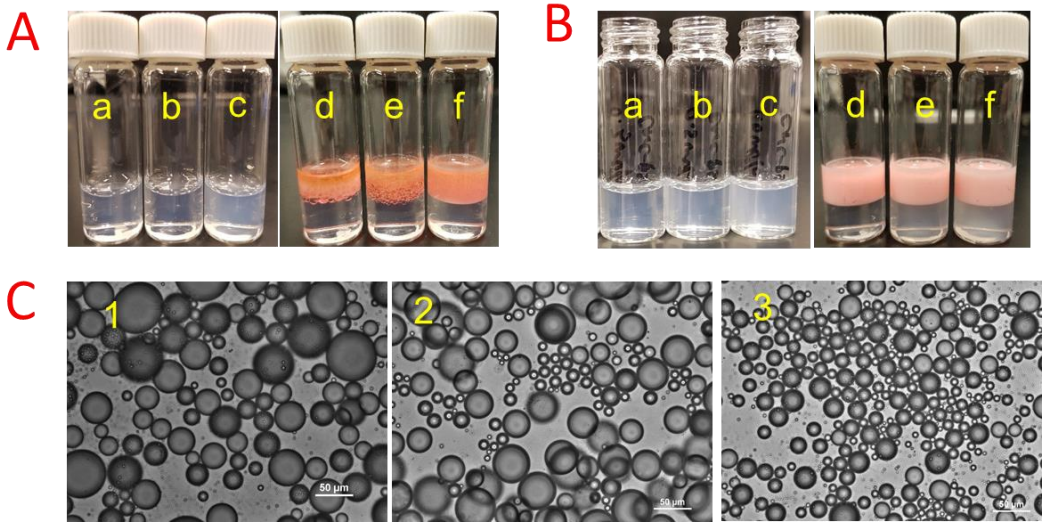

Figure 3.4 Photographs of (A) pristine CNC and (B) CNC-PS from room temperature (a: 0.3 wt%, b: 0.5 wt%, c: 1.0 wt%) suspensions as well as mixture after emulsifications (toluene water ratio 1:2, d: 0.3 wt%, e: 0.5 wt%, f: 1.0 wt%); (C) Optical micrographs of emulsions stabilized by CNC-PS from room temperature at different concentrations (toluene water ratio 1:2, 1: 0.3 wt%, 2: 0.5 wt%, 3: 1.0 wt%)

In order to gain a better understanding on the stability of the emulsions, the percentage height of emulsion phase over total mixture (H%) was visually evaluated, and the data are presented in Figure 3.5(B). For toluene emulsions stabilized by CNC-PS (r.t.), the H % for all the emulsions decreased rapidly within a storage period of approximately 15 mins, and followed by a slower decrease, and beyond 3 days, the H % remained constant. By increasing the nanoparticle concentrations, a progressive reduction in H % was observed (Figure 3.5 (B)). Similar phenomena were observed for other Pickering type emulsions stabilized by different nanoparticles.[148,185] In addition, the H % of all the stable emulsions turned to around 50 % after storage for 3 months, thus the oil fraction in the formulated emulsions is 66.7 % according to Eq. (3.2).

In addition to toluene, hexadecane was used as the organic phase in preparing the Pickering emulsions. It was evident that the emulsion stability was improved when compared to toluene, and the creaming rate was much lower. This could be attributed to toluene possesses a higher polarity than hexadecane; i.e. toluene ($\varepsilon = 2.38$; $\mu = 0.43$), and hexadecane ($\varepsilon = 2.05$; $\mu = 0.06$), where the polarity of each solvent is being expressed by its dielectric constant ε and dipole moment μ. At

concentrations below 0.5 wt%, the H% of the creaming layer of the emulsions decreased rapidly in the initial 30 mins, followed by a slower decrease. For emulsions with nanoparticle concentrations greater than 0.8 wt%, mild creaming was observed, where only a 4 % change in height was recorded after 4 hours for emulsions stabilized by 1 wt% CNC-PS (r.t.) (see Figure 3.5 (D)). The differences in the creaming behavior at low particle concentrations could be attributed to the effect of droplet size. It was found that the droplet size of emulsions stabilized by CNC-PS (r.t.) were much smaller when hexadecane was used instead of toluene (Figure 3.6 (A)). The droplet size decreased from 21 to 4.8 μm when concentrations was increased from 0.2 to 1.0 wt% (Figure 3.6 (B)). Once the concentration approached 0.5 wt%, further increase in the concentration did not result in a substantial reduction in the droplet size. Therefore, the surface coverage ratio at 0.5 wt% nanoparticles is 50 %, which was determined by Eq. (3.1). It means 50 % surface coverage is sufficient to stabilize 1 mL hexadecane. When the oil droplets have been sufficiently covered by the nanoparticles, a further increase in concentration will only lead to the excess nanoparticles being dispersed in the continuous phase. This will increase the volume fraction of particles, which will result in an increase the viscosity of the emulsion system. The creaming rate can be better understood from the Stokes equation, as shown in Eq. (3.3). In addition, similar with toluene-water emulsions, all the stable hexadecane-water emulsions had a H % around 50 % after three months storage, thus the oil fraction in the formulated emulsions was 66.7 % according to Eq. (3.2).

$$V = \frac{2r^2(\rho-\rho_0)g}{9\eta} \qquad (3.3)$$

where V is the creaming rate, r is the droplet radius, ρ is the density of the droplet, ρ_0 is the density of the dispersion medium, η is the viscosity of the continuous phase and g is the local acceleration due to gravity.

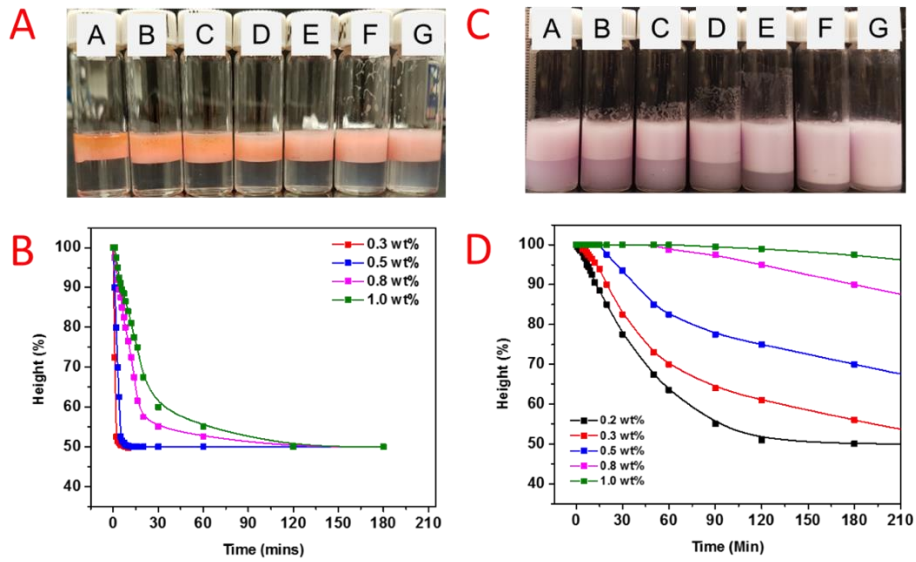

Figure 3.5 Optical micrographs of toluene (A) and hexadecane (C) in water emulsions stabilized by CNC-PS from room temperature at different concentrations (oil water ratio 1:2, A: 0.05; B: 0.1; C: 0.2; D: 0.3; E: 0.5; F: 0.8; G: 1.0 wt%). Creaming profile of toluene (B) and hexadecane (D) in water Pickering emulsion stabilized by CNC-PS from room temperature at different concentrations.

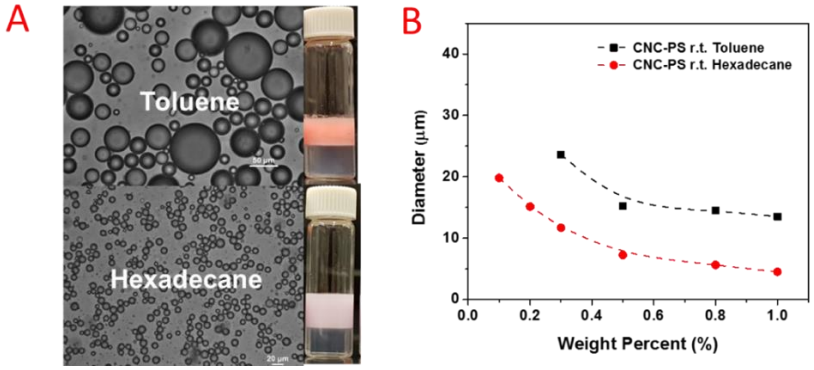

Figure 3.6 (A) Optical micrographs of toluene (up) and hexadecane (bottom) in water emulsions stabilized by 0.3 wt% CNC-PS from room temperature. (B) Droplet size dependence on nanoparticle content in the water phase in an emulsion containing toluene or hexadecane with a 1:2 oil to water ratio.

The effects of salt concentration on the stability of Pickering emulsions have been previously described in the literature.[156,179,185] By screening the charge of the sulfate groups on the surface of

CNC, the introduction of salt lowers the zeta potential of charged particles that favours the inter-particle interactions at the oil-water interface that enhances the stability of the emulsion. When salt was added to CNC-PS from r.t., similar behavior was observed. As shown in Figure 3.7, the zeta potential decreased when the salt concentration was increased. A visible increase in the viscosity was also observed with the increase in salt concentration, due to aggregation and network formation of the CNC particles and the emulsion droplets. Different amounts of NaCl were added to 0.5 wt% of CNC-PS (r.t.), and their impact on the stability of toluene-in-water emulsions were investigated. As discussed earlier, the addition of salt induced the aggregation of CNC, resulting in the increase in the turbidity of the dispersion (Figure 3.8 (A)). Figure 3.8 (B) and 3.8 (C) illustrate the decrease in the creaming rate and the emulsion droplet size (15.6 to 11.3 μm) caused by the increase in the salt concentration from 0 to 50 mM. However, beyond 50 mM, a further increase in the salt concentration did not have an impact on the creaming process. This trend is consistent with the trend observed from the zeta potential measurements. The reduction in the creaming rate could be correlated to the reduction in the size of the emulsion droplet and the increase in the viscosity of the continue phase as governed by the Stokes equation (Eq. (3.3)).

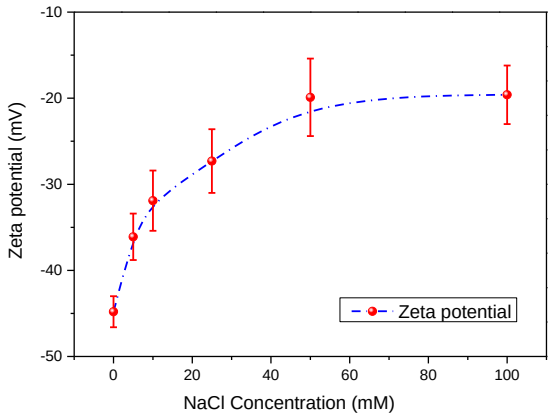

Figure 3.7 Zeta Potential of CNC-PS (0.5 wt%) with various salt concentration

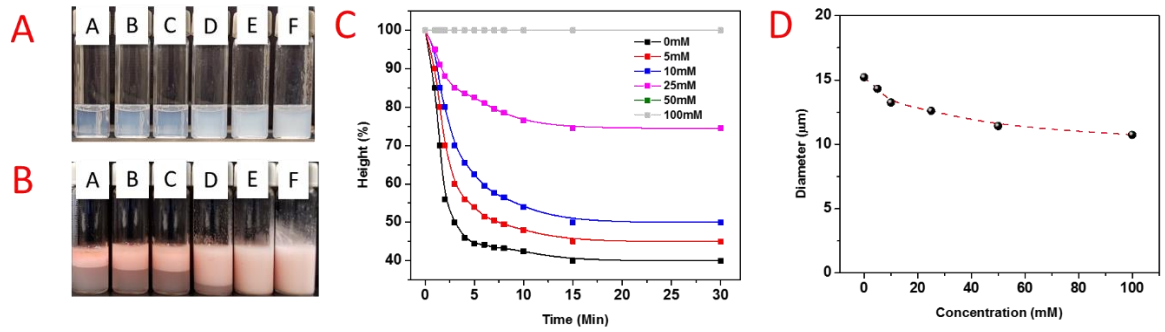

Figure 3.8 (A) Photograph shows the transparency of 0.5 wt% CNC-PS suspensions in different NaCl concentrations (A: 0, B: 5, C: 10, D: 25, E: 50, F: 100 mM); (B) Emulsions with toluene as oil phase (probed with Nile Red) stabilized by CNC-PS suspensions (0.5 wt %) with different NaCl concentrations (A: 0, B: 5, C: 10, D: 25, E: 50, F: 100 mM) after the storage of 1 day; (C) Creaming profile of toluene in water emulsions stabilized by 0.5 wt% CNC-PS and different NaCl concentration; (D) Droplet size dependence on NaCl concentration in the continuous phase while keep the nanoparticle concentration at 0.5 wt% and oil to water ratio 1:2.

3.4.3 Pickering emulsions stabilized by modified CNC with different M_n of polystyrene

In this section, the impact of the molecular weight of polystyrene on the emulsion stability was investigated. Amine terminated polystyrene of different average M_n (5000 vs 10000 Da) were used in the modification at room temperature. The ratio between reactive groups on CNC and polystyrene were kept constant, where the weight ratio between CNC and polystyrene were 10:1 and 5:1 for molecular weight of 5000 and 10000 Da, respectively. Toluene was used as the organic phase since its stability against coalescence can be easily observed. As shown in Figure 3.9 (A), no significant difference in the droplet size was observed for emulsions prepared using the same CNC concentration of 0.8 wt%. In fact, the droplet sizes were slightly larger for emulsions stabilized by nanoparticles prepared using a higher molecular weight polystyrene (Figure 3.9 (B)). We hypothesized that a relatively lower grafting density on cellulose nanocrystals was present when a higher molecular weight polystyrene was used since an increase in the molecular weight will reduce the mobility of the polymer chain during the reaction. The small terminal groups may be buried inside the random polymer coil, making it less accessible for the reaction with the hemiacetal groups on the ends of the CNC. The creaming behavior were also investigated to examine the stability of the emulsions, and this is summarized in Figure 3.10. There was no

significant difference on the creaming profile between emulsions stabilized by these two types of CNC-PS.

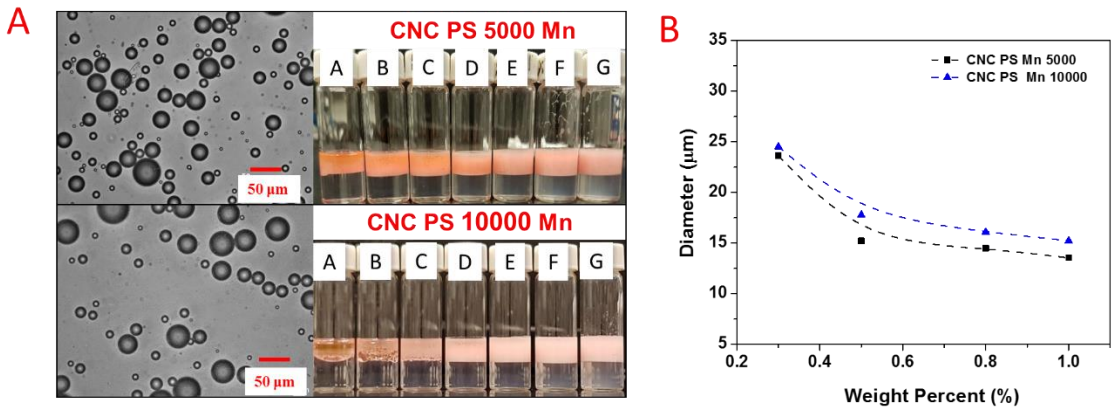

Figure 3.9 Optical micrographs of toluene in water emulsions stabilized by 0.8 wt% CNC-PS (M_n = 5000 Da, up) and CNC-PS (M_n = 10000 Da, bottom). The inserted photograph shows the emulsion stability after 2 weeks with different concentrations of nanoparticles (oil water ratio 1:2, A: 0.05; B: 0.1; C: 0.2; D: 0.3; E: 0.5; F: 0.8; G: 1.0 wt%); (B) Droplet size dependence on nanoparticle content (CNC-PS, M_n=5000 Da, and CNC-PS, M_n=10000 Da) in the water phase.

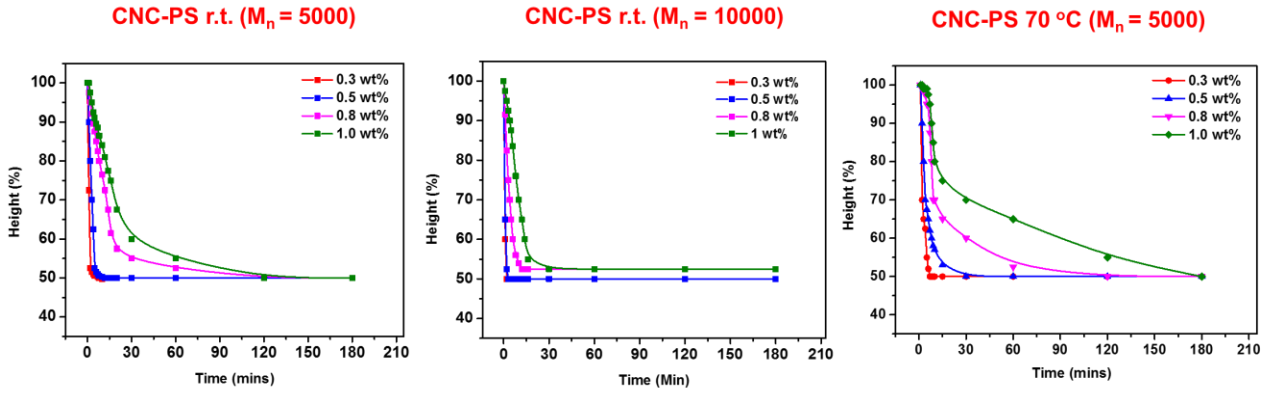

Figure 3.10 Creaming profiles of toluene in water emulsion stabilized by CNC-PS with various reaction conditions (Left) room temperature and PS M_n=5000 Da; (Middle) room temperature and PS M_n=10000 Da; and (Right) 70 °C PS M_n=5000 Da at different concentrations.

3.4.4 Pickering emulsions stabilized by modified CNC prepared at different temperatures

In this study, polystyrene with a M_n of 5000 Da was used and the weight ratio between CNC and polystyrene was fixed at 10:1. Nanoparticles from two different reaction temperatures were compared to assess their capacity to stabilize the toluene-water emulsions. As shown in Figure 3.11 (A), the emulsions stabilized by modified nanoparticles were stable against coalescence when the concentrations were greater than 0.3 wt%. The average droplet size was much smaller for emulsions stabilized by nanoparticles prepared at 70 ^{o}C (Figure 3.11 (B)). At a higher reaction temperature, more polystyrene chains were believed to be grafted onto the cellulose nanoparticles. CNC with a higher density of hydrophobic PS chains will be more favourably partitioned to the oil-water interface. A slight creaming behavior for emulsions was also observed, which may attribute to the size difference between these two systems.

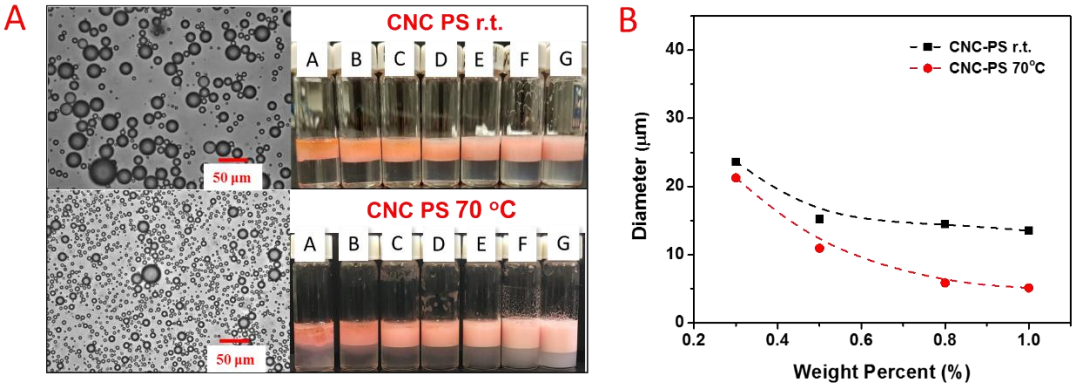

Figure 3.11 (A) Optical micrographs of toluene in water emulsions stabilized by 1.0 wt% CNC-PS (r.t.) (up) and CNC-PS (70 ^{o}C) (bottom). The inserted photograph shows the emulsion stability after 2 weeks with different concentrations of nanoparticles (oil water ratio 1:2, A: 0.05; B: 0.1; C: 0.2; D: 0.3; E: 0.5; F: 0.8; G: 1.0 wt%); (B) Droplet size dependence on nanoparticle content (CNC-PS from r.t. as well as 70 ^{o}C) in the water phase.

3.5 Conclusions

Hydrophobic polystyrene was successfully grafted onto the reducing end of cellulose nanocrystals through a selective-end group modification protocol. The modified nanoparticles displayed favourable surface properties and were capable of stabilizing toluene or hexadecane-in-water emulsions. Both emulsions displayed good stability against coalescence over a period of more than 4 months. When hexadecane was the oil phase, the droplet size of the emulsions was smaller than

toluene, which also displayed a much slower creaming rate. The creaming behavior of the emulsions was inhibited by electrolytes, which screened the charges on CNC surface. This work offers a possible strategy to modify CNC to produce amphiphilic particles for stabilizing Pickering emulsions.

Chapter 4* One Step Synthesis of Green High-Performance Pesticide Nano-dispersion using Cellulose Nanocrystal

Developing novel environmentally friendly nano-sized pesticide formulation is a key focus of sustainable agriculture. In this study, we used cellulose nanocrystal (CNC) as a carrier and dispersing agent for two model water insoluble pesticides (i.e. Deltamethrin and Permethrin) to formulate organic solvent and surfactant free pesticide nano-dispersions. The results show that the optimum loading ratio between pesticide and CNC was 1:100 as determined by UV-vis spectrophotometer, dynamic light scattering (DLS), zeta potential, and transmission electron microscopy (TEM). Fourier transform infrared spectroscopy (FTIR) and Isothermal Titration Calorimetry (ITC) results suggested hydrophobic interaction dominated the adsorption process. In addition, both laboratory and field trial tests were conducted to evaluate the pest control efficacy of the nano-dispersion, and it possessed performance better or equal to existing commercial formulations. The nano-dispersion was effective to control diamond back moth (DBM) in cabbage, achieving a mortality percentage of 99%. Consequently, a total cabbage yield of 322.3 kg was obtained for the nano-dispersion treated plot, while that of the commercial formulation treated plot and the control plot was 319.2 kg and 294.28 kg, respectively.

* This chapter is partially adapted from a paper: Chunxia Tang, Jason Pun, and Michael K.C. Tam, "One Step Synthesis of Green High-Performance Pesticide Nano-dispersion using Cellulose Nanocrystal" Manuscript under preparation.

Abstract graphic

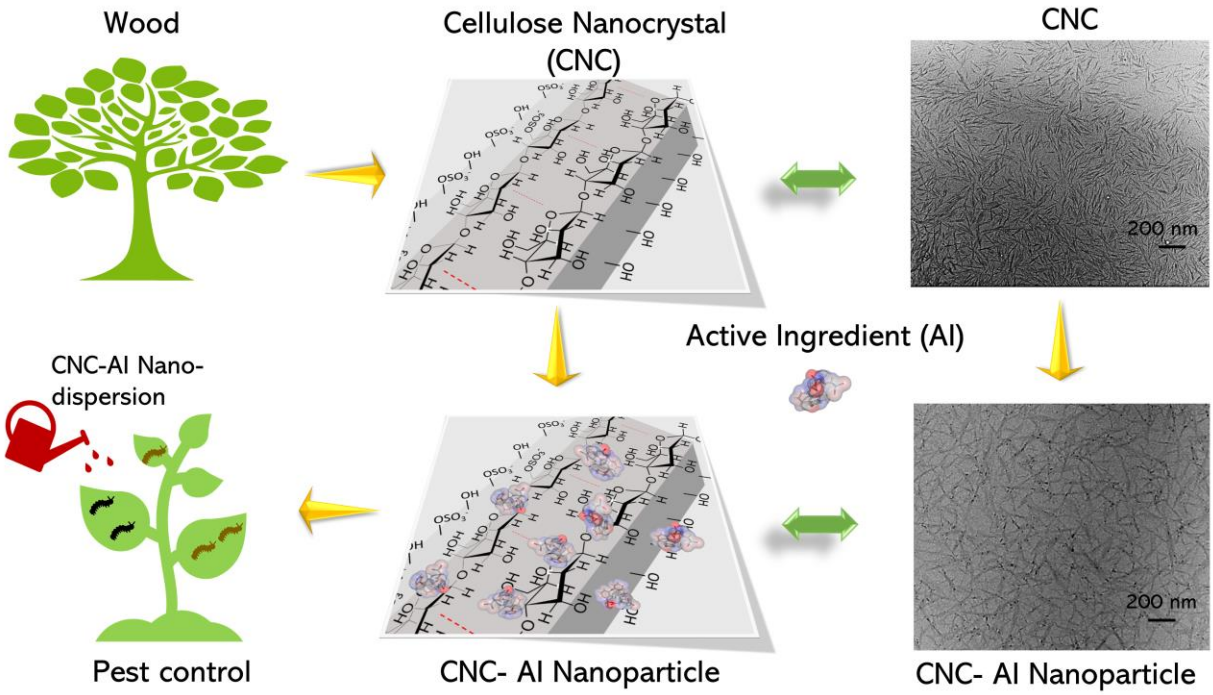

4.1 Introduction

Pesticides are essential compounds to ensure crop yield, and the demand of them has increased due to population growth and arable land reduction across the world.[186] However, poor water solubility of the majority of pesticides has greatly limited their water dispersity, and consequently their pest control efficacies.[187] Therefore, pesticides are often formulated as emulsifiable concentrate (EC), suspension concentrate (SC), wettable powder (WP), microemulsions, etc. in order to enhance their water dispersity.[58] Meanwhile, large amount of solvents and surfactants are consumed during the production of the pesticide formulations. For example, organic solvents such as toluene and xylene, and synthetic surfactants are commonly required to dissolve the pesticides and maintain droplet stability in EC and emulsion formulations.[1] These organic solvents possess strong toxicity and volatility, which are potential risks to the end users. In addition, environmental pollution is another problem associated with the application of such pesticide formulations via spraying due to the leaching of pesticides and those un-green adjuvants.[7]

In recent years, great efforts have been devoted to develop environmentally-friendly pesticide formulations, aiming at reducing/avoiding the use of toxic organic solvents and surfactants.[188,189] Inspired by recent advances in nanotechnology and material science, nano-pesticides have received much attention due to their unique surface to volume properties.[1,53,190] In contrast, bulk pesticide crystals generally possess diameters up to hundreds of macro-meters, which are difficult to yield stable aqueous dispersions. Two pathways are commonly used to prepare nano-pesticides: grind pesticide crystals to nano-sized particles and precipitate the pesticide solution in a non-solvent. The former requires high energy input and additional steps to produce stable formulation, while the latter can produce stable nano-dispersion in one step when stabilizers are present in the non-solvent.[191] Nanomaterials can play the role as stabilizers or carriers in the precipitation step due to their excellent colloidal stabilities and large surface areas. Moreover, they can help reduce the pesticide particle size as well as increase its dispersity and stability.[192,193]

A wide variety of materials have been demonstrated as pesticide carriers: Inorganic materials, such as clay, mesoporous silica, and layered double hydroxides;[194,195] Synthetic polymers/ co-polymers, e.g., poly (ethylene glycol) (PEG), poly-ε-caprolactone (PCL), and polymethylmethacrylate (PMMA)- polystyrene copolymers;[196,197] Natural polymers, like chitosan, lignin, cellulose derivatives, alginate, etc.[17,18] Among them, biomass-based polymers are usually considered as sustainable, biodegradable and environmentally friendly materials. Therefore, they are highly

desirable as alternative green carriers for pesticides to replace emulsion based products that are formulated using toxic-organic-solvents.[5,53,198]

Cellulose is one of the most abundant bio-mass based polymers on earth. However, cellulose based nanoparticles are rarely used for pesticide application. Very recently, some new cellulose-based nanoparticles became commercially available, which also offered a great opportunity for development of "greener" pesticide systems, i.e. organic solvent- and surfactant-free pesticide formulations. Cellulose nanocrystal (CNC) is one of these very promising candidates, which is obtained by the acid hydrolysis of native cellulose using an aqueous inorganic acid, such as sulfuric acid.[200] Under the acidic environment, the amorphous regions of native cellulose are dissociated, leaving behind the highly ordered crystalline domains (commonly referred to as cellulose nanocrystal (CNC)).[21,160,201] Typically, CNC produced from sulfuric acid hydrolysis possesses a width ranging between 5 and 20 nm and length of several hundred nanometers. In addition, the hydrolysis of cellulose using sulfuric acid leads to the formation of sulfate ester groups generating numerous negative charges on the surface of CNC, which promotes homogeneous dispersion of cellulose nanocrystals due to electrostatic repulsion in aqueous solutions.[162,167]

Thus, instead of using polymeric nanoparticles for agrochemicals encapsulation and dispersion, CNC can be an ideal carrier for the preparation of pesticide nano-dispersion due to its biodegradability, biocompatibility, large surface area and excellent colloidal stability. In this study, a universal and cost-effective method was developed to fabricate organic solvent/surfactant-free pesticide nano-dispersion using biomass-based CNC. The preparation conditions, binding mechanism and pest control efficacy in both laboratory and field trial of the nano-dispersion were studied.

4.2 Materials and method

4.2.1 Materials

Sulfated cellulose nanocrystals powder produced by sulfuric acid hydrolysis were provided by Celluforce Inc. Deltamethrin (DEL, solubility in water < 0.002 mg/L at 25 deg C (data from PubChem)) and Permethrin (PER, solubility in water < 0.13 mg/L at 25 deg C (data from PubChem)) were purchased from Sigma-Aldrich in analytical standard. Acetone (ACS reagent, ⩾ 99.5%), ethanol (ACS reagent, ⩾ 99.5%), and potassium bromide (KBr, FTIR grade) were purchased from Sigma Aldrich. A commercial EC formulation of ORTHO® HOME DEFENSE®

MAX^{TM} with permethrin concentration of 0.25% was purchased from Home Depot (USA) for in laboratory pest control test. Another commercial EC formulation Deltamethrin 2.5 EC was used as reference in field trial test. Ultra-pure water (resistivity of 18.2 MΩ.cm) was used to prepare all the aqueous dispersions. Living mealworms and waxworms which have life expectancy of 1 month were purchased from PetSmart (Canada) and stored in the fridge at 4 degree. The worms were taken out from the fridge to at room temperature before the experiment. An average of 30 min and 40 min is needed for mealworms and waxworms to be active, respectively.

4.2.2 Preparation of pesticide nano-dispersion

1 wt% CNC stock dispersion was prepared by dispersing CNC powders into Milli-Q water. DEL or PER dissolved in acetone at various concentrations were mixed with 1 wt% CNC dispersion (containing 0.5 g CNC) at a water to acetone volume ratio of 1 to 2, followed by evaporation in a vacuum oven at 60 °C and vacuum pressure of 15 KPa for 6 hours. The obtained dispersion was denoted as CNC-DEL$_X$ or CNC-PER$_X$, where X represents the mass of pesticide (mg) used. As an example, CNC-DEL$_5$ means nanoparticles prepared by 5 mg DEL and 0.5 g CNC. In comparison, control samples (DEL$_X$) without CNC were formulated by mixing DEL acetone solution with ultrapure water following the same process as described. Solid content of a dispersion was calculated by freeze drying of a known weight of sample.

4.2.3 Characterization of nanoparticles

Dynamic light scattering (DLS) and ζ-potential. The average diameter and zeta potential of the nanoparticles were measured using the Malvern Zetasizer Nano series. Experiments were conducted at 90 degree with a sample concentration of 0.04 wt%. The results were determined from an average of 3 measurements, consisting of 12 runs per measurement.

Turbidity measurement. Turbidity of nano-dispersions (0.45 wt%) were measured by UV-vis spectrophotometer (Cary 100 Bio) at 500 nm. Briefly, 2 mL of sample was transferred to a Quartz cuvette, and the transmittance (%) at 500 nm was recorded. All the measurements were performed 3 times and averages were reported.

Fourier transform infrared spectroscopy (FTIR). FTIR spectra were obtained using a Bruker Tensor 27 spectrometer FT-IR spectrometer with a resolution of 4 cm^{-1} and a scanning number of 32 from 400 to 4000 cm^{-1}. Briefly, freeze-dried samples were mixed with KBr, followed by grinding via mortar and pestle, then compressed into a pellet.

Transmission Electron Microscopy (TEM). To observe the nanoparticle morphologies, 0.01 wt% aqueous dispersions were placed onto the copper grids (200 mesh coated with copper) and allowed to dry at room temperature for TEM characterizations (Philips CM10, 60 Kev).

Isothermal Titration Calorimetry (ITC). MicroCal VP-ITC (Northampton, MA, USA) was used to study the binding mechanism between the pesticide molecules and CNC nanoparticles. CNC stock solution with a concentration of 0.1 mg/mL was prepared by adding CNC water dispersion to equal volume of ethanol. Similarly, 25 µg/mL DEL stock solution was prepared by dissolving DEL in ethanol/ water (1:1, v/v) mixture. The good solubility of DEL in ethanol/water (1:1, v/v) mixture was confirmed by the linearly increased UV adsorption intensity at 277 nm with increasing DEL concentration when it was below 200 µg/mL (See Figure 4.1). To conduct the titration, aliquot of 10 µL was dropped stepwise by an auto injection syringe that contains 280 µL DEL stock solution to a reaction cell contains 1.43 mL CNC stock solution with a 6 min interval. For comparison, background was collected by injection of DEL stock solution to ethanol/ water (1:1, v/v) mixture without CNC following the same method. The temperature was set at 25 °C throughout the titration, and data obtained were plotted with the Origin 7.0 software.

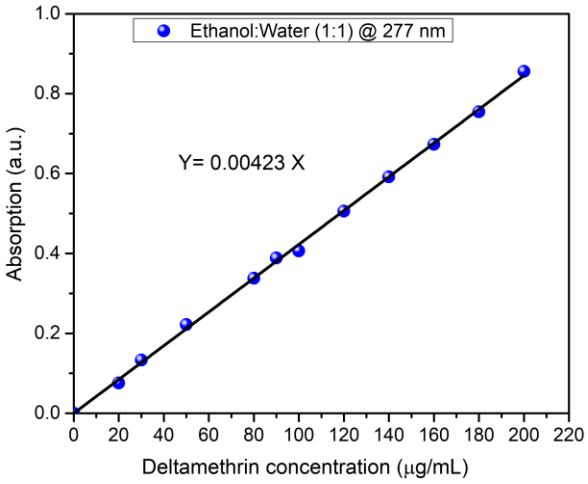

Figure 4.1 UV adsorption curve of DEL in ethanol/water (1:1 v/v) mixture

4.2.4 In laboratory nano-dispersion pest control efficacy evaluation

Before the test, CNC-DEL_5 and CNC-PER_5 nano-dispersions were diluted to 0.1, 0.5, 1.0 and 1.5 wt%, where the corresponding active ingredient (AI) concentration was 9.9 ppm, 49.5 ppm, 99.9 ppm and 150 ppm. To perform the pest control test, fresh spinach leaves were spread on a petri dish (10 cm diameter), then 2 mL of the dispersion was sprayed on the leave surfaces with 1 mL

on the top and 1 mL on the bottom. After that, 20 active worms were placed on top of the leaves, and the survival rate of the worms was recorded at set time intervals. To determine whether a worm was dead, three steps were adopted, i) lightly touch the worm around its body with a wide tip of tweezer, ii) lightly pinch the worm in the stomach and tail with tweezer, iii) lightly lift the worm with tweezer. If there was no movement after the 3 steps, the worm was recorded as dead. In comparison, the pest control efficiency of 1.0 wt% CNC (0 ppm DEL) and DEL_5 control (100 ppm DEL) were also investigated and compared with 1.0 wt% CNC-DEL_5 (99.5 ppm DEL). In addition, the pest control efficiency of CNC-PER_5 was compared with the commercial EC pesticide ORTHO® HOME DEFENSE® MAX™ under the same PER dosage. Both mealworms and waxworms were used for the evaluation.

4.2.5 In field nano-dispersion pest control efficacy test

To examine the efficacy of the developed nano-dispersion, Deltamethrin was selected as a model pesticide for the field trial test, which was conducted in Pobbathiri Tsp, Nay Pyi Taw Region of Myanmar during Winter 2020. This field trial was arranged by our industrial partner, Asiatic Agriculture Industrial Pte Ltd. Three plots (T1, T2 and T3) of 4 m × 3 m were designed for planting of Cabbage, Crown (hybrid), and each of them had 3 replications (R1, R2 and R3). The efficacy of the prepared nano-dispersion was compared with a commercial formulation Deltamethrin 2.5 EC for the control of Diamond back moth caterpillar (DBM) in cabbage. CNC-DEL_5 nano-dispersion was prepared at a concentration of 3.75 g/L prior to spray, and Deltamethrin 2.5 EC was diluted in water with a concentration of 1.5 mL/L to maintain the same AI concentration. The spray volume was set as 100 L / acre for 2 times with an interval of 7 days. The details of treatment applied for each plot is summarized in Table 4.1. To evaluate the DBM control efficacies, 10 heads of cabbage in each replication were selected and the initial number of targeted pests per head was recorded on the 74^{th} day after planting. The first assessment was conducted on the 77^{th} day that was 3 days after first applications, and the second assessment was conducted on the 84^{th} day, which was 3 days after subsequent applications. In the end of the test, cabbages were harvested and the total yield of the three plots were calculated.

Table 4.1 Details of treatment for each plot

Application Time	T1	T2	T3
74th Day	Control	**Deltamethrin 2.5EC** 1.5 mL/L	**CNC-DEL$_5$** 3.75 g/L
81st Day	Control	**Deltamethrin 2.5EC** 1.5 mL/L	**CNC-DEL$_5$** 3.75 g/L

4.3 Results and discussion

The formation process of the nano-dispersion can be illustrated in four stages as shown in Scheme 1. In stage I, pesticide solution was mixed with CNC dispersion, where the pesticide existed in molecular state in acetone/ water (2:1, v/v) mixture. Interaction between pesticide molecules and CNC nanoparticles could occur when they were close enough. The attraction force could attribute to hydrophobic interaction, hydrogen bonding or Van der Waals interaction.[54] In stage II, acetone in the mixture was partially removed at 60 °C, and the mixture still maintained its solubility towards these pesticide molecules. Consequently, more pesticide molecules approached the CNC surface due to their higher concentration. In stage III, as more acetone was evaporated, the solubility of the mixture was significantly reduced. Therefore, small clusters consisted of several molecules were formed. CNC could provide sites for these clusters due to its large surface area and amphiphilic surface. With the evaporation proceeding, more and more pesticide molecules were deposited on the CNC, forming new clusters or adding the existing clusters. In stage IV, acetone was completely removed, thus majority of the pesticide molecules precipitated from the mixture and formed clusters or nanoparticles. Notably, it's impractical to transfer all the pesticide molecules from the mixture to CNC surface. Therefore, while some of the pesticide nanoparticles were deposited on CNC, some were not, and the proportion depends on the ratio between pesticide and CNC.

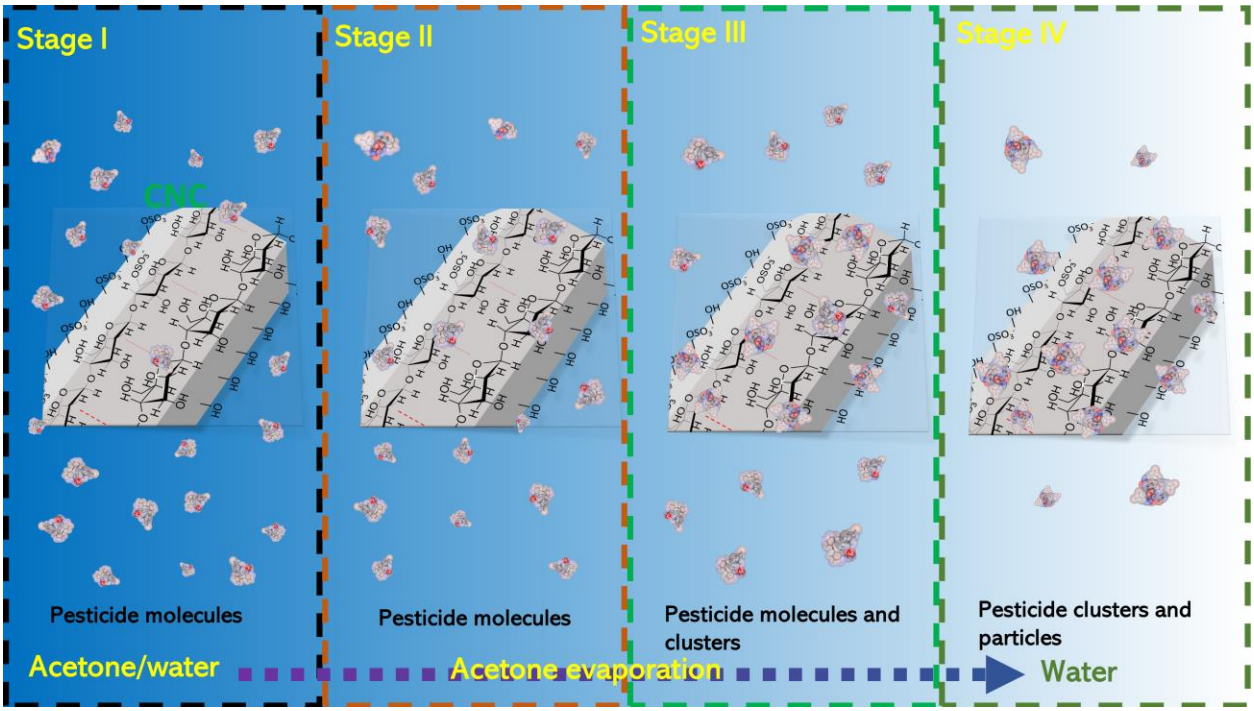

Scheme 4.1 Illustration of the formation process of CNC-AI nano-dispersion.

4.3.1 Optimum loading ratio study

Both Permethrin and Deltamethrin belong to the synthetic pyrethroid pesticides, and they have very similar chemical structure as well as poor water solubility.[202] Here we used Deltamethrin (DEL) as an example to investigate the optimum loading ratio between pesticide and CNC. CNC-DEL_x nano-dispersions were prepared by pesticide with dosages varying from 0 mg to 20 mg and 0.5 g CNC. As shown in the inserted picture in Figure 4.2(A), the turbidity of nano-dispersion increased with DEL dosage, and it was evaluated by measuring the UV transmittance (%) at 500 nm. Seen from Figure 4.2 (A), the transmittance (%) decreased proportionally with DEL dosage, and a rapid transmittance decline was observed when DEL dosage beyond 5 mg, which could be caused by the increased pesticide clusters concentration that scattered more light.

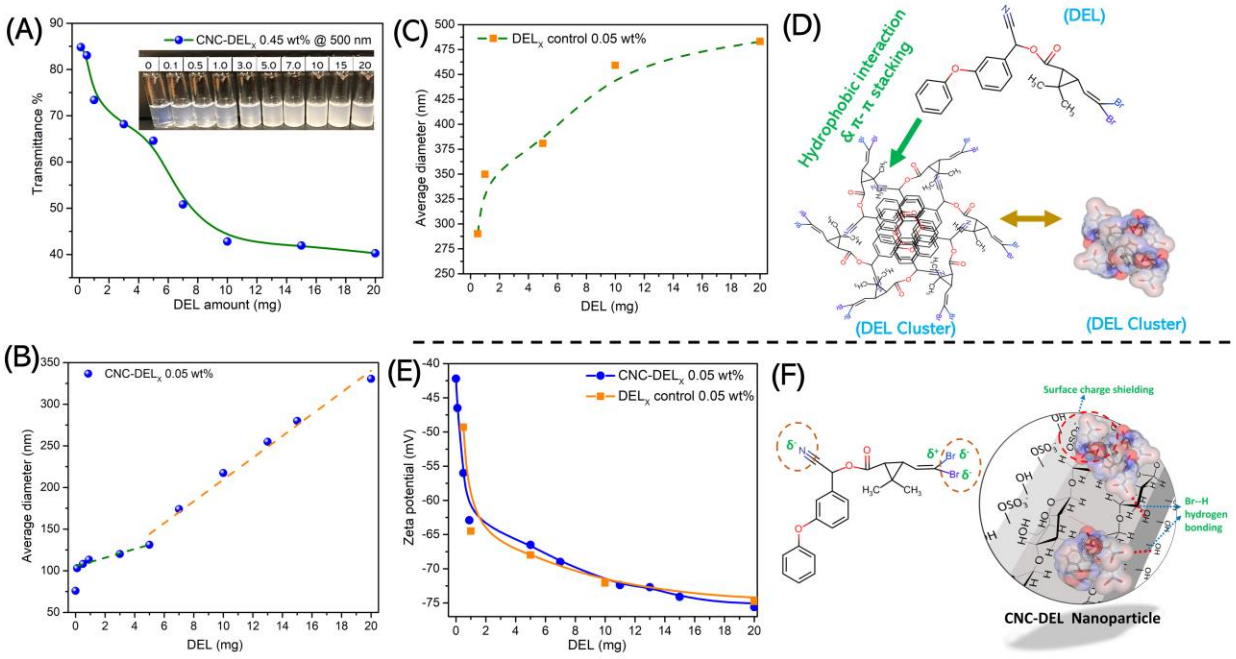

Figure 4.2 (A)Transmittance of CNC-DEL$_X$ nano-dispersion as a function of DEL dose (mg). Inserted picture showing the 0.45 wt% nano-dispersions with different DEL dose (mg). Average hydrodynamic diameter of CNC-DEL$_X$ (B), DEL$_X$ control (C), and their zeta potential values (E). The illustration of DEL clusters formation process (D), electronegative groups on DEL molecules and DEL particle surface charge shielding effect (F).

To examine the particle size, DLS measurements on 0.05 wt% CNC-DEL$_X$ dispersions were conducted at 90 degree. Although CNC is a rod-like nanoparticle, the scattering from DLS measurements at 90 degree were reported to estimate the hydrodynamic diameter of CNC before and after modification.[203,169] From Figure 4.2 (B), we observed that pristine CNC possessed an average hydrodynamic diameter of 75.9 nm, and the diameter clearly increased after loading the DEL. Two distinct increment slopes were observed after the linear fitting was applied to these data. Specifically, the diameter of CNC-DEL$_X$ displayed a faster rate when DEL amount exceeded 5 mg, which might be caused by the formation of larger pesticide clusters during precipitation when pesticide dosage exceeded the loading and dispersing capacity of CNC. The dispersion effect of CNC on DEL particles was further identified by a control experiment. Shown in Figure 4.2 (C), the diameter of DEL$_X$ control without CNC was much larger than CNC-DEL$_X$ under the same DEL content. For example, the diameter of CNC-DEL$_5$ was 131.2 nm, while that of DEL$_5$ was 380.8

nm. The much smaller size demonstrated that CNC could significantly reduce DEL particle size as a dispersing agent, however, larger DEL clusters/particles were produced without CNC due to the overgrowth of the clusters. The possible formation process of DEL clusters is illustrated in Figure 4.2 (D), which shows the self- assembly of hydrophobic DEL molecules to clusters by hydrophobic interaction or π- π stacking interaction during acetone evaporation. DEL molecules continued to deposit on the formed small clusters without the presence of CNC, resulting in large clusters. Furthermore, DLS results indicated that CNC had limited surface/sites as dispersing agent. For 0.5 g CNC, it was effective for dispersing/loading up to 5 mg DEL. A further addition would significantly increase the particle size, causing the loss in colloidal stability, consequently the phase separation during formulation storage.

Surface charge is another important parameter to evaluate the stability of pesticide formulation as high surface charge could introduce strong electrostatic repulsion between particles. Pristine CNC possessed excellent colloidal stability due to its negatively charged sulfate ester groups, which yielded a zeta potential of -42.2 mV as shown from Figure 4.2 (E). The absolute zeta potential value of CNC-DEL_X increased with DEL dosage, which was probably caused by the increased amount of DEL particles. The surface charge of DEL particles might be attributed to the polar groups (-CN, -Br) on DEL molecules. As discussed earlier, the DEL clusters were formed by self-assembly of DEL molecules, where the hydrophobic domains of DEL molecules formed the core and the polar groups were on the outside facing the polar solvent (Figure 4.2 (D)). N and Br are strong electronegative elements that can attract electrons; therefore, the electrons of C atom were strongly attracted by N and Br in -C≡N and -C=C $(Br)_2$ groups (see Figure 4.2 (F)). The negative zeta potential values from DEL_X control further supported the conclusion. Similar to CNC-DEL_X, the surface charge of DEL_X control also increased with DEL dosage, which was probably due to more -C≡N and -C=C $(Br)_2$ groups present in larger particles. Interestingly, the zeta potential value of CNC-DEL_X was very close to DEL_X control. This might be caused by the loaded DEL particles shielding the negative sulfate ester groups on CNC (illustrated in Figure 4.2 (F)).

In summary, the optimum loading mass of DEL was considered as 5 mg when 0.5 g CNC was used. This ratio was adopted in the following studies as it produced nanoparticles with smaller size as well as more negative zeta potential, which are important parameters to prepare stable formulations.

4.3.2 Nano-particle morphology and size distribution study

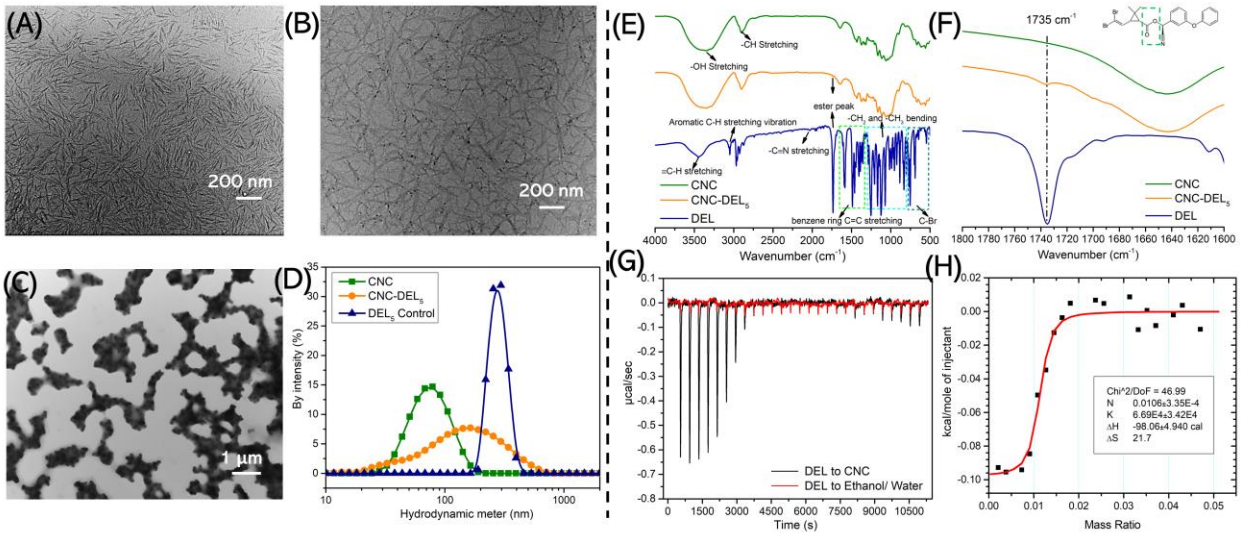

Figure 4.3 TEM images of pristine CNC (A), CNC-DEL$_5$ (B), DEL$_5$ control (C), and particle size distribution of 0.05 wt% of these dispersions by intensity (D). FTIR pattern of CNC, CNC-DEL$_5$ and DEL (E), and a magnified region (F). Calorimetric curve of injection of DEL solution to ethanol/ water mixture (red) and to CNC (black) (G) and integral plot after subtracting background (H).

Pristine CNC is a rod-like nanoparticle with an average length of 200-400 nm and width of 5-20 nm as seen in Figure 4.3 (A) determined from TEM analyses. Its dispersing and loading capacity towards DEL particles were evident as demonstrated by the uniformly distributed DEL nanoparticles on CNC (Figure 4.3 (B)). However, significant aggregation of DEL particles was observed when CNC was absent. From Figure 4.3 (C), we observed that DEL$_5$ control exhibited much larger particle size than CNC-DEL$_5$, which further confirmed the dispersing effect of CNC. DLS measurements were further conducted to analyze their particle sizes. From Figure 4.3 (D), we observed that pristine CNC possessed a single peak with an average hydrodynamic diameter of 75.9 nm, and the peak became broader and the average hydrodynamic diameter increased to 131.2 nm for CNC-DEL$_5$. In the scenario of DEL$_5$ control, the average hydrodynamic diameter of DEL particles was much larger with a size of 380.8 nm.

4.3.3 Binding mechanism study

There are some studies that reported that pristine CNC could be used as carrier for hydrophobic compounds, however, the interaction mechanism between CNC and hydrophobic molecules was

not clearly explained.[204–207] Herein, FTIR was used to investigate the bonding information before and after loading DEL on CNC. As shown in Figure 4.3(E), a small peak at 1735 cm^{-1} was observed in CNC-DEL_5, which belongs to the ester group on DEL. A magnification from 1800 cm^{-1} to 1600 cm^{-1} is shown in Figure 4.3 (F). Interestingly, no other characteristic peaks belonging to DEL were observed on CNC-DEL_5, which was probably due to the low concentration of DEL in the CNC-DEL_5. In addition, we expected that hydrogen bonding could exist between CNC and DEL particles when they are very close as illustrated in Figure 4.2 (F). Overall, FTIR results suggested the interaction between CNC and DEL was physical, and no chemical bond was formed.

To further examine the interaction mechanism between CNC and DEL molecules, ITC was used to monitor the heat change associated with the interaction.[208] A typical curve (in red color) of titrating concentrated DEL solution to ethanol/water mixture without CNC is shown in Figure 4.3 (G), where the heat released was due to dilution. In the presence of CNC, obvious enthalpy change was observed as a function of time or DEL concentration as shown by the black spectra in Figure 4.3(G). The distinct enthalpy difference in the first 5000 s indicated that some forms of interaction occurred between CNC and DEL molecules. After 5000 s, the enthalpy was almost overlapped with the background, suggesting these interactions had ceased with when additional DEL was titrated to the CNC solution. After subtracting the background, the integrations of the peak areas were plotted and shown in Figure 4.3 (H). The enthalpy change was negative, i.e. -98.06±4.94 cal, suggesting the interaction was exothermic.[209] Also, the small association constant K_a (6.69 ± 3.42) $\cdot 10^4$ indicated the binding force was a weak force. It seems that one type of binding interaction was present as the data could be fitted to a one site binding model.[210–212] Since no hydrogen bonding peak was observed from the FTIR spectra, hydrophobic interaction would be the only likely driving force for the binding. Recent studies on CNC revealed that CNC is an amphiphilic system, where the axial direction of the rings formed by -CH were hydrophobic and the hydroxyl groups are hydrophilic.[213–215,216] However, the specific hydrophobic plane of CNC is still being debated. For example, Capron et al. reported that plane (200) was hydrophobic,[213,215] while a recent work based on molecular dynamic simulation concluded that both plane (100) and (010) of CNC were amphiphilic.[214] In other words, there is no standard method to calculate the content of the hydrophobic domains on CNC. Therefore, the X axis of Figure 4.3 (H) was designated as the mass ratio between DEL and CNC. N is known as stoichiometric, which represents the molar ratio between the ligand and receptor when the sites of receptor are saturated.

Here, N represented the mass ratio between DEL and CNC when the sites on CNC were saturated, and it was around 0.0106. This result was consistent with the optimum loading ratio determined by DLS measurements in section 4.3.1.

4.3.4 In laboratory nano-dispersion pest control efficacy evaluation

Both Permethrin and Deltamethrin are wide spectrum pesticides, and their mode of action is mainly based on contact and stomach toxicity. The pest control efficacies of CNC-DEL_5 and CNC-PER_5 nano-dispersion were evaluated with two types of worms, i.e. mealworms and waxworms. Mealworms are the larval of the mealworm beetles, and waxworms are the caterpillar larvae of wax moths. Figure 4.4 (A) illustrates the pest control experiment of CNC-DEL_5 nano-dispersion at different concentrations and two control samples in real time. The effect of CNC-DEL_5 concentration on mealworms mortality is shown in Figure 4.4 (B). Clearly, the living worm ratio decreased from 65% to 45% with CNC-DEL_5 concentration increasing from 0.1 wt% to 1.0 wt%. The increased efficacy was mainly due to the increased DEL dosage in a 2 mL dispersion. Notably, the 1.0 wt% dispersion displayed very fast knockdown effect, as 55% mortality was achieved in 60 mins.

For comparison, the efficacies of CNC and DEL_5 control were also investigated and compared with 1.0 wt% CNC-DEL_5, and the results are shown in Figure 4.4 (C). It is evident that CNC did not show effective pest control efficacy, only 5% mortality was observed during the 2 hours observation, which was probably caused by natural death of the worms. In contrast, DEL_5 control (contains100 ppm DEL) exhibited effective pest control efficacy, where 30% mortality was achieved in 2 hours. However, CNC-DEL_5 still possessed the strongest pest control efficacy when compared with DEL_5 control under the same DEL dosage. The superior performance was probably attributed to the smaller DEL particle size in CNC-DEL_5, yielding a larger surface area for contact with the worms.

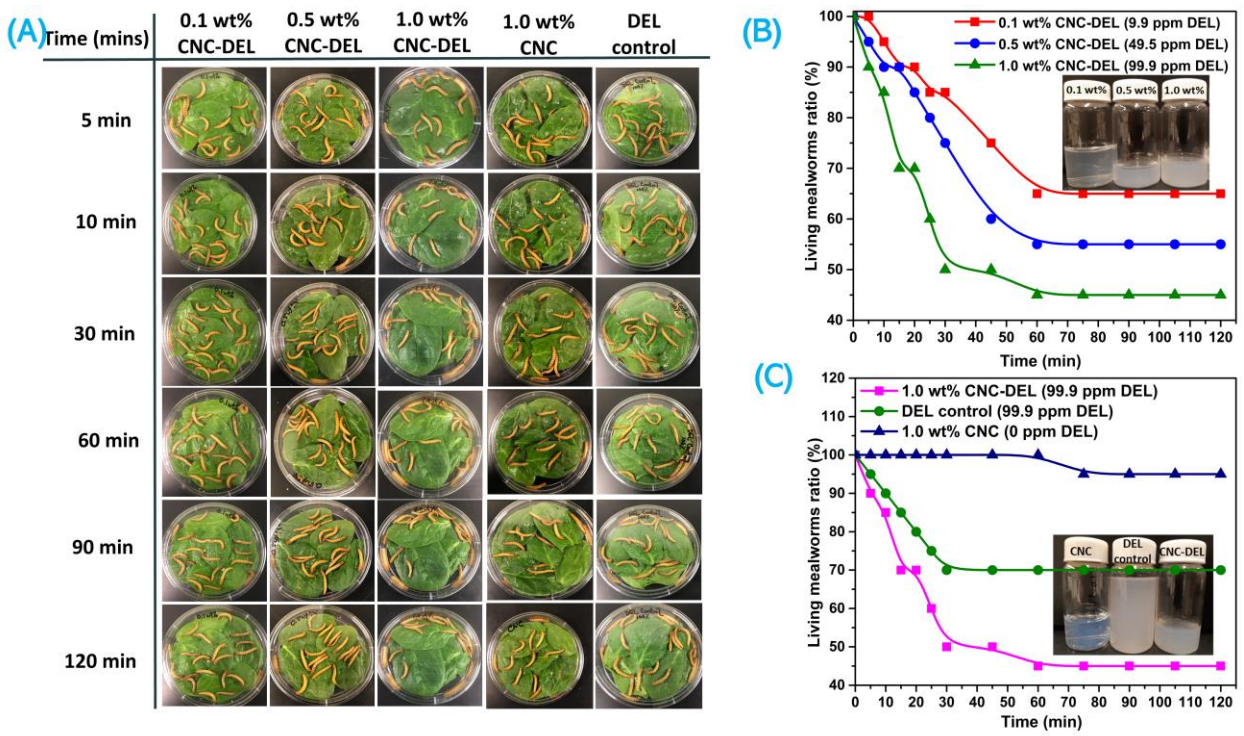

Figure 4.4 (A) Optical pictures of mealworms mortality in real time, (B) living mealworms ratio of 0.1 wt% CNC-DEL_5, 0.5 wt% CNC-DEL_5, and 1.0 wt% CNC-DEL_5 dispersion as a function of time, and the insert shows the three dispersions, (C) living mealworms ratio of 1.0 wt% CNC, DEL_5 control, and 1.0 wt% CNC-DEL_5 dispersion as a function of time, and the inserted picture shows the three dispersions.

Similarly, the pest control efficacy of CNC-PER_5 at different concentrations were also studied and compared with a commercial EC pesticide formulation whose active ingredient is also permethrin. The efficacy was also dominated by PER concentration as shown in Figure 4.5. Moreover, the 1.0 wt% CNC-PER_5 achieved a comparable mortality (around 55%) to the commercial formulation (containing 100 ppm PER).

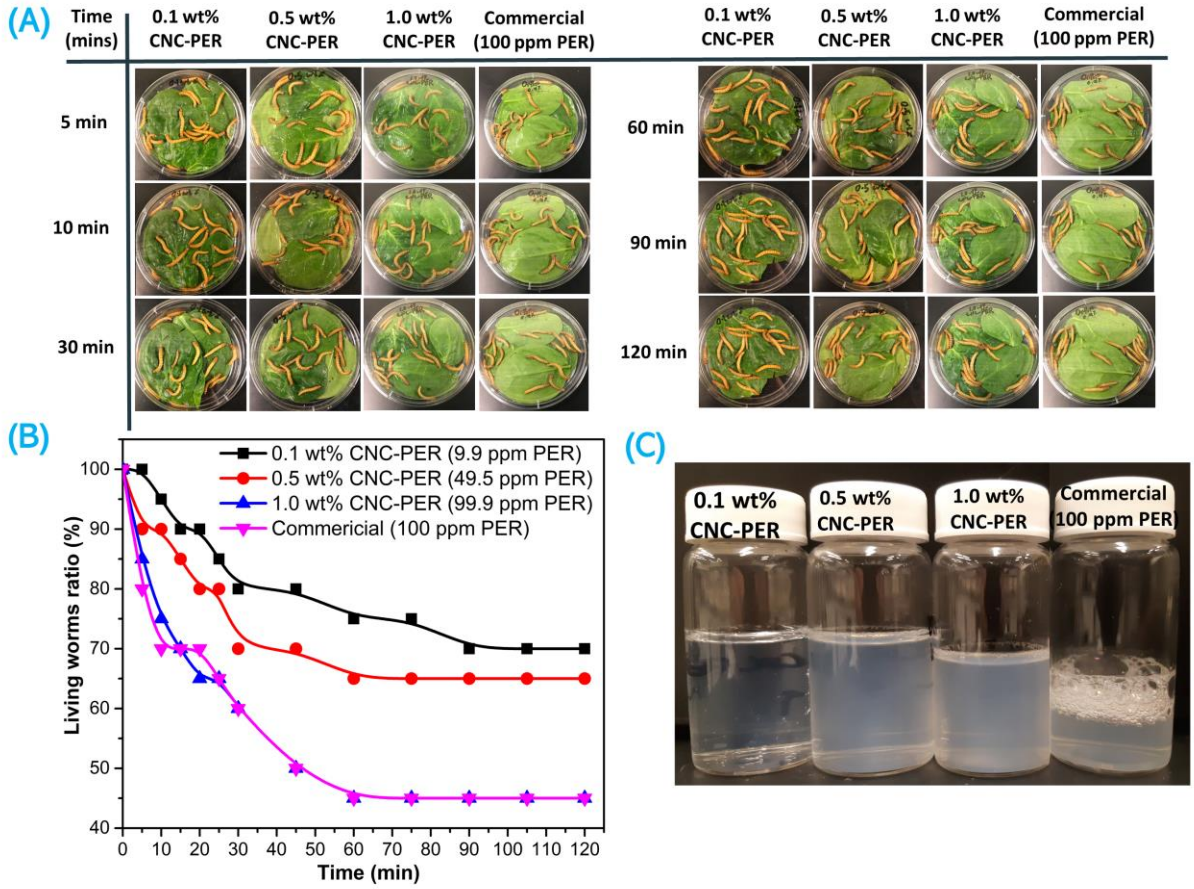

Figure 4.5 (A) Optical pictures of mealworms mortality in real time, (B) living mealworms ratio of 0.1 wt% CNC-PER_5, 0.5 wt% CNC-PER_5, 1.0 wt% CNC-PER_5 dispersion and the commercial EC formulation as a function of time, and (C) picture showing the four pesticide formulations.

For a more comprehensive assessment of the formulation performance, efficacy tests were also conducted on a larger body weight worm, i.e. waxworm. The living waxworm ratios of 1.5 wt% CNC-PER_5 (150 ppm PER) and commercial formulation (150 ppm PER) as a function of time of are shown in Figure 4.6. It is evident that the commercial EC formulation displayed faster knockdown effect as 75% of the waxworms were killed in 2 hours, while CNC-DEL_5 formulation achieved 70% mortality in 3 hours. The faster knockdown effect of commercial formulation was probably due to the presence of large amounts of organic solvents.

Overall, in laboratory worm test, the results suggested that the CNC-DEL_5/ PER_5 nano-dispersion displayed good pest control performance. Besides, the current method possessed many advantages,

such as; no organic solvents and surfactants were used, simple preparation process, which meet the sustainable agriculture and 'green chemistry' concept.

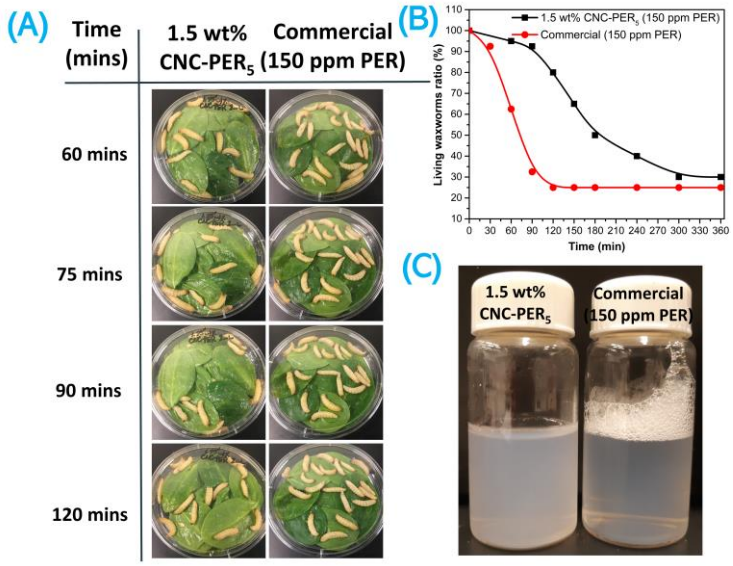

Figure 4.6 (A) Optical pictures showing the state of waxworms treated with 1.5 wt% CNC-PER_5 and commercial (150 ppm PER) at different time, (B) living waxworm ratio of the two samples in real time, and (C) picture of the two formulations.

4.3.5 Large scale field trials of the nano-dispersion for evaluating pest control efficacy

The three plots of 4 m × 3 m land designed for planting of cabbage is shown in Figure 4.7 (A). 3.75 g/L CNC-DEL_5 nano-dispersion and 1.5 mL/L commercial Deltamethrin 2.5 EC were sprayed on cabbages as shown in Figure 4.7 (B) on the 74^{th} day and 81^{st} day after planting. 10 heads of cabbages in each replication were selected and the targeted pests per head before and after treatments were recorded in Table 4.2. Figure 4.7 (C) shows a demonstration of target pest counting on a selected cabbage and Figure 4.7 (D) is a close view of larvaes on the leaf. The mean number of target pest/head of cabbage of each plot before and after treatment is summarized in Figure 4.7 (E). It is evident that the cabbage plot treated with CNC-DEL_5 nano-dispersion (T3) displayed the lowest number of larvae infestation per head of cabbage, followed by that treated with Deltamethrin 2.5EC (T2). Control plot (T1) showed the highest number of larvae infestation per head throughout the whole data collection and assessment period. The mortality percentage of T2 and T3 was 96% and 99% as calculated based on the mean number of target pest/head before and after treatment. It is evident that the CNC-DEL_5 nano-suspension possessed comparable pest

control efficacy to the commercial Deltamethrin 2.5 EC formulation. In addition, the cabbage yield is shown in Figure 4.7 (F), where we observe a total yield of T3 is 322.3 Kg, followed by T2 with 319 Kg and T1 with 294.28 Kg. Such results suggested that the developed CNC-DEL_5 nano-dispersion is very effective to control the diamond back moth (DBM) in cabbage, and consequently increase cabbage yield. The nano-dispersion can be widely applied to other types of crops and pests by simply changing the active ingredient on CNC during the nano-dispersion preparation.

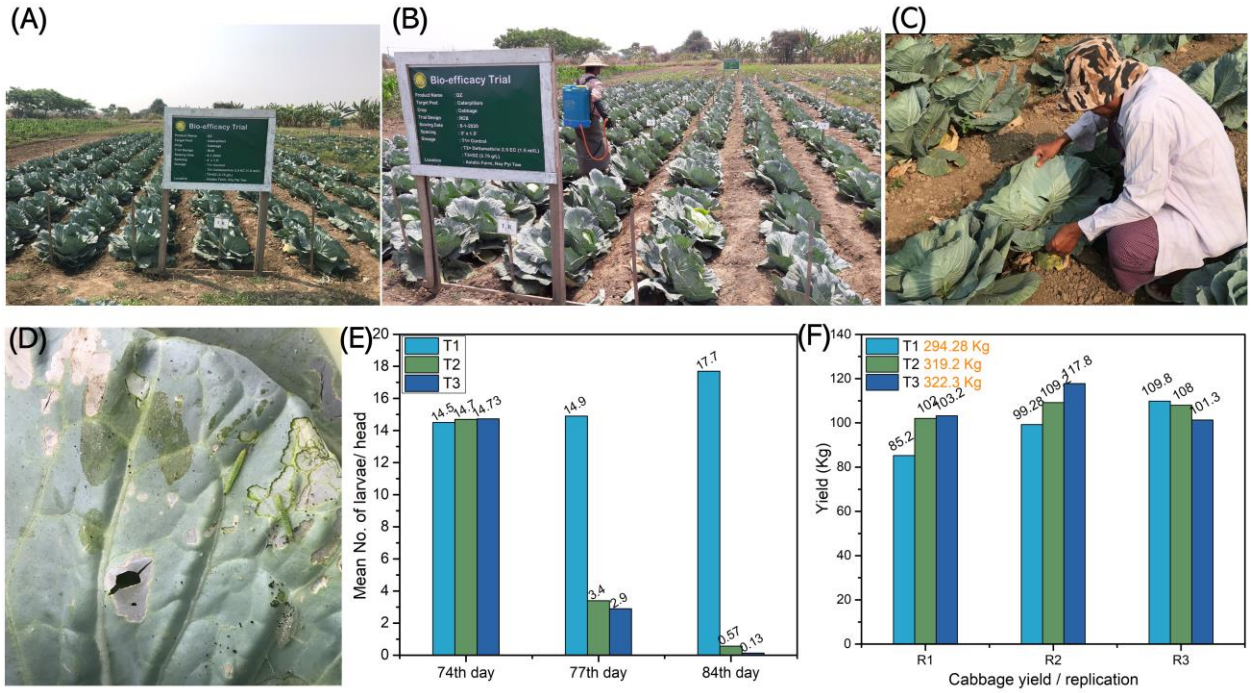

Figure 4.7 (A) An overview of the plots planted with cabbage, (B) demonstration of spray experiment during the test, (C) demonstration of target pest counting, (D) a close view of the larvae on the leaf. (E) Mean number of larvae per head of cabbage in each plot before and after treatments, (F) A summary of cabbage yield in 3 replications of each plot treated with different formulations.

Table 4.2 Mean number of target pests/ head of cabbage in each plot before and after treatments

Data collection date	20.3.2020										
			Before treatment(initial data)								
Number of Pest per plant											
T 1	**S 1**	**S 2**	**S 3**	**S 4**	**S 5**	**S 6**	**S 7**	**S 8**	**S 9**	**S 10**	**Means**
R1	5	15	17	23	10	14	16	22	14	11	14.7
R2	22	23	20	24	15	13	12	23	0	17	16.9
R3	14	22	12	0	13	15	11	0	18	14	11.9
								Average of T 1			**14.50**
T 2	**S 1**	**S 2**	**S 3**	**S 4**	**S 5**	**S 6**	**S 7**	**S 8**	**S 9**	**S 10**	**Means**
R1	46	8	16	14	18	0	3	20	20	11	15.6
R2	14	15	7	26	11	44	10	15	9	9	16.0
R3	5	24	22	13	5	10	13	17	5	11	12.5
								Average of T 2			**14.70**
T 3	**S 1**	**S 2**	**S 3**	**S 4**	**S 5**	**S 6**	**S 7**	**S 8**	**S 9**	**S 10**	**Means**
R1	3	5	6	17	14	20	**13**	2	8	10	9.8
R2	22	21	31	15	28	7	1	16	9	17	16.7
R3	44	12	10	4	15	31	18	12	15	16	17.7
								Average of T 3			**14.733**

Data collection date	23.3.2020										
			1st time after treatment								
Number of Pest per plant											
T 1	S 1	S 2	S 3	S 4	S 5	S 6	S 7	S 8	S 9	S 10	Means
R1	13	8	26	14	23	14	15	11	12	14	15
R2	15	12	20	24	23	4	13	14	11	12	14.8
R3	20	14	13	2	21	24	7	13	20	15	14.9
								Average of T 1			14.90
T 2	S 1	S 2	S 3	S 4	S 5	S 6	S 7	S 8	S 9	S 10	Means
R1	0	4	5	3	3	7	5	4	4	1	3.6
R2	4	1	8	7	3	4	0	4	0	2	3.3
R3	0	1	6	5	3	0	2	7	4	5	3.3
								Average of T 2			3.40
T 3	S 1	S 2	S 3	S 4	S 5	S 6	S 7	S 8	S 9	S 10	Means
R1	4	2	5	6	3	3	4	4	3	1	3.5
R2	0	0	3	3	0	4	4	0	3	4	2.1
R3	3	0	4	3	7	0	3	3	4	4	3.1
								Average of T 3			2.9

Data collection date	30.3.2020										
			2nd time after treatment								
Number of Pest per plant											
T 1	S 1	S 2	S 3	S 4	S 5	S 6	S 7	S 8	S 9	S 10	Means
R1	33	13	34	13	11	21	12	4	23	15	17.9
R2	30	21	10	30	12	10	14	21	11	7	16.6
R3	20	32	11	8	31	37	8	21	10	8	18.6
								Average of T 1			17.70
T 2	S 1	S 2	S 3	S 4	S 5	S 6	S 7	S 8	S 9	S 10	Means
R1	0	1	0	0	0	1	2	1	0	0	0.5
R2	1	0	0	0	0	1	1	2	0	0	0.5
R3	1	1	0	2	2	1	0	0	0	0	0.7
								Average of T 2			0.57
T 3	S 1	S 2	S 3	S 4	S 5	S 6	S 7	S 8	S 9	S 10	Means
R1	0	0	1	0	0	0	0	0	0	0	0.1
R2	0	0	0	1	1	0	0	0	0	0	0.2
R3	1	0	0	0	0	0	0	0	0	0	0.1
								Average of T 3			0.133

4.4 Conclusions

We developed a simple and scalable process to produce organic solvents- and surfactants- free pesticide nano-dispersion using cellulose nanocrystal (CNC) as carrier and dispersing agent. FTIR and ITC studies suggested that the attraction between hydrophobic pesticide molecules and CNC was dominated by hydrophobic interaction. The optimum loading mass ratio between deltamethrin and CNC was 1:100 as determined by DLS and ITC results. In addition, both laboratory and field trial tests have suggested that the nano-dispersion possessed excellent pest control efficacy that was comparable to commercial formulations. Besides, the small particle size and high zeta potential value of CNC-DEL_5 nanoparticle are very important properties to produce a stable dispersion that can be stored long term. In summary, the nano-dispersion is very promising for replacing conventional pesticide formulations due to its simple preparation process, environmentally friendly material, odorless ingredients, and excellent pest control efficacy.

Chapter 5* Shape Recoverable and Mechanically Robust Cellulose Aerogel Beads for Efficient Removal of Copper ions

Developing bio-based absorbents with high removal capacity towards heavy metals is one of the key strategies to manage water pollution worldwide. Robust cellulose aerogel beads (CGP, diameter of 3~4 mm) with high amine content were prepared by cross-linking polyethylenimine (PEI) to cellulose nanofibrils (CNF) using 3-Glycidyloxypropyl) trimethoxysilane (GPTMS). The mass ratio between PEI and GPTMS (1:1 or 3:1), crosslinking mechanism, morphologies, elemental compositions, total amine contents, mechanical strengths as well as the adsorption capacity and kinetic of the aerogel beads were investigated. Small CGP beads possessed several desirable characteristics, such as high amine group content (5.74 mmol/g for CGP3 beads), large maximum Cu (II) adsorption capacity (163.40 mg/g for CGP3 beads), very fast adsorption rate (< 10 h to reach equilibrium), high shape recovery (2.00 % plastic deformation for CGP3 beads at 50% strain), robust mechanical strength (stress around 10.5 KPa at 50% strain), and they could be regenerated and reused.

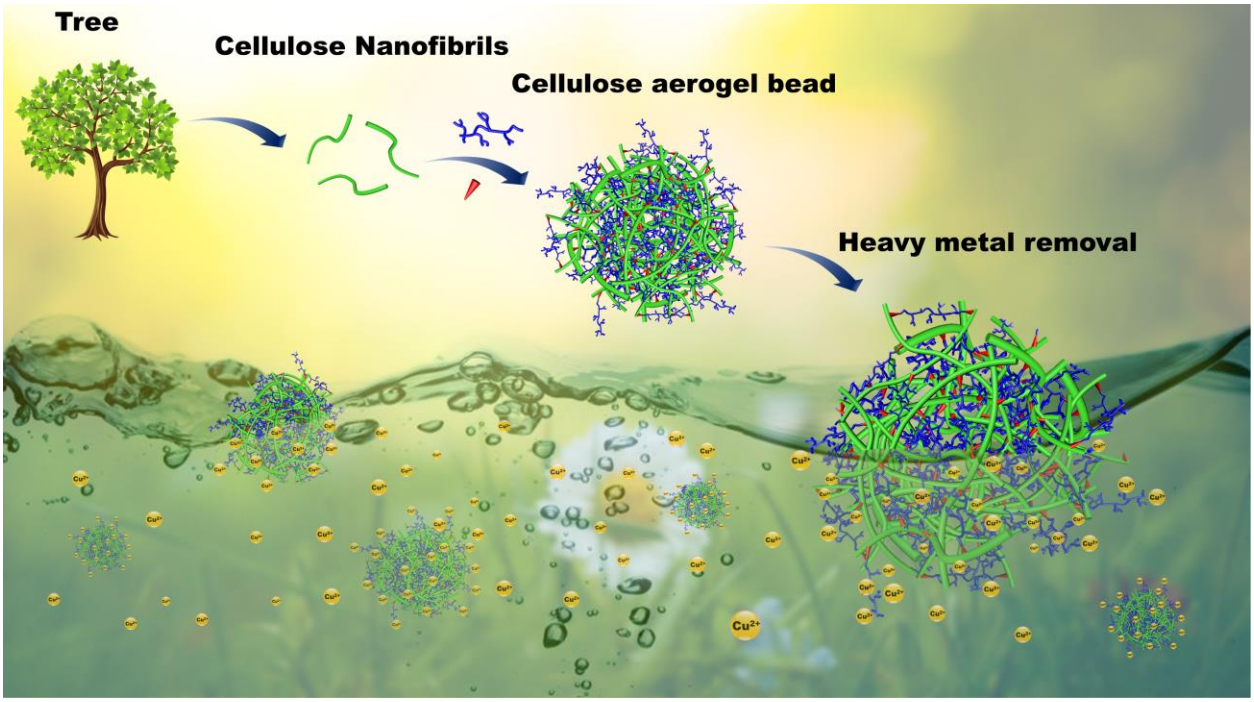

* This chapter is adapted from a paper: Tang, C.; Brodie, P.; Li, Y.; Grishkewich, N. J.; Brunsting, M.; Tam, K. C. Shape Recoverable and Mechanically Robust Cellulose Aerogel Beads for Efficient Removal of Copper Ions. Chem. Eng. J. 2020, 124821.

5.1 Introduction

Heavy metals (e.g., Pb (II), Cu (II), Cr (VI)) are serious water pollutants that threaten human health due to their high toxicity, non-degradability and bio-accumulation. [217] Various technologies have been adopted to remove the metal ions from wastewater, such as ion-exchange, chemical precipitation, flocculation, membrane separation and adsorption. [218] Among them, adsorption is an efficient and economical approach since it is easy to design and operate. [219] Absorbents, such as activated carbon, clay, biochar and polymers are widely used for wastewater treatment.[220] However, most of these commercial absorbents consisted of powders, which have poor recyclability, low removal efficiency and high cost.[221] Besides, the poor recyclability of these powders can cause the secondary pollution. Therefore, novel absorbents that can satisfy the practical requirements are necessary.

Aerogels are highly interconnected porous solid materials that possess many advantages, such as ultralow density, high surface area and adsorption capacity and ease of separation from the bulk aqueous solutions. [222] These unique properties make aerogels ideal absorbents for water treatment. Many materials have been demonstrated to be effective for preparing aerogel absorbents, e.g., graphene oxide, silica, polymers and bio-mass based materials.[223–225] In recent years, intense studies have been devoted to bio-mass based materials due to their low cost, bio-degradability as well as abundant surface reactive groups.[226]

Cellulose is an environmentally friendly compound derived from natural resources, such as trees and agriculture biomass.[58] Depending on the size and aspect ratio, cellulose materials can be classified into cellulose fibers (mainly used for papermaking), microcrystalline cellulose (MCC), cellulose nanofibrils (CNF) and cellulose nanocrystals (CNC).[59,201] CNF exhibits its unique properties to prepare aerogels due to its high aspect ratio, abundant surface hydroxyl groups, and structural flexibility.[227] However, physically crosslinked CNF aerogel such as pure CNF entangled aerogels or polymers (e.g., PVA, PEG, gelatin) blended CNF aerogels are easy to dissociate in water due to the hydrogen bonding interaction between its hydroxyl groups and water molecules. [227] Chemical crosslinking is an effective and commonly used approach to enhance cellulose aerogel wet mechanical strength via the formation of robust covalent bonding. In general, surface modification of CNF with crosslinking sites such as silyl, amine, epoxy, carboxyl or aldehyde groups is necessary to build up robust and functionalized CNF aerogels.[222]

Considering the low adsorption capacity of hydroxyls groups on CNF towards metal ions, modification of CNF with crosslinkers containing carboxylic, amine or phosphate groups is an effective strategy to enhance its heavy metals removal capacity as well as wet mechanical property.[217] For example, Zhang et al. prepared a CNF aerogel absorbent that possessed both carboxyl and amino groups by grafting polyethylenimine (PEI) on TEMPO- oxidized CNF, achieving a maximum Cu (II) capacity of 52.32 mg/g;[228] Tang et al. introduced PEI on CNF using polydopamine as crosslinker to produce CNF aerogel absorbent, which achieved a maximum Cu (II) adsorption capacity of 103.5 mg/g;[229] Li et al. mixed PEI with carboxylated-CNF *via* physical crosslinking to prepare aerogel absorbent with a Cu (II) absorption capacity of 175.44 mg/g.[230] However, similar to these mentioned CNF aerogels, most CNF aerogel absorbents reported in literature are monoliths. Although these monoliths exhibited high adsorption capacity, the adsorption kinetics is slow due to the long diffusion path. Since the removal rate is a critical parameter to improve its efficiency, this can be achieved by reducing the diffusion path length.[231] In this study, we grafted a hyperbranched cationic polymer, PEI on CNF using (3-glycidyloxypropyl) trimethoxysilane (GPTMS) as a crosslinker. The obtained mixture was injected into liquid nitrogen for rapid freezing, followed by sublimation to obtain cellulose aerogel beads (diameter between 3-4 mm). The chemical structure and composition, morphology, mechanical property, Cu (II) ion adsorption capacity and mechanism as well as regeneration performance of the aerogel beads were investigated. The novelty of this work comprise of: (1) cellulose aerogel beads was used instead of cellulose aerogel monoliths for Cu (II) removal to improve the removal efficiency by reducing copper ion diffusion path length; (2) small beads with larger surface to volume ratio than monoliths that enhanced the adsorption rate; (3) a scalable and simple one pot chemical crosslinking reaction conducted at room temperature and in aqueous solution was proposed; (4) the mechanical performance of the aerogel beads were precisely quantified, and to our knowledge, this is the first reported study; (5) the beads possessed excellent adsorption, regeneration and mechanical property, which is very promising for packed column adsorption.

5.2 Materials and Methods

5.2.1 Materials

CNF slurry was obtained from the Process Development Center (University of Maine), and the detailed production process was reported previously.[201] (3-glycidyloxypropyl) trimethoxysilane

(GPTMS), branched- polyethylenimine (b-PEI, M_w 750,000 Da), copper (II) sulfate pentahydrate, sodium hydroxide (NaOH), hydrochloride acid (HCl, 37%), potassium bromide (KBr), humic acid and ethylenediaminetetraacetic acid (EDTA) were purchased from Sigma Aldrich. Milli-Q water (conductivity of 15 μs/cm) was used to prepare the aqueous dispersions.

5.2.2 Preparation of cellulose aerogel beads/monoliths

GPTMS was dropwise added to the CNF dispersion (1 wt%) under magnetic stirring at room temperature with a mass ratio of CPTMS: CNF = 1:1, and the mixture was further stirred for 2 hours to allow the GPTMS hydrolyzed and condensed on CNF. Then, b-PEI solution (20 wt%) was added to the mixture with a mass ratio of CNF: GPTMS: PEI = 1:1:1 or 1:1:3, followed by stirring for 30 min at R.T. The obtained mixture was introduced to liquid nitrogen via a syringe pump at a controlled rate to form uniform spherical beads. Afterwards, these frozen beads were subjected to freeze drying at -45 ℃ to produce the aerogel beads. The obtained aerogel beads are denoted as CGP1 (CNF: GPTMS: PEI mass ratio of 1:1:1), and CGP3 (CNF: GPTMS: PEI mass ratio of 1:1:3). In comparison, aerogel beads without PEI were also prepared, and designated as CG (CNF: GPTMS mass ratio of 1:1). CGP1 aerogel monolith with a dry mass of 100 mg was prepared by freezing a scintillation vial (diameter of 28 mm) containing the reaction mixture in liquid nitrogen, followed by freeze drying at -45 ℃.

5.2.3 Characterization

Fourier transform infrared spectroscopy (FTIR) spectra were obtained using the Bruker Tensor 27 spectrometer FT-IR spectrometer with a resolution of 4 cm^{-1} and a scanning number of 32 from 400 to 4000 cm^{-1}. Briefly, pellets were prepared by mixing an amount of freeze-dried aerogel beads with KBr, finely ground in mortar and pestle then compressed into a pellet. It's worthy to note that all the beads samples were dialyzed in Milli-Q water to remove the unreacted CPTMS/ PEI before the characterization.

Scanning electron microscopy (SEM) equipped with EDS was used to examine the morphologies and elemental composition of the aerogel beads. The dried aerogel beads were sputtered with gold and visualized in a Carl Zeiss NTS GmbH instrument with an acceleration voltage of 5 keV.

The amine contents of the beads were quantitatively determined via a conductometric-potentiometric titration method using a Metrohm 809 Titrando auto-titrator (Switzerland). Samples were dialyzed in Milli-Q water until the conductivity remained constant prior to the

titration. Known mass of dry beads or PEI solution was placed in the vessel and 25 mL Milli-Q water was added. Then, 0.1M HCl was used to adjust the pH to 3.5 followed by titration with 0.01M NaOH. The amine content of the sample was calculated using Eq. (5.1):

$$Amine\ content\ (mmol/g)\ = \frac{V\ (NaOH)\times 0.01}{m} \quad (5.1)$$

where V(mL) is the NaOH volume and m (g) is the dry weight of the sample.

The compressive strength of the aerogel beads was evaluated in a Microtester G2 (CellScale Biomaterials Testing, Waterloo). To fully cover the beads, a 5 mm × 5 mm steel platen was selected and glued on the cantilever. The beads were placed under the steel plate and the compressive tests were conducted in a water bath. All compression tests were performed in a displacement-controlled mode, with images, displacement (δ) and applied force (F) in real time recorded during the compress. The strain (Ɛ) and stress (σ) were calculated by assuming all the beads were perfectly spherical and the contact area was fixed during the compression. Here, we use the maximum contact area to calculate the stress as shown in the following equations:

$$Ɛ\ (\%) = 100\ \times \delta/D \quad (5.2)$$

$$S\ (mm^2) = \pi(D/2)^2 \quad (5.3)$$

$$\sigma\ (\mathrm{Pa}) =\ 10^6 \times F/S \quad (5.4)$$

where D (mm) is the diameter of the bead, and F (N) is the force applied at real time.

5.2.4 Adsorption experiments

5.2.4.1 Adsorption pH, absorbent dosage and ionic strength study

To study the optimized pH for adsorption, 100 mg dry beads were massed and dialyzed in Milli-Q water before immersing in 50 mL 100 ppm Cu (II) solution. The initial pH (pH_i) of the solution was adjusted from 3 to 6.2 by using 0.1M HCl or NaOH. The concentration of Cu (II) in the mixture was monitored by a Copper Ion Selective Electrode (Cu-ISE, Cole-Parmer®). Besides, the pH of the solution during adsorption was recorded by a pH electrode and the value at equilibrium (pH_e) was reported. Also, the conductivity of the solution during adsorption was recorded by a conductivity electrode. The adsorption capacity q_e (mg/g) was calculated by Eq. (5.5) as follows:

$$q_e = \frac{(C_0 - C_e)}{m} V \quad (5.5)$$

where C_0 (mg/L) and C_e (mg/L) are the initial and equilibrium concentrations, respectively; q_e (mg/g) is the adsorption capacity at equilibrium; V(L) represents the solution volume of Cu (II) ions and m (g) represents the mass of the aerogel adsorbent.

The effect of absorbent dosage (20 mg to 100 mg CGP1 beads) and ionic strength (100 mg CGP1 beads, 0 M to 0.5M NaCl) were investigated in 10 mL 100 ppm Cu (II) solution under pH 5.6 and 25 ℃, and the corresponding equilibrium adsorption capacities q_e (mg/g) were also calculated by Eq. (5.5).

5.2.4.2 Adsorption isothermal and thermodynamic study

20 mg absorbents were immersed 15 mL Cu (II) solutions with concentration ranging from 50 ppm to 400 ppm to study the adsorption isothermal. The adsorption experiments were carried out at 25 ℃ with initial pH of 5.6. The adsorption behavior was described by Langmuir and Freundlich isotherm models:

$$\frac{C_e}{q_e} = \frac{C_e}{q_m} + \frac{1}{K_L q_m} \quad (5.6)$$

$$logq_e = logK_F + nlogC_e \quad (5.7)$$

where q_m is the maximum adsorption capacity of the absorbent, and K_L and K_F is the binding constant of the Langmuir and Freundlich equation, respectively; n is the Freundlich model represents the empirical parameter.

To investigate the adsorption thermodynamic, 20 mg CGP1 beads was immersed in 20 mL Cu (II) with varying concentrations and the adsorption experiments were carried out at 25 ℃, 30 ℃ and 35 ℃, respectively. The thermodynamic parameters (ΔG°, ΔH°, and ΔS°) were calculated by equations as follows:

$$Kc = 63.546 \times 55.5 \times 1000 \times K_L \quad (5.8)$$

$$\Delta G° = -RTlnK_C \quad (5.9)$$

$$\Delta G° = \Delta H° - T\Delta S° \quad (5.10)$$

$$lnK_C = \frac{-\Delta H°}{R} \cdot \frac{1}{T} + \frac{\Delta S°}{R} \quad (5.11)$$

Where K_L (L/mg) is Langmuir constant determined from Langmuir adsorption isothermal; K_C is thermodynamic equilibrium constant that is dimensionless, and the factor 63.546 is the molar weight of Cu and 55.5 is the number of moles of pure water per liter. ΔG°, ΔH°, and ΔS° refers to Gibbs energy, enthalpy and entropy change respectively. R is a universal gas constant 8.3144 J/mol×K, T (K) is absolute temperature.

5.2.4.3 Adsorption kinetics study

100 mg CGP1 absorbent was added to 50 mL 100 ppm Cu (II) solution at pH 5.6 and 25℃, and the mixture was stirred continuously until the adsorption reached equilibrium. The adsorption data were fitted to the pseudo-first order kinetic model (Eq. (5.12)), pseudo-second order kinetic model (Eq. (5.13)), and intra- particle diffusion model (Eq. (5.14)):

$$\ln(q_e - q_t) = lnq_e - k_1 t \quad (5.12)$$

$$\frac{t}{q_t} = \frac{1}{(k_2 q_e^2)} + \frac{t}{q_e} \quad (5.13)$$

$$q_t = K_{id} t^{0.5} + C \quad (5.14)$$

where q_t (mg/g) is the adsorption capacity at time t, and k_1 and k_2 are the rate constants for the pseudo-first order adsorption and pseudo-second order adsorption kinetic models, respectively. K_{id} is the rate constant (g mg^{-1} min^{-1}) of intra-particle diffusion kinetics.

5.2.4.4 Simulated wastewater treatment

The simulated wastewater was prepared by addition of a common Natural Organic Matter (NOM), humic acid, to Cu (II) solutions (from 50 ppm to 400 ppm). The adsorption experiment was conducted by immersing 20 mg CGP1 beads in 10 mL Cu (II) solutions containing 50 ppm humic acid at pH 5.6 and 25 ℃. The adsorption capacity was calculated by Eq. (5.5).

5.2.5 Regeneration study

The aerogel beads after Cu (II) adsorption were immersed in 0.1 M EDTA solution to remove the Cu (II). A clear color transition from bright blue to colorless was observed during the regeneration process. Afterwards, the beads were recovered using a mesh and squeezed by hand to remove the excessed solution, followed by soaking in Milli-Q water several times to elute the salts until the conductivity became constant. The regenerated beads were subjected to adsorption process and the regeneration process was repeated for five cycles.

5.3 Results and discussion

The preparation process and formation mechanism of the aerogel beads are illustrated in Schematic 1. Under aqueous condition, GPTMS hydrolyzed to form silicon hydroxyl groups that further reacted with the hydroxyl groups on CNF via condensation reaction.[75] The epoxy groups on the other end of GPTMS were reacted sequentially with the amine groups on PEI *via* the ring open reaction, to form robust networks. The proposed chemical structure of the network is shown in section (b) in Schematic 5.1. To form spherical porous beads, liquid nitrogen was chosen as the cold source and freezing bath due to its extreme low temperature and neglectable capillary force. Many studies have reported that the high temperature gradient created by liquid nitrogen could induce the rapid ice crystals nucleation speed and result in lots of small crystal domains, which is crucial to yield porous aerogel with small pore size after sublimation.[84,232,233] As the reaction mixture dropped to liquid nitrogen, small ice crystal domains formed within the network and forced the cross-linked CNF fibers to aggregate to form pores with thin walls. Porous cellulose aerogel beads with small pore size were produced when these small ice crystal domains were removed by sublimation via a freeze- drying process.[234]

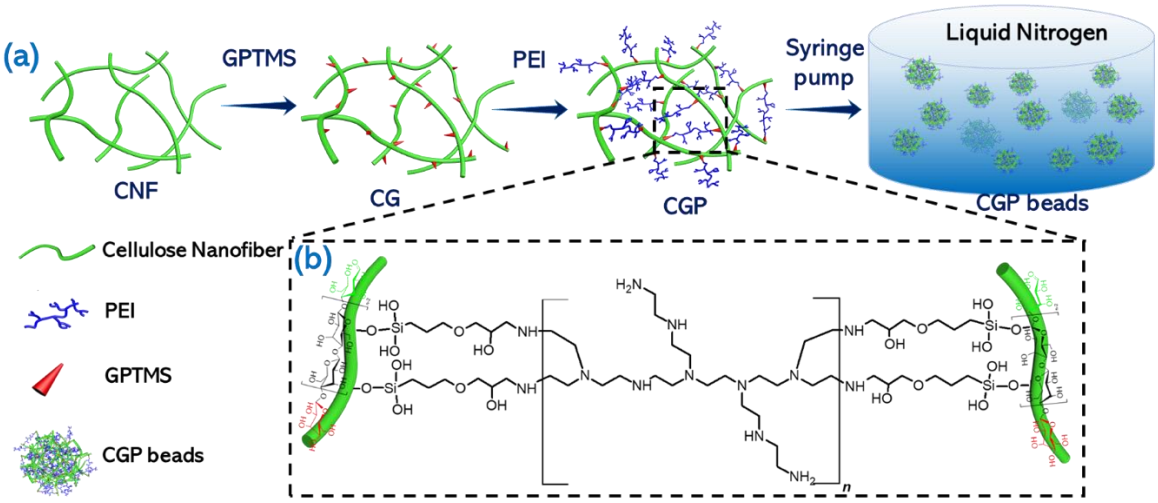

Schematic 5.1 Illustration of the preparation and chemical structure of the CGP beads

5.3.1 Characterizations of the aerogel beads

To verify the cross-linking reaction between CNF, GPTMS and PEI, Fourier-transform infrared spectroscopy (FTIR) was used to detect the characteristic peaks or formed covalent bonds, and the results are shown in Figure 1. Compared to pristine CNF aerogel, CG aerogel displayed three peaks at 1200, 900, and 851 cm^{-1} (see Figure 5.1(a)), which were assigned to the characteristic peaks of

epoxy groups on GPTMS.[235] After further modification with PEI (see CGP1 and CGP3 in Figure 5.1(b)), the peak at 851 cm^{-1} vanished due to the ring open reaction, while some typical peaks belong to PEI were evident. For example, the new peak at 3280 cm^{-1} is due to the N-H stretching vibration of secondary amine; new peaks at 1570 cm^{-1} and 1475 cm^{-1} are attributed to the N-H bending vibration, and the new peak at 820 cm^{-1} is assigned to N-H wagging vibration; Also, the intensity of C-H stretching vibration peaks at 2935 cm^{-1} and 2867 cm^{-1} increased due to the aliphatic -CH_2-CH_2- spacer in PEI; Another new peak at 1316 cm^{-1} belongs to C-N stretching vibration. The presence of new peaks and disappearance of epoxy groups confirmed the successful cross-linking reaction. In addition, compared to CGP1, CGP3 displayed stronger N-H bending vibration intensity, which may ascribe to the higher amine content.

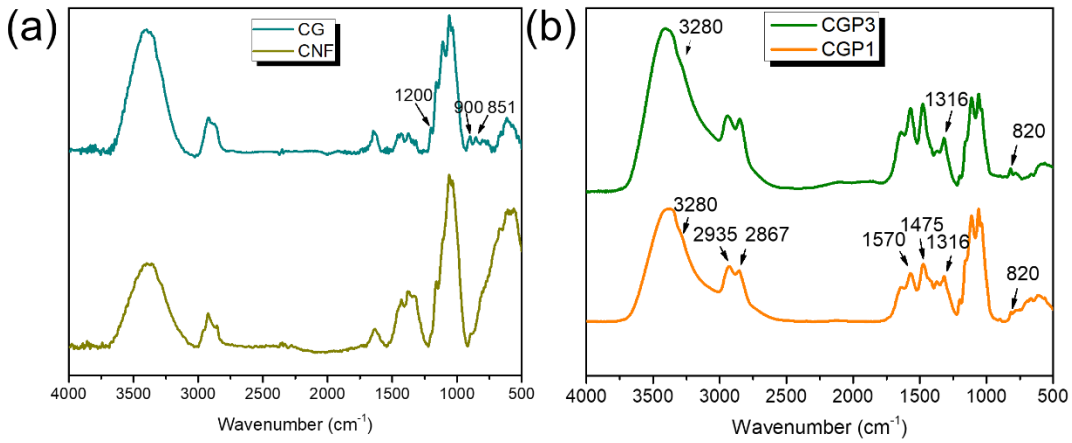

Figure 5.1 (a) FTIR patterns of CNF and CG, (b) FTIR patterns of CGP1 and CGP3 aerogel beads.

Amine group content is a critical parameter in terms of improving the aerogel adsorption capacity as it exhibits strong chelation ability towards Cu (II) ions. Therefore, in this study we could increase the amine content by tuning the mass ratio of PEI to GPTMS (1:1 or 3:1). From the conductometric-potentiometric titration results shown in Figure 5.2 (a), we noted that PEI displayed three pKas (8.75, 6.37 and 4.25) due to the branched structure containing primary, secondary and tertiary amine groups.[236] The amounts of each amine groups were calculated and summarized in Figure 5.2 (d), where the molar ratio of primary: secondary: tertiary is approximately 1:2:1. In contrast, CGP1 aerogel beads did not display the 3 regimes (Figure 5.2 (b)), where no primary amine groups were detected. The possible reason is that most of primary

amine groups had reacted with the epoxy groups since they are more reactive compared to the secondary and tertiary amines,[75] and the residual amounts of primary amine could not be measured by the titration method. Overall, CGP1 aerogel beads contained a total amine content of 2.67 mmol/g, with 1.50 mmol/g -NH- that would mainly contribute to Cu (II) ions adsorption because of the high steric hindrance of tertiary amine. By increasing the mass ratio of PEI: GPTMS to 3:1, the amine contents in CGP3 aerogel beads were significantly enhanced, with primary, secondary and tertiary amines of 1.50, 2.24 and 2.00 mmol/g, respectively. The high amine content of the aerogel beads is the basis for high Cu (II) ions removal capacity and efficiency. In addition, most studies (listed in Table 5.2) using absorbents containing PEI did not quantitatively measure the 3 types of amines, which is the first time such information is quantified for this aerogel.

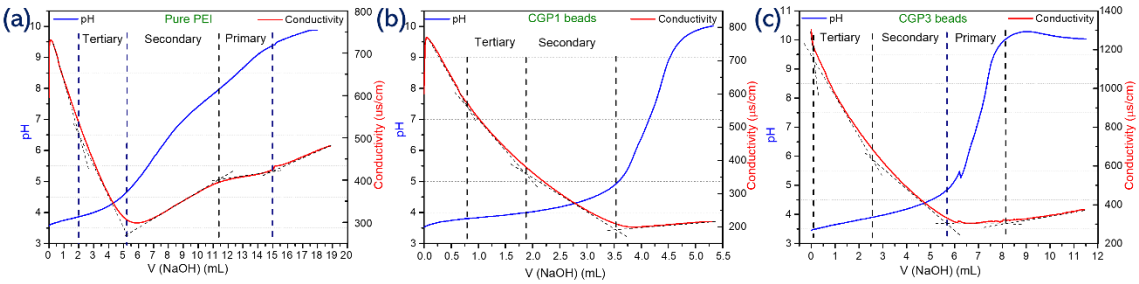

(d)

	Pure PEI	CGP1 beads	CGP3 beads
Primary amine	5.72 mmol/g	0.00 mmol/g	1.50 mmol/g
Secondary amine	9.80 mmol/g	1.50 mmol/g	2.24 mmol/g
Tertiary amine	5.72 mmol/g	1.17 mmol/g	2.00 mmol/g

Figure 5.2 Conductometric- potentiometric titration curve of (a) pure PEI, (b) CGP1 beads, (c) CGP3 beads, and (d) a summary of the amine species and their contents for pure PEI, CGP1 beads, and CGP3 beads.

The morphologies of these aerogel beads were visualized by SEM, and results indicated that all the aerogel beads possessed three-dimensional porous structure but their morphology differed greatly. From Figure 5.3 (a), we observed that pure CNF aerogel consisted of fibrillated and sheet-like structure in the network, where the fibril structure dominated.[83] The fiber bundles interconnected loosely to form porous networks. In contrast, the CG aerogel possessed a denser structure with larger amounts of fiber sheets. This is associated with the crosslinking effect of GPTMS, which brought the fibers closer to form sheets during freezing. The crosslinking effect was more pronounced after the modification with PEI. As shown in Figure 5.3 (c) for CGP1, the

sheets were closely connected with a dense network, where less fiber bundles were evident. Furthermore, there are no individual fiber when the mass ratio of PEI:GPTMS was increased to 3:1. The fibers were tightly crosslinked constituting porous skeletons as seen from Figure 5.3 (d). In addition, the elemental composition of each aerogel was analyzed by EDS, and they are presented in Figure 5.3 (a'-d'). Pure CNF is composed by repeating glucose units comprising of atomic C, H, O. The element analysis result shown in Figure 5.3 (a') is consistent with the expected atomic C, O with neglectable N element. After modification with GPTMS, the Si signal appeared (Figure 5.3 (b')) and it consisted of 14.26 wt% of the total elements. Further grafting PEI increased the N signal intensity to 4.62 wt% of the total elements (see Figure 5.3 (c')). Similarly, the N content in CGP3 aerogel beads increased to 24.22 wt% (see Figure 5.3 (d')), which is much higher than CGP1 and consistent with the titration results. All the results further confirmed the crosslinking reaction was successful and it was effective to prepare the amine-rich porous aerogels.

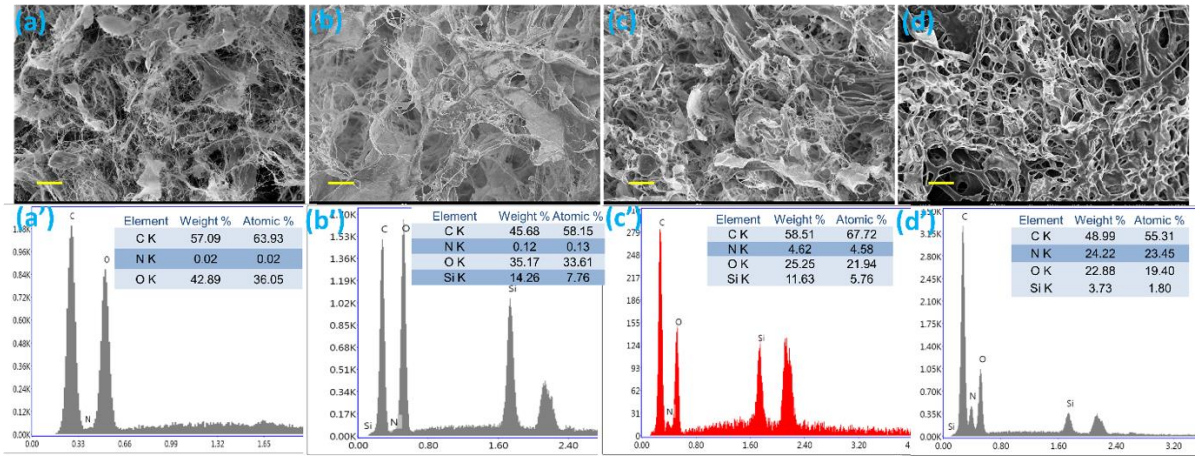

Figure 5.3 SEM images of the aerogel beads surface. (a) pure CNF bead, (b) CG bead, (c) CGP1 bead and (d) CGP3 bead. Scale bar: 20 μm. EDX element analysis and the composition table of (a') pure CNF bead, (b') CG bead, (c') CGP1 bead and (d') CGP3 bead.

Wet mechanical stability is another important factor on the recyclability of the absorbents as they could withstand the stress and deformation during adsorption.[231] Compressive stress (σ)-strain (ε) measurements were performed to evaluate the mechanical properties of the aerogel beads. It should be noted that pure CNF aerogel bead broke easily once placed in water due to the hydrogen bonding formed between the hydroxyl groups on CNF and water molecules. However, after crosslinked with GPTMS and PEI, CNF beads possessed excellent wet mechanical strength as the fibers were linked by robust covalent bonding that could prevent the aerogel disintegration from

hydrogen bonding attraction. The stress (σ)-strain (ε) curves at different strains (Ɛ: 20, 30, 40 and 50%) of CG and CGP1are shown in Figure 5.4 (a) and 5.4 (b). The curves possessed three distinct regions: In the first region, the compressive stress increased linearly with compressive strain, suggesting the beads are elastic when the compressive strain was below 12% for CG and 26% for CGP1; In the second region, the curves displayed a plateau region as the stress increased slightly with compressive strain, which was associated with the gradual collapse of the porous structure in the aerogels; As strain exceeded 25% for CG and 40% for CGP1, the stress showed a dramatic increase as the beads went through a densification process after the complete collapse of the porous structure.[237,238]

Figure 5.4 (c) shows a cyclic stress (σ)-strain (ε) test at a constant strain of 50% for CG, CGP1 and CGP3 beads, where distinct stress difference among the beads was seen. CGP3 bead possessed the most robust mechanical property due to its high crosslinking density. The plastic deformation (refers to the ratio of permanent deformation height to the original height), maximum stress and energy loss coefficient (the area ratio of hysteresis loops to compress curves) of the beads in each cycle were calculated and presented in Figure 5.4 (d), 5.4 (e) and 5.4 (f). From Figure 5.4 (d), the two CGP beads exhibited much smaller plastic deformation compared to CG bead, highlighting their excellent shape recovery property. Specifically, the plastic deformation of CG bead increased from 10.35% (1^{st} cycle) to 12.38% (10^{th} cycle), while that of CGP1 slightly increased from 2.25% (1^{st} cycle) to 2.48% (10^{th} cycle) and that of CGP3 remained around 2.00% without changing. Besides, CGP3 beads displayed the largest maximum stress among the three beads (see Figure 5.4 (e)), indicating the stable structural robustness. Energy loss coefficient is another factor to evaluate aerogel elasticity and mechanical compressibility.[239] Shown in Figure 5.4 (f), the energy loss coefficient of CG bead was much higher than the CGP beads and it decreased from 0.51(1^{st} cycle) to 0.46 (10^{th} cycle). The higher energy dissipation revealed the viscoelastic characteristics of CG beads, and the large plastic deformation was one form of energy conversion. For CGP1, the energy loss coefficient decreased from 0.32 to 0.30, which is small compared to other CNF aerogels, [237,240,241] suggesting the excellent compressibility of the beads. CGP3 displayed a slightly higher energy coefficient (0.33) than CGP1, which might be caused by the high stress at 50% strain (3 times higher than CGP1). The low energy loss coefficient suggested the CGP beads possessed excellent elasticity and compressibility, as the beads could bear high stress by bending the fiber networks, thereby reducing the extent of deformation. All the results further support the conclusion

that crosslinking with PEI is a very effective strategy to increase the amine content and also to improve the wet mechanical strength and shape recovery property of the beads.

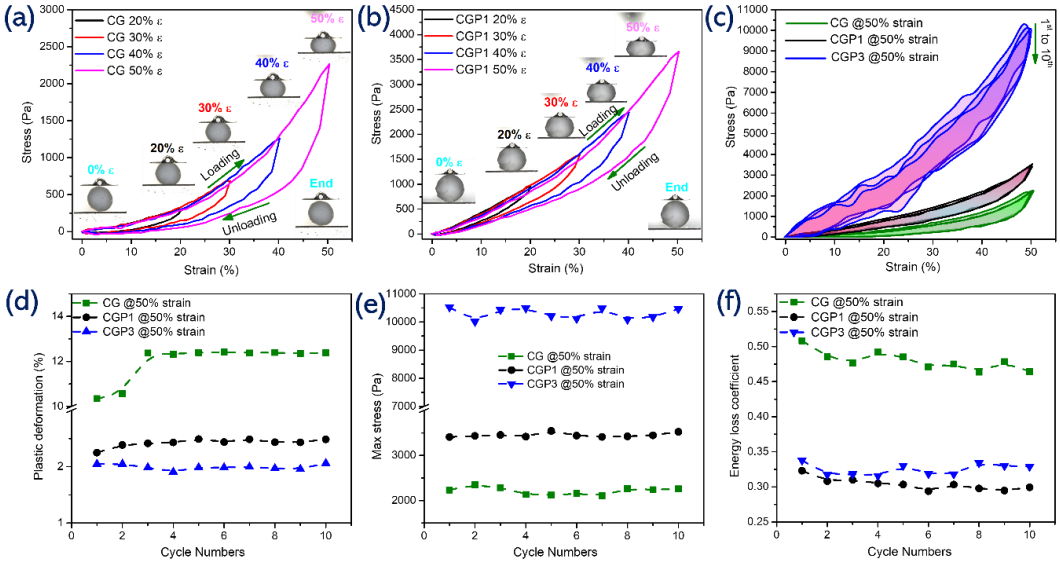

Figure 5.4 Mechanical compression of the aerogel beads. (a) Strain- stress curve of CG with different strain (Ɛ: 20, 30, 40 and 50%), (b) strain- stress curve of CGP1 with different strain (Ɛ: 20, 30, 40 and 50%), (c) Cyclic test of CG, CGP1 and CGP3 at strain of 50%, (d) plastic deformation, (e) max stress and (f) energy loss coefficient of CG, CGP1 and CGP3 at different cycles with a strain of 50%.

5.3.2 Copper adsorption experiments

5.3.2.1 Effect of pH, dosage and ionic strength

The initial pH of the copper solution has a critical effect on the absorbent adsorption performance as it determines the form of copper species as well as the electrostatic repulsive forces between the absorbents and Cu (II) ions. For example, Cu (II) ions transformed to Cu $(OH)_2$ when the pH exceeded 6.5.[219] Therefore, we fixed the initial pH between 3 to 6.2 to study its effect on the bead adsorption capacity. The results are shown in Figure 5.5 (a), where q_e was smaller at low pH due to the strong electrostatic repulsive force between positively charged PEI and Cu^{2+} ions. PEI became protonated at pH below 9.5 (determined from the titration curve), and the protonation degree increased inversely proportional to the pH, hence a suitable pH range of between 5.0 to 6.2 was selected to conduct the adsorption studies. At a pH of 5.6, the adsorption capacity was determined to be 47.5 mg/g while at pH 6.2 a value of 48.5 mg/g was observed, hence no pH

adjustment was necessary. The adsorption data at pH 5.6 is shown in Figure 5.5 (b), where the Cu^{2+} concentration continuously decreased during the adsorption. The CGP aerogel beads transformed from white to bright blue as the adsorption experiment progressed (shown in the inserted picture, due to the complexation of Cu (II) ions with the amine groups on PEI chains.[219]

In addition to Cu (II) ions concentration, we also monitored the pH and conductivity of the mixture during the adsorption process (Figure 5.5 (c)). With the removal of Cu (II) ions, the conductivity of the mixture decreased while the pH increased. The former was due to the contribution of Cu (II) ions to the conductivity. As for the pH, the sustained increased from 5.6 to 7.0 suggested that the adsorption was not dominated by H^+ exchange, but rather by the coordination/ chelation between the amine groups and Cu (II) ions. The increase in the pH could be associated to (i) the shifting of the equilibrium of Cu (II) ion hydrolysis during adsorption, and (ii) the removal of the H^+ by the protonation of the amine groups facilitated by the chelation of Cu^{2+} ions and the nitrogen atom. A control experiment was conducted by immersing CGP1 beads in pure Milli-Q water without Cu (II) ions, and the pH and conductivity were recorded as plotted in Figure 5.5 (d). The conductivity remained constant at around 15 μs/cm during the experiment, indicating no electrolytes (such as free PEI molecules) were released. However, the pH showed a progressing increase from 6.4 to 7.4 after the beads was immersed in the solution, suggesting a slow protonation of the amine groups. Furthermore, to further confirm the above observation, we examined the pH before and after adsorption under different initial pH conditions (Figure 5.5 (e)), and all the pH at equilibrium were in the narrow range of 6- 6.5.

From the above results, we concluded the followings: (1) the PEI protonation and Cu (II) adsorption processes occurred simultaneously, and (2) the adsorption is dominated by coordination/ chelation of amine groups and Cu (II) ions. A suggestion for practical applications of PEI based absorbents is to maintain a constant pH at the optimal value, thereby improving the adsorption capacity since the pH of the solution might change during adsorption.

The effect of absorbent dosage was studied by varying CGP1 beads mass from 20 mg to 100 mg with a fixed Cu (II) solution volume of 10 mL. Seen from Figure 5.5 (f), the equilibrium adsorption capacity of CGP1 beads remained increasing when the absorbent dosage below 60 mg and decreased when further increased absorbent dosage. This may be due to the unsaturated Cu (II) adsorption under higher absorbent dosage. By contrast, the Cu (II) ions removal efficiency

increased constantly with absorbent dosage, yielding 97.26% removal percentage when 100 mg absorbent was used.

Ionic strength is another parameter that could affect the absorbents performance. Figure 5.7 (a) shows the effect of NaCl concentration (0 M, 0.01 M, 0.1 M, 0.25 M and 0.5 M) on CGP1 beads adsorption capacity. It's seen that the equilibrium adsorption capacity decreased from 48.38 mg/g to 8.33 mg/g as NaCl concentration increased from 0 M to 0.5 M. The results indicated that the aerogel adsorption performance was significantly affected when strong ionic strength presented. It might be caused by extreme high concentration of counter ion Cl^- (17,750 ppm for 0.5 M NaCl, which is 177.5 times higher than Cu (II)) that shielded the positive charged amine groups.

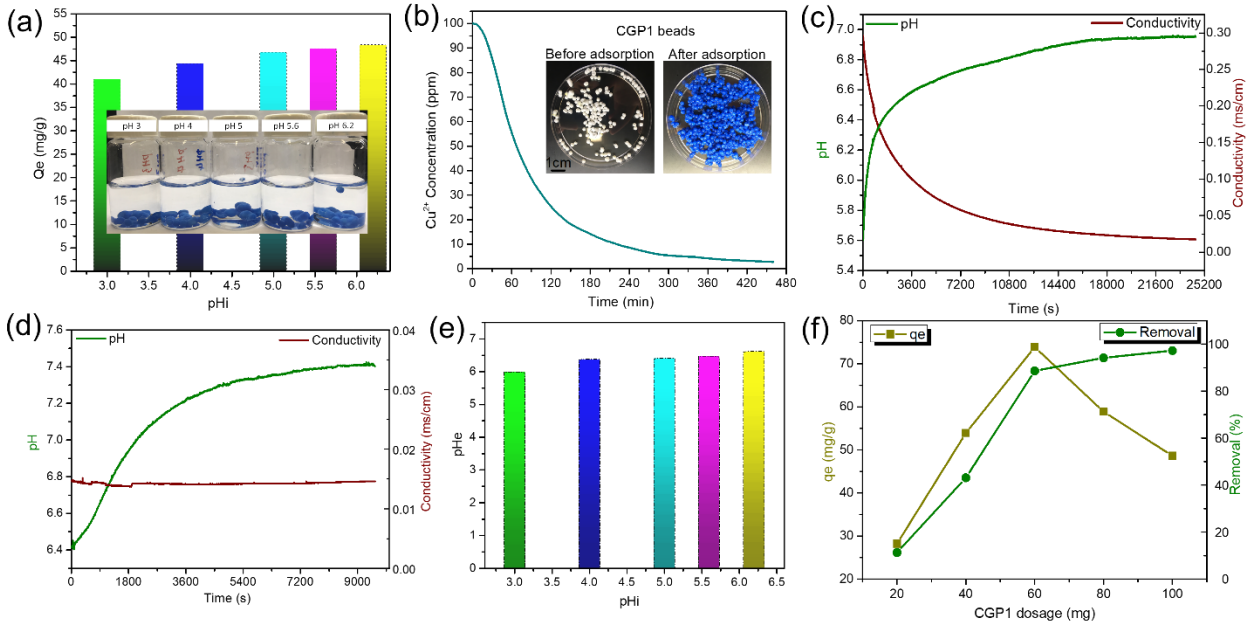

Figure 5.5 (a) Effect of initial pH on the adsorption capacity and (b) concentration of Cu (II) ions during adsorption at initial pH 5.6 (100 mg CGP1 beads, R.T., and 50 mL 100 ppm Cu). (c) pH and conductivity curves during adsorption (100 mg CGP1 beads, R.T., 50 mL 100 ppm Cu and initial pH of 5.6). (d) pH and conductivity curves in Milli-Q water (100 mg CGP1 beads, R.T., and 50 mL Milli-Q water). (e) pH values at adsorption equilibrium with different initial pHs. (f) Effect of absorbent dosage on Cu (II) adsorption capacity and removal percentage (20 mg to 100 mg CGP1 beads, 25 °C, 10 mL 100 ppm Cu and initial pH of 5.6).

5.3.2.2 Adsorption isothermal and thermodynamic study

Adsorption isothermal analyses were carried out to examine the adsorption capacity and interactive behaviors between the adsorbent and Cu (II) ions. Figure 5.6 (a) shows that the equilibrium adsorption capacity increased rapidly at low Cu (II) ions concentration then slowly increased for both CGP1 and CGP3 beads. The adsorption data were further fitted to the Langmuir and Freundlich model as shown in Figure 5.6 (b) and 5.6 (c). Clearly, the Langmuir isothermal model better described the adsorption data, indicating the adsorption sites were homogeneously distributed in the aerogels and the adsorption was monolayer.[217] The parameters for the fittings are summarized in Table 5.1. The maximum adsorption capacity of the beads was calculated according to the Langmuir model, yielding 126.10 mg/g and 163.40 mg/g for CGP1 and CGP3 respectively. The larger adsorption capacity of CGP3 beads compared to CGP1 was due to its higher amine content. In addition, our maximum adsorption capacities were higher than many PEI-based materials reported in the literature (Table 5.2).

Thermodynamic study is very essential to understand the energetic changes during the adsorption process. By investigating the adsorption isothermals at different temperatures (Figure 5.7 (b)), lnKc versus 1/T was plotted as shown in Figure 5.7 (c), from where the thermodynamic parameters (i.e., $\Delta G°$, $\Delta H°$, and $\Delta S°$) can be calculated according to Eq. (5.8) to Eq. (5.11).[242] As shown in Table 5.3, the negative $\Delta G°$ indicated the spontaneous adsorption process, and it increased as temperature went higher. In addition, the negative value of $\Delta H°$ suggested the adsorption was an exothermic process, and it is more favorable at room temperature than higher temperature.

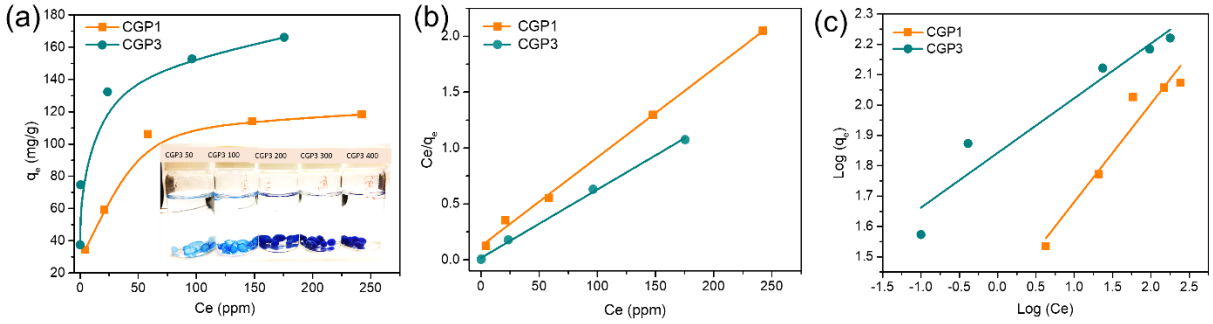

Figure 5.6 (a) Adsorption isothermal of CGP beads, (b) adsorption data fitted with Langmuir isothermal model, (c) adsorption data fitted with the Freundlich model.

Table 5.1 Langmuir and Freundlich constants of CGP1 and CGP3 beads for Cu (II) ion adsorption

Samples	Langmuir isotherm			Freundlich isotherm		
	K_L	q_m (mg/g)	R^2	K_F	n	R^2
CGP1	0.06	126.10	0.99	22.78	0.32	0.92
CGP3	0.38	163.40	0.99	69.55	0.18	0.91

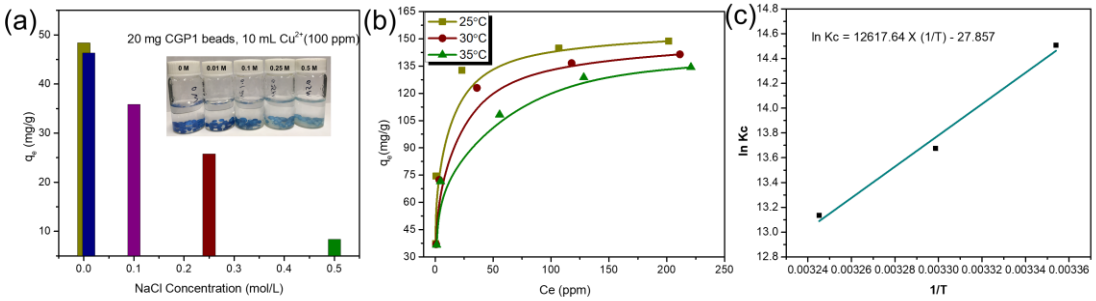

Figure 5.7 (a) Effect of ionic strength on the CGP1 beads adsorption capacity (20 mg CGP1 beads, 10 ml 100 ppm Cu (II) solution). (b) Adsorption isothermal of 20 mg CGP1 beads at different temperatures (20 mL Cu (II) solutions, pH 5.6). (c) Plot of ln K_C versus 1/T for Cu (II) ions adsorption of CGP1 aerogel beads at different temperatures

5.3.2.3 Effect of Cu (II) ions on beads morphology and mechanical property

The morphologies and elemental compositions of the CGP beads after adsorption were examined and shown in Figure 5.8. The structure of the aerogel beads was more compact after the adsorption studies as seen in Figure 5.8 (a) and 5.8 (b), which might be attributed to the bridging effect of the absorbed Cu (II) ions. These Cu (II) ions could crosslink the amine groups to produce the densely porous networks. Thus, the presence and distribution of Cu (II) ions was further confirmed by elemental analysis and EDS mapping. From Figure 5.8 (a') and 5.8 (b'), the proportion of Cu (II) ions in CGP1 and CGP3 beads was 10.28 wt% and 15.99 wt% respectively. In addition, the absorbed Cu (II) ions were uniformly distributed in the aerogel networks as revealed by the EDS mapping images shown in Figure 5.8 (a") and 5.8 (b"), indicating the adsorption sites were homogenously distributed in both aerogels.

Table 5.2 Comparison of the maximum adsorption capacities for Cu (II) ions from various reported sorbents with this study

Material	pH	q_{max} (mg/g)	References
TEMPO-CNF-TMPTAP-PEI	5.5	485.44	[217]
Gelatin-glutaraldehyde-PEI	4.6	61.2	[243]
TEMPO-CNF-glutaraldehyde-PEI	5.0	52.32	[228]
cellulose/alginate-glutaraldehyde-PEI	5.5	177.1	[244]
CNF-PDA-PEI	4.0	103.5	[229]
Polyethyleneimine-bacterial cellulose (PEI-BC)	4.5	148.0	[245]
TEMPO-NFC-PEI	5.0	175.44	[230]
Soybean protein -ECH-PEI	5.5	136.2	[219]
CS/GO aerogel beads	4.9	457.5	[246]
CGP1 beads	5.6	126.10	this study
CGP3 beads	5.6	163.40	this study

Table 5.3 Thermodynamic parameters of Cu (II) adsorption by CGP1 beads

Temperature	**K_C**	**$\Delta G°$ (kJ/mol)**	**$\Delta H°$ (kJ/mol)**	**$\Delta S°$ (kJ/mol)**
298.15 K	2.00×10^6	-35.96	-104.9	-231.6
303.15 K	8.70×10^5	-33.91		
308.15 K	5.06×10^5	-32.56		

To further explore the crosslinking effect of Cu (II) ions, the compressive strain- stress of CGP1 beads after Cu (II) adsorption with initial Cu (II) concentration of 0 ppm- 400 ppm were measured, and data are shown in Figure 5.9 (a). At fixed strain of 50%, the stresses of the wet beads after Cu adsorption were significantly higher than before the adsorption, and the stress was proportional to Cu (II) ion concentration as more Cu (II) ions were absorbed. The increased stress was caused by the crosslinking effect of Cu (II) ions, which could bring the amine groups nearby closely and form a more compacted network due to the strong coordination bonding between Cu (II) ions and amine groups.

5.3.2.4 Adsorption mechanism

The adsorption mechanism was investigated by FTIR based on CGP beads before and after the adsorption. In Figure 5.9 (b), an intense peak appeared after adsorption at 625 cm^{-1} in both CGP1 and CGP3 curves, which was due to the complex of Cu and amine groups.[219] In addition, the N-H bending vibration peak at 1570 cm^{-1} faded and the intensity of C-N stretching peak at 1316 cm^{-1}

decreased in both CGP1 and CGP3 curves after Cu adsorption.[247] Also, two N-H stretching vibration peaks at 3215 & 3125 cm^{-1} were observed in the CGP3 beads after the adsorption, which might be caused by the Cu (II) ion. In contrast, no clear change was evident for CGP1 after adsorption, which indirectly confirmed the titration results that CGP1 beads possessed lower amounts of primary amine groups. All these changes suggested that the amine groups participated in the adsorption. Except for the amine groups, the vibration peak of C-O-C on the glucose units at 1060 cm^{-1} decreased significantly, suggesting that the O also participated in the adsorption process. The electron configuration of Cu^{2+} is [Ar] $3d^9$, who has one empty 4S and three empty 4P orbitals. Typically, Cu^{2+} has 4 or 6 coordination numbers depending on the orbital hybridization. Among them, 2 or 4 sites coordinated with the amine groups and the residuals were occupied by the oxygen containing groups (e.g., -OH, C=O, C-O, and H_2O). [217]

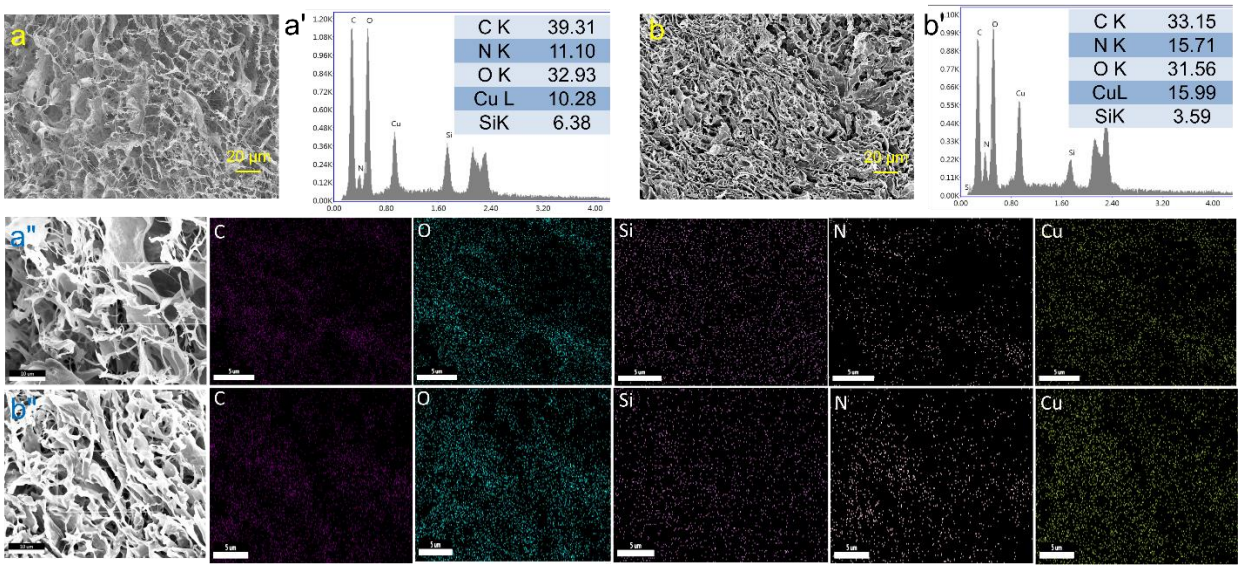

Figure 5.8 SEM images of the cross section of (a) CGP1 and (b) CGP3 beads after Cu (II) adsorption, scale bar 20 µm. Element composition by weight % of (a') CGP1 and (b') CGP3 beads after Cu (II) adsorption. EDS mapping of C, O, Si, N, Cu of (a') CGP1 and (b') CGP3 beads after Cu (II) adsorption, scale bar 10 µm for selected areas and 5 µm for mapping images.

5.3.2.5 Kinetics study

CGP1 aerogel beads was used to study the adsorption kinetics, and Figure 5.10 (a) shows its absorption kinetics under different initial Cu (II) concentrations. It's seen that all the adsorptions

were fast in the first 120 min and no more than 10 h was needed to reach the equilibrium. In comparison, as shown in Figure 5.9 (c), equal amount of CGP1 aerogel monolith possessed a much longer adsorption time (>16 h) than CGP1 beads (< 8h, Figure 5.5 (b)) under the same condition. These results demonstrated that our CGP aerogel beads possessed a faster and more efficient than previous reported studies. [217,219,226,229,230,243,245,248] The reasons for the high adsorption rates are: (1) small size of the absorbents possessed high surface area that greatly increased the contact area for the binding of Cu (II) ions, (2) more functional groups on the surface to rapidly capture the ions, and (3) the small size of the beads greatly reduced the Cu (II) ion diffusion path. The adsorption kinetic of CGP1 beads in 100 ppm Cu (II) is shown in Figure 5.10 (b). Clearly, the adsorption rate was very fast in the first 120 min, after it decreased to a slower rate. To elucidate the adsorption behavior on Cu (II) ions, the adsorption data was fitted to Pseudo-first and Pseudo-second order models as shown in Figure 5.10 (c), and the fitting parameters are shown in Table 5.4. The results suggested the data obeyed the Pseudo-second order model better, indicating the adsorption process was chemical adsorption.

To further examine the diffusion mechanism in the Cu (II) ions uptake process, the intra-particle diffusion model was evaluated. As shown in Figure 5.10 (d), the plots of q_t versus $t^{0.5}$ yielded three linear regions, which are assigned to three stages of diffusion of Cu (II) ions: (1) external diffusion from bulk solution to the surface of the aerogel, (2) internal diffusion from the surface to the inner section of the beads once the surface sites are saturated, (3) slow diffusion until the beads become saturated.[229,247] The slopes of the three stages were calculated from the intraparticle diffusion model and summarized in Table 5.4. It is evident that $K_{id,1} > K_{id,2} > K_{id,3}$, suggesting the adsorption rate in the first stage was very fast, much larger than the second and third stage. The results indicated that the adsorption was chemisorption process and was affected by pore diffusion, consistent with most PEI based absorbents listed in Table 5.2.

Table 5.4 Parameters of Pseudo- first- order, Pseudo- second- order and Intra-particle diffusion for CGP1 beads adsorption kinetics

Samples	Pseudo-first- order		Pseudo-second- order		Intra-particle diffusion (g mg-1 min-1)		
	K_1	R^2	K_2	R^2	$K_{id,1}$	$K_{id,2}$	$K_{id,3}$
CGP1	0.00588	0.967	0.00040	0.999	4.516	1.518	0.358

5.3.2.6 Simulated wastewater treatment

Natural organic matter (NOM), such as humic acid, fulvic acid and non- humic substances, is one of the main components in industry wastewater.[249,250] In this study, we simulated real wastewater by addition of 50 ppm humic acid to various concentration of Cu (II) solutions to evaluate the CGP1 beads adsorption capacity. Shown in Figure 5.9 (d), the adsorption capacity of CGP1 beads increased with increasing initial Cu (II) concentration in the presence of 50 ppm humic acid, which was slightly lower when compared to the adsorption capacity without humic acid. The reduced adsorption capacity may be due to the interference effect of humic acid, which could occupy the positive charged amine groups of CGP absorbents as well as attract Cu (II) ions because of its inherent negative charge. Nevertheless, the results suggested the CGP beads possessed excellent adsorption performance and could be considered as a promising absorbent in real wastewater treatment.

5.3.3 Regeneration study

Except for high adsorption capacity, an excellent absorbent should possess excellent recyclability in order to satisfy the criteria of sustainability and economics. The absorbed Cu (II) ions can be easily removed from the absorbents using ethylenediaminetetraacetic acid (EDTA), which is a strong chelation agent for Cu (II) ions. The adsorption performance of the regenerated CGP1 beads was evaluated and shown in Figure 5.9 (e). No clear reduction in the adsorption capacity was observed during the five regeneration cycles, which is likely a result of the structural stability and excellent chelation property of the aerogel beads. The excellent regeneration property, small size as well as high removal efficiency and capacity of the CGP beads pave the foundations for practical applications.

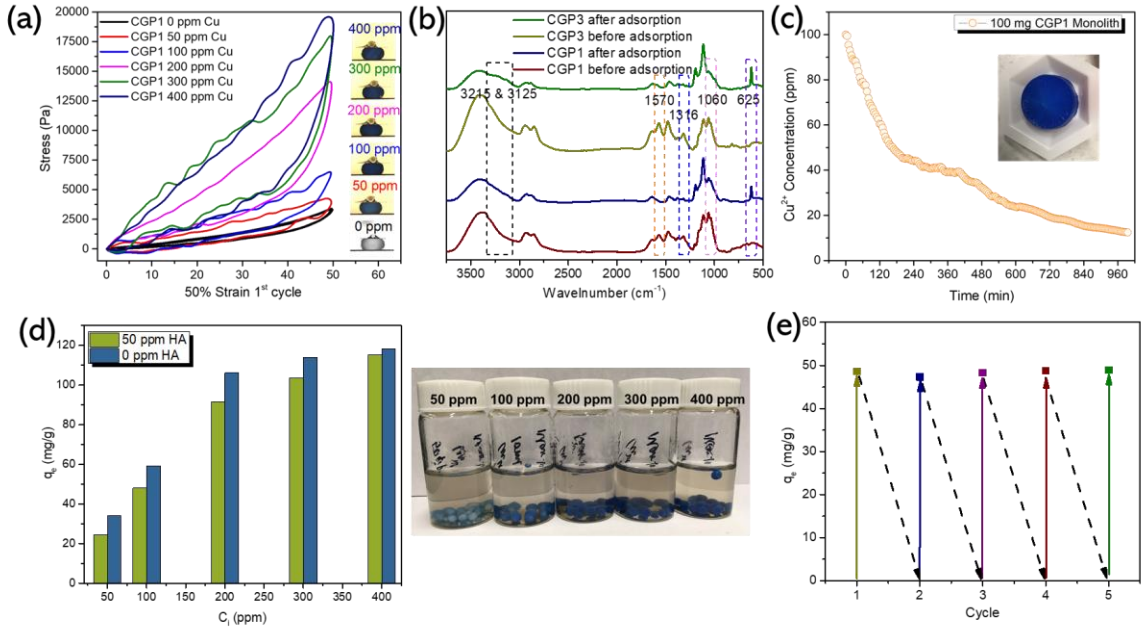

Figure 5.9 (a) Compressive strain-stress curves of CGP1 beads after Cu (II) adsorption in 0-400 ppm copper solution, (b) FTIR patterns of CGP1 and CGP3 beads before and after adsorption in 100 ppm Cu (II) solution, (c) adsorption kinetic of CGP1 monolith (100 mg aerogel with diameter of 28 mm, pH 5.6, 50 mL 100 ppm Cu (II) solution), (d) comparison of CGP1 beads adsorption capacity in simulated wastewater containing different concentration of NOM (0 ppm and 50 ppm humic acid) and Cu (II) (50 ppm to 400 ppm), (e) five cycles of regeneration study for CGP1 beads (100 mg absorbents, 50 mL 100 ppm copper solution, at R.T. and pH 5.6).

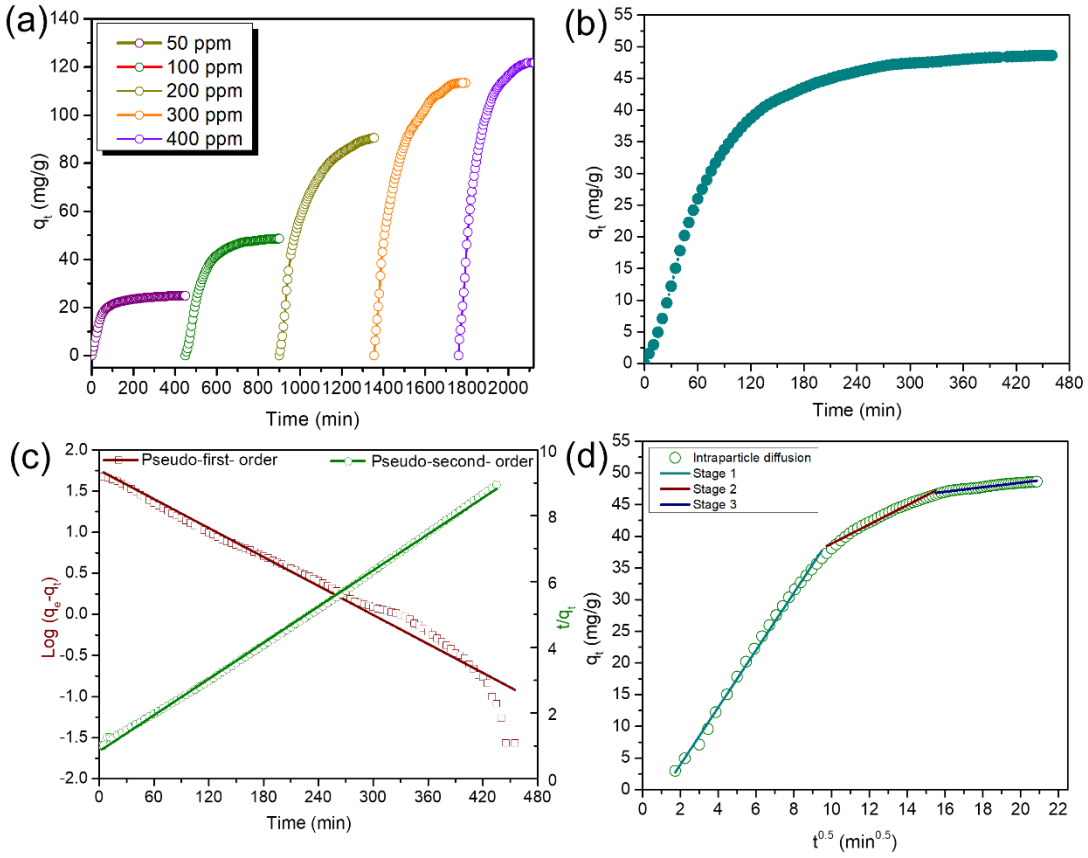

Figure 5.10 (a) adsorption kinetics of CGP1 beads in Cu (II) solution with different initial concentration (50-400 ppm), (b) adsorption kinetics of CGP1 beads in 100 ppm Cu (II) solution and (c) the data fitted to Pseudo- first- order and Pseudo- second order models and (d) the data fitted to intraparticle diffusion model.

5.4 Conclusions

In this study, a sustainable bio-based material, cellulose nanofibril (CNF), was used as a scaffold to prepare aerogel as absorbents for heavy metal removal. The high Cu (II) adsorption capacity of the absorbents was achieved by introducing branched PEI on the CNF with GPTMS as crosslinker. By increasing the mass ratio of PEI to GPTMS from 1:1 to 3:1, the total amine content of the CGP aerogel beads was increased from 2.67 to 5.74 mmol/g, resulting in the enhancement of Cu (II) adsorption capacity from 126.10 to 163.40 mg/g; A denser aerogel network with increased mechanical strength was prepared. The Cu (II) adsorption kinetic is a driven by chemisorption, and both the amine and oxygen containing groups were involved in the chelation process. The

intra-particle model revealed that the adsorption process is pore diffusion controlled. The aerogel network became more compact after Cu (II) adsorption yielding a higher compressive stress due to the crosslinking effect of Cu (II) ions. In addition, the pH of the mixture was altered during the adsorption in the PEI based absorbents, hence maintaining a constant pH is important for improving the adsorption capacity. Overall, the prepared CGP aerogel beads are promising systems due to the simple preparation method, room temperature reaction, high adsorption capacity, fast removal rate, robust mechanical strength as well as excellent regeneration property.

Chapter 6* Carboxylated Cellulose Cryogel Beads via a One-step Ester Crosslinking of Maleic Anhydride for Copper Ions Removal

In this study, we developed a one-step protocol to prepare highly carboxylated and chemically crosslinked cellulose nanofibril (CNF) cryogel beads using maleic anhydride (MA). Fourier transform infrared spectroscopy (FTIR) and conductometric-potentiometric titration results confirmed the presence of carboxyl groups and ester linkages produced simultaneously during the ring open reaction of MA, yielding a carboxylic content of up to 2.78 mmol/g. The effect of CNF concentration on the morphology and wet mechanical strength of the crosslinked cryogel beads were also investigated, and results suggested that higher CNF concentration yielded a compact network that displayed a maximum compressive stress of 2800 Pa at 60% strain. In addition, the heavy metal ions (i.e., Cu (II)) removal capacity, kinetics, mechanism as well as the recyclability of the resulted CNF-MA cryogel beads were examined.

Abstract graphic

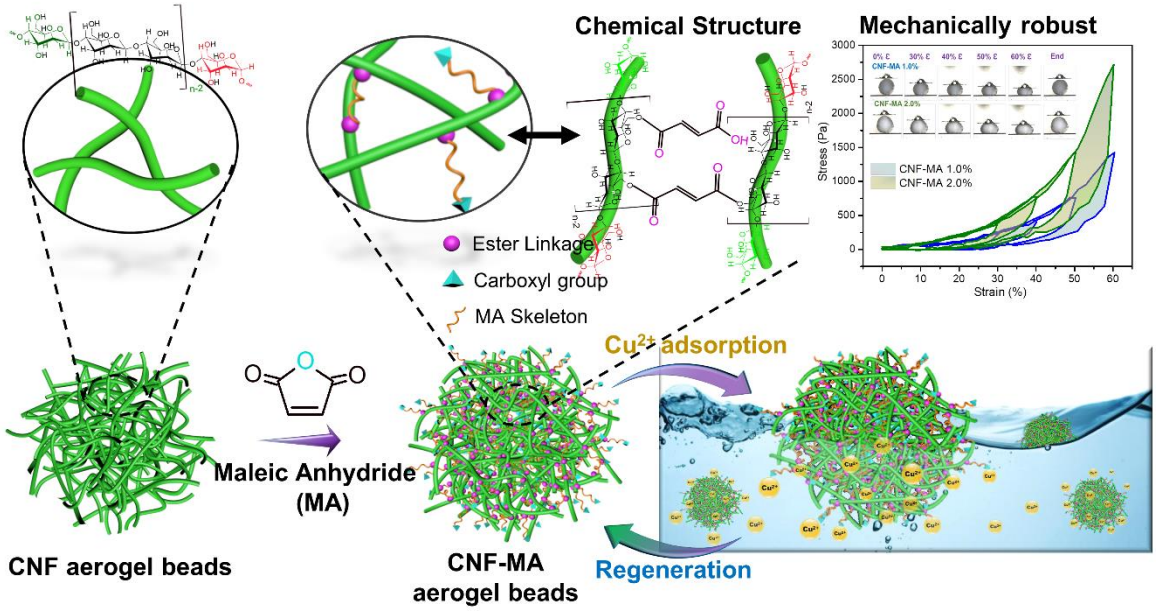

* This chapter is adapted from a paper: Tang, C.; Brodie, P.; Brunsting, M.; Tam, K. C. Carboxylated Cellulose Cryogel Beads via a One-Step Ester Crosslinking of Maleic Anhydride for Copper Ions Removal. Carbohydr. Polym. 2020, 242 (02), 116397.

6.1 Introduction

With the rapid development of urbanization, heavy metal ions (such as copper (II), lead (II), and chromium (VI)) produced from mining, machinery manufacturing and chemical engineering processes have been discharged causing serious water pollution worldwide.[251] Strategies associated with the removal of these toxic heavy metals include ion exchange, chemical precipitation, flocculation, membrane separation and adsorption. Among them, adsorption is widely adopted due to its ease of operation and scale up.[224] Activated carbon and petroleum-based polymers are commonly used absorbents or flocculants. However, their low adsorption capacity, high cost, poor recyclability and non-degradability make them a less attractive choice.[217] Therefore, novel absorbents that satisfy all the practical requirements should be developed for future applications.

Cellulose nanomaterial is one of the potential alternatives as it is abundant on earth, renewable and bio-degradable.[173] As one of the promising nanomaterials, cellulose has been widely explored in many areas, from waste water treatment,[252] energy storage,[253] oil recovery,[59] biomedical,[254] agriculture to food additives. [58,255] Depending on the aspect ratio, wood derived cellulose materials can be classified into four categories: cellulose fiber (CF) produced from bleached pulp, microcrystalline cellulose (MCC), cellulose nanofibrils (CNF) and cellulose nanocrystals (CNC). For wastewater treatment application, cellulose nanomaterials (CNF and CNC) possess advantages over others because of their larger specific surface area and abundant surface hydroxyl groups.[251] Nevertheless, pristine cellulose nanomaterials have low removal capacity due to the low affinity of hydroxyl groups towards heavy metals. Therefore, decorating functional groups on cellulose nanomaterials is necessary to improve their adsorption capacity.[217]

Carboxylation is an effective way to introduce adsorption sites on cellulose nanomaterials considering their abundant surface hydroxyl groups.[256] To date, several methods have been successfully demonstrated for preparing carboxylated cellulose nanomaterials absorbents, including 2,2,6,6-tetramethylpiperidine-1-oxyl (TEMPO) radical oxidation, ammonium persulfate (APS) oxidation, periodate-chlorite oxidation, carboxymethylation, esterification, and organic carboxylic acid hydrolysis.[257] For example, Qin et al. prepared carboxylated CNF via the carboxymethylation with monochloroacetic acid, achieving a carboxyl content of 2.70 mmol/g and Cu (II) removal capacity of 115.30 mg/g;[258] Wang et al. produced carboxylate CNF from citric/

hydrochloric acid hydrolysis, yielding a carboxyl content of 1.18 mmol/g and Cu (II) removal capacity of 45.05 mg/g;[259] In another study, carboxylated CNC was produced by Fe^{2+}/H_2O_2 oxidation, yielding a carboxyl content of 2.20 mmol/g and a Cu (II) removal capacity of 51.10 mg/g; [260] Li et al. adopted TEMPO-oxidation to prepare carboxylate CNF, producing a carboxyl content of 1.40 mmol/g and achieving Cu (II) removal capacity of 102.90 mg/g.[261] However, most of the reported cellulose nanomaterial- based absorbents directly used their single fibril form, which are difficult to recover due to their submicron size.

Assembling these single fibers into an cryogel is an excellent approach to address this issue as cryogel that consists of an interconnected porous solid material can be readily separated from the bulk solution.[83] When it comes to the fabrication of cryogel, CNF exhibits unique property, such as structural flexibility and high aspect ratio, which favors the formation of highly entangled networks.[201] However, physically crosslinked CNF cryogel is easy to disintegrate in water as a result of hydrogen bonding formed between water molecules and carboxyl/hydroxyl groups on the carboxylated CNF. [217] Chemical crosslinking is necessary to produce stronger network in order to improve the stability and recyclability of the CNF cryogel.[262] Generally, most studies adopted a two steps process to prepare carboxylated and chemically crosslinked CNF cryogel: firstly, carboxylated CNFs are prepared and they are crosslinked using crosslinkers such as organic silica or epichlorohydrin, which require various chemicals, solvents, water and time.[75,219] In addition, most of these cryogels are monoliths, which usually take long time to achieve adsorption equilibrium due to the long diffusion path length.

In this study, we developed an efficient and simple and one step procedure to prepare carboxyl decorated and chemically crosslinked CNF cryogel beads. Pristine CNF cryogel beads (average diameter of 3 mm) were prepared by extruding the CNF slurry solution into liquid nitrogen followed by freeze drying, and maleic anhydride (MA) was used as the crosslinker. The CNF cryogel beads were immersed in molten maleic anhydride for 4 h at 120 °C to prepare robust carboxylated CNF cryogel beads. The chemical structure, elemental composition, morphology, mechanical property, Cu (II) ion adsorption capacity and mechanism as well as recovery performance of the cryogel beads were investigated. The novelty of this work is the carboxyl functionalization and ester crosslinking of CNF cryogel beads that was achieved in a one-step ring opening reaction of MA. Besides, several advantages associated with this method are: (1) the one

step reaction is straightforward, where no toxic organic solvent and catalyst (e.g., DMF, DMSO and Pyridine) are needed; (2) CNF cryogel beads were used instead of CNF cryogel monoliths for Cu (II) removal to improve the removal efficiency by reducing copper ion diffusion path length; (3) The CNF beads were easily recovered from MA solution by a mesh after the reaction and the MA solution could be reused for subsequent reaction; (4) Instead of using week acid solutions (e.g., citric acid, oxalic acid, maleic acid, etc.) to prepare carboxylated CNF,[257,259,263] we used molten acid anhydride as the solvent and a high temperature (120 ℃) to improve the esterification efficiency and avoid further hydrolysis as minimal water was present in the reaction mixture;[264,265] and (5) the mechanical performance of the CNF cryogel beads was measured, a characteristic that was not often determined.

6.2 Material and methods

6.2.1 Materials

CNF slurry was obtained from the Process Development Center (University of Maine), and the detailed production process was reported previously.[201] Maleic anhydride (MA, 99%), Acetone (ACS agent, ≥ 99.5%), copper (II) sulfate pentahydrate, sodium hydroxide (NaOH), hydrochloric acid (HCl, 37%), potassium bromide (KBr, FTIR grade), and ethylenediaminetetraacetic acid disodium (EDTA-Na_2) were purchased from Sigma Aldrich. Ultrapure water (conductivity of 15 μs/cm) was used to prepare the aqueous dispersions.

6.2.2 Preparation of carboxylated CNF cryogel beads

Well-dispersed CNF slurry (with a concentration of 0.5 wt% to 2.0 wt%) was transferred to a 50 mL plastic syringe injector connected to a 200 μL plastic pipette tip (cut to an inner tip dimension of 1 mm). The slurry was dispensed at a controlled rate (80 mL/ hour) into liquid nitrogen via a syringe pump to produce uniform spherical beads. The frozen beads were subjected for freeze drying at -45 ℃ for 4 days to produce pristine CNF cryogel beads. To prepare carboxylated CNF cryogel beads, pristine CNF cryogel beads were mixed with excessive amount of MA at a mass ratio of CNF:MA = 1:50, and reacted at 120 ℃ for 4 h under occasional stirring.[264] The beads were separated from the MA solution using a steel mesh and thoroughly washed by acetone, followed by soaking in acetone overnight to remove the unreacted MA. The residual MA solution can be reused for the next reaction. Hereafter, the washed beads were dried in vacuum oven at 60 ℃, and

the beads were denoted as CNF-MA X, where X represents the initial concentration of CNF used. For example, CNF-MA 1.0 % means the carboxylate CNF beads prepared from 1.0 % CNF.

6.2.3 Characterization

All the CNF-MA X beads were dialyzed in ultrapure water until the conductivity became constant, confirming the complete removal of free MA molecules and other chemicals prior to the characterization.

Fourier transform infrared spectroscopy (FTIR) spectra were obtained using the Bruker Tensor 27 spectrometer FT-IR spectrometer with a resolution of 4 cm^{-1} and a scanning number of 32 from 400 to 4000 cm^{-1}. Briefly, pellets were prepared by mixing freeze-dried cryogel beads with KBr, finely ground in mortar and pestle then compressed into a pellet.

Scanning electron microscopy (SEM) equipped with an Energy Dispersive X-Ray Spectroscopy (EDS) was used to examine the morphologies and elemental composition of the cryogel beads. The dried spherical cryogel beads were sputtered with gold and the exterior surfaces were visualized in a Carl Zeiss NTS GmbH instrument with an acceleration voltage of 5 keV. To examine the distribution of Cu (II) ions in the interior of the cryogel, the CNF-MA beads before and after Cu (II) adsorption were cut into hemispheres after frozen in liquid nitrogen, and the cross sections were subjected to elemental analysis.

The carboxyl contents of the beads were quantitatively determined using a conductometric-potentiometric titrator (Metrohm 809 Titrando auto-titrator (Switzerland)). Samples were dialyzed in ultrapure water until the conductivity remained constant prior to the titration. A known mass of dry beads was placed in a 100 mL vessel containing 25 mL ultrapure water. Then, 0.1 M HCl was used to adjust the pH to 3.5, which was then titrated with 0.01 M NaOH. The carboxyl content of the sample was calculated using Eq. (6.1):

$$carboxyl\ content\ (mmol/g) = V\ (NaOH) \times 0.01/m \qquad (6.1)$$

where V (mL) is the volume of NaOH and m (g) is the dry weight of the sample. The titration for each sample was repeated twice. To measure the total carbonyl content (TCC), a known mass of dry beads was treated with 0.5 M NaOH to cleave the ester linkages, which was then titrated with 0.5 M HCl. The TCC was also calculated based on the same principle as outlined in Eq. (6.1).

The compressive strengths of the CNF-MA X cryogel beads were evaluated using a Microtester G2 (CellScale Biomaterials Testing, Waterloo). To fully cover the beads, a 4 mm × 4 mm steel platen was selected and glued to the cantilever (diameter of 0.5588 mm). The beads were placed under the steel plate and the compressive tests were conducted in a water bath. All compressive tests were performed in displacement control mode with loading and recovery duration of 30 s. The images, displacement (δ) and applied force (F) in real time recorded during the compression. The strain (Ɛ) and stress (σ) were calculated by assuming all the beads were perfectly spherical and the contact area was fixed during the compression. Here, we use the maximum contact area to calculate the stress as shown in the following equations:

$$Ɛ\ (\%) = 100\ \times \delta/D \tag{6.2}$$

$$S\ (mm^2) = \pi(D/2)^2 \tag{6.3}$$

$$\sigma\ (\text{Pa}) = \ 10^6 \times F/S \tag{6.4}$$

where D (mm) is the diameter of the bead measured by the machine, and F (N) is the force applied at real time.

The densities of the cryogel beads were calculated using the dry mass and volume (where the bead diameter was measured in the wet state). Also, the porosity could be estimated using Eq. (6.5) according to Buchtová & Budtova (2016).

$$Porosity\ \% \ = (1 - \frac{\rho_{beads}}{\rho_{cellulose}}) \times 100 \tag{6.5}$$

where $\rho_{cellulose}$ is 1.5 g/cm^3.

6.2.4 Adsorption experiments

6.2.4.1 Adsorption pH study

To study the optimized pH for adsorption, 100 mg dry CNF-MA 1 % beads were added and dialyzed in ultrapure water before immersing in 50 mL 100 ppm Cu (II) solution. The initial pH (pH_i) of the solution was adjusted from 3 to 6.2 using either 0.1 M HCl or NaOH. The concentration of Cu (II) in the mixture was monitored using a Copper Ion Selective Electrode (Cu-ISE, Cole-Parmer®). Besides, the pH of the solution during adsorption was recorded by a pH electrode and the value at equilibrium (pH_e) was reported. Also, the conductivity of the solution

during adsorption was recorded by a conductivity probe. The adsorption capacity q_e (mg/g) was calculated using Eq. (6.6):

$$q_e = \frac{(C_0 - C_e)}{m} V \quad (6.6)$$

where C_0 (mg/L) and C_e (mg/L) are the initial and equilibrium concentrations, respectively; q_e (mg/g) is the adsorption capacity at equilibrium; V (L) represents the solution volume of Cu (II) ions and m (g) represents the mass of the cryogel adsorbent.

6.2.4.2 Adsorption isothermal study

100 mg CNF-MA 1 % or CNF-MA 2 % beads were immersed 50 mL Cu (II) solutions with concentration ranging from 50 to 400 ppm to study the isothermal adsorption. The adsorption experiments were carried out at 25 ℃ with an initial pH of 5.6. The adsorption behavior was described by the non-linear forms of Langmuir and Freundlich isotherm models: [267]

$$q_e = \frac{q_m K_L C_e}{1 + K_L C_e} \quad (6.7)$$

$$q_e = K_F C_e^n \quad (6.8)$$

where q_m is the maximum adsorption capacity of the absorbent, and K_L and K_F is the binding constant of the Langmuir and Freundlich equation, respectively; n is the Freundlich model represents the empirical parameter.

6.2.4.3 Adsorption kinetic study

100 mg CNF-MA 2 % beads were added to 50 mL of 200 ppm Cu (II) solution at pH 5.6 and 25 ℃, and the mixture was continuously stirred until the adsorption approached equilibrium. The adsorption data was fitted to the non- linear forms of pseudo-first order kinetic model, pseudo-second order kinetic model, and intra-particle diffusion model described in Eqs. (6.9), (6.10), and (6.11) respectively:

$$q_t = q_e(1 - e^{-k_1 t}) \quad (6.9)$$

$$q_t = \frac{q_e^2 k_2 t}{1 + k_2 q_e t} \quad (6.10)$$

$$q_t = K_{id} t^{0.5} + C \quad (6.11)$$

where q_t (mg/g) is the adsorption capacity at time t, and k_1 and k_2 are the rate constants for the pseudo-first order adsorption and pseudo-second order adsorption kinetic models, respectively. K_{id} is the rate constant (g mg^{-1} min^{-1}) of intra-particle diffusion kinetics.

6.2.5 Recovery study

The 100 mg CNF-MA 2% beads after Cu (II) adsorption were immersed in 0.1 M EDTA-Na_2 solution to remove the Cu (II) ions. Afterwards, the beads were recovered using a mesh and hand squeezed to remove the excessive solution, and then soaked in ultrapure water several times to elute the salts until the conductivity became constant. The recovered beads were subjected to adsorption in 50 mL 200 ppm Cu (II) solution at pH 5.6 and 25 ℃, and the recovery process was repeated four times.

6.3 Results and discussion

The preparation process and formation mechanism of the CNF-MA cryogel beads are illustrated in Figure 6.1. The CNF fibers used in this experiment exhibited an average length of tens of micrometers and average width of tens of nanometers as shown in the TEM image. These noodles like fibers tended to form interconnected networks due to their high aspect ratio and structural flexibility. Uniformed spherical beads were produced by injecting the CNF slurry into liquid nitrogen, and the extreme low temperature induced the rapid growth of ice crystals within the networks.[262] The ice crystals further promoted the aggregation of CNF fibers to form pore walls, and porous cryogel beads with an average diameter of 3 mm were obtained when the ice crystals were removed by sublimation in a freeze dryer.[75] The size of the beads was limited by the nozzle diameter and the injection method, which could range from several micrometers to several millimeters as reported by many previous studies.[92,254,268,269]

Acid anhydrides, such as succinic anhydride (SA) and maleic anhydride (MA) were reported to be effective in introducing carboxyl groups onto cellulose nanomaterials *via* a ring open reaction.[270–272] However, most of those previous works focused on producing individual carboxylated CNC or CNF whiskers using acid anhydrides without studying the effect of crosslinking. Herein, we selected MA as a model acid anhydride to study their dual functions. In contrast to previous reports that used solvents, such as DMF or DMSO, we directly mixed molten MA and CNF cryogel beads since MA has a moderate melting point (52.8 ℃). The advantages of this method are: (1) toxic solvents are not needed; (2) no catalyst is needed as anhydride is very reactive; (3) the integrity of

CNF cryogel beads can be maintained in molten MA due to the higher interfacial tension between beads and MA compared to DMF or DMSO; (4) the residual MA solvent can be recycled. In addition, we propose two types of reaction occurring during the ring open reaction at high temperature (120 ℃): (1) one end of MA graft onto CNF via esterification with hydroxyl groups while the other end remained as carboxyl groups; (2) both ends of MA grafted onto CNF via esterification produced ester crosslinked CNF fibers, where the chemical structure of CNF-MA beads is shown in Figure 6.1.

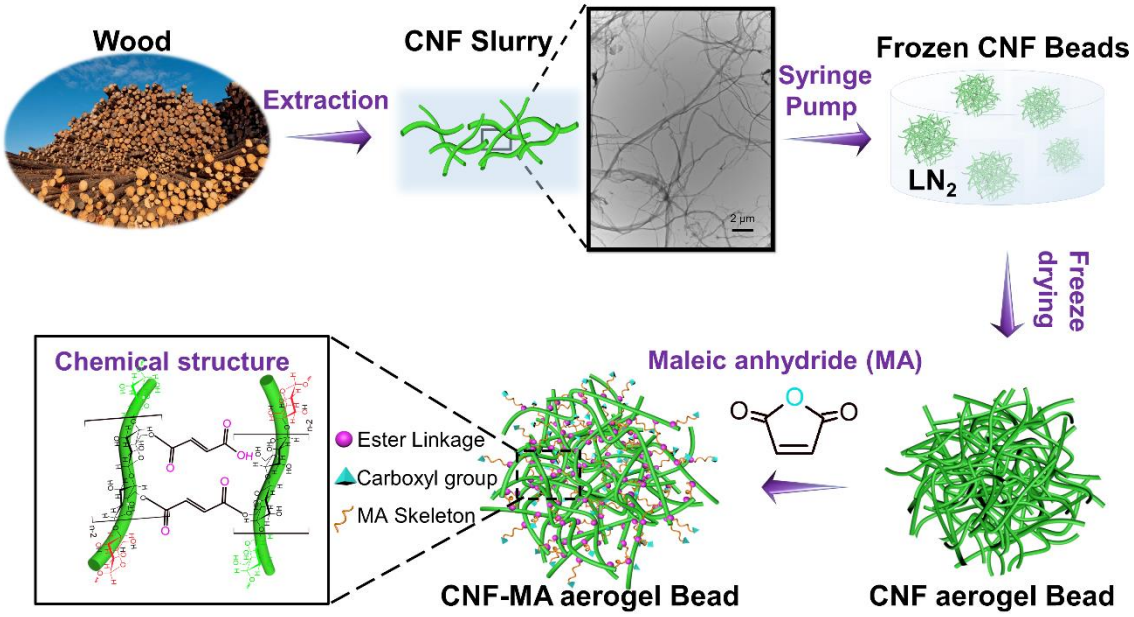

Figure 6.1 Schematic illustration of the preparation process and proposed chemical structure of the CNF-MA beads

6.3.1 Characterization

To verify the formation of ester and carboxyl groups, we performed FTIR to confirm the characteristic peaks. In Figure 6.2 A, an intense new peak at 1726 cm^{-1} appeared in CNF-MA 1.0 % assigned to C=O stretching vibration when compared to pristine CNF. In addition, the presence of =CH bending vibration of MA at 821 cm^{-1} and the absence of anhydride peak at 1780 cm^{-1} indicated no free MA molecules existed in CNF-MA 1 % and MA was successfully grafted onto CNF. However, it was difficult to identify the ester bond (-COO-) and carboxylic acid (-COOH) peaks as they overlapped at 1726 cm^{-1}. To separate the peaks, we further treated the CNF-MA 1%

beads with 0.01 M NaOH to convert the -COOH to -COONa groups, [273] which produced a peak at 1570 cm^{-1} as shown in Figure 6.2 A, and the remained peak at 1726 cm^{-1} was attributed to ester bond. These results suggested that MA was successfully grafted onto CNF via esterification, simultaneously producing ester linkage and carboxylic groups.

Carboxyl content is an important parameter for Cu (II) ions adsorption. Conductometric-potentiometric titration was conducted to measure the carboxyl content of the beads, and the results are shown in Figure 6.2 B to 6.2 D. Pristine CNF possessed negligible carboxyl content of 0.16 mmol/g (see Figure 6.2 B), while CNF-MA 1 % and CNF-MA 2 % possessed a carboxyl content of 2.45 mmol/g and 2.78 mmol/g respectively (see Figure 6.2 C and 6.2 D). To verify the presence of ester crosslinking, we treated the CNF-MA 2 % beads with 0.5 M NaOH to cleave the ester linkages, releasing the di-carboxylic maleic acid (Na form), which was then titrated with 0.5 M HCl to determine the total carbonyl content (TCC). As shown in Figure 6.3, the TCC of CNF-MA 2 % was approximately 11.11 mmol/g, which was much higher than the TCC prior to cleavage (5.56 mmol/g), suggesting the existence of ester crosslinking in the beads. The significantly higher degree of substitution indicated that both primary and secondary hydroxyl groups at the C_3 and C_2 positions have also participated in the esterification reaction, and similar phenomenon was also reported by Sehaqui et al when they used succinic anhydride to prepare carboxylated CNF.[271]

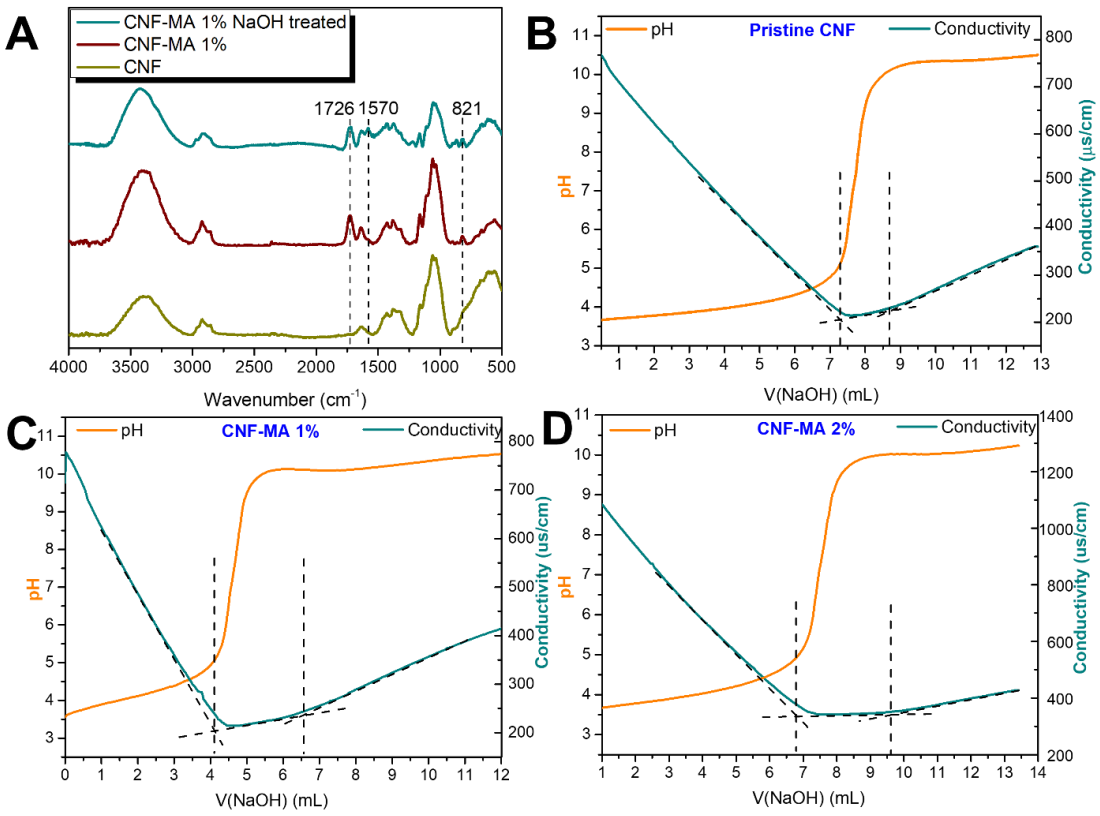

Figure 6.2 FTIR patterns of pristine CNF, CNF-MA 1 % and 0.01 M NaOH treated CNF-MA 1 % (A), and conductometric- potentiometric titration curve of 86 mg pristine CNF (B), 9.8 mg CNF-MA 1 % (C) and 10 mg CNF-MA 2 % (D).

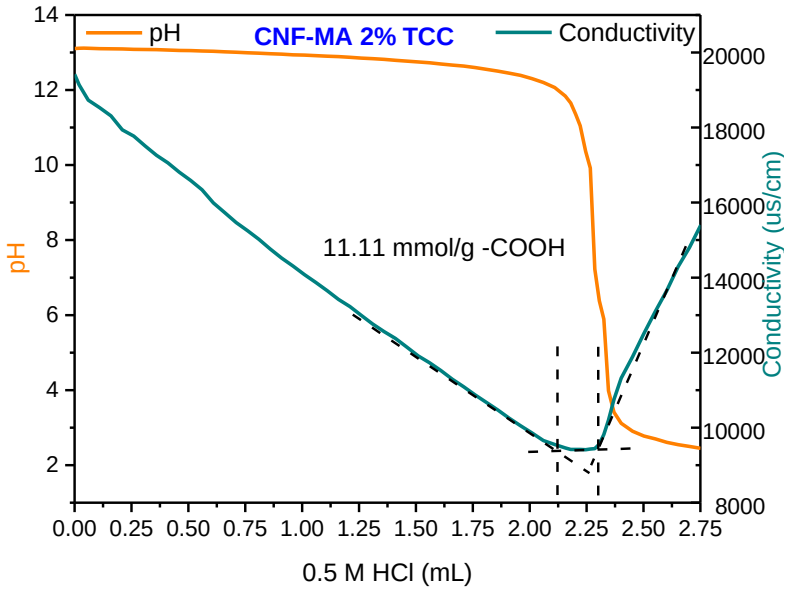

Figure 6.3 Conductometric- potentiometric titration curve of 8.1 mg 0.5 M NaOH treated CNF-MA 2% beads

The morphologies of these cryogel beads were visualized by SEM, and the results indicated that all the cryogel beads displayed randomly oriented three-dimensional porous structure as shown in Figure 6.4 and Figure 6.5. The surface of pristine CNF cryogel beads comprised of fibril and fiber sheet structure, where the fibril structure was dominant. The network was more compact at higher CNF content (Figure 6.4 B and Figure 6.5 C, C'), which was consistent with previous reported studies. [227,274] It is worthy to note that fiber length has an impact on the network density as cryogel beads prepared by shorter CNF fibers (~ several micrometers) usually possessed more porous morphologies due to the inadequate entanglement.[92,269] After modification with MA, the cryogel bead surfaces consisted of more CNF bundles as highlighted in the magnified image (Figure 6.4 B') and fiber sheet structure, which is attributed to the crosslinking effect of MA. This phenomenon was more pronounced in CNF-MA 2 % as large number of fiber bundles and fiber sheets are observed in Figure 6.5D and Figure 6.5D' due to the higher CNF concentration. In addition, the interior of the beads possessed the same fiber organization as the bead surface (see Figure 6.5 B", C" and D"), indicating the fibril and fiber sheet structure were uniformly distributed in the network.

The pores morphologies of these cryogel beads were also investigated. As evident from Figure 6.4 and Figure 6.5, all the pores were comprised of fibrillar and columnar structure in both the surface and the interior of the beads, where the fibrillar structure dominated. Generally, most of the reported CNF cryogels possessed a combination of fibrillar, columnar or honeycomb pore structure, depending on their freezing methods.[83,275,276] It should be noted here, the morphologies of the pores in our beads were identical throughout the beads due to its spherical shape.

Besides, the elemental composition of the beads before and after modification were investigated by EDS elemental analysis. From Figure 6.4 C, Figure 6.4 A", Figure 6.4 B", all samples only contained C and O elements, suggesting no other elements, such as Cu^{2+} were introduced to the samples.

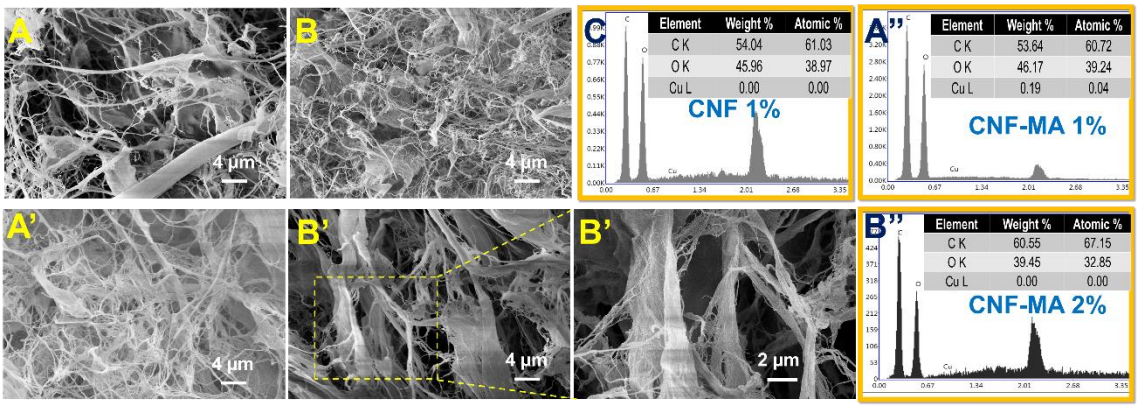

Figure 6.4 SEM images of the cryogel beads surface. CNF 1 % and CNF-MA 1 % (A and A'), CNF 2 % and CNF-MA 2 % (B and B'). EDS elemental analysis of pristine CNF 1% (C), CNF-MA 1 % (A") and CNF-MA 2 % (B").

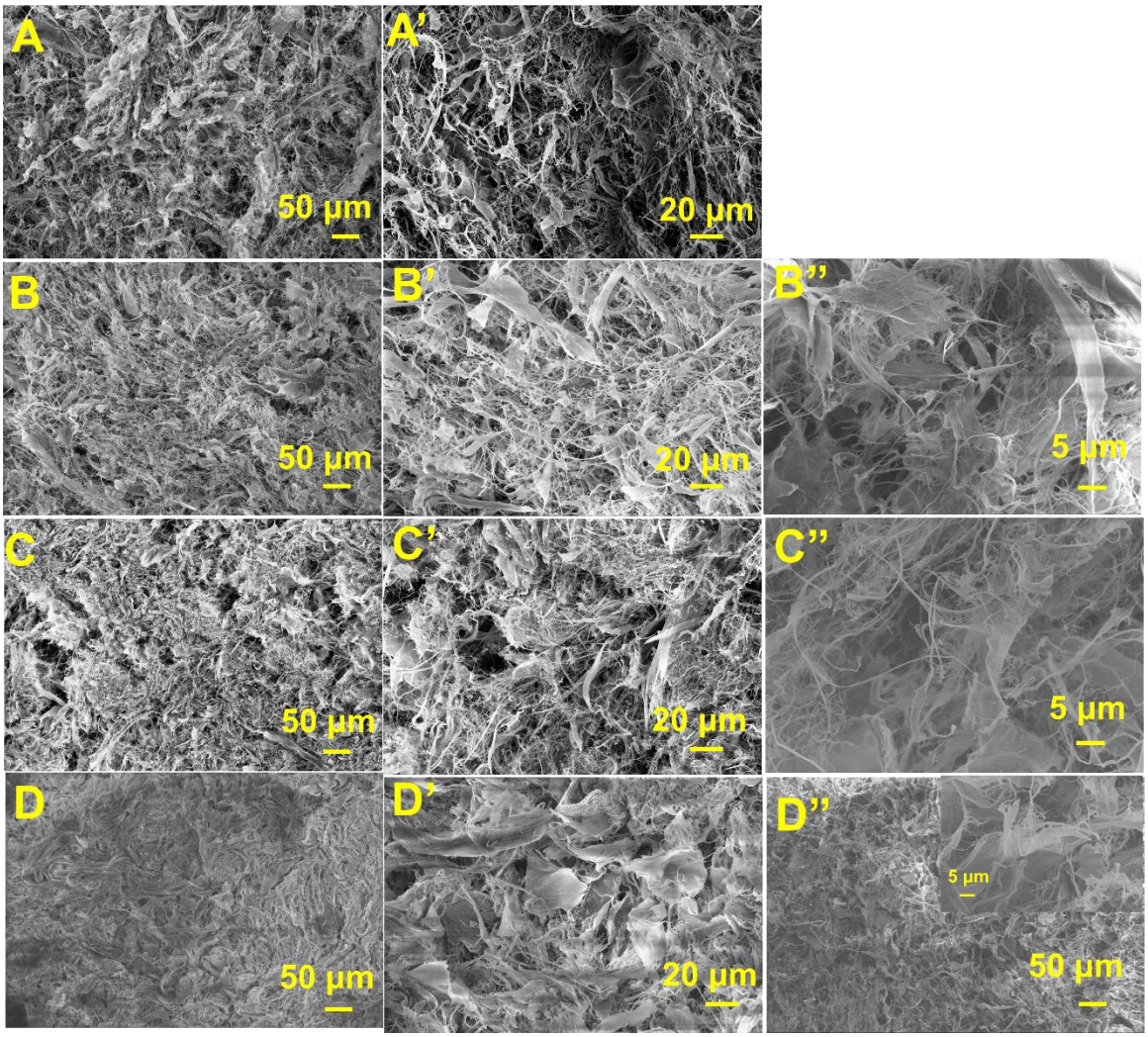

Figure 6.5 SEM images of cryogel beads surfaces at different magnifications: CNF 1 % (A and A'), CNF-MA 1 % (B and B'), CNF 2 % (C and C') and CNF-MA 2 % (D and D'), and the cross sections CNF-MA 1 % (B"), CNF 2 % (C") and CNF-MA 2 % (D").

Table 6.1 A summary of the density and porosity of cryogel beads with different CNF concentrations

	Density (g/cm^3)	Porosity (%)
CNF-MA 0.5 %	0.0187	98.75
CNF-MA 1.0 %	0.0343	97.71
CNF-MA 1.5 %	0.0657	95.62
CNF-MA 2.0 %	0.0778	94.81

Mechanical characteristic, especially the wet strength, is very critical for the cryogel absorbents in terms of their recyclability.[217] Therefore, compressive strain (Ɛ)- stress (σ) measurements were performed to evaluate the mechanical properties of the cryogel beads. It should be noted that pristine CNF cryogel bead could not be measured as it broke when placed in water. In contrast, CNF-MA beads possessed excellent wet stability and their structural integrity was preserved even after vigorously mixed in water (see Figure 6.6 I). The strain (Ɛ)- stress (σ) curves at different strain (Ɛ: 30%, 40%, 50% and 60%) of CNF-MA X are shown in Figure 6.6 A and Figure 6.6 B. Generally, the compressive stress increased with CNF concentration, where CNF-MA 1.5 % and CNF-MA 2.0 % possessed similar strength, and they were much higher than CNF-MA 1.0 % and CNF-MA 0.5 %. Higher CNF concentration contributed to a more compact network as evident by the increased density shown in Table 6.1, which greatly improved the cryogel mechanical strength. The beads shrunk significantly when 0.5 % and 1.0 % CNF were used as seen in Figure 6.6 I. In addition, the plastic deformations of each sample under given compressive strain are summarized in Figure 6.6 C, where we can see the CNF content dominated the beads shape recovery property. For example, at 60 % strain, CNF-MA 0.5 % displayed a plastic deformation of 32.16 %, while that of CNF-MA 1.0%, CNF-MA 1.5 % and CNF-MA 2.0 % was 23.03 %, 20.06 % and 17.78 %, respectively.

In addition, the compressive curves possessed three distinct regions: In the first region, the compressive stress increased linearly with strain, suggesting that the beads were elastic at the compressive strain below 5 % for CNF-MA 0.5 %, 8 % for CNF-MA 1.0 %, 15 % for CNF-MA 1.5 % and CNF-MA 2.0 %; In the second region, the curves displayed a plateau region as the stress increased slightly with compressive strain, which was associated with the gradual collapsed of the pores in the cryogels; When the strain exceeded 50 %, the stress for all beads increased dramatically as the beads undergo a densification stage where the pores completely collapsed. [239,241]

The cyclic test results at fixed stain of 60 % of all the beads are shown in Figure 6.6 D and Figure 6.6 E, and the corresponding plastic deformations, max stresses and energy loss coefficients during 10 cycles were calculated and presented in Figure 6.6 F, Figure 6.6 G and Figure 6.6 H. All the samples exhibited a slightly increased plastic deformation in the beginning and then approached a plateau. Among them, CNF-MA 0.5% displayed the largest deformation ratio of 37.34% after 10

cycles due to its lower density and higher porosity (Table 6.1), while that of CNF-MA 2.0% maintained a value of 17.99%. The better shape recovery property of CNF-MA 2 % was due to its denser network compared to others, which also yielded the largest stress of around 2800 Pa after 10 compression cycles. The energy loss coefficient is another factor that provides information on the cryogel elasticity and mechanical compressibility.[237,238] In Figure 6.6 H, the energy loss coefficient of CNF-MA 0.5 % beads was much larger than other beads, revealing its inherent viscoelasticity and further explaining its poor shape recovery property. For CNF-MA 1.5 % and CNF-MA 2.0 % beads, their energy loss coefficients were identical compared to CNF-MA 1.0 % (all decreased from around 0.61 to 0.56 in 10 cycles), as their networks dissipated energy during the compression due to the frictions between the denser fibers. Nevertheless, their energy losses were relatively lower than CNF-MA 0.5 % beads, suggesting the better compressibility of these beads.

All the results supported the conclusion that crosslinking with MA and increasing CNF concentration were effective to not only increase the carboxyl content but also to improve the wet mechanical strength and shape recovery property of the beads.

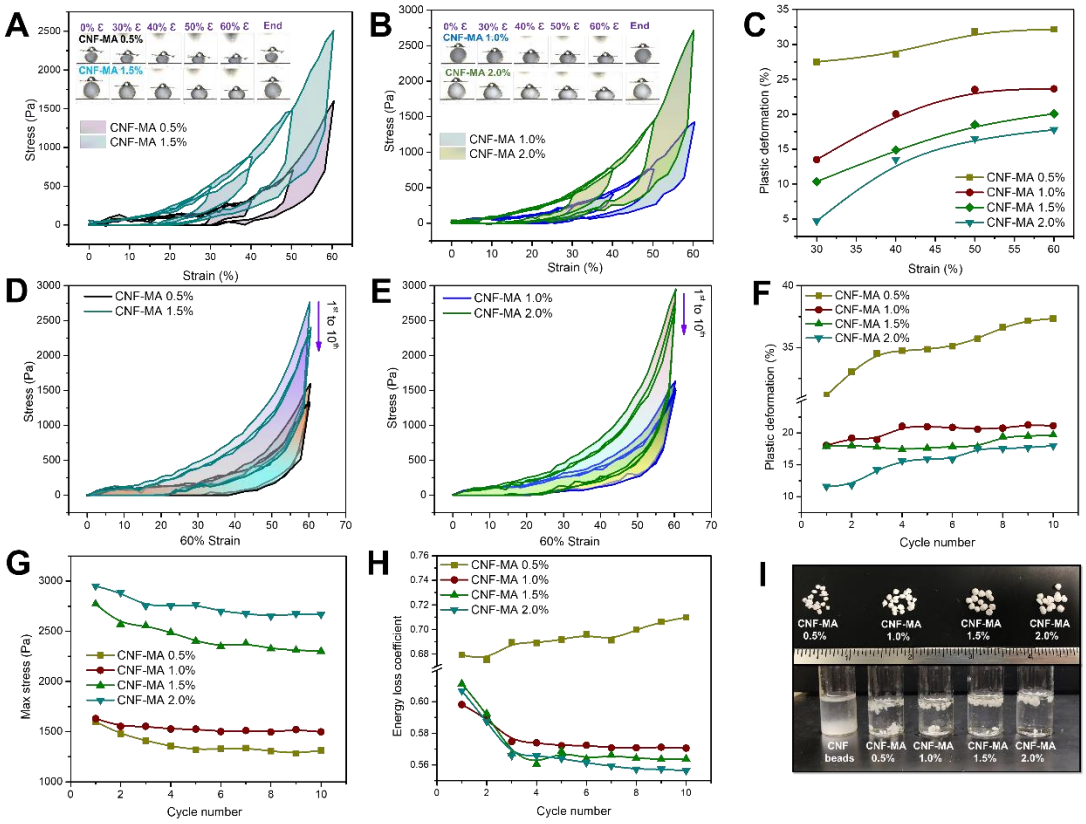

Figure 6.6 Mechanical compression tests of the cryogel beads. Strain- stress curve of (A) CNF-MA 0.5 % and 1.5 % and (B) CNF-MA 1.0 % and 2.0 % with different strain (Ɛ: 30 %, 40 %, 50 % and 60 %,); (C) plastic deformation of all beads with different strain; Cyclic test of (D) CNF-MA 0.5 % and 1.5 % and (E) CNF-MA 1.0 % and 2.0 % at strain of 60 %; Plastic deformation (F), max stress (G) and energy loss coefficient (H) of all beads at different cycles with a strain of 60 %. (I) Photos of CNF-MA X beads (top) and 2 % CNF beads & CNF-MA X beads after vigorously shaking in water (bottom).

6.3.2 Copper adsorption experiments

6.3.2.1 Effect of pH

The initial pH of the copper solution greatly affects the absorbents adsorption performance as it determines the form of copper species as well as the electrostatic interaction strength between the absorbents and Cu (II) ions.[217] Generally, Cu (II) ions start to transform to Cu $(OH)_2$ at pH above 6.0, thus we set the initial pH between 3 to 6.2 for studying the corresponding beads adsorption capacity. As shown in Figure 6.7A, distinct adsorption capacities were observed at different initial

pH. The adsorption capacity at equilibrium increased when the initial pH value was increased from 3.0 to 5.6, due to the deprotonation carboxylic groups at higher pH. At 6.2, the adsorption capacity decreased slightly and this was due to the formation of Cu $(OH)_2$. Therefore, a pH of 5.6 was set as the optimized initial pH for conducting the adsorption studies. As seen in Figure 6.7B, the Cu (II) concentration decreased continuously during the adsorption, with the bead color changing from white to light blue (insert in Figure 6.7B).

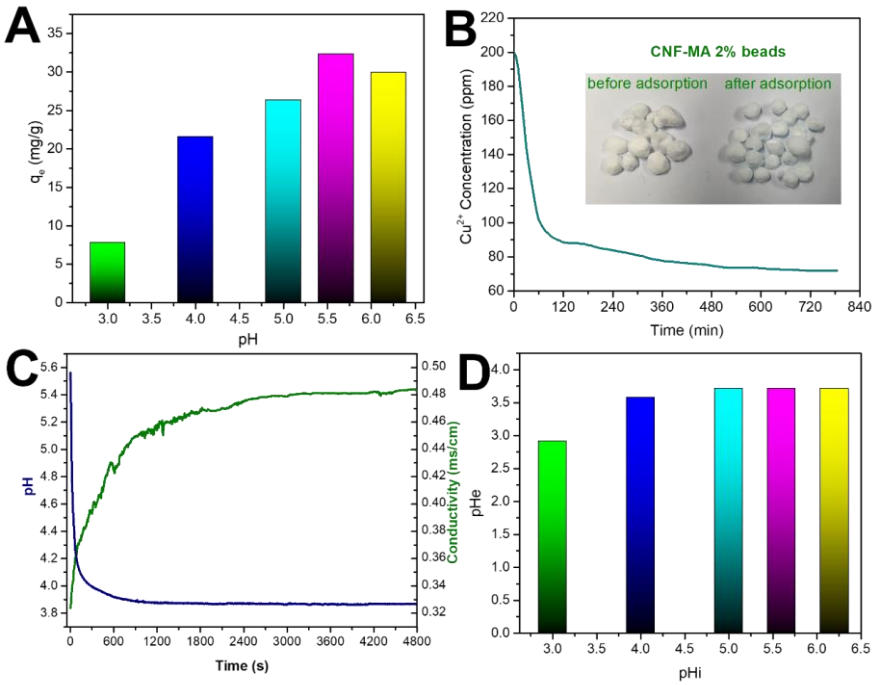

Figure 6.7(A) Effect of initial pH on the adsorption capacity (100 mg CNF-MA 1 % beads, 100 ppm Cu^{2+}), (B) concentration of Cu (II) ions during adsorption at initial pH 5.6 (100 mg CNF-MA 2 % beads), (C) pH and conductivity of the mixture during adsorption (initial pH of 5.6), (D) pH values at adsorption equilibrium at different initial pH (100 mg CNF-MA 1 % beads).

In addition to Cu (II) ions concentration, we also monitored the pH and conductivity of the solution mixture during adsorption as shown in Figure 6.7C, and the conductivity increased while the pH decreased, in contrast to the removal of Cu (II) ions. The continuous decrease of pH indicated the adsorption was dominated by ion-exchange between H^+ and Cu^{2+}. One possible reason for the higher conductivity is the released of H^+ ions driven the Cu (II) hydrolysis, which produced more mobile Cu (II) ions that contributed to conductivity. We also monitored the pH before and after

adsorption at different initial pH conditions (Figure 6.7D), where the pH at equilibrium were in the range of 2.8- 3.7.

6.3.2.2 Isothermal Adsorption

Isothermal adsorption analysis was conducted to examine the adsorption capacity of the beads and interactive behavior between the adsorbents and Cu (II) ions at different carboxyl content. In Figure 6.8, the q_e of CNF-MA 1 % and CNF-MA 2 % beads increased rapidly at low Cu (II) ion concentration then slowly increased to plateau. The adsorption data were further fitted to the Langmuir and Freundlich model as shown in Figure 6.8A and Figure 6.8B. Apparently, The Langmuir model fitted better to the data, indicating the adsorption sites were homogeneously distributed in the cryogels and the adsorption was monolayer. The parameters for both fittings are summarized in Table 6.2(A). The maximum adsorption capacities of the cryogel beads determined from the Langmuir model were 60.92 mg/g and 84.12 mg/g for CNF-MA 1 % and CNF-MA 2 %, respectively. The larger adsorption capacity of CNF-MA 2 % beads was ascribed to its higher carboxyl content as well as its denser network that could retain more Cu (II) ions. Our maximum adsorption capacities are higher than many reported carboxylated CNF based absorbents as summarized in Table 6.2(B), highlighting the advantage of high carboxyl contents as well as crosslinked porous networks.

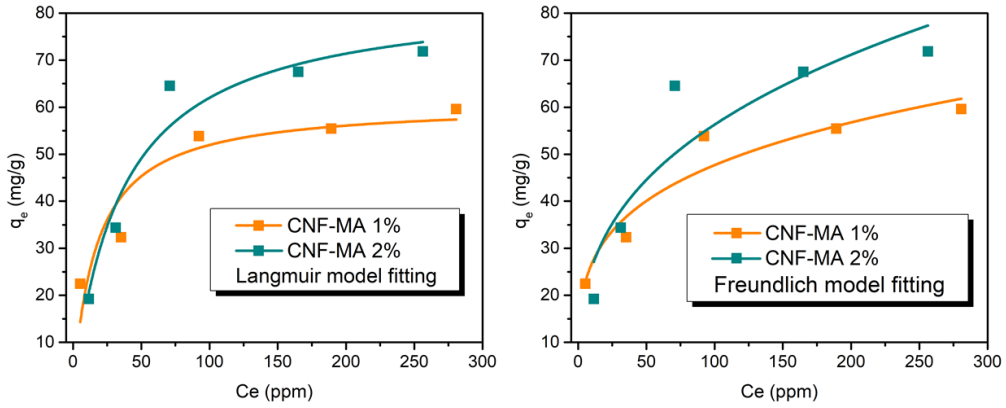

Figure 6.8 (A) Adsorption isothermal of CNF-MA 1 % and CNF-MA 2 % beads fitted with the Langmuir model and (B) fitted with the Freundlich model.

Table 6.2 (A): Langmuir and Freundlich constants of CNF-MA 1% and CNF-MA 2% beads for Cu (II) ion adsorption

Samples	Langmuir isotherm			Freundlich isotherm		
	K_L	q_m (mg/g)	R^2	K_F	n	R^2
CNF-MA 1 %	0.03	60.92	0.91	14.97	0.25	0.81
CNF-MA 2 %	0.01	84.12	0.94	11.87	0.34	0.81

Table 6.2 (B): Comparison of the maximum Cu (II) adsorption capacities from various reported carboxylate cellulose absorbents with this study

Material	Carboxylic content (mmol/g)	pH	q_{max} (mg/g)	References
TEMPO-CNF fibers	1.40	5.0	102.90	(Li et al., 2019)
Carboxymethylated cellulose fiber	1.05	6.0	23.48	(Wang, Liu, Duan, Sun, & Xu, 2019)
Carboxylate CNC	2.20	/	51.10	[260]
Carboxymethylated CNF	2.70	5.0	115.30	[252]
TEMPO-CNF/GO membrane	/	5.7	63.50	[278]
Carboxylate CNF	1.18	/	45.05	(Wang et al., 2018)
CNF-MA 1% beads	2.45	5.6	60.92	this study
CNF-MA 2% beads	2.78	5.6	84.12	this study

Table 6.2 (C): Parameters of pseudo- first- order, pseudo- second- order and intra-particle diffusion for CNF-MA 2% beads adsorption kinetics

Sample	Pseudo-first- order			Pseudo-second- order			Intra-particle diffusion		
	K_1	R^2	q_e	K_2	R^2	q_e	$K_{id,1}$	$K_{id,2}$	$K_{id,3}$
CNF-MA 2%	12.154	0.1580	59.19	0.0005	0.9603	66.83	9.1808	0.7366	0.2648

6.3.2.3 Adsorption kinetics

CNF-MA 2 % beads were used to study the adsorption kinetics. In Figure 6.9A, the beads displayed a rapid adsorption rate in the first 120 min that slowly approached an equilibrium within 500 min. The fast adsorption rate was due to: (1) the small beads possessing larger surface area that greatly increased the contact area towards Cu (II) ions; (2) the small beads with carboxyl groups could efficiently capture Cu (II); (3) the small beads greatly reduced the Cu (II) ions diffusion path length that in turn saturated the beads quickly.[268] To evaluate the Cu (II) adsorption behavior of these cryogel beads, the adsorption data was further fitted to pseudo- first order and pseudo-second order models as shown in Figure 6.9A, and the fitting parameters are summarized

in Table 6.2(C). The results suggested the data could be described better by the pseudo-second order model, indicating that the adsorption process was chemical adsorption.

To further examine whether the pore diffusion alters the Cu (II) ion adsorption process, intra-particle diffusion model was used to analyze the adsorption data.[247] As shown in Figure 6.9B, the plots of q_t versus $t^{0.5}$ yielded three linear regions, which corresponded to the three stage diffusion of Cu (II) ions: (1) external diffusion from bulk solution to the surface of the beads, (2) diffusion from the surface to the inner of the beads through pores, (3) slow diffusion to reach the equilibrium. The slopes of the three stages corresponding to the diffusion rate were calculated from the intraparticle diffusion model and summarized in Table 6.2(C). We noted that $K_{id,1} > K_{id,2} > K_{id,3}$, suggesting the adsorption rate at first stage was very fast, compared to the second and third stage. The results suggested that the pore diffusion also controlled the adsorption process, which agreed with most of cryogel absorbents.[254,279]

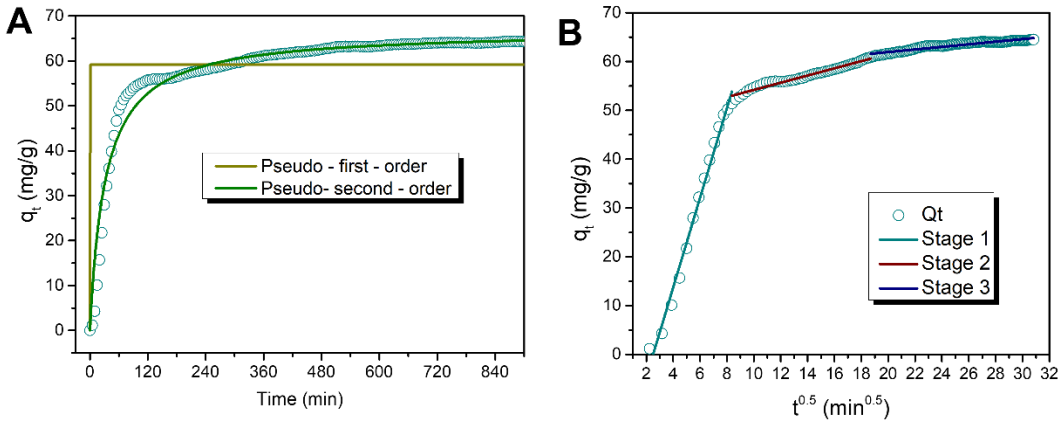

Figure 6.9 (A) Adsorption kinetics of 100 mg CNF-MA 2 % beads in 50 mL 200 ppm Cu (II) solution fitted to pseudo- first- order and pseudo- second order models and (B) the data fitted to intraparticle diffusion model.

6.3.2.4 Elemental composition of beads after adsorption

To verify the presence of Cu ions in the beads, the elemental composition of the bead cross sections after Cu adsorption were examined by EDS mapping as shown in Figure 6.10. Clearly, the Cu signals were observed in both beads, yielding a value of 1.15 wt% and 4.59 wt% for CNF-MA 1 % and CNF-MA 2 % respectively, while no Cu signals were detected before the adsorption as shown

in Figure 6.4A" and Figure 6.4B". The higher Cu content in CNF-MA 2 % further confirmed its higher adsorption capacity. In addition, the EDS mapping indicated that the Cu ions were uniformly distributed in the network and exhibited consistent shapes with the networks, suggesting the homogenous distribution of adsorption sites in the beads.

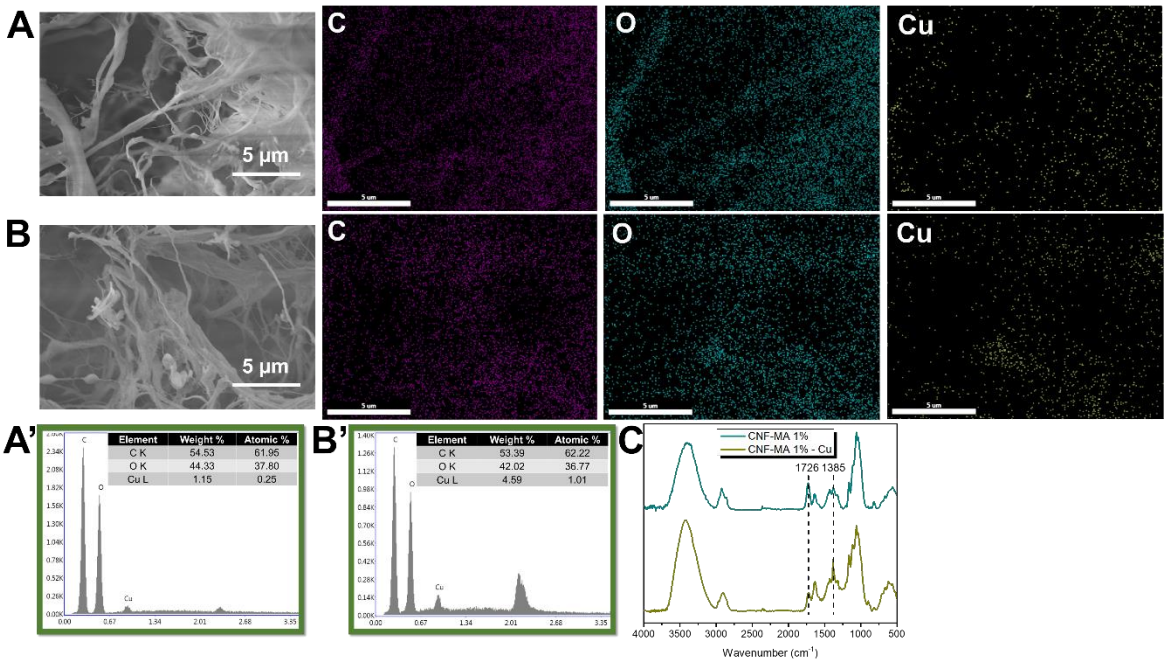

Figure 6.10 EDS mapping and the element composition of the cross section of CNF-MA 1 % (A and A') and CNF-MA 2 % (B and B') beads after Cu adsorption, and FTIR of CNF-MA 1 % before and after Cu adsorption (C).

6.3.2.5 Adsorption mechanism

As discussed earlier, the continuous reduction in the pH during the adsorption shown in Figure 6.7 (C) is associated to the ion-exchange between H^+ of protonated carboxylic groups and Cu^{2+}. Such interaction dominates the adsorption due to the higher ionic strength of Cu^{2+}. For the deprotonated carboxylic groups, electrostatic attraction between the negative charged $-COO^-$ groups and positive charged Cu^{2+} ions was responsible for the adsorption. In addition, the FTIR of the CNF-MA 1 % beads before and after Cu adsorption were also investigated to elucidate the adsorption mechanism. In Figure 6.10 C, the intensity of C=O stretching vibration peak at 1726 cm^{-1} was significantly reduced after adsorption, while the -OH bending vibration peak at 1385 cm^{-1} was greatly enhanced.

The results indicated that the Cu^{2+} ions were simultaneously captured by the carboxyl and hydroxyl groups via ionic complexation.

3.3 Recovery study

An excellent absorbent should not only possess high adsorption capacity, but also good recyclability considering the sustainability and economic factors. EDTA- Na_2 was selected as the desorption agent due to its strong chelation effect towards Cu^{2+} compared to the electrostatic interaction of the carboxylic groups. The recoverable characteristics of CNF-MA 2 % beads was evaluated and shown in Figure 6.11, where we observed that the equilibrium adsorption capacity decreased from 68 mg/g to around 45 mg/g after 4 cycles. The reduced adsorption capacity might be caused by the lower carboxyl content. As discussed earlier, the pH of the system decreased to around 3.5 during the adsorption, resulting in the slow cleavage of the ester bonds and the beads disintegrated into some small pieces as observed in the four cycles recovery study. These small pieces could not be recovered by the mesh, resulting in the observed reduction of the carboxyl contents. Our results indicated that the CNF-MA cryogel beads possessed excellent recyclability characteristics when compared to other carboxylated CNF absorbents listed in Table 6.2 (B).

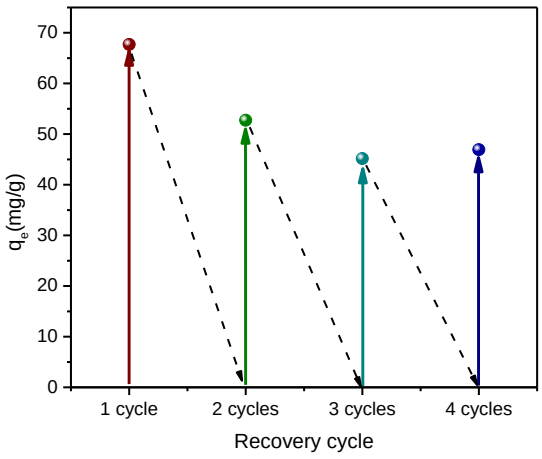

Figure 6.11 Four cycles of recovery study of CNF-MA 2 % beads (100 mg absorbents, 50 mL 200 ppm copper solution, at R.T. and pH 5.6)

6.4 Conclusions

In this study, robust carboxylated cellulose nanofibril (CNF) cryogel beads were prepared in one step via a ring open reaction of maleic anhydride (MA). The method used molten MA as solvent and reactant, which simultaneously crosslinked the CNF cryogel beads and imparted carboxyl groups onto the cryogels. The method is efficient and environmentally friendly as no organic solvents or catalysts are needed and the MA could be recycled. The CNF-MA cryogel beads possessed a carboxyl content of up to 2.78 mmol/g, yielding a high Cu (II) adsorption of 82.17 mg/g. In addition, the cryogel beads displayed excellent mechanical strength in water as a result of the ester crosslinking, yielding a maximum stress of 2800 Pa under 60 % strain. The Cu (II) adsorption was a chemisorption process, where both carboxyl and hydroxyl groups participated in the complexation. The intra-particle model revealed that the adsorption process was also affected by pore diffusion. Overall, the prepared CNF-MA cryogel beads are promising absorbents for heavy metals removal due to its fast removal rate, robust mechanical strength as well as excellent recyclability. In addition, organic solvent and catalyst were not required.

Chapter 7* Ambient amphiphilic and underwater super-oleophobic carboxylated cellulose aerogel for multiple applications

Abstract

Developing filters for both oil-in-water and water-in oil emulsion separation is challenging as dual wettability of the filter is required. In this study, ambient amphiphilic cellulose aerogels were prepared by crosslinking cellulose nanofibrils (CNF) with dicarboxylated-PEGs of different molecular weights. The aerogels at dry state displayed excellent uptake capacity for various solvents of different polarities (from 0.1 to 10.2), and then released the absorbed oils in water. The results show that crosslinkers with smaller molecular weight possessed higher crosslinking activity capacity. Both crosslinking degree and network density contributed to the mechanical strength of the aerogel. These aerogels could effectively remove both emulsified oil and water droplets from water and oil, respectively. The aerogel displayed better separation efficiency for SDS and CNC stabilized oil-in-water emulsions than CTAB and Tween 80. It was found that the size of the emulsion droplet and its interaction with the aerogel determined the water permeation flux and separation efficiency. For water-in-oil emulsions, the viscosity of the oil had a significant effect on the permeate flux. A separation efficiency of more than 97% was achieved for all studied water-in-oil emulsions.

* This chapter is adapted from a paper: Chunxia Tang, Xinmei Yan, Hua Fan, Vivek Maheshwari and Kam Chiu Tam "Ambient amphiphilic and underwater super- oleophobic cellulose aerogel for multiple emulsions separation" Manuscript under preparation.

Application 1: Emulsion separation

7.1 Introduction

The discharge of oily wastewater containing emulsions and oil spills during marine transportation have been one of the major sources of water pollution for decades. Removal of emulsions from oily wastewater is a global challenge especially for surfactant stabilized emulsions due to their good stabilities and micro- or nano-droplet sizes.[11] In recent years, emulsions stabilized by solid particles, namely Pickering emulsions, have attracted much attention from researchers as they exhibit better stability over surfactants.[59] Pickering emulsions could be a new source of pollutants to water streams in the future that need to be considered. In another aspect, water will also be a pollutant when it exists in oils particularly in fuels regardless of whether they are free, solubilized, or emulsified. It causes microbial growth and corrosion that could further damage vehicle engine system.[127,128] Therefore, the removal of emulsified oil and water droplets is of great significance for environmental management as well as oil purification industries.

Traditional methods, such as centrifugation, oil skimming, and floatation for oil/water mixture separation are not suitable for separating emulsions.[12] Since the first report of artificial superhydrophobic and superhydrophilic mesh by Jiang et al. in 2004 and 2011,[280,281] respectively, filters with super-wettability and defined pore size were constructed for emulsion separation by either blocking oil or water droplets permeate through the filter.[11] In the scenario of oil-in-water emulsion separation, superhydrophilic filters possess intrinsic advantages over superhydrophobic filters due to their low oil adhesion and high water affinity properties. On the other hand, superhydrophobic filters are widely adopted for oil spill cleanup and water-in-oil emulsion separation.[130] Hydrophilic compounds and fluoride based hydrophobic materials were commonly used to produce these superwetting filters.[11] In recent years, smart filters with dual emulsion separation functions have drawn extensive interests. Stimuli-responsive compounds, such as PDMAEMA, PNIPAM, TiO_2, ZnO, were adopted to fabricate such smart surfaces. A wettability transition was achieved when the filters were subjected to external stimuli, for example pH, temperature, gas, and light.[140]

Compared with 3D porous filters (e.g., foams, sponges, or aerogels) that possess large surface areas, 2D filters (e.g., polymeric membranes and filter papers) exhibit lower water or oil absorbency, smaller pore size and shorter filtration channels. They can be easily fouled and

blocked by water or oil droplets and surfactants, comprising its long term separation flux and efficiency performance.[12] Two strategies are generally used to prepare superwetting 3D porous filters: (1) assemble hydrophilic/hydrophobic skeleton materials to porous network using a bottom up approach. For example, Xiao et al. prepared superhydrophilic aerogel by coating polydopamine (PDA) and polyethyleneimine (PEI) on freeze dried graphene/ cellulose acetate nanofibers aerogel.[282] (2) Modify commercial sponges with hydrophilic or hydrophobic components, e.g., Lv et al. constructed a 3D multiscale superhydrophilic sponge by coating PDA, PEI and layered double hydroxide (LDH) nano- scrolls on a commercial poly(melamine formaldehyde) sponge.[12] Various materials have been reported to prepare the aerogel skeleton, e.g., polyurethane, melamine resin, polydimethylsiloxane, polyacrylamide (PAM), poly (acrylic acid) (PAA), graphene, chitosan, alginate, and cellulose, etc.[222] Among them, cellulose consisting of repeating glucose units is the most abundant natural resource on earth.[103] The benefits are biodegradable, abundant, flexible, and intrinsic hydrophilic properties, cellulose fibers are popular as skeletons to prepare porous membranes, papers, aerogels, and hydrogels for wastewater treatment applications.[120]

However, cellulose fiber-based 3D porous filters are less reported for oily wastewater treatment compared to their applications in oil spill cleanup according to a literature survey by Web of science. In summary, 18 journal papers reported superhydrophilic cellulose filter/membrane/sponge/aerogel/foam from 2015 to the present, while the number of their superhydrophobic counterpart was 64 as shown in Figure 7.1. Among these superhydrophilic cellulose aerogels, only 3 were applied for oil-in-water emulsion separation.[132,140,283] For these reported superhydrophobic cellulose aerogels, the majority of them were used for oil spill cleanup as well as for water-in-oil emulsions separation. However, a large amounts of energies, chemicals, solvents are consumed, and complicated processes are required to transform the intrinsic hydrophilic cellulose to superhydrophobic. In addition, superhydrophobic filters are not efficient for oil-in-water emulsion separation due to the high interfacial tension between water and superhydrophobic surface. In conclusion, there are no reported study on the use of cellulose aerogel for both oil-in-water and water-in-oil emulsion separation without external stimuli.

Therefore, it is meaningful to take advantage of the intrinsic hydrophilic property of cellulose and exploit its potentials in multiple applications including oil-in-water emulsion separation, water-in-oil emulsion separation, and oil spill cleanup. Firstly, chemical crosslinking treatment is required

to prepare a mechanically robust cellulose aerogel, to prevent the disintegration of aerogel induced by the hydrogen bonding between cellulose fibers and water molecules. In this study, dicarboxylated-PEGs were synthesized and further used as crosslinkers to prepare robust ambient amphiphilic and underwater superoleophobic cellulose aerogels for various types of solvents absorption as well as emulsion separation. Besides, the effects of crosslinker length on the mechanical strength of the aerogel and underwater oil droplet adhesion force, emulsifier type on oil-in-water emulsion separation flux and efficiency, and oil type on water-in-oil emulsion separation flux and efficiency were investigated.

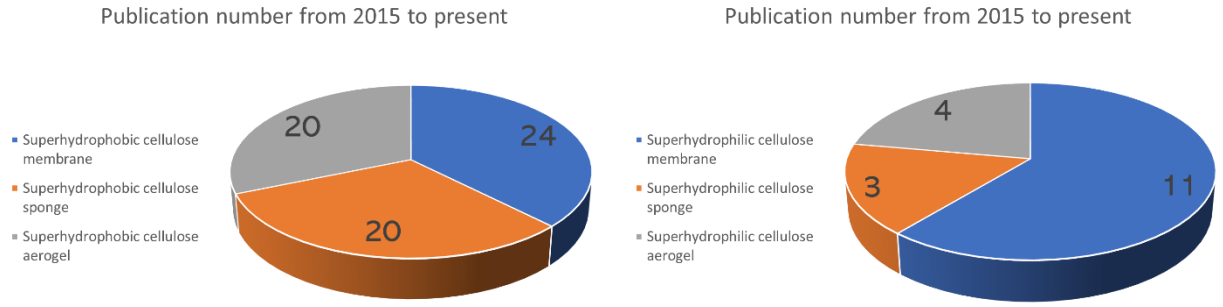

Figure 7.1 Number of publications with the topic of “Super hydrophobic” or “Superhydrophilic” and topic “cellulose filter” or “cellulose membrane” or “cellulose sponge” or “cellulose aerogel” from 2015 to present by a literature search using Web of science.

7.2 Experimental section

7.2.1 Materials

Cellulose nanofibrils (CNF) slurry was purchased from the Process Development Center of University of Maine, and the production process was reported previously.[201] Cellulose nanocrystals powder was provided by Celluforce Inc. Poly(ethylene glycol) (average Mn = 600, 1500, 3350, 8000), maleic anhydride (MA, 99%), sodium hydroxide pellets (NaOH, anhydrous), Nile red, 4-(Dimethylamino)pyridine (DMAP, ReagentPlus®, ≥99%), hexadecyltrimethylammonium bromide (CTAB, ≥ 98%), sodium dodecyl sulfate (SDS, ACS agent, ≥ 99%), TWEEN® 80, dichloromethane (CH_2Cl_2, anhydrous, ≥99.8%), diethyl ether, acetone (ACS agent, ≥ 99.5%), hexane (anhydrous, 95%), toluene (ACS reagent, ≥99.5%), and chloroform-d (99.8 atom % D) were purchased from Sigma Aldrich. Ultrapure water (conductivity of 15 μs/cm) was used to prepare the aqueous dispersions.

7.2.2 Preparation of dicarboxylated-PEGs

To prepare dicarboxylated-PEG, PEGs (average M_n = 600, 1500, 3350, 8000 Da) were dissolved in CH_2Cl_2, followed by the addition of excessive amount of maleic anhydride at a molar ratio of MA : PEG = 4 : 1. The reaction was performed at room temperature for 3 days in the presence of DMAP catalyst. Then, the dicarboxylated-PEGs were precipitated from CH_2Cl_2 using cold diethyl ether as anti-solvent. After 3 cycles of precipitation and washing, the purified products were dried in a vacuum oven at 40 ℃. Notably, the dicarboxylated- PEGs were denoted as PM 600, PM 1500, PM 3350, PM 8000, according to the molecular weight of PEG used in the reaction.

7.2.3 Preparation of crosslinked cellulose aerogels

Pristine CNF aerogel monolith with a dry mass of 75 mg was prepared as template before crosslinked with dicarboxylated-PEGs. Briefly, 5 g CNF slurry was transferred into a scintillation vial with a diameter of 23 mm, and immersed in liquid nitrogen and consequently it was freeze dried at -45 ℃. To prepare crosslinked cellulose aerogel, dicarboxylated-PEG was dissolved in acetone, which was then added to the dried CNF aerogel monolith of a molar ratio of crosslinker: glucose unit = 1 : 8. The chemical crosslinking reaction was conducted at 120 ℃ for 3 hours. Then, the aerogel was washed with acetone 5 times and soaked in acetone overnight to remove the unreacted crosslinkers. Finally, the aerogel was dried in a vacuum oven at 60 ℃, and the final products were denoted as CPM 600, CPM 1500, CPM 3350, CPM 8000, depending on the choice of the crosslinker. In addition, a higher reaction ratio (1 : 1) was performed between PM 600 and CNF followed the same procedure as described, and the produced aerogel was named as CPM 600 H.

7.2.4 Physical properties measurement

The crosslinker weight fraction (CL%) of the aerogel was determined by calculating the weight difference of the aerogel before and after the crosslinking reaction. Water uptake capacity was measured by immersing the aerogels in water, and the weight at equilibrium was determined. The aerogel bulk density was calculated based on its dry mass and volume. Also, the porosity can be estimated by Eq. (7.1) according to Buchtová & Budtova et al.[266]

$$Porosity\ \% = \left(1 - \frac{\rho_{aerogel}}{\rho_{cellulose}}\right) \times 100 \qquad (7.1)$$

where $\rho_{cellulose}$ is 1.5 g/cm^3.

7.2.5 Oil absorption and recovery

To study the oil absorption capacity of the aerogels, the pre-weighted aerogels in dry state were fully immersed in CH_2Cl_2, toluene or hexane for 5 min. Then, the increase in the weight was measured, and the oil absorption capacity was determined by Eq. (7.2):

$$Oil\ absorption\ capacity\ (g/g) = (w_1 - w_0)/w_0 \quad (7.2)$$

where w_0 and w_1 are the aerogel weight before and after oil absorption.

The absorbed oil was released into the water by placing the aerogel in a scintillation vial (diameter of 23 mm) containing 10 mL water. After 10 mins, the recovered oil volume was determined by the height of oil layer and the base area of the vial. Then, the recovered oil ratio (%) was determined by Eq. (7.3):

$$\text{Recovered oil ratio } (\%) = (v\rho/(w_1 - w_0)) \times 100\% \quad (7.3)$$

where v and ρ is the volume and density of the released oil, respectively.

7.2.6 Preparation of emulsions

Toluene in water emulsions stabilized by different surfactants (CTAB, or SDS, or Tween 80) were prepared by mixing 1 mL toluene (dyed with Nile red) with 100 mL MilliQ water containing 30 mg surfactant by a IKA high speed homogenizer for 2 min, then sonicated by a probe sonicator for 1 min to produce uniform and stable oil-in-water emulsions. Similarly, CNC stabilized toluene in water Pickering emulsions were prepared by mixing 1 mL toluene with 100 mL MilliQ water containing 50 mg, 100 mg, or 200 mg CNC. Water-in-oil emulsions were prepared by mixing 1 mL water with 100 g oil (vegetable oil, diesel oil or hexane) containing 30 mg Span 80.

7.2.7 Emulsion separation experiment

To evaluate the emulsion separation performance of an aerogel, the aerogel was loaded in a 30 mL AIR-TITE luer slip syringe with an inner diameter of 22.6 mm. Then, 10 mL emulsions were poured into the syringe. The aerogels were pre-soaked in water before loading into the syringe for oil-in-water emulsion separation, while the aerogels were used in dry state for water-in-oil emulsion separation. All the separation processes were gravity driven. The permeate flux ($L/(m^2 \cdot h)$) was calculated using Eq. (7.4):

$$Flux = \frac{V}{At} \quad (7.4)$$

where V (L) is the emulsion volume permeated through the aerogel at the testing time, A is the effective filtration area of the aerogel (m^2), and t is the testing time (h). Herein, we calculated the initial flux at the 1st min and overall flux when the filtration completed to evaluate the comprehensive performance of the aerogel. Consequently, the separation efficiencies for toluene-in-water emulsions were determined by monitoring toluene concentration before and after filtration by a UV–vis spectroscopy (Lambda 950, US) at 261 nm. For water-in-oil emulsions, the separation efficiencies were evaluated by measuring the water content before and after filtration using a C20 Karl Fisher™ auto-titrator. Then, the emulsion separation efficiency (R (%)) was calculated by using Eq. (7.5):

$$R\ (\%) = \left(1 - \frac{C_P}{C_0}\right) \times 100\% \qquad (7.5)$$

where C_0 and C_p are the toluene or water content in the original emulsion and in the filtrate, respectively.

7.2.8 Characterization

^{1}H Nuclear magnetic resonance (NMR) was conducted to confirm the presence of MA on PEG skeleton. Samples were dissolved in chloroform-d, and the spectra were recorded on a Bruker Advance 300 MHz spectrometer. The grafting ratios or modification degrees of MA on PEGs were determined by measuring their carboxyl contents, which was achieved by using a conductometric-potentiometric titrator (Metrohm 809 Titrando auto-titrator (Switzerland)). The cyclic compressive strengths at 50 % strain of the aerogels in wet state were evaluated using a Universal Mechanical Tester (CETR). Scanning electron microscopy (SEM) was used to examine the morphologies of the aerogels. The aerogels were sputtered with gold and the cross sections were visualized in a Zeiss Ultraplus field- emission SEM instrument with an acceleration voltage of 5 keV. BET Surface areas of the aerogels were measured by a surface area analyzer (Gemini VII 2390) with N_2 adsorption under a series of relative pressures. Underwater oil adhesion forces of the aerogels were measured by DCAT 11 (Data Physics). A drop of CH_2Cl_2 (5 μL) was suspended on a RG 2 Du Noüy ring as probe, which was controlled to contact the aerogel surface with a relative speed of 0.005 mm/s. Contact angle measurements were performed using an optical tensiometer. Underwater oil contact angle of aerogels was measured by injection of 5 μL CH_2Cl_2 or toluene or hexane on the surface of aerogel that was immersed in water. The morphologies of all the

emulsions were visualized by optical microscope (Nikon Elipse Ti–S) at 400 X magnification without dilution. Oil-in-water emulsion droplet size was measured by a particle size analyzer (Anton Paar).

7.3 Results and discussion

7.3.1 Synthesis of crosslinkers with different lengths

The modification process of PEGs is illustrated in Figure 7.2 (A). As reported previously, maleic anhydride (MA) could react with hydroxyl groups via the ring open reaction, simultaneously producing an ester linkage and a free carboxyl group.[119] Here, MA was grafted on the PEG skeleton by reacting with the two hydroxyl groups on both ends of the PEG chains, yielding dicarboxylated-PEGs that could further crosslink with cellulose nanofibrils (CNF) via the esterification reaction. The presence of MA on PEG skeleton and modification degree was confirmed by ^{1}H NMR and conductometric-potentiometric titration, respectively. From Figure 7.2 (B), characteristic peaks belong to carboxyl groups and CH=CH skeleton of MA were observed at the chemical shift of 8.133 to 8.157 ppm and 6.166 to 6.383 ppm for all modified PEGs,[284] while no such peaks were observed in pristine PEGs as shown in Figure 7.3. In addition, the characteristic peak of the formed ester linkage from 4.315 to 4.344 ppm provided a clear evidence of the successful modification. Carboxyl content of the modified PEGs were measured to evaluate their modification degrees. Shown in Figure 7.2 (C), the experimental carboxyl content of PM 600, PM 1500, PM 3350, and PM 8000 was 2.53, 1.44, 0.59, and 0.25 mmol/g, respectively, which are very close to their theoretical content. Details of the titration curve for each crosslinker can be found in Figure 7.4 (A). The results suggest that the modification degrees for the four PEGs were 100 %, indicating that all the hydroxyl groups on the end of PEGs were completely replaced by carboxyl groups.

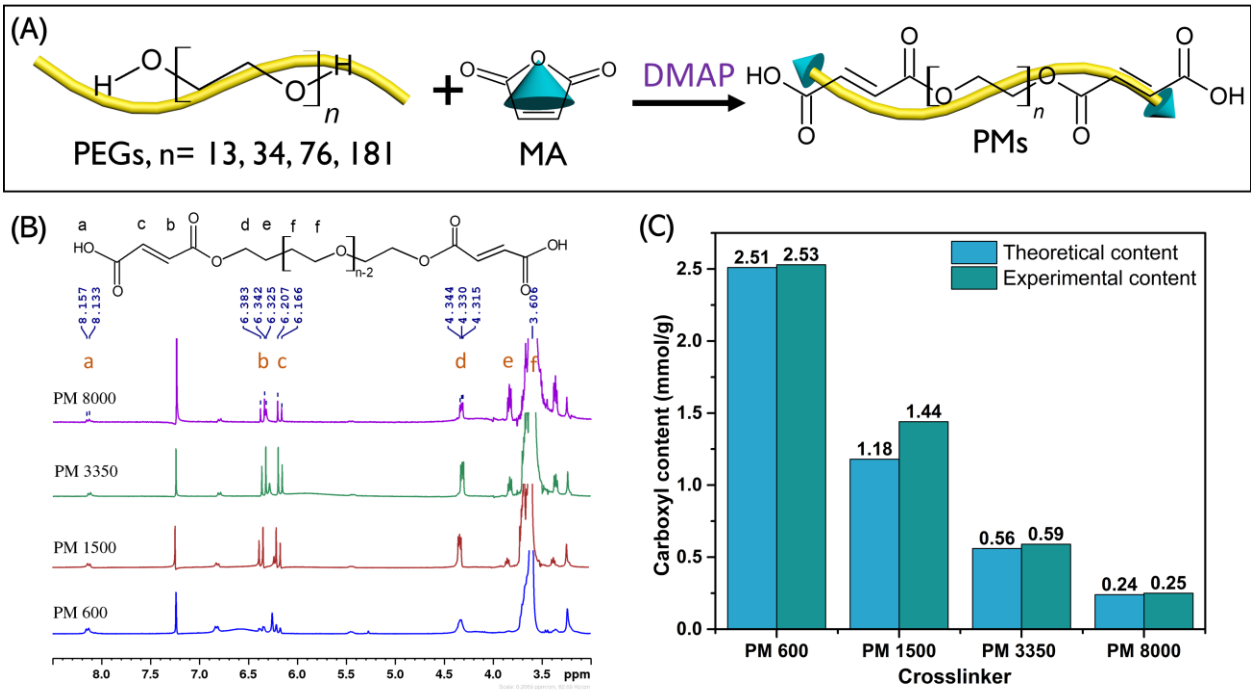

Figure 7.2 (A) Reaction scheme of grafting MA on PEG with different molecule weight, (B) ^{1}H NMR spectrums of modified PEGs of different lengths, (C) Carboxyl contents of MA modified PEGs from theoretical and experimental calculations.

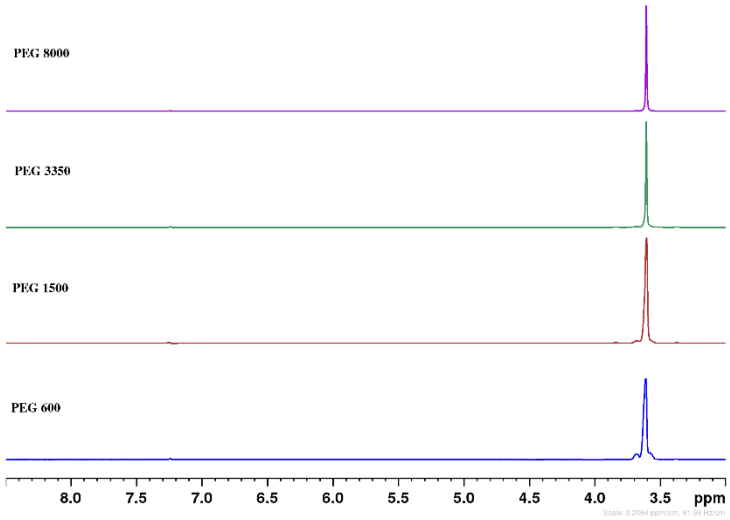

Figure 7.3 ^{1}H NMR spectrums of pristine PEGs of different molecule weight

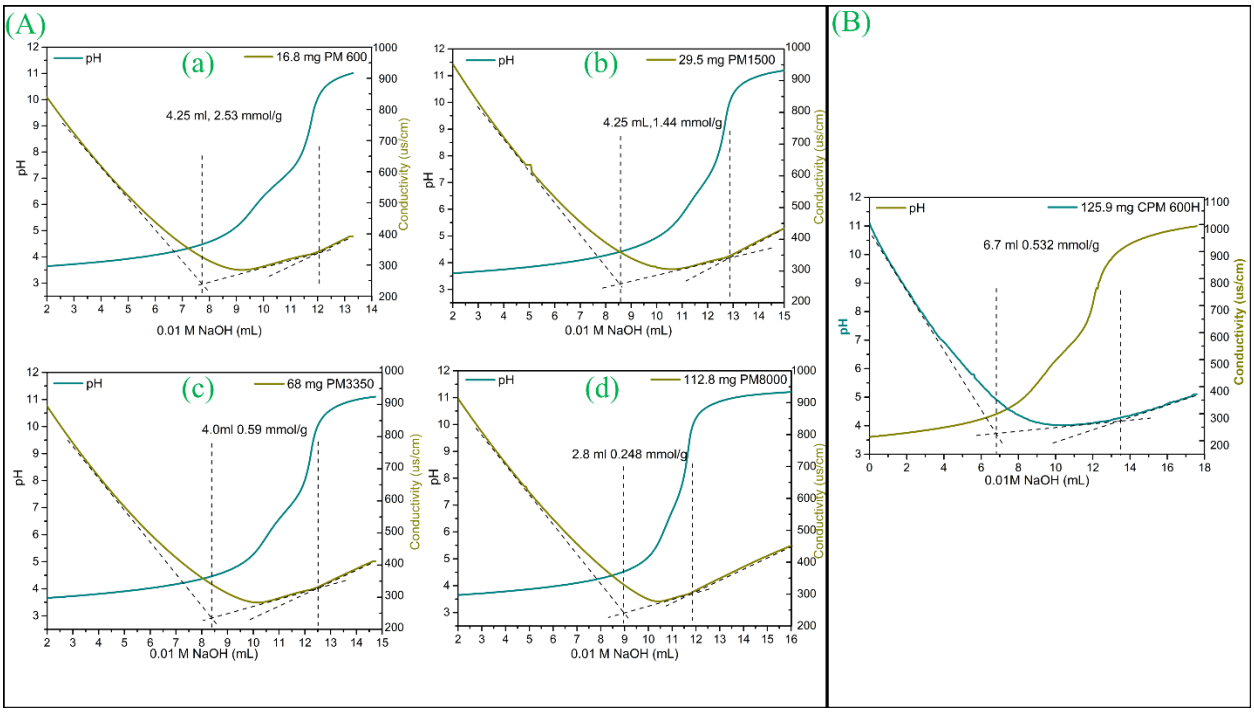

Figure 7.4 Conductometric-potentiometric titration curves for crosslinkers (A) PM 600 (a), PM 1500 (b), PM 3350 (c), PM 8000 (d), and (B) CPM 600 H (b).

7.3.2 Synthesis of crosslinked cellulose aerogels

It's known that physically crosslinked CNF aerogel is easily disintegrated under water due to the hydrogen bonding attraction between cellulose fibers and water molecules.[120] Thus, chemical crosslinking treatment was necessary to produce a mechanically robust cellulose aerogel for emulsion separation. Herein, pristine CNF aerogel was crosslinked with dicarboxylated-PEGs *via* esterification reaction between the hydroxyl groups on CNF and carboxyl groups on PMs at 120 °C as illustrated in Figure 7.5 (A) and 7.5 (B). 10 cycles compressive test at 50 % strain of crosslinked aerogels shown in Figure 7.5 (C) demonstrated their excellent mechanical property under wet state. All aerogels could recover to over 85 % of its original height after 10 compression cycles.

To investigate the effect of crosslinker length on the aerogel strength, we synthesized crosslinked aerogel solely by maleic anhydride using the same reaction ratio with PMs (1:8) for comparison. As evident from Figure 7.5 (C), all the aerogels crosslinked with PMs exhibited higher compressive strength ((b) to (e)) compared to MA ((a)), and their maximum strengths at 50 % strain are listed in Table 7.1. However, the max strength did not improve much when we increased the PM crosslinker length by tuning PEG M_n from 600 to 8000 Da, which indicated that the

mechanical strength was not dominated by crosslinker length. We further analyzed the crosslinker weight fraction (CL %) in the crosslinked aerogels by calculating the increase in weight after purification, and the results are summarized in Table 7.1. With the increasing in the PM length, the number of PMs in the aerogel decreased after considering the MW of the PMs. Longer crosslinkers experienced lower crosslinking reaction due to steric hindrance compared to crosslinkers of smaller MW, thus producing a looser crosslinked network. The number of crosslinkers in the CM aerogel was similar with CPM 600, but much higher than CPM 1500, 3350 and 8000. The stronger network of CPM 600 over CM was due to the higher network density contributed by PEG chains, the same results were observed for CPM 1500, 3350, and 8000.

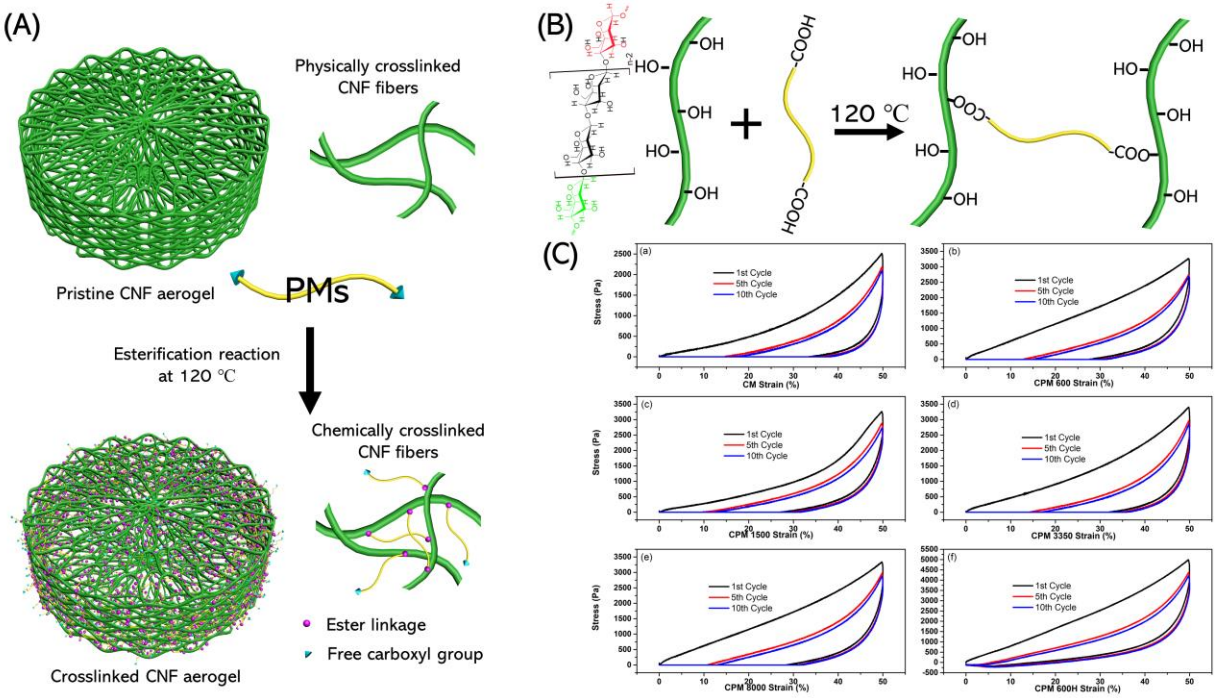

Figure 7.5 (A) Schematic of the synthesis process PMs crosslinked CNF aerogel by esterification reaction, (B) an illustration of crosslinking reaction between CNF fibers and dicarboxylated- PEGs, (C) cyclic compressive test of aerogels crosslinked by (a) MA, (b) PM 600, (c) PM 1500, (d) PM 3350, (e) PM 8000, and (f) higher molar ratio of PM 600, at 50% strain in wet state.

In conclusion, both crosslinking degree and network density contributed to the mechanical strength of the aerogel. To produce a much stronger network, we increased the reaction molar ratio of PM 600 to CNF from 1:8 to 1:1. The resulting CPM 600 H exhibited a higher density and CL % than

CPM 600, consequently a much higher mechanical strength around 4984.87 pa at 50 % strain as seen from Table 7.1.

Table 7.1 A summary of physical properties of crosslinked aerogels

Aerogel	Bulk density (mg/cm^3)	Porosity (%)	CL (%)	Water uptake (g/g)	Surface area (m^2/g)	Max strength (Pa)
CM	20.16	98.66	0.92	58.10	14.68	2517.59
CPM 600	22.10	98.57	11.45	54.93	17.43	3268.54
CPM 1500	23.06	98.33	11.66	52.77	24.68	3263.73
CPM 3350	23.31	98.57	9.71	50.98	12.15	3403.33
CPM 8000	24.22	98.34	20.47	56.13	4.81	3335.90
CPM 600 H	24.60	98.38	20.47	44.27	11.10	4984.87

7.3.3 Morphologies of the crosslinked aerogels

Pristine CNF aerogel was produced by sublimation of ice crystal templates using the freeze dry technique that yielded a porous network consisting of fibril and fiber sheet structure as seen in Figure 7.6 (A). Subsequently, it was used as template for the synthesis of crosslinked aerogels. After chemical crosslinking, the porous structures were preserved for all the CPM aerogels as evident from Figure 7.6 (A) to 7.6 (G). A porosity greater than 98% was achieved for all the CPM aerogels, which are summarized in Table 7.1. Notably, the networks were denser than that of pristine CNF aerogel due to the presence of crosslinkers as observed from the SEM images. However, one cannot tell the pore size of these aerogels from these images as the pores were formed by randomly entangled fibers. It is evident that the macropores dominated the porous structure in all the aerogels as shown by the magnified images in Figure 7.6 (a) to 7.6 (g). Meanwhile, mesopores were also evident from the fiber sheets, and an example from CPM 600 H is shown in Figure 7.6 (g').

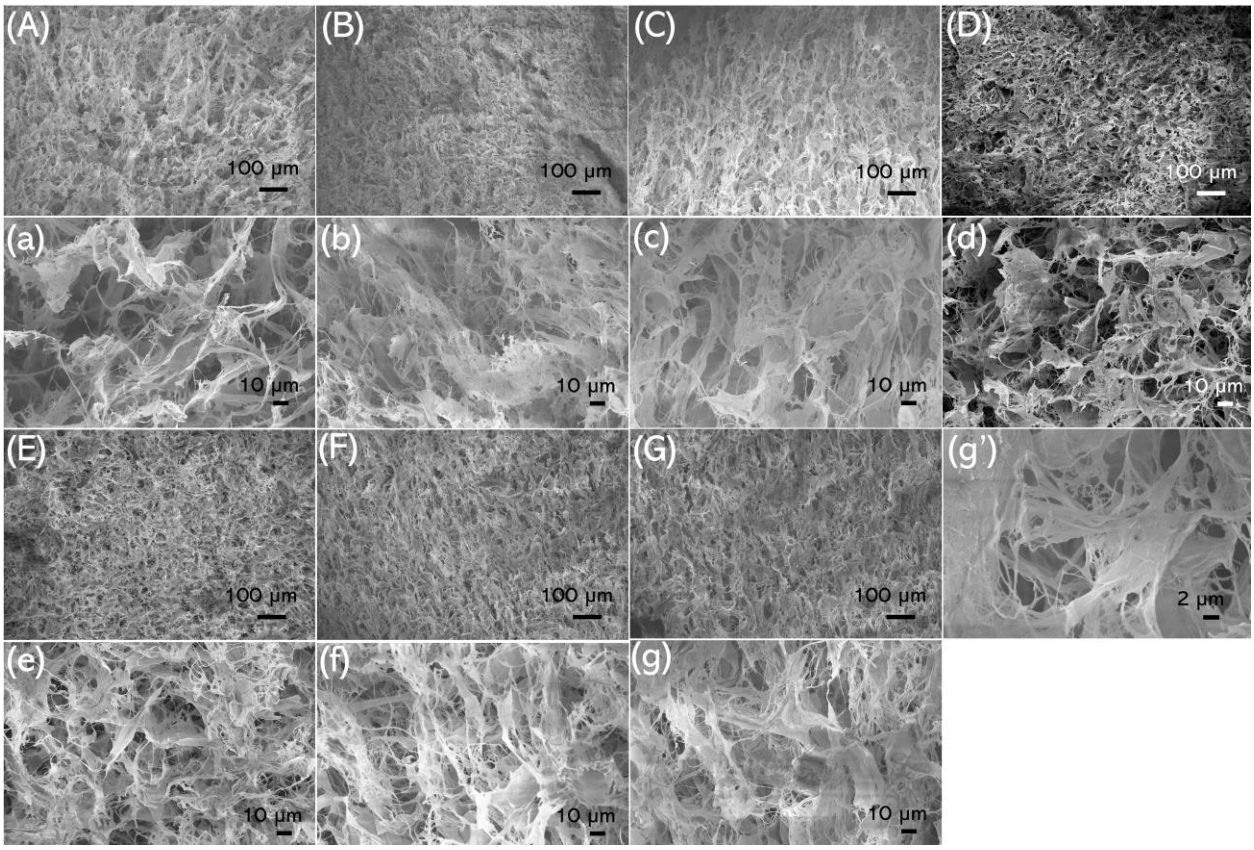

Figure 7.6 SEM images of aerogels at low magnification and a closer view of pristine CNF aerogel (A and a), CM aerogel (B and b), CPM 600 aerogel (C and c), CPM 1500 aerogel (D and d), CPM 3350 aerogel (E and e), CPM 8000 aerogel (F and f), CPM 600 H aerogel (G and g) and a view at high magnification (g').

7.3.4 Characterization of aerogel wettability

The wettability of the PM crosslinked aerogels was tested in dry and wet state. At dry state, the porous aerogels displayed excellent uptake capacity towards different solvents including water (δ= 10.2), dichloromethane (δ= 3.1), toluene (δ= 2.4), and hexane (δ= 0.1) as summarized in Table 7.1 and (1) in Figure 7.7 (A). These solvents were selected to represent a broad class of solvent types spanning a wide range of polarities (δ). Generally, aerogels with lower crosslinking degree and network density exhibited higher solvent uptake capacity regardless of the solvent polarity. The results suggest that the aerogels were amphiphilic at dry state that could be wetted by both water and oils, where the absorbed toluene and hexane oils were 100 % released immediately from all CPM aerogels when they were immersed in water ((2) in Figure 7.7 (A)). The phenomenon suggested the aerogels possessed underwater oleophobic property ((3) in Figure 7.7 (A)), which

further shows the ambient amphiphilic and underwater oleophobic property of the CPM aerogels. As evident from left to right, the aerogel in dry state could absorb toluene oil (stained with Nile red), then released the absorbed toluene oil by absorbing water once the aerogel was contacted with water. Furthermore, no oil trace was left on the aerogel when it was retrieved from the water phase to air and re-immersed into the oil/water mixture. Similar phenomenon was also observed by Wang et al. with the cellulose sponge.[132] Such characteristics make the CPM aerogels very promising as absorbents for oil spill cleanup and oil recovery, and very promising in self-cleaning applications.

Interestingly, the CH_2Cl_2 recovery ratio varied among the CPM aerogels. Seen from Figure 7.7 (A), (2)), CPM 8000 did not release any CH_2Cl_2, while other CPM aerogels released most of the absorbed CH_2Cl_2, which was lower than for toluene and hexane. This could be due to the higher density of CH_2Cl_2 (1.33 g/cm^3) compared to water, which retarded the water replacement process compared to toluene (0.867 g/cm^3) and hexane (0.655 g/cm^3), which has a much lower density than CH_2Cl_2. For aerogel with denser networks such as CPM 600 H, it needed a longer time to replace the trapped CH_2Cl_2. Therefore, less CH_2Cl_2 were released compared to the other CPM aerogels within the same time period. However, there may exist other reasons to account for the 0 % CH_2Cl_2 release behavior of CPM 8000 during our 3 days observation. It is known that PEG chain is composed of alternative hydrophobic ethylene units and hydrophilic oxygen atoms, which is responsible for its amphoteric character.[285] The fraction of hydrophobic domains increased with MW, resulting in a reduced water solubility of PEG with higher MW. Hence, PM 8000 (with higher MW) could trap CH_2Cl_2 within the network since CPM 8000 contained 20.47 wt% of PM 8000.

To confirm the underwater oleophobic property of CPM aerogels, underwater oil contact angles (OCA) of these aerogels were measured using CH_2Cl_2, toluene and hexane. As shown in Figure 7.7 (B), all the CPM aerogels displayed OCA greater than 150° for CH_2Cl_2, indicating these aerogels possessed underwater super-oleophobic property. The superhydrophilicity could be attributed to the rough surface and hydrophilic PEG and CNF components in the aerogel. In addition, the OCAs slightly decreased for the CPM aerogel with higher crosslinker length, probably due to the increased fraction of hydrophobic domains in the aerogel. A higher crosslinking degree would increase the fraction of hydrophobic domains as more ester groups were

formed. Therefore, a lower underwater CH_2Cl_2 contact angle of CPM 600 H compared to CPM 600 was observed. Furthermore, CPM 600 H and CPM 8000 were taken as representatives to evaluate the underwater toluene and hexane contact angle of CPM aerogels. Clearly, they possessed OCAs greater than 165° for both oils, which could be attributed to the lower polarity of the two oils as well as the decreased affinity of PMs for both oils. In summary, the underwater oil contact angle measurements support the conclusion that the CPM aerogels possessed underwater super-oleophobic characteristics.

More interestingly, it was found that the CH_2Cl_2 droplet pinned on CPM 8000 regardless of whether it was placed at a 90° angle or pulled by a needle tip during the underwater oil contact angle measurements as shown in Figure 7.7 (C). In contrast, the oil droplet could roll easily using the needle tip for other CPM aerogels. The oil adhesive force between the oil droplet and CPM aerogel surface was measured using a high-sensitivity microelectromechanical balance system. From Figure 7.7 (B), CPM 8000 exhibited a very high CH_2Cl_2 droplet adhesion force (126.03 μN), followed by CPM 600 H (73.50 μN), while all the other aerogels possessed adhesion force lower than 1 μN. The high underwater oil adhesion property of CPM 8000 could be used for underwater oil droplet manipulation.[286] As demonstrated in Figure 7.7 (D), the CPM 8000 aerogel could uptake a CH_2Cl_2 droplet from the vial bottom without rolling off.

The different adhesive force among CPM aerogels was caused by the crosslinkers as CPM aerogels were prepared by the crosslinking of pristine CNF aerogel with different crosslinker length. As discussed earlier, the hydrophobic domain fraction increased with PEG length and ester content, which enhanced the affinity of aerogel towards CH_2Cl_2. As seen from Figure 7.8 (A) and 7.8 (B), the aerogels crosslinked with shorter crosslinkers (CPM 600 and CPM 1500) possessed strong affinity to water, thus resulting in an ultralow oil adhesion (both were 0.29 μN). For CPM 3350, it showed a slightly lower oil contact angle than CPM 600 and 1500, yet it still possessed very strong affinity for water and low oil adhesion (0.69 μN). Such low adhesion superwetting state is called the Cassie state. When the crosslinker length was increased further increased, alternative hydrophobic and hydrophilic regimes were formed on the CPM 8000 surface. The hydrophobic domains could be wetted by oil, while the hydrophilic fractions still possessed strong water affinity that could not be wetted by oil as illustrated in Figure 7.8 (D). Such state is called the transitional state between Cassie state and Wenzel state.[287]

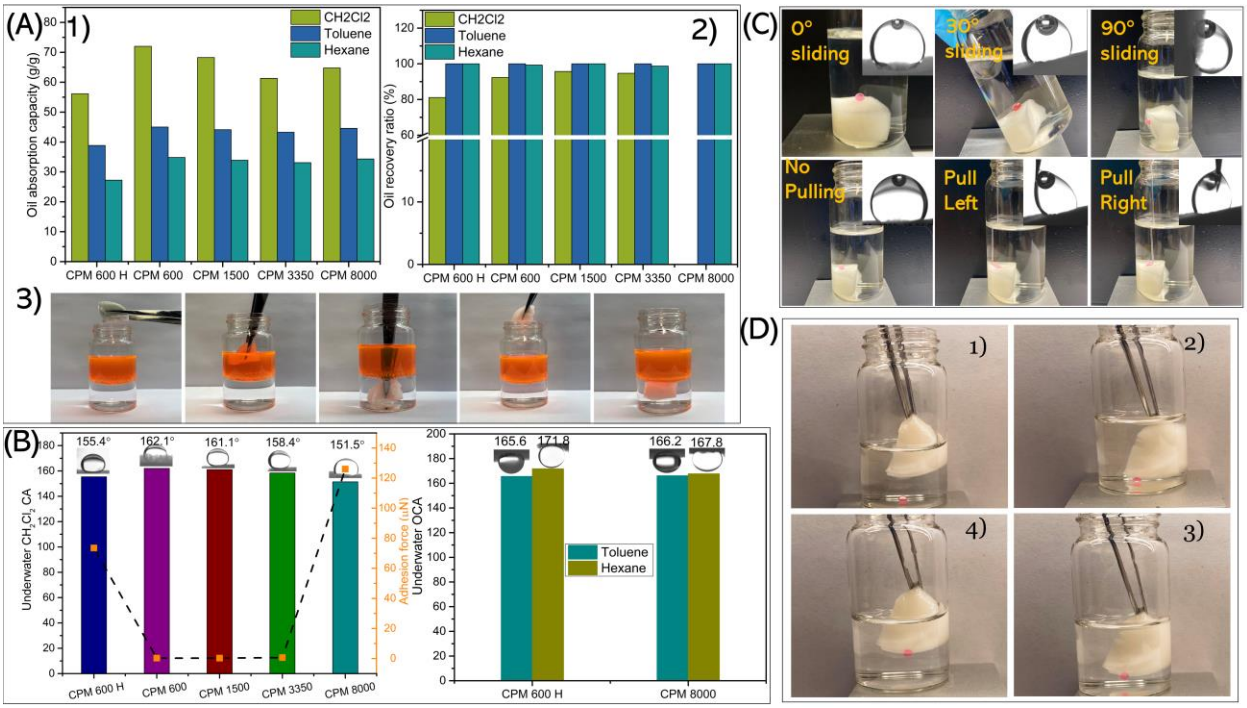

Figure 7.7 (A) Oil absorption capacity 1) and oil release property 2) of CPM aerogels for CH_2Cl_2, toluene and hexane, and 3) a demonstration of ambient amphiphilic and underwater oleophobic property using CPM 600 H aerogel and toluene (dyed with Nile red) / water mixture. (B) Underwater oil contact angle and oil adhesion force measurement of CPM aerogels using CH_2Cl_2 (left), and underwater toluene and hexane contact angle of CPM 600 H and CPM 8000 (right). (C) A demonstration of high underwater CH_2Cl_2 adhesive property of CPM 8000 at different sliding angles and pulling directions. (D) A demonstration of a potential application of CPM 8000 for underwater oil droplet manipulation.

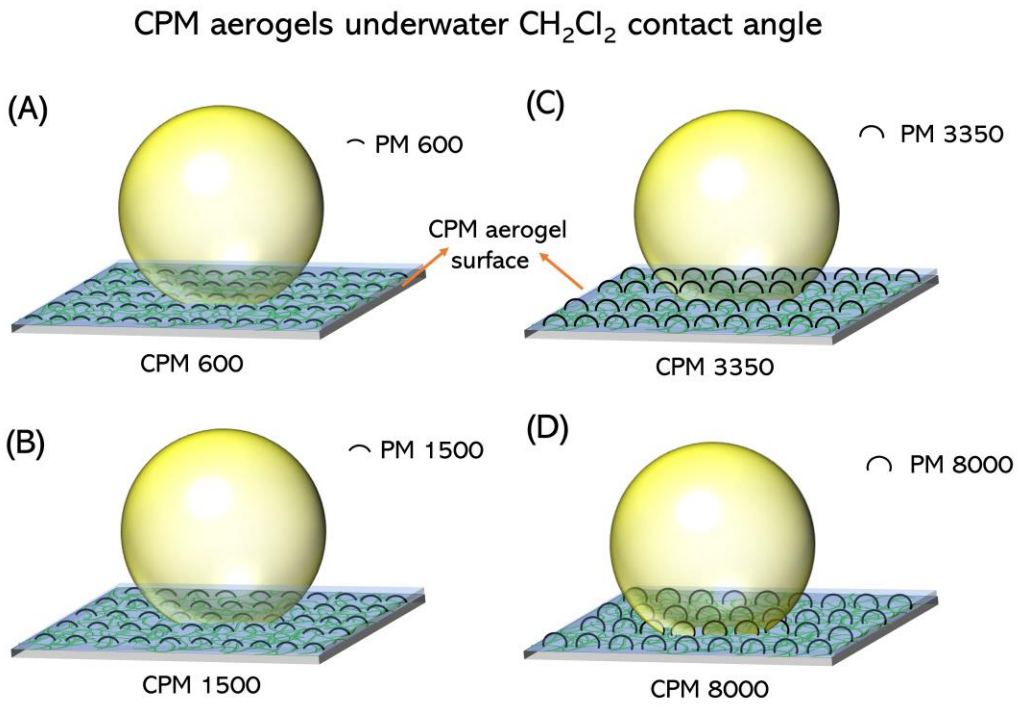

Figure 7.8 Schematic illustration of underwater oil adhesion property of CPM aerogels with different crosslinker length.

7.3.5 Oil-in-water emulsions separation

7.3.5.1 Surfactant stabilized oil-in-water emulsions separation

The potential of amphiphilic and porous CPM aerogels for emulsions separation was investigated. Toluene-in-water emulsions stabilized by cationic surfactant CTAB (CTAB SE), anionic surfactant SDS (SDS SE) and nonionic surfactant Tween 80 (Tween 80 SE) as shown in Figure 7.9 (A) were used to evaluate the CPM aerogels emulsion separation efficiency. An average droplet size of 4.50 µm, 6.20 µm, and 1.88 µm was achieved for 0.03 wt% CTAB SE, 0.03 wt% SDS SE and 0.03 wt% Tween 80 SE respectively (Figure 7.9 (B)). To eliminate the effect of electrostatic interaction between emulsion droplet and aerogel, Tween 80 SE was used to investigate the separation performance among these CPM aerogels. Notably, all the emulsion separation experiments were driven by gravity. From Figure 7.9 (C), we observed that all CPM aerogels exhibited a higher initial water flux than their overall flux. The decline could be caused by the continuing reduction in the height of the emulsion as well as pore blocking caused by oil droplets accumulation during filtration. As the separation of oil droplets is based on the size sieving effect

of the filter,[287] therefore, medium and tiny oil droplets could be trapped within the network or permeated through the aerogel with the water, while larger oil droplets were excluded and retained on the top of the filter as illustrated in Figure 7.9 (D). Among the tested CPM aerogels, CPM 600 H possessed the highest rejection efficiency of 77.38%, closely followed by CPM 8000 of 75.21 %. CPM 1500 exhibited the lowest rejection efficiency of 39.54 %, whereas the highest initial water flux of 1155.30 L/(m^2·h) and overall flux of 1050.60 L/(m^2·h). Such inverse relation between oil rejection efficiency and water permeation flux was observed in all the CPM aerogels. The better emulsion rejection performance of CPM 600 H and CPM 8000 compared to the others were attributed to their denser network that could trap more oil droplets within the aerogel network.

One could imagine that the emulsion separation efficiency is not only associated with the inherent property of the filter, but it is also highly correlated with the emulsion droplet size and surfactant type. The 77.38% filtration efficiency of CPM aerogels for Tween 80 SE stabilized emulsion was probably due to the small oil droplet size. Therefore, CPM 600 H was selected to study the effect of surfactant types on its separation performance. CTAB SE and SDS SE were used for the study. Similarly, higher initial fluxes than overall fluxes were observed from Figure 7.9 (E) for all types of emulsions. Compared with Tween 80 SE, CPM 600 H exhibited a much higher emulsion rejection efficiency for both CTAB and SDS SEs. The larger average droplet size of the two emulsions compared to Tween 80 SE could contribute to the separation efficiency according to the size sieving theory. Electrostatic interaction between oil droplets and the aerogel is another factor that affects the separation performance. As the CPM aerogels were synthesized by crosslinking of dicarboxylated PEGs (PMs) with CNF, some PMs would only have one end grafted on the CNF while the other end remained as free carboxyl groups as illustrated in Figure 7.5 (A). Therefore, all CPM aerogels with carboxyl groups might affect their emulsion separation performances when an ionic surfactant was used as the emulsifier.

CPM 600 H possesses a carboxylic content of 0.532 mmol/g according to the conductometric-potentiometric titration result shown in Figure 7.4 (B). As illustrated in Figure 7.9 (F), the negatively charged aerogel could attract CTAB stabilized emulsions via electrostatic attraction, trapping the tiny droplets within the aerogel to yield an emulsion rejection efficiency of 89.5%. On the other hand, the aerogel would repel the SDS stabilized emulsions via electrostatic repulsion, yielding a higher separation efficiency of 92.03%. Nile red was dissolved in toluene during the

emulsion preparation step to facilitate the visualization of the oil droplets. The top, bottom, and side views of CPM 600 H after filtration were examined to further confirm its separation performance. The aerogel exhibited a pink top and side face as well as partially clean bottom after CTAB SE filtration, a pink top and a slight pink side face, while fully clean bottom after SDS SE filtration, complete pink surfaces after Tween 80 SE filtration. The results suggested that the majority of CTAB SE was retained in the aerogel network, while the majority of SDS SE were excluded outside the aerogel, and Tween 80 SE permeated through the aerogel. The lower overall water flux of CTAB SE filtration (412.61 L/(m^2·h)) compared to SDS SE and Tween 80 SE was probably caused by the trapped oil droplets. Besides, the transparent CTAB and SDS SE filtrates were subjected to optical microscopy assessment, where no oil droplets were observed under 400 X magnification (see Figure 7.10), which confirmed that the permeated oil droplets were very small (nano-size). However, micron- sized oil droplets (around 4 μm) were observed for the Tween 80 SE filtrate. This further demonstrates that the charge interaction between surfactant and aerogel could enhance emulsion separation efficiency of the aerogel.

In addition, the recyclability of the aerogel was investigated after the filtration tests. The recovery was performed by rinsing the aerogel with acetone for 1 min, followed by rinsing with water for 1 min, and it was then subjected for CTAB SE filtration. The process was repeated for 5 cycles, and the flux for each cycle is shown in Figure 7.11. A decreased flux was observed with cycle times, which was ascribe to the accumulated CTAB surfactants in aerogel network that blocked the pores.

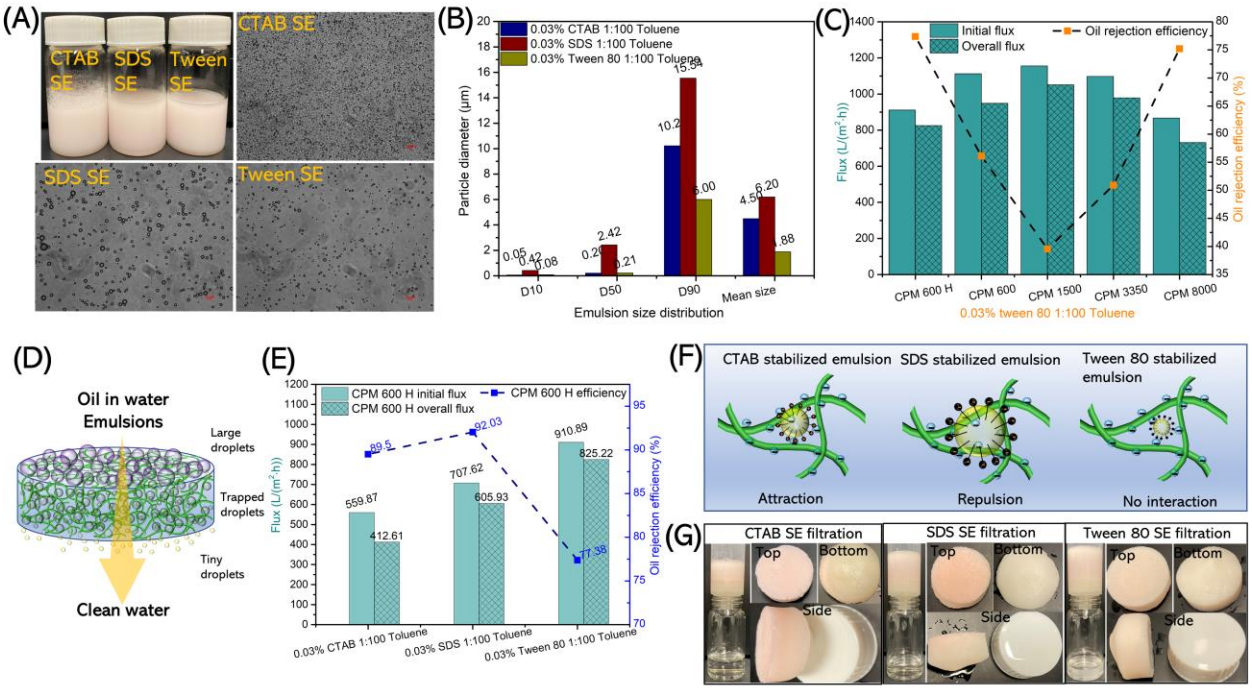

Figure 7.9 (A) A photo of 0.03 wt% CTAB, 0.03 wt% SDS, 0.03 wt% Tween 80 stabilized toluene-in-water emulsions and their corresponding optical microscopic images (scale bar 10 μm). (B) Emulsion droplet size distribution of the three emulsions. (C) Filtration flux and oil separation efficiency of all CPM aerogels toward 0.03 wt% Tween 80 SE. (D) Schematic illustration of emulsion separation process using CPM aerogel. (E) Filtration flux and emulsion separation efficiency of CPM 600 H aerogel toward 0.03 wt% CTAB, SDS and Tween 80 SEs. (F) Schematic illustration of the interaction between negatively charged aerogel and CTAB SE, SDS SE and tween 80 SE. (G) The top, bottom, and side views of CPM 600 H aerogel after CTAB SE, SDS SE and tween 80 SE filtration.

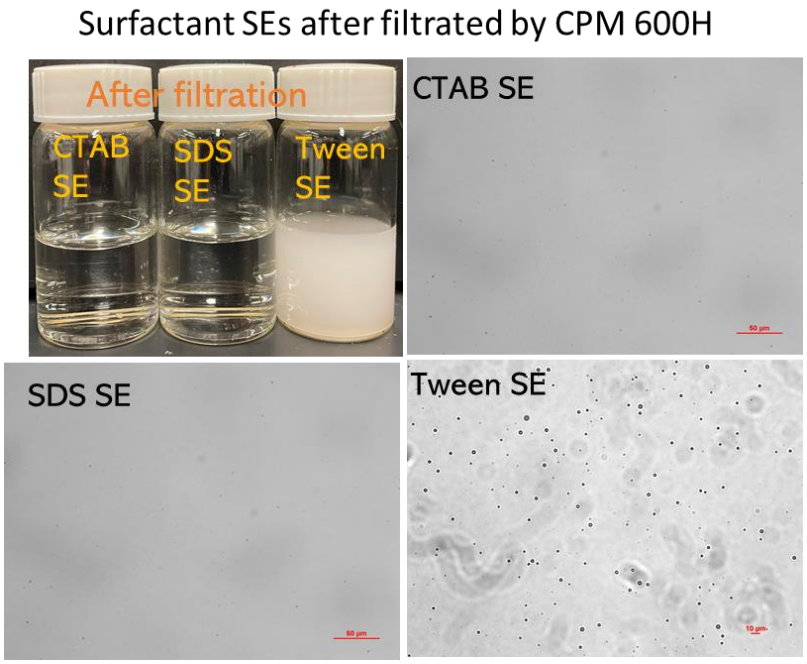

Figure 7. 10 A photo of 0.03 wt% CTAB, 0.03 wt% SDS, 0.03 wt% Tween 80 stabilized toluene-in-water emulsions and their corresponding optical microscope images after filtrated by CPM 600 H aerogel (scale bar 10 μm). Note: the microscope was contaminated, and the background contained stain marks. Repeat experiment is being performed.

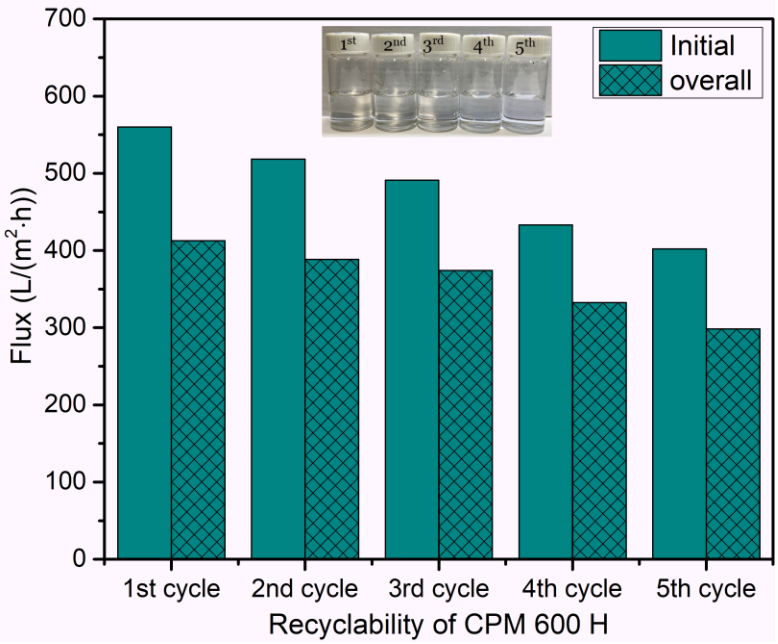

Figure 7.11 Recyclability tests of CPM 600 H aerogel for CTAB SE filtration

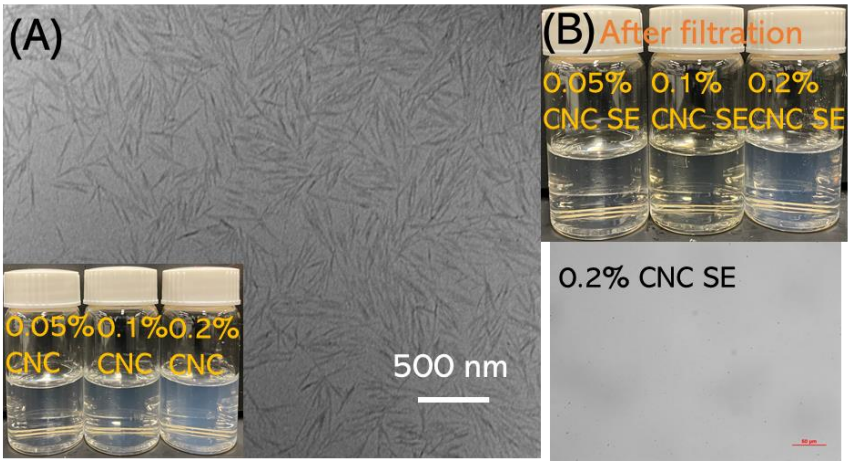

Figure 7.12 (A) TEM image of CNC nanoparticle (inserted picture is CNC dispersion with different concentration), (B) A photo of 0.05 wt%, 0.1 wt%, 0.2 wt% CNC stabilized toluene in water emulsions and their corresponding optical microscope images after filtrated by CPM 600 H aerogel (scale bar 10 μm). Note: the microscope was contaminated, and the background contained stain marks. Repeat experiment is being performed.

7.3.5.2 CNC stabilized oil-in-water emulsions separation

Cellulose nanocrystal (CNC) is a rod like nanoparticle that possesses an average length of 200 nm and width around 10 nm as observed by TEM (Figure 7.12). It is widely used as emulsifier for Pickering emulsion preparation in recent years.[201] Herein, we used CNC stabilized toluene-in-water emulsions (CNC SE) as a model to evaluate the Pickering emulsion separation performance of CPM 600 H aerogel. Toluene-in-water Pickering emulsions stabilized by 0.05, 0.1 and 0.2 wt% CNC were prepared, and their corresponding morphologies were observed by optical microscope as shown in Figure 7.13 (A). The mean droplet size of the three emulsions was 9.09 μm, 8.25 μm and 7.38 μm as shown in Figure 7.13 (B). Compared with surfactants SE, CNC SEs possessed larger mean droplet sizes, yielding a higher emulsion separation efficiency (> 92%). A clear reduction in the water flux was observed when the CNC concentration was increased from 0.05 to 0.1 wt%, which decreased slightly when it further increased to 0.2 wt%. As the emulsion droplet did not change much, the reduced water flux was probably caused by the retained CNC nanoparticles within the aerogel. Similarly, the top, bottom, and side face of the aerogel after filtration were examined to track the emulsion droplets. Figure 7.13 (D) shows an example from 0.2% CNC SE filtration, where a clean bottom and partially clean side face were observed. It further confirmed majority of emulsion droplets were retained in the aerogel. However, the filtrate

was turbid compared with filtrates from 0.05% CNC SE and 0.1% CNC SE (Figure 7.12). The filtrate was further analyzed by optical microscope, and no oil droplets were observed (Figure 7.12). Therefore, the turbidity was probably caused by the tiny droplets or CNC nanoparticles.

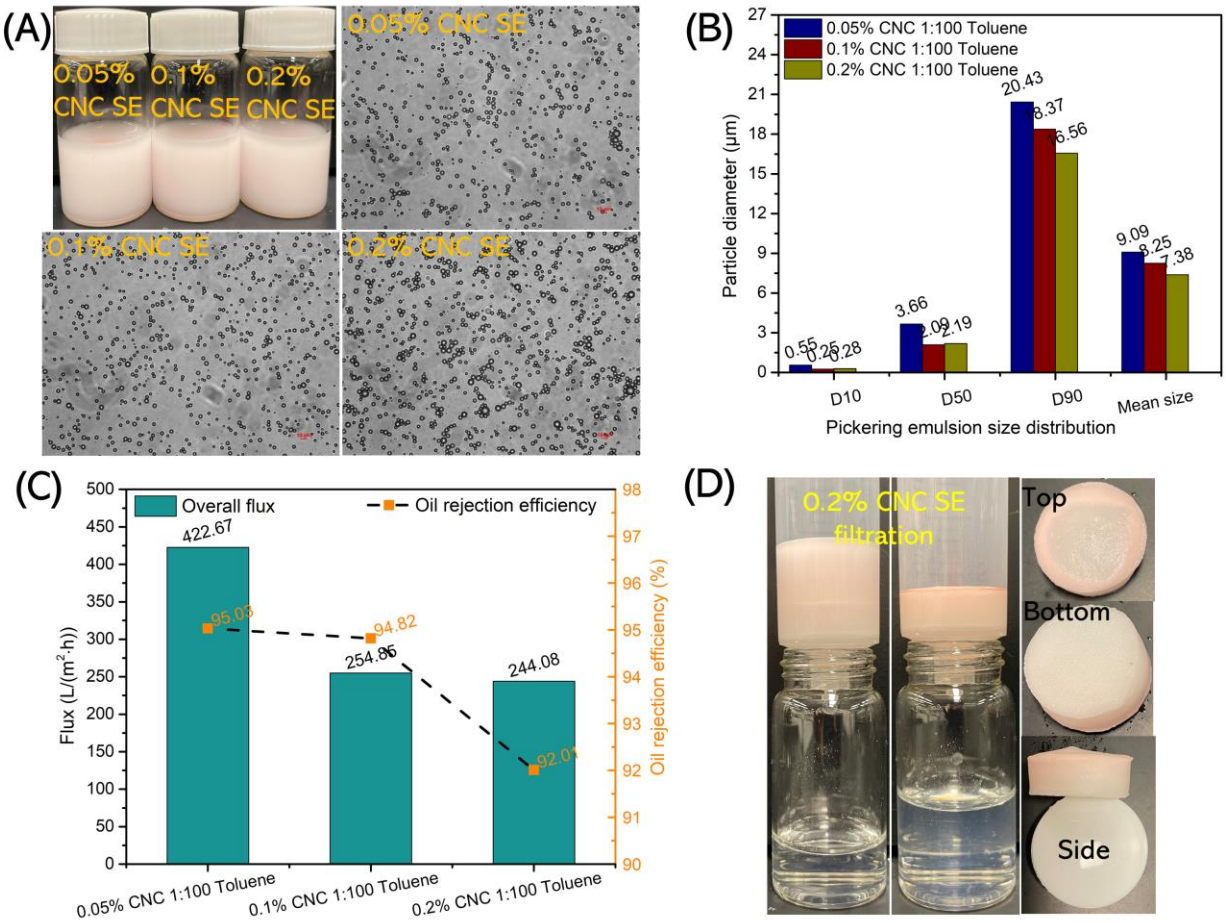

Figure 7.13 (A) Pictures of 0.05 wt% CNC SE, 0.1 wt% CNC SE, 0.2 wt% CNC SE and their corresponding optical microscope images (scale bar 10 μm). (B) Emulsion droplet size distribution of the three emulsions. (C) Filtration flux and oil separation efficiency of CPM 600 H aerogels toward the CNC SEs. (D) A demonstration of CPM 600 H aerogel for 0.2% CNC SE filtration, and the top, bottom, side views of CPM 600 H aerogel after filtration.

7.3.6 Water-in-oil emulsions separation

As the aerogel possessed ambient amphiphilic and underwater super-oleophobic property, it could be used to remove water droplets from oil. Water-in-oil emulsions prepared using vegetable oil, diesel, and hexane as well as their morphologies before filtration are shown in Figure 7.14 (A). As the continuous phase, oil could wet and permeate through the dry aerogel, while water droplets

were trapped in the network during filtration due to size sieving effect. A white layer was formed on the top surface of CPM 600 H aerogel during the filtration, which further confirmed the trapped water droplets (Figure 7.14 (C)). After filtration, clean oils were obtained for all three emulsions as seen from Figure 7.14 (A). The original emulsions and their filtrates were further analyzed by optical microscope. All the emulsions showed the presence of water droplets before filtration (Figure 7.14 (B)), while no water droplets were found in the filtrates (Figure 7.15). Furthermore, the separation efficiencies were calculated by measuring the water content before and after filtration, where greater than 97% removal efficiency was achieved for all emulsions (Figure 7.14 (D)).

The oil permeation flux was also evaluated during the filtration (Figure 7.14 (D)). Among the three oils, hexane exhibited the highest overall permeation flux of 1371.90 L/(m^2·h)), followed by diesel fuel of 496.48 L/(m^2·h)) and soybean oil 5.80 L/(m^2·h)). According to Hagen-Poiseuille equation (Flux = $p\pi r^2\Delta P/8\mu L$), flux is correlated to the porosity (p), pore radius (r), and thickness (L) of a filter, and pressure drop (ΔP) as well as liquid viscosity (μ).[12] For a given aerogel, p, r and L are fixed parameters. ΔP is determined by the oil density for the same volume of emulsions. The density of hexane, diesel and soybean oil is 0.655 g/cm^3, 0.85 g/cm^3, and 0.917 g/cm^3, respectively. μ is liquid viscosity, which is 0.30 mPa·s for hexane at 25 ℃, 3.35 mPa·s for diesel fuel at 25 ℃ and 40.6 mPa·s for soybean oil at 30 ℃. Therefore, the significant higher flux of oil-in-hexane emulsions was associated with its lower viscosity.

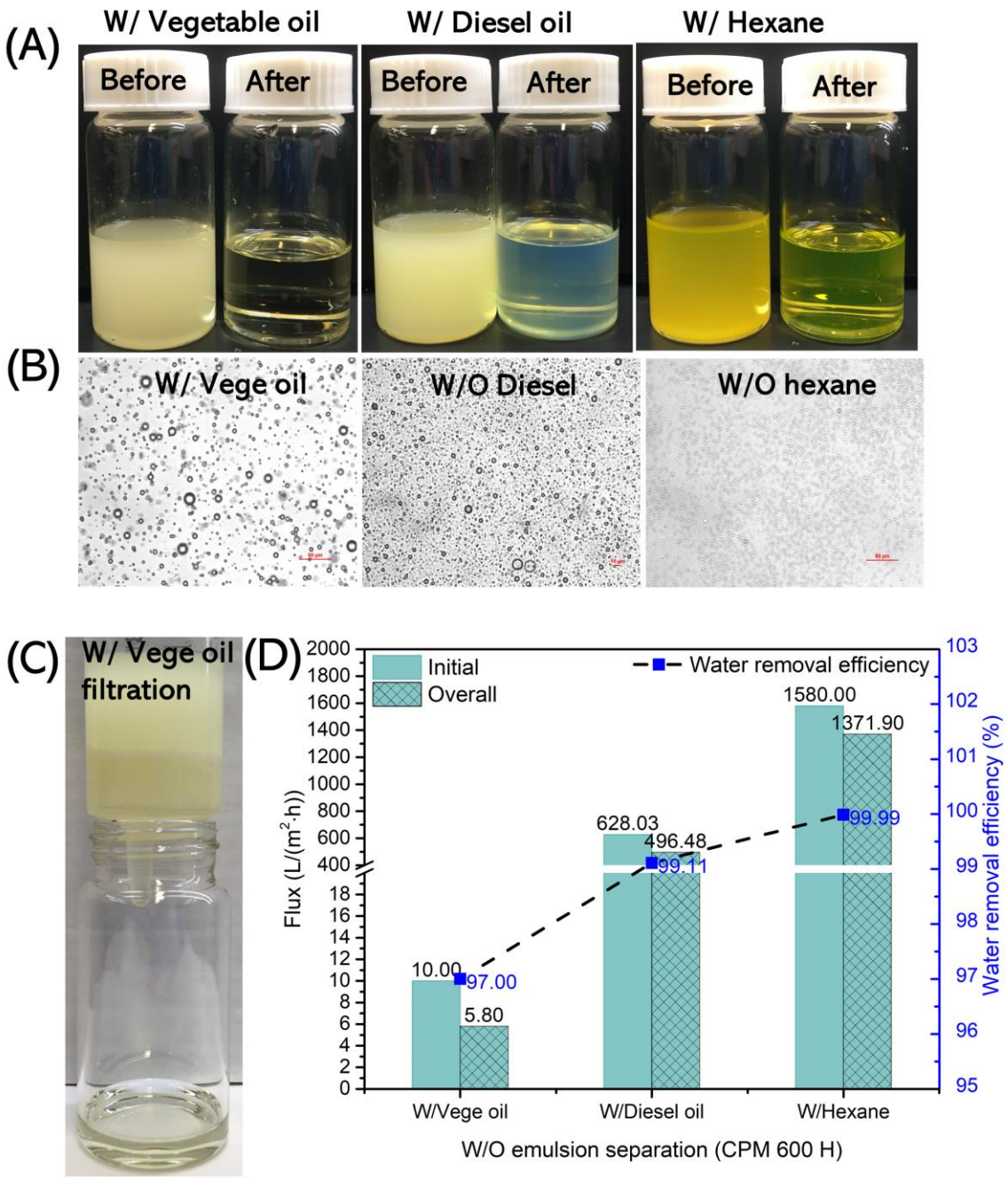

Figure 7.14 (A) Picture of water-in-vegetable oil, water-in-diesel, water-in-hexane emulsions before and after filtration, and (B) their corresponding optical microscopic images before filtration (scale bar 10 μm). (C) A demonstration of CPM 600 H aerogel for water-in-vegetable oil emulsion filtration. (D) Filtration flux and oil separation efficiency of CPM 600 H aerogels toward the water-in-oil emulsions.

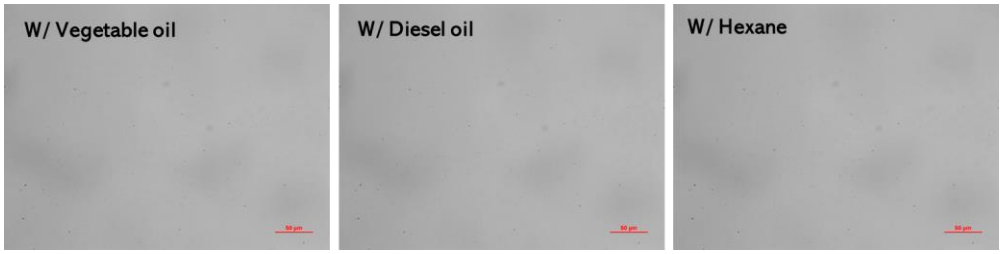

Figure 7.15 (A) Optical microscopic images water-in-vegetable oil, water-in-diesel, water-in-hexane emulsions after filtration through CPM 600 H aerogel (scale bar 10 μm). Note: the microscope was contaminated, and the background contained stain marks. Repeat experiment is being performed.

7.4 Conclusions

In this study, we have successfully synthesized a series of crosslinkers of different length by grafting maleic anhydride on PEGs (MW = 600, 1500, 3350, 8000 Da). These dicarboxylated-PEGs were further used as crosslinkers for cellulose nanofibrils (CNF) to prepare mechanically robust cellulose aerogels through an esterification reaction. The results showed that the crosslinking activity decreased with increasing crosslinker length. Both crosslinking degree and network density contributed to the mechanical strength of an aerogel. The as prepared aerogels possessed amphiphilic property that could uptake solvents with a wide range of polarities (from 0.1 to 10.2). They also exhibited underwater super-oleophobic property, which allowed the aerogels to release the absorbed oils in water. Ultralow underwater oil adhesion force was achieved for aerogels with shorter crosslinker length and lower crosslinking degree, while CPM 8000 aerogel showed high underwater oil adhesion force. Such amphiphilic aerogels were effective for both oil-in-water and water-in-oil emulsions separation. The separation efficiency for oil-in-water emulsions is a combination effect of size sieving and electrostatic interaction between oil droplets and the negatively charged aerogel. The aerogel also demonstrated excellent separation performance for cellulose nanocrystal stabilized oil-in-water Pickering emulsions. For water-in-oil emulsions, the viscosity of oil showed a significant effect on the permeate flux. Overall, the aerogels are very promising for oil spill cleanup and recovery, for self- cleaning, and for multiple emulsion separation applications.

Application 2: Plant growth

7.5 Introduction

According to the discussion in Chapter 1, it was stated that 187 million metric tons of fertilizer, nearly four million tonnes of pesticides, 2.7 trillion cubic meters of water (about 70% of all freshwater consumptive use globally) are needed to produce three billion metric tons of crops per year.[8] In addition to the large consumption of agrochemicals, water consumption is another critical issue that needs attention, especially with the associated changes arising from climate change.[9] Research into advanced water retention systems have been conducted to enhance crop production yield.[7] Superabsorbent hydrogel (SAH) as soil conditioner and nutrients carrier have attracted increasing attention due to their super water adsorption and retention property. It can reduce water irrigation frequency, which is favorable in arid regions. SAH is 3D matrix composed of synthetic or natural hydrophilic polymers, such as polyacrylamide (PAM), polyacrylic acid (PAA), chitosan, gelatin, cellulose, etc., by physical or chemical crosslinking. However, synthetic polymers like PAM and PAA are non-biodegradable in soil although they possess excellent property to prepare SAH.

Incorporating natural degradable polymers in the synthesis of SAH can reduce soil contamination. Polysaccharides, such as cellulose, alginate, chitosan, and lignin are very promising materials to fabricate SAH due to their hydrophilicity, degradability, and reactivity. For example, Calcagnile et al. fabricated a SAH based on 1-ethyl-3-(3-dimethylaminopropyl) carbodiimide hydrochloride (WSC) crosslinked CMC and HEC,[288] where the SAH could enhance the soil water retention efficiency, which further promoted the growth of tomatoes. Senna et al. prepared amphoteric biodegradable hydrogel (HEDTA) by crosslinking cellulose acetate with ethylenediaminetetraacetic dianhydride (EDTAD).[289] The water retention and slow release capability of HEDTA was tested in the planting of eucalyptus during the dry season. The average height and stem diameter of eucalyptus seedlings suggested the effectiveness of the resulting HEDTA hydrogel.

In this study, the CPM aerogels have demonstrated excellent water absorption capacity according to the results shown in Table 7.1. It also has carboxyl groups that could capture nutrient ions and reduce the loss of nutrients when the land is being irrigated. Therefore, its potential as water and nutrients retention platform is being explored.

7.6 Methods

7.6.1 Water absorption capacity measurement

Water uptake capacity of CPM 600 H aerogel, cotton, paper towel, and soil were measured by immersing the samples in water, and the gained weight at equilibrium was calculated by Eq. (7.6).

$$Water\ absorption\ capacity\ (g/g) = (w_1 - w_0)/w_0 \qquad (7.6)$$

where w_0 and w_1 are the sample weight before and after water absorption.

7.6.2 Plant growth experiment

Pea seeds were disinfected by soaking the seeds into 0.1% NaClO solution for 10 minutes, followed by rinsing with DI water prior to use. The seeds were transferred onto a constant wetted filter paper and incubated at 24 ℃ for 24 hrs to initiate the germination of the seeds, and those showing white buds will be subsequently selected and planted. As illustrated in Figure 7.16 (B) and (C), 1000 g of soil was placed in each pot, with 500 g on the top layer mixed with 0, 15, and 30 CPM 600 H aerogels of 23 mm. Then, 5 pea seeds were buried 1 cm from the top, and it was irrigated with 200 ml Hoagland solution on the planting day. The humidity, light duration and density, temperature and watering details during growth period were monitored as summarized in Table 7.2. On the 36^{th} day, the seedlings were harvested, and the total fresh weight, average shoot/root length, average diameter of seedlings from each pot were measured.

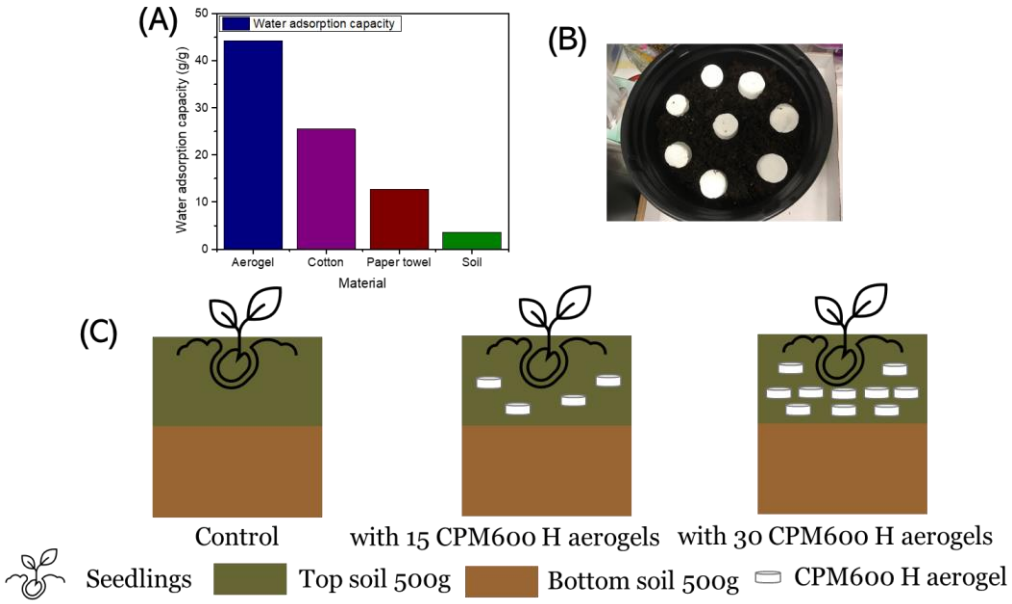

Figure 7.16 (A) Water adsorption capacity of CPM 600 H aerogel, cotton, paper towel, and soil. (B) A photo of aerogel containing pot. (C) Illustration of seeds planting in each pot.

Table 7.2 A summary of seed growth condition

	L- temp C	H-temp C	Humidity %	Day/night	Watering	Light intensity
Sep 4	19	21	43	16/8	200 ml	8000 lux
Sep 5	19	20	53	16/8	0 ml	8000 lux
Sep 6	19	21	42	16/8	0 ml	8000 lux
Sep 7	19	20	60	16/8	0 ml	8000 lux
Sep 8	19	20	53	16/8	0 ml	8000 lux
Sep 9	19	20	53	16/8	0 ml	8000 lux
Sep 10	19	20	56	16/8	0 ml	8000 lux
Sep 11	19	21	44	16/8	100 ml	8000 lux
Sep 12	19	21	52	16/8	0 ml	8000 lux
Sep 13	19	20	55	16/8	0 ml	8000 lux
Sep 14	19	21	41	16/8	100 ml	8000 lux
Sep 15	19	21	50	16/8	0 ml	8000 lux
Sep 16	19	21	55	16/8	0 ml	8000 lux
Sep 17	19	21	43	16/8	100 ml	8000 lux
Sep 18	19	21	30	16/8	0 ml	8000 lux
Sep 19	19	21	28	16/8	0 ml	8000 lux
Sep 20	18	21	28	16/8	100 ml	8000 lux
Sep 21	19	21	36	16/8	100 ml	8000 lux
Sep 22	18	21	41	16/8	0 ml	8000 lux
Sep 23	18	20	54	16/8	0 ml	8000 lux
Sep 24	19	20	59	16/8	100 ml	8000 lux
Sep 25	19	20	54	16/8	100 ml	8000 lux
Sep 26	19	20	57	16/8	0 ml	8000 lux
Sep 28	19	21	56	16/8	100 ml	8000 lux

7.7 Results and discussion

Figure 7.16 (A) shows that the aerogel demonstrated much higher water adsorption capacity than cotton, paper towel and soil, which was mainly due to its high porosity and superhydrophilicity. After planting, the germination rate of seeds and the morphology of seedlings in each pot were monitored each day. As shown in Figure 7.17 (A), on the 4th day after planting, there were 2 seeds, 4 seeds and 5 seeds germinated in the control pot, pot with 15 aerogels and pot with 30 aerogels respectively. The same germination rate was maintained until harvest. The details of gemination rate in each pot during the first week is shown in Figure 7.17 (B). As these pots were not watered until the 7th day after planting (see Table 7.2), the faster germination rate in aerogel containing pots suggested that the aerogels could retain water and promote seed germination.

On the 36th day after planting, the seedlings were harvested as shown in Figure 7.17 (A). The total fresh weight, average shoot/root length, and average diameter of seedlings from each pot were measured and summarized in Figure 7.17 (C). Clearly, seedlings from the pot containing 30 aerogels possessed highest fresh weight and length compared to the others. In addition to the excellent water absorption capacity, the aerogels could capture the nutrient ions from the Hoagland solution via the carboxyl groups. Such synergetic characteristic promoted the rapid growth of seedlings, which is very promising as nutrients delivery and water retention platforms.

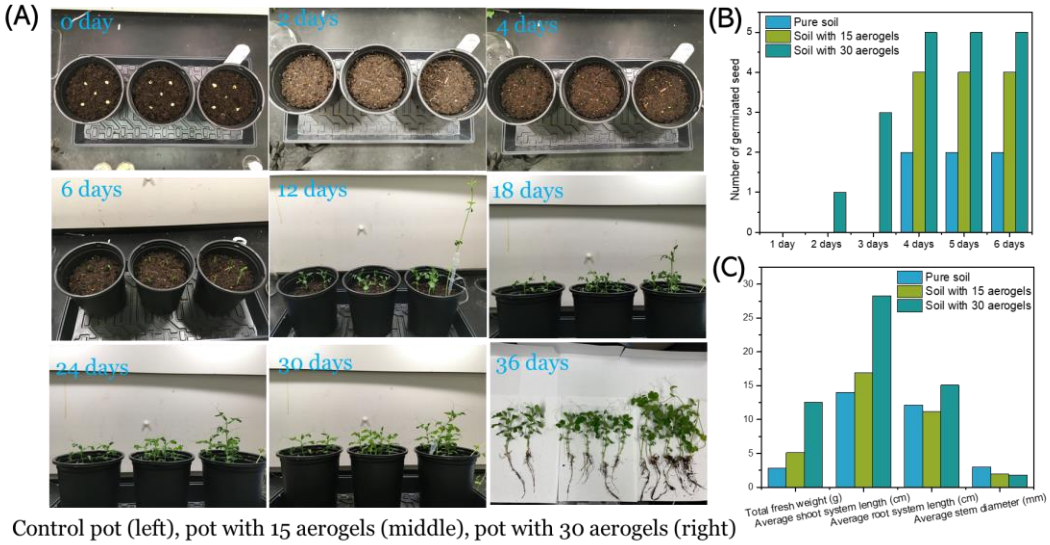

Figure 7.17 (A) Morphology of seedlings in each pot during the 36 days growth period. (B) Germination rate of seeds in each pot in the first 6 days. (C) Fresh weight, average shoot/ root length, and average diameter of seedlings from each pot after harvesting.

7.8 Conclusions

In this study, superhydrophilic and carboxylated CPM 600 H aerogel was used as a platform for water and nutrients retention to facilitate plant growth. The aerogel showed much higher water absorption capacity compared with soil and other types of absorbents. Plant growth experiment suggested the aerogel could retain water and promote seed germination. A faster germination rate was observed from the pot containing 30 aerogels. In addition, the aerogels could capture the nutrient ions from the Hoagland solution via the carboxyl groups, thereby promoting the seedling growth rate. After harvesting, plants from pots with 30 aerogels possessed highest fresh weight and length compared to the others. Such results suggested the aerogel possess potential in agricultural applications.

Chapter 8 General conclusions and perspectives for future study

8.1 General conclusions and contributions

In this thesis, the environmental pollution caused by the overuse of pesticide formulation, wastewater discharge and non-degradable materials are discussed in Chapter 1. From a detailed literature review described in Chapter 2, we concluded that cellulose nanomaterials (CNs) are sustainable and biodegradable biomass derived materials. They are very promising for use as Pickering emulsifiers, drug carriers, and skeletons for designing porous aerogels for pollutants adsorption and filtration. Based on these characteristics, several systems were developed as described in Chapter 3 to Chapter 7 to reduce environmental pollution. The major conclusions and contributions associated with each chapter are described below:

In Chapter 3, an amphiphilic CNC was synthesized by grafting aminated polystyrene (PS-NH_2) on its reducing end via reductive amination reaction. The end aldehyde content of the pristine CNC was confirmed by two methods. The CHC method revealed an aldehyde content on the reducing end of pristine CNC was 24.5 μmol/g, while the PT method gave a value of 31.08 μmol/g. After modification at room temperature, the aldehyde content decreased from 24.5 to 11.4 μmol/g, confirming that the reaction was successful. The results further showed that prolonging reaction time and increasing reaction temperature were effective ways to increase the grating ratio. PS-NH_2 with longer chain displayed lower reactivity compared with PS-NH_2 with shorter chain.

In terms of Pickering emulsion preparation, end modified CNC produced more stable toluene-in-water emulsion when compared to pristine CNC. With increasing emulsifier concentration, a smaller emulsion droplet size and slower creaming rate was observed. Under the same emulsifier concentration, hexadecane-in-water emulsions exhibited smaller emulsion droplet size compared to toluene-in-water emulsions. Adding electrolytes would screen the charges on the CNC surface, yielding emulsions with much smaller size and slower creaming rate. All the results suggested that the end modified CNCs are effective emulsifiers to prepare stable oil-in-water emulsions for various types of oils. It also showed excellent encapsulation capability for a model hydrophobic compound (Nile red) without coalescence over a period of more than 4 months, hence such a system is very promising for preparing emulsified concentrate formulations for pesticide encapsulation.

The major contributions of this chapter include: (1) a new approach for end-modification of CNC, which expanded its potential applications; (2) the content of end aldehyde group was precisely measured, providing more information for understanding the basic property of CNC; (3) the application of end modified CNC as Pickering emulsifier was investigated, which has not been reported; 4) sustainable material, such as CNC was used as emulsifier to replace petroleum derived surfactants, which is promising for preparing novel pesticide emulsions.

In Chapter 4, a scalable and novel solution to prepare organic solvent- and surfactant- free pesticide nano-dispersion using cellulose nanocrystals as carriers is described. Two model water-insoluble pesticides (Deltamethrin and Permethrin) were used in this study. The optimum loading mass ratio between deltamethrin and CNC was 1:100 as determined by DLS and ITC. FTIR and ITC studies suggested that the attraction between hydrophobic pesticide molecules and CNC was dominated by hydrophobic interaction. CNC acted as carrier and dispersing agent during the preparation, leading to the formation of nano-sized pesticide particles. Besides, the small particle size and high zeta potential value of pesticide@CNC are very important properties to yield a stable dispersion that can be stored over an extended period.

In laboratory tests, the nano-dispersion possessed excellent pest control efficacy on both mealworms and waxworms, which was comparable to commercial formulations. The efficacy of the prepared nano-dispersion was also investigated in a field trial, where comparable performance with a commercial formulation Deltamethrin 2.5 EC for the control of Diamond back moth caterpillar (DBM) in cabbage was observed. In summary, the nano-dispersion is very promising to replace the conventional pesticide formulations due to its simple preparation process, environmentally friendly material, odorless ingredients, and excellent pest control efficacy.

The major contributions of this chapter include: (1) this is the first reported study on the loading capacity of pristine CNC for water insoluble compound; (2) the interaction between CNC and water insoluble compound was investigated; 3) a novel, universal, and cost-effective technique was developed to fabricate pesticide nano-dispersion using biobased CNC; 4) the current formulation is organic solvent- and surfactant-free, which greatly reduces environmental pollutions.

In Chapter 5, aminated cellulose aerogel beads were prepared by the injection of polyethylenimine (PEI) and 3-glycidyloxypropyl) trimethoxysilane (GPTMS) crosslinked CNF dispersion into liquid nitrogen, followed by freeze drying. Robust cellulose aerogel beads (CGP, diameter of 3~4

mm) with high amine content were produced for heavy metal ions (i.e., Cu^{2+}) removal. Both the amine content and mechanical strength were significantly increased when the mass ratio of PEI and GPTMS was between 1:1 to 3:1. The high amine content (5.74 mmol/g) of CGP3 beads displayed several desirable characteristics, such as large maximum Cu (II) adsorption capacity (163.40 mg/g), very fast adsorption rate (< 10 h to reach equilibrium), high shape recovery (2.00 % plastic deformation at 50% strain), robust mechanical strength (stress around 10.5 KPa at 50% strain), and they could be regenerated and reused.

The Cu (II) adsorption kinetic is driven by chemisorption, and both the amine and oxygen containing groups were involved in the chelation process. The intra-particle model revealed that the adsorption process is pore diffusion controlled. Thermodynamic study showed that the adsorption was more favorable at room temperature than at higher temperature. In addition, the pH of the mixture was altered during the adsorption in the PEI based absorbents, hence maintaining a constant pH is important to improve the adsorption capacity. Moreover, the resulting aerogel beads possessed excellent adsorption performance even in the presence of natural organic matter, which is very promising for wastewater treatment.

The major contributions of this chapter include: (1) a simple and scalable preparation method was developed to prepare cellulose aerogel with high amine content and high mechanical strength; (2) a new approach to prepare cellulose aerogel beads was developed; 3) the mechanical strength of small cellulose aerogel bead was precisely measured, and to our knowledge, this is the first reported study; (4) the adsorption performance between aerogel beads and monolith was compared, providing insights for the improvement of the adsorption rate.

In Chapter 6, a one-step protocol to prepare highly carboxylated and chemically crosslinked cellulose nanofibril (CNF) cryogel beads using maleic anhydride (MA) was developed. Conductometric-potentiometric titration results confirmed that 2.78 mmol/g carboxyl groups were present in the cryogel. A maximum compressive stress of 2800 Pa at 60% strain was observed when 2 wt% CNF was used to prepare the cryogel. The cryogel beads possessed Cu (II) adsorption of 82.17 mg/g at the optimized adsorption condition. The Cu (II) adsorption was a chemisorption process, where both carboxyl and hydroxyl groups participated in the complexation. The intra-particle model revealed that the adsorption process was also affected by pore diffusion. Overall, the prepared CNF-MA cryogel beads are promising absorbents for heavy metals removal due to

its fast removal rate, robust mechanical strength as well as excellent recyclability. In addition, organic solvent and catalyst were not required.

The major contributions of this chapter include: (1) a straightforward one-step reaction was developed for preparing chemically crosslinked carboxylated cellulose aerogel beads; (2) no toxic organic solvent and catalyst (e.g., DMF, DMSO and Pyridine) were used in the reaction; (3) Instead of using week acid solutions (e.g., citric acid, oxalic acid, maleic acid, etc.) to prepare carboxylated CNF, we used molten acid anhydride as the solvent and at higher temperature (120 ℃) to improve the esterification efficiency and to avoid further hydrolysis as minimal water was present in the reaction mixture;

In Chapter 7, ambient amphiphilic cellulose aerogels were prepared by crosslinking cellulose nanofibrils (CNF) with dicarboxylated-PEGs of different lengths. The crosslinking activity decreased with increasing crosslinker length due to steric hindrance. Both crosslinking degree and network density contributed to the mechanical strength of the aerogel. The as prepared aerogels possessed amphiphilic property that could uptake solvents of a wide range of polarities (from 0.1 to 10.2). They also exhibited underwater super-oleophobic property, which allowed the aerogels to release the absorbed oils into water. Such amphiphilic aerogels were effective for both oil-in-water and water-in-oil emulsion separation. The separation efficiency for oil-in-water emulsions is a combination effect of size sieving and electrostatic interaction between oil droplets and the negatively charged aerogel. For water-in-oil emulsions, the viscosity of the oil had a significant effect on the permeate flux. Overall, the aerogels are very promising for oil spill cleanup and recovery, for self-cleaning, and for multiple emulsion separation applications.

In another application, the water absorption capacity of CPM 600 H aerogel was compared with soil and other types of absorbents. The aerogel could promote seed germination and seedling growth by retaining water and nutrients in its network during irrigation.

The major contributions of this chapter include: (1) the effect of crosslinker length on its crosslinking capacity and the mechanical strength of the resulted aerogel was investigated, which has not been reported for cellulose based aerogel; (2) a new type of ambient super amphiphilic cellulose aerogel was developed for both emulsified oil-in-water and water-in-oil emulsion separation, which has not been reported for cellulose aerogels; (3) the as prepared aerogel showed potential for oily waste water, oil purification, oil spill cleanup, and self-cleaning applications; (4)

the application of cellulose aerogel as water and nutrients retention platform for promoting seed germination and seedling growth was first reported.

8.2 Recommendations for future studies

In summary, the thesis focused on reducing environmental pollution firstly by the development of novel pesticide formulation using sustainable cellulose nanomaterials, and cellulose nanomaterial-based absorbent and filters for wastewater treatment. Beyond a better understanding of the property and application of CNs, the results obtained in the research work also inspire us to explore this subject further in future. The recommendations are suggested below:

In Chapter 3, the packing behavior of end-modified CNC on oil/ water interface, i.e., standing upright or along with its backbone axis or in between, could be investigated and discussed. Besides, a comparison between the stability as well as the pest control efficacy of the resulting Pickering emulsions and a diluted commercial emulsified concentrate could be performed. To formulate a more stable and non-creaming Pickering emulsion, the addition of salts or other commercial thickeners could be effective strategies.

In Chapter 4, the loading capacity of CNC for more types of pesticides can be examined, along with a conclusion describing its relationship with the intrinsic property of the pesticides. The stability of the nano-dispersion, on whether the pesticide can be released from CNC during storage, should be investigated. It could provide a better understanding on the overall performance of the nano-dispersion. A powder form product can be considered for long term storage. Furthermore, an environmentally-responsive system that responds to temperature, UV, etc. can be designed by decorating responsive moieties such as poly(N-isopropylacrylamide) (PNIPAAm), azobenzene, on the CNC before or after loading the pesticides.

In Chapter 5 and 6 that describe the preparation of aerogel beads, a microfluidic device can be adopted for large scale production of uniform beads. A comparative study of the size effect on the adsorption capacity should be performed. In terms of applications, these beads can also be loaded in a column to conduct filtration studies, where the adsorption performance of the aerogel beads in wastewater can also be studied.

There are some inspirations from Chapter 7: cellulose aerogels could recover nutrients (e.g., Cu^{2+}, PO_4^{3-}, NH_4^{+}) from wastewater, and further applied as water retention absorbent and fertilizers delivery platform for promoting plant growth.

The challenges that still exist in water treatment despite the fact that many absorbents have been developed. Some of the challenges are listed below:

1) Complexity of wastewater. In research papers, usually one type or two types of pollutants were studied. However, various types of pollutants may coexist in the wastewater, which could impact the performance of the absorbents.
2) Poor stability of absorbents. The wastewater could be in acidic or alkaline condition, leading to the breakdown of the absorbents that have poor mechanical strength.
3) Poor efficiency. In research papers, adsorption study is widely used to evaluate the performance of absorbents, which could take more than 10 hours to reach the equilibrium. In practice, such method is not efficient to treat large volume of wastewater. Therefore, future research may focus more on absorbents that can be used in filtration.
4) Secondary contamination. In many studies, the post- treatment for absorbents/ adsorbents contain pollutants was not mentioned. This corresponds to moving the pollutants from one place to another, causing secondary contamination. More advanced systems are desired to collect and degrade pollutants in a single process.

References

(1) Zhao, X.; Cui, H.; Wang, Y.; Sun, C.; Cui, B.; Zeng, Z. Development Strategies and Prospects of Nano-Based Smart Pesticide Formulation. *J. Agric. Food Chem.* **2018**, *66* (26), 6504–6512. https://doi.org/10.1021/acs.jafc.7b02004.

(2) Wang, Y.; Wang, A.; Wang, C.; Cui, B.; Sun, C.; Zhao, X.; Zeng, Z.; Shen, Y.; Gao, F.; Liu, G.; et al. Synthesis and Characterization of Emamectin-Benzoate Slow-Release Microspheres with Different Surfactants. *Sci. Rep.* **2017**, *7* (1), 1–9. https://doi.org/10.1038/s41598-017-12724-6.

(3) Zhang, H.; Qin, H.; Li, L.; Zhou, X.; Wang, W.; Kan, C. Preparation and Characterization of Controlled-Release Avermectin/Castor Oil-Based Polyurethane Nanoemulsions. *J. Agric. Food Chem.* **2018**, *66* (26), 6552–6560. https://doi.org/10.1021/acs.jafc.7b01401.

(4) Li, Y.; Zhou, M.; Pang, Y.; Qiu, X. Lignin-Based Microsphere: Preparation and Performance on Encapsulating the Pesticide Avermectin. *ACS Sustain. Chem. Eng.* **2017**, *5* (4), 3321–3328. https://doi.org/10.1021/acssuschemeng.6b03180.

(5) Li, Y.; Yang, D.; Lu, S.; Lao, S.; Qiu, X. Modified Lignin with Anionic Surfactant and Its Application in Controlled Release of Avermectin. *J. Agric. Food Chem.* **2018**, *66* (13), 3457–3464. https://doi.org/10.1021/acs.jafc.8b00393.

(6) Liang, J.; Yu, M.; Guo, L.; Cui, B.; Zhao, X.; Sun, C.; Wang, Y.; Liu, G.; Cui, H.; Zeng, Z. Bioinspired Development of P(St-MAA)-Avermectin Nanoparticles with High Affinity for Foliage to Enhance Folia Retention. *J. Agric. Food Chem.* **2018**, *66* (26), 6578–6584. https://doi.org/10.1021/acs.jafc.7b01998.

(7) Nuruzzaman, M.; Rahman, M. M.; Liu, Y.; Naidu, R. Nanoencapsulation, Nano-Guard for Pesticides: A New Window for Safe Application. *J. Agric. Food Chem.* **2016**, *64* (7), 1447–1483. https://doi.org/10.1021/acs.jafc.5b05214.

(8) Lowry, G. V.; Avellan, A.; Gilbertson, L. M. Opportunities and Challenges for Nanotechnology in the Agri-Tech Revolution. *Nat. Nanotechnol.* **2019**, *14* (6), 517–522. https://doi.org/10.1038/s41565-019-0461-7.

(9) Martin, E.; Lalley, J.; Wang, W.; Nadagouda, M. N.; Sahle-Demessie, E.; Chae, S. R. Phosphate Recovery from Water Using Cellulose Enhanced Magnesium Carbonate Pellets: Kinetics, Isotherms, and Desorption. *Chem. Eng. J.* **2018**, *352* (June), 612–624. https://doi.org/10.1016/j.cej.2018.06.183.

(10) D6699a6dc01ad1edaa04efd755fcde03d5887e19 @ Www.Fao.Org.

(11) Zhang, W.; Liu, N.; Cao, Y.; Lin, X.; Liu, Y.; Feng, L. Superwetting Porous Materials for Wastewater Treatment: From Immiscible Oil/Water Mixture to Emulsion Separation. *Adv. Mater. Interfaces* **2017**, *4* (10). https://doi.org/10.1002/admi.201700029.

(12) Lv, W.; Mei, Q.; Xiao, J.; Du, M.; Zheng, Q. 3D Multiscale Superhydrophilic Sponges with Delicately Designed Pore Size for Ultrafast Oil/Water Separation. *Adv. Funct. Mater.* **2017**, *27* (48), 1704293. https://doi.org/https://doi.org/10.1002/adfm.201704293.

(13) Ahmad, M.; Rajapaksha, A. U.; Lim, J. E.; Zhang, M.; Bolan, N.; Mohan, D.; Vithanage, M.; Lee, S. S.; Ok, Y. S. Biochar as a Sorbent for Contaminant Management in Soil and Water: A Review. *Chemosphere* **2014**, *99*, 19–33.

https://doi.org/10.1016/j.chemosphere.2013.10.071.

(14) Fahmy, T. Y. A.; Fahmy, Y.; Mobarak, F.; El-Sakhawy, M.; Abou-Zeid, R. E. Biomass Pyrolysis: Past, Present, and Future. *Environ. Dev. Sustain.* **2020**, *22* (1), 17–32. https://doi.org/10.1007/s10668-018-0200-5.

(15) Rajinipriya, M.; Nagalakshmaiah, M.; Robert, M.; Elkoun, S. Importance of Agricultural and Industrial Waste in the Field of Nanocellulose and Recent Industrial Developments of Wood Based Nanocellulose: A Review. *ACS Sustain. Chem. Eng.* **2018**, *6* (3), 2807–2828. https://doi.org/10.1021/acssuschemeng.7b03437.

(16) García, A.; Gandini, A.; Labidi, J.; Belgacem, N.; Bras, J. Industrial and Crop Wastes: A New Source for Nanocellulose Biorefinery. *Ind. Crops Prod.* **2016**, *93*, 26–38. https://doi.org/10.1016/j.indcrop.2016.06.004.

(17) Mishra, S.; Kharkar, P. S.; Pethe, A. M. Biomass and Waste Materials as Potential Sources of Nanocrystalline Cellulose: Comparative Review of Preparation Methods (2016 – Till Date). *Carbohydr. Polym.* **2019**, *207* (November 2018), 418–427. https://doi.org/10.1016/j.carbpol.2018.12.004.

(18) Foster, E. J.; Moon, R. J.; Agarwal, U. P.; Bortner, M. J.; Bras, J.; Camarero-Espinosa, S.; Chan, K. J.; Clift, M. J. D.; Cranston, E. D.; Eichhorn, S. J.; et al. Current Characterization Methods for Cellulose Nanomaterials. *Chem. Soc. Rev.* **2018**, *47* (8), 2609–2679. https://doi.org/10.1039/c6cs00895j.

(19) Moon, R. J.; Martini, A.; Nairn, J.; Simonsen, J.; Youngblood, J. Cellulose Nanomaterials Review: Structure, Properties and Nanocomposites. *Chem. Soc. Rev.* **2011**, *40* (7), 3941–3994. https://doi.org/10.1039/C0CS00108B.

(20) Trache, D.; Hussin, M. H.; Haafiz, M. K. M.; Thakur, V. K. Recent Progress in Cellulose Nanocrystals: Sources and Production. *Nanoscale* **2017**, *9* (5), 1763–1786. https://doi.org/10.1039/c6nr09494e.

(21) Moon, R. J.; Martini, A.; Nairn, J.; Simonsen, J.; Youngblood, J. *Cellulose Nanomaterials Review: Structure, Properties and Nanocomposites*; 2011; Vol. 40. https://doi.org/10.1039/c0cs00108b.

(22) Elazzouzi-Hafraoui, S.; Nishiyama, Y.; Putaux, J.-L.; Heux, L.; Dubreuil, F.; Rochas, C. The Shape and Size Distribution of Crystalline Nanoparticles Prepared by Acid Hydrolysis of Native Cellulose. *Biomacromolecules* **2008**, *9* (1), 57–65. https://doi.org/10.1021/bm700769p.

(23) Zimmermann, T.; Pöhler, E.; Geiger, T. Cellulose Fibrils for Polymer Reinforcement. *Adv. Eng. Mater.* **2004**, *6* (9), 754–761.

(24) Isogai, A.; Saito, T.; Fukuzumi, H. TEMPO-Oxidized Cellulose Nanofibers. *Nanoscale* **2011**, *3* (1), 71–85.

(25) Nechyporchuk, O.; Belgacem, M. N.; Bras, J. Production of Cellulose Nanofibrils: A Review of Recent Advances. *Ind. Crops Prod.* **2016**, *93*, 2–25. https://doi.org/10.1016/j.indcrop.2016.02.016.

(26) Moon, R. J.; Martini, A.; Nairn, J.; Simonsen, J.; Youngblood, J. *Cellulose Nanomaterials Review: Structure, Properties and Nanocomposites*; 2011; Vol. 40. https://doi.org/10.1039/c0cs00108b.

(27) Postek, M. T.; Vladár, A.; Dagata, J.; Farkas, N.; Ming, B.; Wagner, R.; Raman, A.; Moon, R. J.; Sabo, R.; Wegner, T. H. Development of the Metrology and Imaging of Cellulose

Nanocrystals. *Meas. Sci. Technol.* **2010**, *22* (2), 24005.

(28) Mohammed, N.; Grishkewich, N.; Tam, K. C. Cellulose Nanomaterials: Promising Sustainable Nanomaterials for Application in Water/Wastewater Treatment Processes. *Environ. Sci. Nano* **2018**, *5* (3), 623–658. https://doi.org/10.1039/c7en01029j.

(29) Heise, K.; Delepierre, G.; King, A. W. T.; Kostiainen, M. A.; Zoppe, J.; Weder, C.; Kontturi, E. Chemical Modification of Reducing End-Groups in Cellulose Nanocrystals. *Angew. Chemie - Int. Ed.* **2021**, *60* (1), 66–87. https://doi.org/10.1002/anie.202002433.

(30) Tao, H.; Lavoine, N.; Jiang, F.; Tang, J.; Lin, N. Reducing End Modification on Cellulose Nanocrystals: Strategy, Characterization, Applications and Challenges. *Nanoscale Horizons* **2020**, *5* (4), 607–627. https://doi.org/10.1039/d0nh00016g.

(31) Huang, J. L.; Li, C. J.; Gray, D. G. Cellulose Nanocrystals Incorporating Fluorescent Methylcoumarin Groups. *ACS Sustain. Chem. Eng.* **2013**, *1* (9), 1160–1164. https://doi.org/10.1021/sc400074e.

(32) Arcot, L. R.; Lundahl, M.; Rojas, O. J.; Laine, J. Asymmetric Cellulose Nanocrystals: Thiolation of Reducing End Groups via NHS–EDC Coupling. *Cellulose* **2014**, *21* (6), 4209–4218. https://doi.org/10.1007/s10570-014-0426-9.

(33) Villares, A.; Moreau, C.; Cathala, B. Star-like Supramolecular Complexes of Reducing-End-Functionalized Cellulose Nanocrystals. *ACS Omega* **2018**, *3* (11), 16203–16211. https://doi.org/10.1021/acsomega.8b02559.

(34) Zhao, X.; Chen, Z.; Lin, N.; Ma, J. Water Redispersion and Cytotoxicity of Reducing End-Modified Cellulose Nanocrystals by Grafting Long-Chain Poly(Ethylene Oxide). *Int. J. Biol. Macromol.* **2021**, *180*, 143–151. https://doi.org/10.1016/j.ijbiomac.2021.03.010.

(35) Heise, K.; Koso, T.; Pitkänen, L.; Potthast, A.; King, A. W. T.; Kostiainen, M. A.; Kontturi, E. Knoevenagel Condensation for Modifying the Reducing End Groups of Cellulose Nanocrystals. *ACS Macro Lett.* **2019**, *8* (12), 1642–1647. https://doi.org/10.1021/acsmacrolett.9b00838.

(36) Wu, J.; Ma, G.-H. Recent Studies of Pickering Emulsions: Particles Make the Difference. *Small* **2016**, *12* (34), 4633–4648. https://doi.org/10.1002/smll.201600877.

(37) Binks, B. P. Particles as Surfactants - Similarities and Differences. *Curr. Opin. Colloid Interface Sci.* **2002**, *7* (1–2), 21–41. https://doi.org/10.1016/S1359-0294(02)00008-0.

(38) Kalashnikova, I.; Bizot, H.; Cathala, B.; Capron, I. New Pickering Emulsions Stabilized by Bacterial Cellulose Nanocrystals. *Langmuir* **2011**, *27* (12), 7471–7479. https://doi.org/10.1021/la200971f.

(39) Kalashnikova, I.; Bizot, H.; Cathala, B.; Capron, I. Modulation of Cellulose Nanocrystals Amphiphilic Properties to Stabilize Oil/Water Interface. *Biomacromolecules* **2012**, *13* (1), 267–275. https://doi.org/10.1021/bm201599j.

(40) Cherhal, F.; Cousin, F.; Capron, I. Structural Description of the Interface of Pickering Emulsions Stabilized by Cellulose Nanocrystals. *Biomacromolecules* **2016**, *17* (2), 496–502. https://doi.org/10.1021/acs.biomac.5b01413.

(41) Du Le, H.; Loveday, S. M.; Singh, H.; Sarkar, A. Pickering Emulsions Stabilised by Hydrophobically Modified Cellulose Nanocrystals: Responsiveness to PH and Ionic Strength. *Food Hydrocoll.* **2020**, *99* (August 2019). https://doi.org/10.1016/j.foodhyd.2019.105344.

(42) Hiranphinyophat, S.; Asaumi, Y.; Fujii, S.; Iwasaki, Y. Surface Grafting Polyphosphoesters

on Cellulose Nanocrystals to Improve the Emulsification Efficacy. *Langmuir* **2019**, *35* (35), 11443–11451. https://doi.org/10.1021/acs.langmuir.9b01584.

(43) Seabra, A. B.; Bernardes, J. S.; Fávaro, W. J.; Paula, A. J.; Durán, N. Cellulose Nanocrystals as Carriers in Medicine and Their Toxicities: A Review. *Carbohydr. Polym.* **2018**, *181* (October 2017), 514–527. https://doi.org/10.1016/j.carbpol.2017.12.014.

(44) Wijaya, C. J.; Saputra, S. N.; Soetaredjo, F. E.; Putro, J. N.; Lin, C. X.; Kurniawan, A.; Ju, Y. H.; Ismadji, S. Cellulose Nanocrystals from Passion Fruit Peels Waste as Antibiotic Drug Carrier. *Carbohydr. Polym.* **2017**, *175*, 370–376. https://doi.org/10.1016/j.carbpol.2017.08.004.

(45) Sun, B.; Hou, Q.; He, Z.; Liu, Z.; Ni, Y. Cellulose Nanocrystals (CNC) as Carriers for a Spirooxazine Dye and Its Effect on Photochromic Efficiency. *Carbohydr. Polym.* **2014**, *111*, 419–424. https://doi.org/10.1016/j.carbpol.2014.03.051.

(46) Shi, Z.; Tang, J.; Chen, L.; Yan, C.; Tanvir, S.; Anderson, W. A.; Berry, R. M.; Tam, K. C. Enhanced Colloidal Stability and Antibacterial Performance of Silver Nanoparticles/Cellulose Nanocrystal Hybrids. *J. Mater. Chem. B* **2015**, *3* (4), 603–611. https://doi.org/10.1039/C4TB01647E.

(47) Jackson, J. K.; Letchford, K.; Wasserman, B. Z.; Ye, L.; Hamad, W. Y.; Burt, H. M. The Use of Nanocrystalline Cellulose for the Binding and Controlled Release of Drugs. *Int. J. Nanomedicine* **2011**, *6*, 321–330. https://doi.org/10.2147/ijn.s16749.

(48) Taheri, A.; Mohammadi, M. The Use of Cellulose Nanocrystals for Potential Application in Topical Delivery of Hydroquinone. *Chem. Biol. Drug Des.* **2015**, *86* (1), 882–886. https://doi.org/10.1111/cbdd.12466.

(49) Qing, W.; Wang, Y.; Wang, Y.; Zhao, D.; Liu, X.; Zhu, J. The Modified Nanocrystalline Cellulose for Hydrophobic Drug Delivery. *Appl. Surf. Sci.* **2016**, *366*, 404–409. https://doi.org/10.1016/j.apsusc.2016.01.133.

(50) Tang, C.; Wang, Y.; Long, Y.; An, X.; Shen, J.; Ni, Y. Anchoring 20(R)-Ginsenoside Rg3 onto Cellulose Nanocrystals to Increase the Hydroxyl Radical Scavenging Activity. *ACS Sustain. Chem. Eng.* **2017**, *5* (9). https://doi.org/10.1021/acssuschemeng.6b02996.

(51) Salimi, S.; Sotudeh-Gharebagh, R.; Zarghami, R.; Chan, S. Y.; Yuen, K. H. Production of Nanocellulose and Its Applications in Drug Delivery: A Critical Review. *ACS Sustain. Chem. Eng.* **2019**, *7* (19), 15800–15827. https://doi.org/10.1021/acssuschemeng.9b02744.

(52) Lin, N.; Dufresne, A. Nanocellulose in Biomedicine: Current Status and Future Prospect. *Eur. Polym. J.* **2014**, *59*, 302–325. https://doi.org/10.1016/j.eurpolymj.2014.07.025.

(53) Athanassiou, C. G.; Kavallieratos, N. G.; Benelli, G.; Losic, D.; Usha Rani, P.; Desneux, N. Nanoparticles for Pest Control: Current Status and Future Perspectives. *J. Pest Sci. (2004).* **2018**, *91* (1), 1–15. https://doi.org/10.1007/s10340-017-0898-0.

(54) Tang, C.; Wang, Y.; Long, Y.; An, X.; Shen, J.; Ni, Y. Anchoring 20(R)-Ginsenoside Rg3 onto Cellulose Nanocrystals to Increase the Hydroxyl Radical Scavenging Activity. *ACS Sustain. Chem. Eng.* **2017**, *5* (9), 7507–7513. https://doi.org/10.1021/acssuschemeng.6b02996.

(55) Sarlak, N.; Taherifar, A.; Salehi, F. Synthesis of Nanopesticides by Encapsulating Pesticide Nanoparticles Using Functionalized Carbon Nanotubes and Application of New Nanocomposite for Plant Disease Treatment. *J. Agric. Food Chem.* **2014**, *62* (21), 4833–4838. https://doi.org/10.1021/jf404720d.

(56) Nörnberg, A. B.; Gehrke, V. R.; Mota, H. P.; Camargo, E. R.; Fajardo, A. R. Alginate-Cellulose Biopolymeric Beads as Efficient Vehicles for Encapsulation and Slow-Release of Herbicide. *Colloids Surfaces A Physicochem. Eng. Asp.* **2019**, *583* (August), 123970. https://doi.org/10.1016/j.colsurfa.2019.123970.

(57) Alonso-Díaz, A.; Floriach-Clark, J.; Fuentes, J.; Capellades, M.; Coll, N. S.; Laromaine, A. Enhancing Localized Pesticide Action through Plant Foliage by Silver-Cellulose Hybrid Patches. *ACS Biomater. Sci. Eng.* **2019**, *5* (2), 413–419. https://doi.org/10.1021/acsbiomaterials.8b01171.

(58) Tang, C.; Li, Y.; Pun, J.; Mohamed Osman, A. S.; Tam, K. C. Polydopamine Microcapsules from Cellulose Nanocrystal Stabilized Pickering Emulsions for Essential Oil and Pesticide Encapsulation. *Colloids Surfaces A Physicochem. Eng. Asp.* **2019**, *570*. https://doi.org/10.1016/j.colsurfa.2019.03.049.

(59) Tang, C.; Spinney, S.; Shi, Z.; Tang, J.; Peng, B.; Luo, J.; Tam, K. C. Amphiphilic Cellulose Nanocrystals for Enhanced Pickering Emulsion Stabilization. *Langmuir* **2018**, *34* (43). https://doi.org/10.1021/acs.langmuir.8b02437.

(60) Mossa, A. T. H. Green Pesticides: Essential Oils as Biopesticides in Insect-Pest Management. *J. Environ. Sci. Technol.* **2016**, *9* (5), 354–378. https://doi.org/10.3923/jest.2016.354.378.

(61) Shin, J.; Na, K.; Shin, S.; Seo, S. M.; Youn, H. J.; Park, I. K.; Hyun, J. Biological Activity of Thyme White Essential Oil Stabilized by Cellulose Nanocrystals. *Biomolecules* **2019**, *9* (12), 1–13. https://doi.org/10.3390/biom9120799.

(62) Mikulcová, V.; Bordes, R.; Kašpárková, V. On the Preparation and Antibacterial Activity of Emulsions Stabilized with Nanocellulose Particles. *Food Hydrocoll.* **2016**, *61*, 780–792. https://doi.org/10.1016/j.foodhyd.2016.06.031.

(63) Tang, C.; Li, Y.; Pun, J.; Sameh, A.; Osman, M.; Tam, K. C. Polydopamine Microcapsules from Cellulose Nanocrystal Stabilized Pickering Emulsions for Essential Oil and Pesticide Encapsulation. *Colloids Surfaces A* **2019**, *570* (March), 403–413. https://doi.org/10.1016/j.colsurfa.2019.03.049.

(64) Kadam, S. L.; Yadav, P.; Bhutkar, S.; Patil, V. D.; Shukla, P. G.; Shanmuganathan, K. Sustained Release Insect Repellent Microcapsules Using Modified Cellulose Nanofibers (MCNF) as Pickering Emulsifier. *Colloids Surfaces A Physicochem. Eng. Asp.* **2019**, *582* (August), 123883. https://doi.org/10.1016/j.colsurfa.2019.123883.

(65) Elabasy, A.; Shoaib, A.; Waqas, M.; Shi, Z.; Jiang, M. Cellulose Nanocrystals Loaded with Thiamethoxam: Fabrication, Characterization, and Evaluation of Insecticidal Activity against Phenacoccus Solenopsis Tinsley (Hemiptera: Pseudococcidae). *Nanomaterials* **2020**, *10* (4), 5–7. https://doi.org/10.3390/nano10040788.

(66) Xiang, S.; Ma, X.; Liao, S.; Shi, H.; Liu, C.; Shen, Y.; Lv, X.; Yuan, M.; Fan, G.; Huang, J.; et al. Cellulose Nanocrystal Surface Cationization: A New Fungicide with High Activity against Phycomycetes Capsici. *Molecules* **2019**, *24* (13). https://doi.org/10.3390/molecules24132467.

(67) Pang, L.; Gao, Z.; Zhang, S.; Li, Y.; Hu, S.; Ren, X. Preparation and Anti-UV Property of Modified Cellulose Membranes for Biopesticides Controlled Release. *Ind. Crops Prod.* **2016**, *89*, 176–181. https://doi.org/10.1016/j.indcrop.2016.05.014.

(68) Patil, M. D.; Patil, V. D.; Sapre, A. A.; Ambone, T. S.; Torris, A. T.; Shukla, P. G.; Shanmuganathan, K. Tuning Controlled Release Behavior of Starch Granules Using

Nanofibrillated Cellulose Derived from Waste Sugarcane Bagasse. *ACS Sustain. Chem. Eng.* **2018**, *6* (7), 9208–9217. https://doi.org/10.1021/acssuschemeng.8b01545.

(69) Mattos, B. D.; Magalhães, W. L. E. Biogenic Nanosilica Blended by Nanofibrillated Cellulose as Support for Slow-Release of Tebuconazole. *J. Nanoparticle Res.* **2016**, *18* (9). https://doi.org/10.1007/s11051-016-3586-8.

(70) Zhao, S.; Malfait, W. J.; Guerrero-Alburquerque, N.; Koebel, M. M.; Nyström, G. Biopolymer Aerogels and Foams: Chemistry, Properties, and Applications. *Angew. Chemie - Int. Ed.* **2018**, *57* (26), 7580–7608. https://doi.org/10.1002/anie.201709014.

(71) Ahankari, S.; Paliwal, P.; Subhedar, A.; Kargarzadeh, H. Recent Developments in Nanocellulose-Based Aerogels in Thermal Applications: A Review. *ACS Nano* **2021**. https://doi.org/10.1021/acsnano.0c09678.

(72) Zheng, Q.; Cai, Z.; Gong, S. Green Synthesis of Polyvinyl Alcohol (PVA)–Cellulose Nanofibril (CNF) Hybrid Aerogels and Their Use as Superabsorbents. *J. Mater. Chem. A* **2014**, *2* (9), 3110–3118.

(73) Lewis, L.; Hatzikiriakos, S. G.; Hamad, W. Y.; Maclachlan, M. J. Freeze-Thaw Gelation of Cellulose Nanocrystals. *ACS Macro Lett.* **2019**, 486–491. https://doi.org/10.1021/acsmacrolett.9b00140.

(74) Dong, H.; Snyder, J. F.; Williams, K. S.; Andzelm, J. W. Cation-Induced Hydrogels of Cellulose Nanofibrils with Tunable Moduli. *Biomacromolecules* **2013**, *14* (9), 3338–3345. https://doi.org/10.1021/bm400993f.

(75) Li, Y.; Grishkewich, N.; Liu, L.; Wang, C.; Tam, K. C.; Liu, S.; Mao, Z.; Sui, X. Construction of Functional Cellulose Aerogels via Atmospheric Drying Chemically Cross-Linked and Solvent Exchanged Cellulose Nanofibrils. *Chem. Eng. J.* **2019**, *366* (January), 531–538. https://doi.org/10.1016/j.cej.2019.02.111.

(76) Ebrahimi, A.; Dahrazma, B.; Adelifard, M. Facile and Novel Ambient Pressure Drying Approach to Synthesis and Physical Characterization of Cellulose-Based Aerogels. *J. Porous Mater.* **2020**, *27* (4), 1219–1232. https://doi.org/10.1007/s10934-020-00901-4.

(77) Toivonen, M. S.; Kaskela, A.; Rojas, O. J.; Kauppinen, E. I.; Ikkala, O. Ambient-Dried Cellulose Nanofibril Aerogel Membranes with High Tensile Strength and Their Use for Aerosol Collection and Templates for Transparent, Flexible Devices. *Adv. Funct. Mater.* **2015**, *25* (42), 6618–6626. https://doi.org/10.1002/adfm.201502566.

(78) Sakai, K.; Kobayashi, Y.; Saito, T.; Isogai, A. Partitioned Airs at Microscale and Nanoscale: Thermal Diffusivity in Ultrahigh Porosity Solids of Nanocellulose. *Sci. Rep.* **2016**, *6* (1), 20434. https://doi.org/10.1038/srep20434.

(79) Voon, L. K.; Pang, S. C.; Chin, S. F. Highly Porous Cellulose Beads of Controllable Sizes Derived from Regenerated Cellulose of Printed Paper Wastes. *Mater. Lett.* **2015**, *164*, 264–266. https://doi.org/10.1016/j.matlet.2015.10.161.

(80) Long, L. Y.; Weng, Y. X.; Wang, Y. Z. Cellulose Aerogels: Synthesis, Applications, and Prospects. *Polymers (Basel).* **2018**, *8* (6), 1–28. https://doi.org/10.3390/polym10060623.

(81) Jiang, F.; Hsieh, Y.-L. Super Water Absorbing and Shape Memory Nanocellulose Aerogels from TEMPO-Oxidized Cellulose Nanofibrils via Cyclic Freezing–Thawing. *J. Mater. Chem. A* **2014**, *2* (2), 350–359. https://doi.org/10.1039/C3TA13629A.

(82) Chen, Y.; Fan, D.; Lyu, S.; Li, G.; Jiang, F.; Wang, S. Elasticity-Enhanced and Aligned Structure Nanocellulose Foam-like Aerogel Assembled with Cooperation of Chemical Art

and Gradient Freezing. *ACS Sustain. Chem. Eng.* **2019**, *7* (1), 1381–1388. https://doi.org/10.1021/acssuschemeng.8b05085.

(83) Pan, Z. Z.; Nishihara, H.; Iwamura, S.; Sekiguchi, T.; Sato, A.; Isogai, A.; Kang, F.; Kyotani, T.; Yang, Q. H. Cellulose Nanofiber as a Distinct Structure-Directing Agent for Xylem-like Microhoneycomb Monoliths by Unidirectional Freeze-Drying. *ACS Nano* **2016**, *10* (12), 10689–10697. https://doi.org/10.1021/acsnano.6b05808.

(84) Wang, C.; Chen, X.; Wang, B.; Huang, M.; Wang, B.; Jiang, Y.; Ruoff, R. S. Freeze-Casting Produces a Graphene Oxide Aerogel with a Radial and Centrosymmetric Structure. *ACS Nano* **2018**, *12* (6), 5816–5825. https://doi.org/10.1021/acsnano.8b01747.

(85) Zhang, X.; Zhao, X.; Xue, T.; Yang, F.; Fan, W.; Liu, T. Bidirectional Anisotropic Polyimide/Bacterial Cellulose Aerogels by Freeze-Drying for Super-Thermal Insulation. *Chem. Eng. J.* **2020**, *385* (September 2019), 123963. https://doi.org/10.1016/j.cej.2019.123963.

(86) Jiménez-Saelices, C.; Seantier, B.; Grohens, Y.; Capron, I. Thermal Superinsulating Materials Made from Nanofibrillated Cellulose-Stabilized Pickering Emulsions. *ACS Appl. Mater. Interfaces* **2018**, *10* (18), 16193–16202. https://doi.org/10.1021/acsami.8b02418.

(87) Li, S.; Zhou, C.; He, Y.; Liu, H.; Zhou, L.; Yu, C.; Wei, C.; Wang, C. Novel Nanocellulose/Polymer Composite Aerogel as Solid-State Fluorescence Probe by Pickering Emulsion Route. *Macromol. Mater. Eng.* **2020**, *305* (11), 1–9. https://doi.org/10.1002/mame.202000467.

(88) Cervin, N. T.; Andersson, L.; Ng, J. B. S.; Olin, P.; Bergström, L.; Waìšgberg, L. Lightweight and Strong Cellulose Materials Made from Aqueous Foams Stabilized by Nanofibrillated Cellulose. *Biomacromolecules* **2013**, *14* (2), 503–511. https://doi.org/10.1021/bm301755u.

(89) Cervin, N. T.; Johansson, E.; Benjamins, J. W.; Wågberg, L. Mechanisms behind the Stabilizing Action of Cellulose Nanofibrils in Wet-Stable Cellulose Foams. *Biomacromolecules* **2015**, *16* (3), 822–831. https://doi.org/10.1021/bm5017173.

(90) Cervin, N. T.; Johansson, E.; Larsson, P. A.; Wågberg, L. Strong, Water-Durable, and Wet-Resilient Cellulose Nanofibril-Stabilized Foams from Oven Drying. *ACS Appl. Mater. Interfaces* **2016**, *8* (18), 11682–11689. https://doi.org/10.1021/acsami.6b00924.

(91) Li, Y.; Xiao, H.; Pan, Y.; Wang, L. Novel Composite Adsorbent Consisting of Dissolved Cellulose Fiber/Microfibrillated Cellulose for Dye Removal from Aqueous Solution. *ACS Sustain. Chem. Eng.* **2018**, *6* (5), 6994–7002. https://doi.org/10.1021/acssuschemeng.8b00829.

(92) Cai, H.; Sharma, S.; Liu, W.; Mu, W.; Liu, W.; Zhang, X.; Deng, Y. Aerogel Microspheres from Natural Cellulose Nanofibrils and Their Application as Cell Culture Scaffold. *Biomacromolecules* **2014**, *15* (7), 2540–2547. https://doi.org/10.1021/bm5003976.

(93) Blachechen, L. S.; Fardim, P.; Petri, D. F. S. Multifunctional Cellulose Beads and Their Interaction with Gram Positive Bacteria. *Biomacromolecules* **2014**, *15* (9), 3440–3448. https://doi.org/10.1021/bm5009876.

(94) Guo, D. M.; An, Q. Da; Xiao, Z. Y.; Zhai, S. R.; Shi, Z. Polyethylenimine-Functionalized Cellulose Aerogel Beads for Efficient Dynamic Removal of Chromium(VI) from Aqueous Solution. *RSC Adv.* **2017**, *7* (85), 54039–54052. https://doi.org/10.1039/c7ra09940a.

(95) Levin, D.; Saem, S.; Osorio, D. A.; Cerf, A.; Cranston, E. D.; Moran-Mirabal, J. M. Green Templating of Ultraporous Cross-Linked Cellulose Nanocrystal Microparticles. *Chem.*

Mater. **2018**, *30* (21), 8040–8051. https://doi.org/10.1021/acs.chemmater.8b03858.

(96) Druel, L.; Kenkel, A.; Baudron, V.; Buwalda, S.; Budtova, T. Cellulose Aerogel Microparticles via Emulsion-Coagulation Technique. *Biomacromolecules* **2020**, *21* (5), 1824–1831. https://doi.org/10.1021/acs.biomac.9b01725.

(97) Carpenter, A. W.; De Lannoy, C. F.; Wiesner, M. R. Cellulose Nanomaterials in Water Treatment Technologies. *Environ. Sci. Technol.* **2015**, *49* (9), 5277–5287. https://doi.org/10.1021/es506351r.

(98) Liu, H.; Geng, B.; Chen, Y.; Wang, H. Review on the Aerogel-Type Oil Sorbents Derived from Nanocellulose. *ACS Sustain. Chem. Eng.* **2017**, *5* (1), 49–66. https://doi.org/10.1021/acssuschemeng.6b02301.

(99) Abouzeid, R. E.; Khiari, R.; El-Wakil, N.; Dufresne, A. Current State and New Trends in the Use of Cellulose Nanomaterials for Wastewater Treatment. *Biomacromolecules* **2019**, *20* (2), 573–597. https://doi.org/10.1021/acs.biomac.8b00839.

(100) Mohammed, N.; Grishkewich, N.; Tam, K. C. Cellulose Nanomaterials: Promising Sustainable Nanomaterials for Application in Water/Wastewater Treatment Processes. *Environ. Sci. Nano* **2018**, *5* (3), 623–658. https://doi.org/10.1039/c7en01029j.

(101) Choudhury, R. R.; Sahoo, S. K.; Gohil, J. M. Potential of Bioinspired Cellulose Nanomaterials and Nanocomposite Membranes Thereof for Water Treatment and Fuel Cell Applications. *Cellulose* **2020**, *27* (12), 6719–6746. https://doi.org/10.1007/s10570-020-03253-z.

(102) Mautner, A. Nanocellulose Water Treatment Membranes and Filters: A Review. *Polym. Int.* **2020**, *69* (9), 741–751. https://doi.org/10.1002/pi.5993.

(103) Chen, Y.; Zhang, L.; Yang, Y.; Pang, B.; Xu, W.; Duan, G.; Jiang, S.; Zhang, K. Recent Progress on Nanocellulose Aerogels: Preparation, Modification, Composite Fabrication, Applications. *Adv. Mater.* **2021**, *33* (11), 2005569. https://doi.org/https://doi.org/10.1002/adma.202005569.

(104) Jiang, F.; Dinh, D. M.; Hsieh, Y. Lo. Adsorption and Desorption of Cationic Malachite Green Dye on Cellulose Nanofibril Aerogels. *Carbohydr. Polym.* **2017**, *173*, 286–294. https://doi.org/10.1016/j.carbpol.2017.05.097.

(105) Zhang, J.; Zhang, X.; Tian, Y.; Zhong, T.; Liu, F. Novel and Wet-Resilient Cellulose Nanofiber Cryogels with Tunable Porosity and Improved Mechanical Strength for Methyl Orange Dyes Removal. *J. Hazard. Mater.* **2021**, *416* (March), 125897. https://doi.org/10.1016/j.jhazmat.2021.125897.

(106) Lyu, W.; Li, J.; Zheng, L.; Liu, H.; Chen, J.; Zhang, W.; Liao, Y. Fabrication of 3D Compressible Polyaniline/Cellulose Nanofiber Aerogel for Highly Efficient Removal of Organic Pollutants and Its Environmental-Friendly Regeneration by Peroxydisulfate Process. *Chem. Eng. J.* **2021**, *414* (February), 128931. https://doi.org/10.1016/j.cej.2021.128931.

(107) Wang, Z.; Song, L.; Wang, Y.; Zhang, X. F.; Hao, D.; Feng, Y.; Yao, J. Lightweight UiO-66/Cellulose Aerogels Constructed through Self-Crosslinking Strategy for Adsorption Applications. *Chem. Eng. J.* **2019**, *371* (April), 138–144. https://doi.org/10.1016/j.cej.2019.04.022.

(108) Zhao, D.; Tian, Y.; Jing, X.; Lu, Y.; Zhu, G. PAF-1@cellulose Nanofibril Composite Aerogel for Highly-Efficient Removal of Bisphenol A. *J. Mater. Chem. A* **2019**, *7* (1), 157–164. https://doi.org/10.1039/c8ta09644a.

(109) Geng, B.; Wang, H.; Wu, S.; Ru, J.; Tong, C.; Chen, Y.; Liu, H.; Wu, S.; Liu, X. Surface-Tailored Nanocellulose Aerogels with Thiol-Functional Moieties for Highly Efficient and Selective Removal of Hg(II) Ions from Water. *ACS Sustain. Chem. Eng.* **2017**, *5* (12), 11715–11726. https://doi.org/10.1021/acssuschemeng.7b03188.

(110) Li, J.; Zuo, K.; Wu, W.; Xu, Z.; Yi, Y.; Jing, Y.; Dai, H.; Fang, G. Shape Memory Aerogels from Nanocellulose and Polyethyleneimine as a Novel Adsorbent for Removal of Cu(II) and Pb(II). *Carbohydr. Polym.* **2018**, *196* (April), 376–384. https://doi.org/10.1016/j.carbpol.2018.05.015.

(111) Hong, H. J.; Ban, G.; Kim, H. S.; Jeong, H. S.; Park, M. S. Fabrication of Cylindrical 3D Cellulose Nanofibril(CNF) Aerogel for Continuous Removal of Copper(Cu2+) from Wastewater. *Chemosphere* **2021**, *278*, 130288. https://doi.org/10.1016/j.chemosphere.2021.130288.

(112) Mo, L.; Pang, H.; Tan, Y.; Zhang, S.; Li, J. 3D Multi-Wall Perforated Nanocellulose-Based Polyethylenimine Aerogels for Ultrahigh Efficient and Reversible Removal of Cu(II) Ions from Water. *Chem. Eng. J.* **2019**, *378* (April), 122157. https://doi.org/10.1016/j.cej.2019.122157.

(113) Li, Y.; Guo, C.; Shi, R.; Zhang, H.; Gong, L.; Dai, L. Chitosan/ Nanofibrillated Cellulose Aerogel with Highly Oriented Microchannel Structure for Rapid Removal of Pb (II) Ions from Aqueous Solution. *Carbohydr. Polym.* **2019**, *223* (April), 115048. https://doi.org/10.1016/j.carbpol.2019.115048.

(114) He, X.; Cheng, L.; Wang, Y.; Zhao, J.; Zhang, W.; Lu, C. Aerogels from Quaternary Ammonium-Functionalized Cellulose Nanofibers for Rapid Removal of Cr(VI) from Water. *Carbohydr. Polym.* **2014**, *111*, 683–687. https://doi.org/10.1016/j.carbpol.2014.05.020.

(115) Liang, X.; Liang, B.; Wei, J.; Zhong, S.; Zhang, R.; Yin, Y.; Zhang, Y.; Hu, H.; Huang, Z. A Cellulose-Based Adsorbent with Pendant Groups of Quaternary Ammonium and Amino for Enhanced Capture of Aqueous Cr(VI). *Int. J. Biol. Macromol.* **2020**, *148*, 802–810. https://doi.org/10.1016/j.ijbiomac.2020.01.184.

(116) Zhao, J.; Zhang, X.; He, X.; Xiao, M.; Zhang, W.; Lu, C. A Super Biosorbent from Dendrimer Poly(Amidoamine)-Grafted Cellulose Nanofibril Aerogels for Effective Removal of Cr(Vi). *J. Mater. Chem. A* **2015**, *3* (28), 14703–14711. https://doi.org/10.1039/c5ta03089g.

(117) Lei, C.; Gao, J.; Ren, W.; Xie, Y.; Abdalkarim, S. Y. H.; Wang, S.; Ni, Q.; Yao, J. Fabrication of Metal-Organic Frameworks@cellulose Aerogels Composite Materials for Removal of Heavy Metal Ions in Water. *Carbohydr. Polym.* **2019**, *205* (May 2018), 35–41. https://doi.org/10.1016/j.carbpol.2018.10.029.

(118) Maatar, W.; Boufi, S. Poly(Methacylic Acid-Co-Maleic Acid) Grafted Nanofibrillated Cellulose as a Reusable Novel Heavy Metal Ions Adsorbent. *Carbohydr. Polym.* **2015**, *126*, 199–207. https://doi.org/10.1016/j.carbpol.2015.03.015.

(119) Tang, C.; Brodie, P.; Brunsting, M.; Tam, K. C. Carboxylated Cellulose Cryogel Beads via a One-Step Ester Crosslinking of Maleic Anhydride for Copper Ions Removal. *Carbohydr. Polym.* **2020**, *242* (February), 116397. https://doi.org/10.1016/j.carbpol.2020.116397.

(120) Tang, C.; Brodie, P.; Li, Y.; Grishkewich, N. J.; Brunsting, M.; Tam, K. C. Shape Recoverable and Mechanically Robust Cellulose Aerogel Beads for Efficient Removal of Copper Ions. *Chem. Eng. J.* **2020**, *392* (January), 124821. https://doi.org/10.1016/j.cej.2020.124821.

(121) Komal; Gupta, K.; Kumar, V.; Tikoo, K. B.; Kaushik, A.; Singhal, S. Encrustation of Cadmium Sulfide Nanoparticles into the Matrix of Biomass Derived Silanized Cellulose Nanofibers for Adsorptive Detoxification of Pesticide and Textile Waste. *Chemical Engineering Journal*. 2020. https://doi.org/10.1016/j.cej.2019.123700.

(122) Khalfaoui, M.; Ghali, A. El; Aguir, C.; Mohamed, Z.; Baouab, M. H. V.; Lamine, A. Ben. Study on Adsorption of Herbicide onto Functionalized Cellulose Extracted from Juncus Acutus L. Plant: Experimental Results and Theoretical Modeling. *Ind. Crops Prod.* **2015**, *67*, 169–178. https://doi.org/10.1016/j.indcrop.2015.01.032.

(123) Shang, Y.; Guo, K.; Jiang, P.; Xu, X.; Gao, B. Adsorption of Phosphate by the Cellulose-Based Biomaterial and Its Sustained Release of Laden Phosphate in Aqueous Solution and Soil. *Int. J. Biol. Macromol.* **2018**, *109*, 524–534. https://doi.org/10.1016/j.ijbiomac.2017.12.118.

(124) Wang, X.; Lü, S.; Gao, C.; Feng, C.; Xu, X.; Bai, X.; Gao, N.; Yang, J.; Liu, M.; Wu, L. Recovery of Ammonium and Phosphate from Wastewater by Wheat Straw-Based Amphoteric Adsorbent and Reusing as a Multifunctional Slow-Release Compound Fertilizer. *ACS Sustain. Chem. Eng.* **2016**, *4* (4), 2068–2079. https://doi.org/10.1021/acssuschemeng.5b01494.

(125) Rafieian, F.; Hosseini, M.; Jonoobi, M.; Yu, Q. Development of Hydrophobic Nanocellulose-Based Aerogel via Chemical Vapor Deposition for Oil Separation for Water Treatment. *Cellulose* **2018**, *25* (8), 4695–4710. https://doi.org/10.1007/s10570-018-1867-3.

(126) Zhou, L.; Xu, Z. Ultralight, Highly Compressible, Hydrophobic and Anisotropic Lamellar Carbon Aerogels from Graphene/Polyvinyl Alcohol/Cellulose Nanofiber Aerogel as Oil Removing Absorbents. *J. Hazard. Mater.* **2020**, *388*, 121804. https://doi.org/https://doi.org/10.1016/j.jhazmat.2019.121804.

(127) Fregolente, P. B. L.; Wolf Maciel, M. R.; Oliveira, L. S. Removal of Water Content from Biodiesel and Diesel Fuel Using Hydrogel Adsorbents. *Brazilian J. Chem. Eng.* **2015**, *32* (4), 895–901. https://doi.org/10.1590/0104-6632.20150324s20140142.

(128) Bogalhos, P.; Fregolente, L.; Fregolente, L. V.; Regina, M.; Maciel, W. Water Content in Biodiesel, Diesel, and Biodiesel − Diesel Blends. **2012**.

(129) Nemoto, J.; Saito, T.; Isogai, A. Simple Freeze-Drying Procedure for Producing Nanocellulose Aerogel-Containing, High-Performance Air Filters. *ACS Appl. Mater. Interfaces* **2015**, *7* (35), 19809–19815. https://doi.org/10.1021/acsami.5b05841.

(130) Chu, Z.; Feng, Y.; Seeger, S. Oil/Water Separation with Selective Superantiwetting/Superwetting Surface Materials. *Angew. Chemie - Int. Ed.* **2015**, *54* (8), 2328–2338. https://doi.org/10.1002/anie.201405785.

(131) Ajdary, R.; Tardy, B. L.; Mattos, B. D.; Bai, L.; Rojas, O. J. Plant Nanomaterials and Inspiration from Nature: Water Interactions and Hierarchically Structured Hydrogels. *Adv. Mater.* **2020**, *n/a* (n/a), 2001085. https://doi.org/https://doi.org/10.1002/adma.202001085.

(132) Wang, G.; He, Y.; Wang, H.; Zhang, L.; Yu, Q.; Peng, S.; Wu, X.; Ren, T.; Zeng, Z.; Xue, Q. A Cellulose Sponge with Robust Superhydrophilicity and Under-Water Superoleophobicity for Highly Effective Oil/Water Separation. *Green Chem.* **2015**, *17*, 3093. https://doi.org/10.1039/c5gc00025d.

(133) Yang, S.; Chen, L.; Liu, S.; Hou, W.; Zhu, J.; Zhao, P.; Zhang, Q. Facile and Sustainable Fabrication of High-Performance Cellulose Sponge from Cotton for Oil-in-Water Emulsion Separation. *J. Hazard. Mater.* **2021**, *408* (August 2020), 124408.

https://doi.org/10.1016/j.jhazmat.2020.124408.

(134) He, Z.; Zhang, X.; Batchelor, W. Cellulose Nanofibre Aerogel Filter with Tuneable Pore Structure for Oil/Water Separation and Recovery. *RSC Adv.* **2016**, *6* (26), 21435–21438. https://doi.org/10.1039/C5RA27413C.

(135) Sun, F.; Liu, W.; Dong, Z.; Journal, Y. D.-C. E.; 2017, undefined. Underwater Superoleophobicity Cellulose Nanofibril Aerogel through Regioselective Sulfonation for Oil/Water Separation. *Elsevier*.

(136) Li, Y.; Zhang, H.; Fan, M.; Zhuang, J.; Chen, L. A Robust Salt-Tolerant Superoleophobic Aerogel Inspired by Seaweed for Efficient Oil–Water Separation in Marine Environments. *Phys. Chem. Chem. Phys.* **2016**, *18* (36), 25394–25400. https://doi.org/10.1039/C6CP04284H.

(137) Zhang, H.; Li, Y.; Shi, R.; Chen, L.; Fan, M. A Robust Salt-Tolerant Superoleophobic Chitosan/Nanofibrillated Cellulose Aerogel for Highly Efficient Oil/Water Separation. *Carbohydr. Polym.* **2018**, *200* (July), 611–615. https://doi.org/10.1016/j.carbpol.2018.07.071.

(138) Zhou, S.; You, T.; Zhang, X.; Materials, F. X.-A. A. N.; 2018, undefined. Superhydrophobic Cellulose Nanofiber-Assembled Aerogels for Highly Efficient Water-in-Oil Emulsions Separation. *ACS Publ.*

(139) Li, Z.; Zhong, L.; Zhang, T.; Qiu, F.; Yue, X.; Yang, D. Sustainable, Flexible, and Superhydrophobic Functionalized Cellulose Aerogel for Selective and Versatile Oil/Water Separation. *ACS Publ.* **2019**, *7* (11), 9984–9994. https://doi.org/10.1021/acssuschemeng.9b01122.

(140) Li, Y.; Zhu, L.; Grishkewich, N.; Tam, K. C.; Yuan, J.; Mao, Z.; Sui, X. CO2-Responsive Cellulose Nanofibers Aerogels for Switchable Oil-Water Separation. *ACS Appl. Mater. Interfaces* **2019**, *11* (9), 9367–9373. https://doi.org/10.1021/acsami.8b22159.

(141) Li, Y.; Zhu, L.; Grishkewich, N.; … K. T.-… applied materials &; 2019, undefined. CO2-Responsive Cellulose Nanofibers Aerogels for Switchable Oil–Water Separation. *ACS Publ.*

(142) Li, L.; Rong, L.; Xu, Z.; Wang, B.; Feng, X.; Mao, Z.; … H. X.-C.; 2020, undefined. Cellulosic Sponges with PH Responsive Wettability for Efficient Oil-Water Separation. *Elsevier*.

(143) Jiao, B.; Shi, A.; Qiang, W.; Binks, B. High Internal Phase Pickering Emulsions Stabilized Solely by Peanut Protein Microgel Particles with Multiple Potential Applications. *Angew. Chemie Int. Ed.* **2018**, DOI: 10.1002/anie.201801350. https://doi.org/10.1002/anie.201801350.

(144) Binks, B. P.; Olusanya, S. O. Phase Inversion of Colored Pickering Emulsions Stabilized by Organic Pigment Particle Mixtures. *Langmuir* **2018**, *34* (17), 5040–5051. https://doi.org/10.1021/acs.langmuir.8b00715.

(145) Hu, Z.; Marway, H. S.; Kasem, H.; Pelton, R.; Cranston, E. D. Dried and Redispersible Cellulose Nanocrystal Pickering Emulsions. *ACS Macro Lett.* **2016**, *5* (2), 185–189. https://doi.org/10.1021/acsmacrolett.5b00919.

(146) Binks, B. P. Particles as Surfactants—Similarities and Differences. *Curr. Opin. Colloid Interface Sci.* **2002**, *7* (1–2), 21–41. https://doi.org/10.1016/S1359-0294(02)00008-0.

(147) Aveyard, R.; Binks, B. P.; Clint, J. H. Emulsions Stabilised Solely by Colloidal Particles. *Adv. Colloid Interface Sci.* **2003**, *100–102*, 503–546. https://doi.org/10.1016/S0001-

8686(02)00069-6.

(148) Chevalier, Y.; Bolzinger, M. A. Emulsions Stabilized with Solid Nanoparticles: Pickering Emulsions. *Colloids Surfaces A Physicochem. Eng. Asp.* **2013**, *439*, 23–34. https://doi.org/10.1016/j.colsurfa.2013.02.054.

(149) Wen, C.; Yuan, Q.; Liang, H.; Vriesekoop, F. Preparation and Stabilization of d -Limonene Pickering Emulsions by Cellulose Nanocrystals. *Carbohydr. Polym.* **2014**, *112*, 695–700. https://doi.org/10.1016/j.carbpol.2014.06.051.

(150) Binks, B. P.; Rodrigues, J. A. Double Inversion of Emulsions By Using Nanoparticles and a Di-Chain. **2007**, 5389–5392. https://doi.org/10.1002/anie.200700880.

(151) Bai, L.; Huan, S.; Xiang, W.; Rojas, O. J. Pickering Emulsions by Combining Cellulose Nanofibrils and Nanocrystals: Phase Behavior and Depletion Stabilization. *Green Chem.* **2018**, *20* (7), 1571–1582. https://doi.org/10.1039/c8gc00134k.

(152) Cherhal, F.; Cousin, F.; Capron, I. Structural Description of the Interface of Pickering Emulsions Stabilized by Cellulose Nanocrystals. *Biomacromolecules* **2016**, *17* (2), 496–502. https://doi.org/10.1021/acs.biomac.5b01413.

(153) Capron, I.; Rojas, O. J.; Bordes, R. Behavior of Nanocelluloses at Interfaces. *Curr. Opin. Colloid Interface Sci.* **2017**, *29*, 83–95. https://doi.org/10.1016/j.cocis.2017.04.001.

(154) Tang, J.; Quinlan, P. J.; Tam, K. C. Stimuli-Responsive Pickering Emulsions: Recent Advances and Potential Applications. *Soft Matter* **2015**, *11* (18), 3512–3529. https://doi.org/10.1039/C5SM00247H.

(155) Rayner, M.; Marku, D.; Eriksson, M.; Sjöö, M.; Dejmek, P.; Wahlgren, M. Biomass-Based Particles for the Formulation of Pickering Type Emulsions in Food and Topical Applications. *Colloids Surfaces A Physicochem. Eng. Asp.* **2014**. https://doi.org/10.1016/j.colsurfa.2014.03.053.

(156) Kalashnikova, I.; Bizot, H.; Cathala, B.; Capron, I. Modulation of Cellulose Nanocrystals Amphiphilic Properties to Stabilize Oil/Water Interface. *Biomacromolecules* **2012**, *13* (1), 267–275. https://doi.org/10.1021/bm201599j.

(157) Mattos, B. D.; Greca, L. G.; Tardy, B. L.; Magalhães, W. L. E.; Rojas, O. J. Green Formation of Robust Supraparticles for Cargo Protection and Hazards Control in Natural Environments. *Small* **2018**, *1801256*, 1801256. https://doi.org/10.1002/smll.201801256.

(158) Liu, L.; Hu, Z.; Sui, X.; Guo, J.; Cranston, E. D.; Mao, Z. Effect of Counterion Choice on the Stability of Cellulose Nanocrystal Pickering Emulsions. *Ind. Eng. Chem. Res.* **2018**, *57* (21), 7169–7180. https://doi.org/10.1021/acs.iecr.8b01001.

(159) Hu, Z.; Ballinger, S.; Pelton, R.; Cranston, E. D. Surfactant-Enhanced Cellulose Nanocrystal Pickering Emulsions. *J. Colloid Interface Sci.* **2015**, *439*, 139–148. https://doi.org/10.1016/j.jcis.2014.10.034.

(160) Habibi, Y.; Lucia, L. A.; Rojas, O. J. Cellulose Nanocrystals: Chemistry, Self-Assembly, and Applications. *Chem. Rev.* **2010**, *110* (6), 3479–3500. https://doi.org/10.1021/cr900339w.

(161) Salas, C.; Nypelö, T.; Rodriguez-Abreu, C.; Carrillo, C.; Rojas, O. J. Nanocellulose Properties and Applications in Colloids and Interfaces. *Curr. Opin. Colloid Interface Sci.* **2014**, *19* (5), 383–396. https://doi.org/10.1016/j.cocis.2014.10.003.

(162) Klemm, D.; Kramer, F.; Moritz, S.; Lindström, T.; Ankerfors, M.; Gray, D.; Dorris, A. Nanocelluloses: A New Family of Nature-Based Materials. *Angew. Chemie Int. Ed.* **2011**,

50 (24), 5438–5466. https://doi.org/10.1002/anie.201001273.

(163) Eyley, S.; Thielemans, W. Surface Modification of Cellulose Nanocrystals. *Nanoscale* **2014**, *6* (14), 7764–7779. https://doi.org/10.1039/C4NR01756K.

(164) Moreau, C.; Villares, A.; Capron, I.; Cathala, B. Tuning Supramolecular Interactions of Cellulose Nanocrystals to Design Innovative Functional Materials. *Ind. Crops Prod.* **2016**, *93*, 96–107. https://doi.org/10.1016/j.indcrop.2016.02.028.

(165) Tang, J.; Shi, Z.; Berry, R. M.; Tam, K. C. Mussel-Inspired Green Metallization of Silver Nanoparticles on Cellulose Nanocrystals and Their Enhanced Catalytic Reduction of 4-Nitrophenol in the Presence of β-Cyclodextrin. *Ind. Eng. Chem. Res.* **2015**, *54* (13), 3299–3308. https://doi.org/10.1021/acs.iecr.5b00177.

(166) Sunasee, R.; Hemraz, U. D.; Ckless, K. Cellulose Nanocrystals: A Versatile Nanoplatform for Emerging Biomedical Applications. *Expert Opin. Drug Deliv.* **2016**, *13* (9), 1243–1256. https://doi.org/10.1080/17425247.2016.1182491.

(167) Habibi, Y. Key Advances in the Chemical Modification of Nanocelluloses. *Chem. Soc. Rev.* **2014**, *43* (5), 1519–1542. https://doi.org/10.1039/C3CS60204D.

(168) Tang, J.; Berry, R. M.; Tam, K. C. Stimuli-Responsive Cellulose Nanocrystals for Surfactant-Free Oil Harvesting. *Biomacromolecules* **2016**, *17* (5), 1748–1756. https://doi.org/10.1021/acs.biomac.6b00144.

(169) Tang, J.; Lee, M. F. X.; Zhang, W.; Zhao, B.; Berry, R. M.; Tam, K. C. Dual Responsive Pickering Emulsion Stabilized by Poly[2-(Dimethylamino) Ethyl Methacrylate] Grafted Cellulose Nanocrystals. *Biomacromolecules* **2014**, *15* (8), 3052–3060. https://doi.org/10.1021/bm500663w.

(170) Saito, T.; Kimura, S.; Nishiyama, Y.; Isogai, A. Cellulose Nanofibers Prepared by TEMPO-Mediated Oxidation of Native Cellulose. *Biomacromolecules* **2007**, *8* (8), 2485–2491. https://doi.org/10.1021/bm0703970.

(171) Peddireddy, K. R.; Nicolai, T.; Benyahia, L.; Capron, I. Stabilization of Water-in-Water Emulsions by Nanorods. *ACS Macro Lett.* **2016**, *5* (3), 283–286. https://doi.org/10.1021/acsmacrolett.5b00953.

(172) Tang, J.; Sisler, J.; Grishkewich, N.; Tam, K. C. Functionalization of Cellulose Nanocrystals for Advanced Applications. *J. Colloid Interface Sci.* **2017**, *494*, 397–409. https://doi.org/10.1016/j.jcis.2017.01.077.

(173) Klemm, D.; Heublein, B.; Fink, H.-P.; Bohn, A. Cellulose: Fascinating Biopolymer and Sustainable Raw Material. *Angew. Chemie Int. Ed.* **2005**, *44* (22), 3358–3393. https://doi.org/10.1002/anie.200460587.

(174) Eichhorn, S. J. Cellulose Nanowhiskers: Promising Materials for Advanced Applications. *Soft Matter* **2011**, *7* (2), 303–315. https://doi.org/10.1039/C0SM00142B.

(175) Du, W.; Guo, J.; Li, H.; Gao, Y. Heterogeneously Modified Cellulose Nanocrystals-Stabilized Pickering Emulsion: Preparation and Their Template Application for the Creation of PS Microspheres with Amino-Rich Surfaces. *ACS Sustain. Chem. Eng.* **2017**, *5* (9), 7514–7523. https://doi.org/10.1021/acssuschemeng.7b00375.

(176) Lokanathan, A. R.; Nykänen, A.; Seitsonen, J.; Johansson, L. S.; Campbell, J.; Rojas, O. J.; Ikkala, O.; Laine, J. Cilia-Mimetic Hairy Surfaces Based on End-Immobilized Nanocellulose Colloidal Rods. *Biomacromolecules* **2013**, *14* (8), 2807–2813. https://doi.org/10.1021/bm400633r.

(177) Zoppe, J. O.; Dupire, A. V. M.; Lachat, T. G. G.; Lemal, P.; Rodriguez-Lorenzo, L.; Petri-Fink, A.; Weder, C.; Klok, H.-A. Cellulose Nanocrystals with Tethered Polymer Chains: Chemically Patchy versus Uniform Decoration. *ACS Macro Lett.* **2017**, 892–897. https://doi.org/10.1021/acsmacrolett.7b00383.

(178) Kalashnikova, I.; Bizot, H.; Cathala, B.; Capron, I. New Pickering Emulsions Stabilized by Bacterial Cellulose Nanocrystals. *Langmuir* **2011**, *27* (12), 7471–7479. https://doi.org/10.1021/la200971f.

(179) Zoppe, J. O.; Venditti, R. A.; Rojas, O. J. Pickering Emulsions Stabilized by Cellulose Nanocrystals Grafted with Thermo-Responsive Polymer Brushes. *J. Colloid Interface Sci.* **2012**, *369* (1), 202–209. https://doi.org/10.1016/j.jcis.2011.12.011.

(180) Cunha, A. G.; Mougel, J. B.; Cathala, B.; Berglund, L. A.; Capron, I. Preparation of Double Pickering Emulsions Stabilized by Chemically Tailored Nanocelluloses. *Langmuir* **2014**, *30* (31), 9327–9335. https://doi.org/10.1021/la5017577.

(181) Zhao, H.; Heindel, N. D. Determination of Degree of Substitution of Formyl Groups in Polyaldehyde Dextran by the Hydroxylamine Hydrochloride Method. *Pharm. Res.* **1991**, *08* (3), 400–402. https://doi.org/10.1023/A:1015866104055.

(182) Kalashnikova, I.; Bizot, H.; Bertoncini, P.; Capron, I. Soft Matter Cellulosic Nanorods of Various Aspect Ratios for Oil in Water Pickering Emulsions †. **2013**, 952–959. https://doi.org/10.1039/c2sm26472b.

(183) Schatz, C.; Lecommandoux, S. Polysaccharide-Containing Block Copolymers: Synthesis, Properties and Applications of an Emerging Family of Glycoconjugates. *Macromol. Rapid Commun.* **2010**, *31* (19), 1664–1684. https://doi.org/10.1002/marc.201000267.

(184) Azzam, F.; Heux, L.; Putaux, J. L.; Jean, B. Preparation by Grafting onto, Characterization, and Properties of Thermally Responsive Polymer-Decorated Cellulose Nanocrystals. *Biomacromolecules* **2010**, *11* (12), 3652–3659. https://doi.org/10.1021/bm101106c.

(185) Yang, F.; Liu, S.; Xu, J.; Lan, Q.; Wei, F.; Sun, D. Pickering Emulsions Stabilized Solely by Layered Double Hydroxides Particles: The Effect of Salt on Emulsion Formation and Stability. *J. Colloid Interface Sci.* **2006**, *302* (1), 159–169. https://doi.org/10.1016/j.jcis.2006.06.015.

(186) Jia, X.; Sheng, W. B.; Li, W.; Tong, Y. Bin; Liu, Z. Y.; Zhou, F. Adhesive Polydopamine Coated Avermectin Microcapsules for Prolonging Foliar Pesticide Retention. *ACS Appl. Mater. Interfaces* **2014**, *6* (22), 19552–19558. https://doi.org/10.1021/am506458t.

(187) Rahman, M. M.; Liu, Y.; Naidu, R. Nanoencapsulation , Nano-Guard for Pesticides : A New Window for Safe Application. **2016**. https://doi.org/10.1021/acs.jafc.5b05214.

(188) Wang, C.; Cui, B.; Zhao, X.; Wang, Y.; Zeng, Z.; Sun, C.; Yang, D.; Liu, G.; Cui, H. Optimization and Characterization of Lambda-Cyhalothrin Solid Nanodispersion by Self-Dispersing Method. **2018**, No. June. https://doi.org/10.1002/ps.5122.

(189) Chin, C.; Wu, H.; Wang, S. S. New Approach to Pesticide Delivery Using Nanosuspensions : Research and Applications. **2011**, 7637–7643. https://doi.org/10.1021/ie2001007.

(190) Xiang, Y.; Wang, M.; Sun, X.; Cai, D.; Wu, Z. Controlling Pesticide Loss through Nanonetworks. *ACS Sustain. Chem. Eng.* **2014**, *2* (4), 918–924. https://doi.org/10.1021/sc400513p.

(191) Thorat, A. A.; Dalvi, S. V. Liquid Antisolvent Precipitation and Stabilization of Nanoparticles of Poorly Water Soluble Drugs in Aqueous Suspensions: Recent

Developments and Future Perspective. *Chem. Eng. J.* **2012**, *181–182*, 1–34. https://doi.org/10.1016/j.cej.2011.12.044.

(192) Tong, Y.; Wu, Y.; Zhao, C.; Xu, Y.; Lu, J.; Xiang, S.; Zong, F.; Wu, X. Polymeric Nanoparticles as a Metolachlor Carrier : Water-Based Formulation for Hydrophobic Pesticides and Absorption by Plants. **2017**. https://doi.org/10.1021/acs.jafc.7b02197.

(193) Kamari, S. N. M. Y. A.; Aljafree, N. F. A. A Review of Materials Used as Carrier Agents in Pesticide Formulations. *Int. J. Environ. Sci. Technol.* **2016**, *13* (12), 2977–2994. https://doi.org/10.1007/s13762-016-1096-y.

(194) Li, J.; Li, Y.; Dong, H. Controlled Release of Herbicide Acetochlor from Clay/Carboxylmethylcellulose Gel Formulations. *J. Agric. Food Chem.* **2008**, *56* (4), 1336–1342. https://doi.org/10.1021/jf072530l.

(195) Wen, L. X.; Li, Z. Z.; Zou, H. K.; Liu, A. Q.; Chen, J. F. Controlled Release of Avermectin from Porous Hollow Silica Nanoparticles. *Pest Manag. Sci.* **2005**, *61* (6), 583–590. https://doi.org/10.1002/ps.1032.

(196) Ding, K.; Shi, L.; Zhang, L.; Zeng, T.; Yin, Y.; Yi, Y. Polymer Chemistry Synthesis of Photoresponsive Polymeric Propesticide Micelles Based on PEG for the Controlled Release of a Herbicide †. **2016**, 899–904. https://doi.org/10.1039/c5py01690h.

(197) Cui, H.; Guo, X. Preparation and Characterization of Size-Controlled Nanoparticles for High-Loading λ-Cyhalothrin Delivery through Flash Nanoprecipitation. **2018**. https://doi.org/10.1021/acs.jafc.8b02851.

(198) Chen, N.; Dempere, L. A.; Tong, Z. Synthesis of PH-Responsive Lignin-Based Nanocapsules for Controlled Release of Hydrophobic Molecules. **2016**. https://doi.org/10.1021/acssuschemeng.6b01209.

(199) Li, Y.; Zhou, M.; Pang, Y.; Qiu, X. Lignin-Based Microsphere: Preparation and Performance on Encapsulating the Pesticide Avermectin. **2017**. https://doi.org/10.1021/acssuschemeng.6b03180.

(200) Tang, C.; Spinney, S.; Shi, Z.; Tang, J.; Peng, B.; Luo, J. Amphiphilic Cellulose Nanocrystals for Enhanced Pickering Emulsion Stabilization. *Langmuir* **2018**, *34*, 12897–12905. https://doi.org/10.1021/acs.langmuir.8b02437.

(201) Tang, C.; Chen, Y.; Luo, J.; Low, M. Y.; Shi, Z.; Tang, J.; Zhang, Z.; Peng, B.; Tam, K. C. Pickering Emulsions Stabilized by Hydrophobically Modified Nanocellulose Containing Various Structural Characteristics. *Cellulose* **2019**, *26* (13–14). https://doi.org/10.1007/s10570-019-02648-x.

(202) Yang, Q.; Sun, L.; Zhang, D.; Qian, J.; Sun, Y.; Ma, L.; Sun, J.; Hu, X.; Tan, W.; Wang, W.; et al. Toxicology in Vitro Partial Characterization of Deltamethrin Metabolism Catalyzed by Chymotrypsin. **2008**, *22*, 1528–1533. https://doi.org/10.1016/j.tiv.2008.05.007.

(203) Kedzior, S. A.; Marway, H. S.; Cranston, E. D. Tailoring Cellulose Nanocrystal and Surfactant Behavior in Miniemulsion Polymerization. *Macromolecules* **2017**, *50* (7), 2645–2655. https://doi.org/10.1021/acs.macromol.7b00516.

(204) Lombardo, S.; Chen, P.; Larsson, P. A.; Thielemans, W.; Wohlert, J.; Svagan, A. J. Toward Improved Understanding of the Interactions between Poorly Soluble Drugs and Cellulose Nanofibers. *Langmuir* **2018**, *34* (19), 5464–5473. https://doi.org/10.1021/acs.langmuir.8b00531.

(205) Qing, W.; Wang, Y.; Wang, Y.; Zhao, D.; Liu, X.; Zhu, J. The Modified Nanocrystalline Cellulose for Hydrophobic Drug Delivery. *Appl. Surf. Sci.* **2016**, *366*, 404–409. https://doi.org/10.1016/j.apsusc.2016.01.133.

(206) Jackson, J. K.; Letchford, K.; Wasserman, B. Z.; Ye, L.; Burt, H. M. The Use of Nanocrystalline Cellulose for the Binding and Controlled Release of Drugs. **2011**. https://doi.org/10.2147/IJN.S16749.

(207) Löbmann, K.; Svagan, A. J. Cellulose Nano Fi Bers as Excipient for the Delivery of Poorly Soluble Drugs. *Int. J. Pharm.* **2017**, *533* (1), 285–297. https://doi.org/10.1016/j.ijpharm.2017.09.064.

(208) Tam, K. C.; Wyn-Jones, E. Insights on Polymer Surfactant Complex Structures during the Binding of Surfactants to Polymers as Measured by Equilibrium and Structural Techniques. *Chem. Soc. Rev.* **2006**, *35* (8), 693–709. https://doi.org/10.1039/b415140m.

(209) Lombardo, S. Thermodynamics of the Interactions of Positively Charged Cellulose Nanocrystals with Molecules Bearing Different Amounts of Carboxylate Anions †. **2018**, 17637–17647. https://doi.org/10.1039/c8cp01532e.

(210) Loh, W.; Brinatti, C.; Tam, K. C. Use of Isothermal Titration Calorimetry to Study Surfactant Aggregation in Colloidal Systems. *Biochim. Biophys. Acta - Gen. Subj.* **2016**, *1860* (5), 999–1016. https://doi.org/10.1016/j.bbagen.2015.10.003.

(211) Brinatti, C.; Huang, J.; Berry, R. M.; Tam, K. C.; Loh, W. Structural and Energetic Studies on the Interaction of Cationic Surfactants and Cellulose Nanocrystals. *Langmuir* **2016**, *32* (3), 689–698. https://doi.org/10.1021/acs.langmuir.5b03893.

(212) Chi, K.; Catchmark, J. M. Crystalline Nanocellulose / Lauric Arginate Complexes. **2017**, *175*, 320–329.

(213) Kalashnikova, I.; Bizot, H.; Cathala, B.; Capron, I. Modulation of Cellulose Nanocrystals Amphiphilic Properties to Stabilize Oil / Water Interface. **2012**.

(214) Malaspina, D. C.; Faraudo, J. Molecular Insight into the Wetting Behavior and Amphiphilic Character of Cellulose Nanocrystals. *Adv. Colloid Interface Sci.* **2019**, *267*, 15–25. https://doi.org/10.1016/j.cis.2019.02.003.

(215) Cherhal, F.; Cousin, F.; Capron, I. Structural Description of the Interface of Pickering Emulsions Stabilized by Cellulose Nanocrystals. **2016**. https://doi.org/10.1021/acs.biomac.5b01413.

(216) Medronho, B.; Alves, L.; Costa, C. And Its Interactions to Dissolution , Regeneration ,. **2017**, 23704–23718. https://doi.org/10.1039/C7CP02409F.

(217) Mo, L.; Pang, H.; Tan, Y.; Zhang, S.; Li, J. 3D Multi-Wall Perforated Nanocellulose-Based Polyethylenimine Aerogels for Ultrahigh Efficient and Reversible Removal of Cu(II) Ions from Water. *Chem. Eng. J.* **2019**, *378* (June), 122157. https://doi.org/10.1016/j.cej.2019.122157.

(218) Joseph, L.; Jun, B. M.; Flora, J. R. V.; Park, C. M.; Yoon, Y. Removal of Heavy Metals from Water Sources in the Developing World Using Low-Cost Materials: A Review. *Chemosphere*. Elsevier Ltd August 1, 2019, pp 142–159. https://doi.org/10.1016/j.chemosphere.2019.04.198.

(219) Liu, J.; Su, D.; Yao, J.; Huang, Y.; Shao, Z.; Chen, X. Soy Protein-Based Polyethylenimine Hydrogel and Its High Selectivity for Copper Ion Removal in Wastewater Treatment. *J. Mater. Chem. A* **2017**, *5* (8), 4163–4171. https://doi.org/10.1039/c6ta10814h.

(220) Qin, H.; Hu, T.; Zhai, Y.; Lu, N.; Aliyeva, J. The Improved Methods of Heavy Metals Removal by Biosorbents: A Review. *Environmental Pollution*. Elsevier Ltd March 1, 2020. https://doi.org/10.1016/j.envpol.2019.113777.

(221) Maleki, H. Recent Advances in Aerogels for Environmental Remediation Applications: A Review. *Chemical Engineering Journal*. Elsevier B.V. September 15, 2016, pp 98–118. https://doi.org/10.1016/j.cej.2016.04.098.

(222) Zhao, S.; Malfait, W. J.; Guerrero-Alburquerque, N.; Koebel, M. M.; Nyström, G. Biopolymer Aerogels and Foams: Chemistry, Properties, and Applications. *Angew. Chemie - Int. Ed.* **2018**, *57* (26), 7580–7608. https://doi.org/10.1002/anie.201709014.

(223) Wang, H.; Mi, X.; Li, Y.; Zhan, S. 3D Graphene-Based Macrostructures for Water Treatment. *Adv. Mater.* **2019**, *1806843*, 1–11. https://doi.org/10.1002/adma.201806843.

(224) Liu, H.; Wei, Y.; Luo, J.; Li, T.; Wang, D.; Luo, S.; Crittenden, J. C. 3D Hierarchical Porous-Structured Biochar Aerogel for Rapid and Efficient Phenicol Antibiotics Removal from Water. *Chem. Eng. J.* **2019**, *368*, 639–648. https://doi.org/10.1016/j.cej.2019.03.007.

(225) Wang, K.; Liu, X.; Tan, Y.; Zhang, W.; Zhang, S.; Li, J. Two-Dimensional Membrane and Three-Dimensional Bulk Aerogel Materials via Top-down Wood Nanotechnology for Multibehavioral and Reusable Oil/Water Separation. *Chem. Eng. J.* **2019**, *371*, 769–780. https://doi.org/10.1016/j.cej.2019.04.108.

(226) Xiong, Y.; Wang, C.; Wang, H.; Yao, Q.; Fan, B.; Chen, Y.; Sun, Q.; Jin, C.; Xu, X. A 3D Titanate Aerogel with Cellulose as the Adsorption-Aggregator for Highly Efficient Water Purification. *J. Mater. Chem. A* **2017**, *5* (12), 5813–5819. https://doi.org/10.1039/C6TA10638B.

(227) De France, K. J.; Hoare, T.; Cranston, E. D. Review of Hydrogels and Aerogels Containing Nanocellulose. *Chem. Mater.* **2017**, *29* (11), 4609–4631. https://doi.org/10.1021/acs.chemmater.7b00531.

(228) Zhang, N.; Zang, G. L.; Shi, C.; Yu, H. Q.; Sheng, G. P. A Novel Adsorbent TEMPO-Mediated Oxidized Cellulose Nanofibrils Modified with PEI: Preparation, Characterization, and Application for Cu(II) Removal. *J. Hazard. Mater.* **2016**, *316*, 11–18. https://doi.org/10.1016/j.jhazmat.2016.05.018.

(229) Tang, J.; Song, Y.; Zhao, F.; Spinney, S.; da Silva Bernardes, J.; Tam, K. C. Compressible Cellulose Nanofibril (CNF) Based Aerogels Produced via a Bio-Inspired Strategy for Heavy Metal Ion and Dye Removal. *Carbohydr. Polym.* **2019**, *208* (December 2018), 404–412. https://doi.org/10.1016/j.carbpol.2018.12.079.

(230) Li, J.; Zuo, K.; Wu, W.; Xu, Z.; Yi, Y.; Jing, Y.; Dai, H.; Fang, G. Shape Memory Aerogels from Nanocellulose and Polyethyleneimine as a Novel Adsorbent for Removal of Cu(II) and Pb(II). *Carbohydr. Polym.* **2018**, *196* (February), 376–384. https://doi.org/10.1016/j.carbpol.2018.05.015.

(231) Shan, S.; Tang, H.; Zhao, Y.; Wang, W.; Cui, F. Highly Porous Zirconium-Crosslinked Graphene Oxide/Alginate Aerogel Beads for Enhanced Phosphate Removal. *Chem. Eng. J.* **2019**, *359* (July 2018), 779–789. https://doi.org/10.1016/j.cej.2018.10.033.

(232) Xu, W.; Xing, Y.; Liu, J.; Wu, H.; Cui, Y.; Li, D.; Guo, D.; Li, C.; Liu, A.; Bai, H. Efficient Water Transport and Solar Steam Generation via Radially, Hierarchically Structured Aerogels. *ACS Nano* **2019**, *13* (7), 7930–7938. https://doi.org/10.1021/acsnano.9b02331.

(233) Zhu, X.; Yang, C.; Wu, P.; Ma, Z.; Shang, Y.; Bai, G.; Liu, X.; Chang, G.; Li, N.; Dai, J.; et al. Precise Control of Versatile Microstructure and Properties of Graphene Aerogel via

Freezing Manipulation . *Nanoscale* **2020**, *12* (8), 4882–4894. https://doi.org/10.1039/c9nr07861d.

(234) Erlandsson, J.; Pettersson, T.; Ingverud, T.; Granberg, H.; Larsson, P. A.; Malkoch, M.; Wågberg, L. On the Mechanism behind Freezing-Induced Chemical Crosslinking in Ice-Templated Cellulose Nanofibril Aerogels. *J. Mater. Chem. A* **2018**, *6* (40), 19371–19380. https://doi.org/10.1039/c8ta06319b.

(235) Cheng, H.; Li, Y.; Wang, B.; Mao, Z.; Xu, H.; Zhang, L.; Zhong, Y.; Sui, X. Chemical Crosslinking Reinforced Flexible Cellulose Nanofiber-Supported Cryogel. *Cellulose* **2018**, *25* (1), 573–582. https://doi.org/10.1007/s10570-017-1548-7.

(236) Deng, S.; Ting, Y. P. Characterization of PEI-Modified Biomass and Biosorption of Cu(II), Pb(II) and Ni(II). *Water Res.* **2005**, *39* (10), 2167–2177. https://doi.org/10.1016/j.watres.2005.03.033.

(237) Song, J.; Chen, C.; Yang, Z.; Kuang, Y.; Li, T.; Li, Y.; Huang, H.; Kierzewski, I.; Liu, B.; He, S.; et al. Highly Compressible, Anisotropic Aerogel with Aligned Cellulose Nanofibers. *ACS Nano* **2018**, *12* (1), 140–147. https://doi.org/10.1021/acsnano.7b04246.

(238) Guan, H.; Cheng, Z.; Wang, X. Highly Compressible Wood Sponges with a Spring-like Lamellar Structure as Effective and Reusable Oil Absorbents. *ACS Nano* **2018**. https://doi.org/10.1021/acsnano.8b05763.

(239) Guo, F.; Jiang, Y.; Xu, Z.; Xiao, Y.; Fang, B.; Liu, Y.; Gao, W.; Zhao, P.; Wang, H.; Gao, C. Highly Stretchable Carbon Aerogels. *Nat. Commun.* **2018**, *9* (1), 1–9. https://doi.org/10.1038/s41467-018-03268-y.

(240) Peng, X.; Wu, K.; Hu, Y.; Zhuo, H.; Chen, Z.; Jing, S.; Liu, Q.; Liu, C.; Zhong, L. A Mechanically Strong and Sensitive CNT/RGO-CNF Carbon Aerogel for Piezoresistive Sensors. *J. Mater. Chem. A* **2018**, *6* (46), 23550–23559. https://doi.org/10.1039/C8TA09322A.

(241) Si, Y.; Yu, J.; Tang, X.; Ge, J.; Ding, B. Ultralight Nanofibre-Assembled Cellular Aerogels with Superelasticity and Multifunctionality. *Nat. Commun.* **2014**, *5*. https://doi.org/10.1038/ncomms6802.

(242) Tran, H. N.; You, S. J.; Chao, H. P. Thermodynamic Parameters of Cadmium Adsorption onto Orange Peel Calculated from Various Methods: A Comparison Study. *J. Environ. Chem. Eng.* **2016**, *4* (3), 2671–2682. https://doi.org/10.1016/j.jece.2016.05.009.

(243) Jiang, J.; Zhang, Q.; Zhan, X.; Journal, F. C.-C. E.; 2019, undefined. A Multifunctional Gelatin-Based Aerogel with Superior Pollutants Adsorption, Oil/Water Separation and Photocatalytic Properties. *Elsevier*.

(244) Zhan, W.; Xu, C.; Qian, G.; Huang, G.; Tang, X.; Lin, B. Adsorption of Cu(Ii), Zn(Ii), and Pb(Ii) from Aqueous Single and Binary Metal Solutions by Regenerated Cellulose and Sodium Alginate Chemically Modified with Polyethyleneimine. *RSC Adv.* **2018**, *8* (33), 18723–18733. https://doi.org/10.1039/c8ra02055h.

(245) Jin, X.; Xiang, Z.; Liu, Q.; Chen, Y.; Lu, F. Polyethyleneimine-Bacterial Cellulose Bioadsorbent for Effective Removal of Copper and Lead Ions from Aqueous Solution. *Bioresour. Technol.* **2017**, *244* (June), 844–849. https://doi.org/10.1016/j.biortech.2017.08.072.

(246) Yu, R.; Shi, Y.; Yang, D.; Liu, Y.; Qu, J.; Yu, Z. Z. Graphene Oxide/Chitosan Aerogel Microspheres with Honeycomb-Cobweb and Radially Oriented Microchannel Structures for Broad-Spectrum and Rapid Adsorption of Water Contaminants. *ACS Appl. Mater.*

Interfaces **2017**, *9* (26), 21809–21819. https://doi.org/10.1021/acsami.7b04655.

(247) Zhao, F.; Repo, E.; Song, Y.; Yin, D.; Hammouda, S. Ben; Chen, L.; Kalliola, S.; Tang, J.; Tam, K. C.; Sillanpää, M. Polyethylenimine-Cross-Linked Cellulose Nanocrystals for Highly Efficient Recovery of Rare Earth Elements from Water and a Mechanism Study. *Green Chem.* **2017**, *19* (20), 4816–4828. https://doi.org/10.1039/c7gc01770g.

(248) Cheng, H.; Li, Y.; Wang, B.; Mao, Z.; Xu, H.; Zhang, L.; Zhong, Y.; Sui, X. Chemical Crosslinking Reinforced Flexible Cellulose Nanofiber-Supported Cryogel. *Cellulose* **2018**, *25* (1), 573–582. https://doi.org/10.1007/s10570-017-1548-7.

(249) Barhoumi, A.; Ncib, S.; Chibani, A.; Brahmi, K.; Bouguerra, W.; Elaloui, E. High-Rate Humic Acid Removal from Cellulose and Paper Industry Wastewater by Combining Electrocoagulation Process with Adsorption onto Granular Activated Carbon. *Ind. Crops Prod.* **2019**, *140* (September), 111715. https://doi.org/10.1016/j.indcrop.2019.111715.

(250) Saha, S.; Das, C. Purification of Humic Acids Contained Simulated Wastewater Using Membrane Ultrafiltration. **2017**, 33–40.

(251) Abouzeid, R. E.; Khiari, R.; El-Wakil, N.; Dufresne, A. Current State and New Trends in the Use of Cellulose Nanomaterials for Wastewater Treatment. *Biomacromolecules* **2019**, *20* (2), 573–597. https://doi.org/10.1021/acs.biomac.8b00839.

(252) Qin, F.; Fang, Z.; Zhou, J.; Sun, C.; Chen, K.; Ding, Z.; Li, G.; Qiu, X. Efficient Removal of Cu^{2+} in Water by Carboxymethylated Cellulose Nanofibrils: Performance and Mechanism. *Biomacromolecules* **2019**, *20* (12), 4466–4475. https://doi.org/10.1021/acs.biomac.9b01198.

(253) Shi, K.; Yang, X.; Cranston, E. D.; Zhitomirsky, I. Efficient Lightweight Supercapacitor with Compression Stability. *Adv. Funct. Mater.* **2016**, *26* (35), 6437–6445. https://doi.org/10.1002/adfm.201602103.

(254) Huang, T.; Shao, Y. W.; Zhang, Q.; Deng, Y. F.; Liang, Z. X.; Guo, F. Z.; Li, P. C.; Wang, Y. Chitosan-Cross-Linked Graphene Oxide/Carboxymethyl Cellulose Aerogel Globules with High Structure Stability in Liquid and Extremely High Adsorption Ability. *ACS Sustain. Chem. Eng.* **2019**, *7* (9), 8775–8788. https://doi.org/10.1021/acssuschemeng.9b00691.

(255) Mattos, B. D.; Tardy, B. L.; Magalhães, W. L. E.; Rojas, O. J. Controlled Release for Crop and Wood Protection: Recent Progress toward Sustainable and Safe Nanostructured Biocidal Systems. *J. Control. Release* **2017**, *262* (June), 139–150. https://doi.org/10.1016/j.jconrel.2017.07.025.

(256) Wang, D. A Critical Review of Cellulose-Based Nanomaterials for Water Purification in Industrial Processes. *Cellulose* **2019**, *26* (2), 687–701. https://doi.org/10.1007/s10570-018-2143-2.

(257) Ji, H.; Xiang, Z.; Qi, H.; Han, T.; Pranovich, A.; Song, T. Strategy towards One-Step Preparation of Carboxylic Cellulose Nanocrystals and Nanofibrils with High Yield, Carboxylation and Highly Stable Dispersibility Using Innocuous Citric Acid. *Green Chem.* **2019**, *21* (8), 1956–1964. https://doi.org/10.1039/c8gc03493a.

(258) Qin, F.; Fang, Z.; Zhou, J.; Sun, C. Efficient Removal of Cu2 + in Water by Carboxymethylated Cellulose Nanofibrils : Performance and Mechanism Efficient Removal of Cu 2 + in Water by Carboxymethylated Cellulose Nanofibrils : Performance and Mechanism. **2019**. https://doi.org/10.1021/acs.biomac.9b01198.

(259) Wang, D.; Yu, H.; Fan, X.; Gu, J.; Ye, S.; Yao, J.; Ni, Q. High Aspect Ratio Carboxylated

Cellulose Nanofibers Cross-Linked to Robust Aerogels for Superabsorption-Flocculants: Paving Way from Nanoscale to Macroscale. *ACS Appl. Mater. Interfaces* **2018**, *10* (24), 20755–20766. https://doi.org/10.1021/acsami.8b04211.

(260) Fan, X.-M.; Yu, H.-Y.; Wang, D.-C.; Mao, Z.-H.; Yao, J.; Tam, K. C. Facile and Green Synthesis of Carboxylated Cellulose Nanocrystals as Efficient Adsorbents in Wastewater Treatments. *ACS Sustain. Chem. Eng.* **2019**, *7* (21), 18067–18075. https://doi.org/10.1021/acssuschemeng.9b05081.

(261) Li, M.; Messele, S. A.; Boluk, Y.; Gamal El-Din, M. Isolated Cellulose Nanofibers for Cu (II) and Zn (II) Removal: Performance and Mechanisms. *Carbohydr. Polym.* **2019**, *221*, 231–241. https://doi.org/10.1016/j.carbpol.2019.05.078.

(262) Erlandsson, J.; Pettersson, T.; Ingverud, T.; Granberg, H.; Larsson, P. A.; Malkoch, M.; Wagberg, L. On the Mechanism behind Freezing-Induced Chemical Crosslinking in Ice-Templated Cellulose Nanofibril Aerogels. *J. Mater. Chem. A* **2018**. https://doi.org/10.1039/C8TA06319B.

(263) Chen, L.; Zhu, J. Y.; Baez, C.; Kitin, P.; Elder, T. Highly Thermal-Stable and Functional Cellulose Nanocrystals and Nanofibrils Produced Using Fully Recyclable Organic Acids. *Green Chem.* **2016**, *18* (13), 3835–3843. https://doi.org/10.1039/c6gc00687f.

(264) Aklog, Y. F.; Nagae, T.; Izawa, H.; Morimoto, M.; Saimoto, H.; Ifuku, S. Preparation of Chitin Nanofibers by Surface Esterification of Chitin with Maleic Anhydride and Mechanical Treatment. *Carbohydr. Polym.* **2016**, *153*, 55–59. https://doi.org/10.1016/j.carbpol.2016.07.060.

(265) Wang, Q.; Yan, X.; Chang, Y.; Ren, L.; Zhou, J. Fabrication and Characterization of Chitin Nanofibers through Esterification and Ultrasound Treatment. *Carbohydr. Polym.* **2018**, *180* (June 2017), 81–87. https://doi.org/10.1016/j.carbpol.2017.09.010.

(266) Buchtová, N.; Budtova, T. Cellulose Aero-, Cryo- and Xerogels: Towards Understanding of Morphology Control. *Cellulose* **2016**, *23* (4), 2585–2595. https://doi.org/10.1007/s10570-016-0960-8.

(267) Tran, H. N.; You, S. J.; Hosseini-Bandegharaei, A.; Chao, H. P. Mistakes and Inconsistencies Regarding Adsorption of Contaminants from Aqueous Solutions: A Critical Review. *Water Res.* **2017**, *120*, 88–116. https://doi.org/10.1016/j.watres.2017.04.014.

(268) Tang, C.; Brodie, P.; Li, Y.; Grishkewich, N. J.; Brunsting, M.; Tam, K. C. Shape Recoverable and Mechanically Robust Cellulose Aerogel Beads for Efficient Removal of Copper Ions. *Chem. Eng. J.* **2020**, 124821. https://doi.org/10.1016/j.cej.2020.124821.

(269) Zhang, F.; Ren, H.; Dou, J.; Tong, G.; Deng, Y. Cellulose Nanofibril Based-Aerogel Microreactors: A High Efficiency and Easy Recoverable W/O/W Membrane Separation System. *Sci. Rep.* **2017**, *7* (January), 1–7. https://doi.org/10.1038/srep40096.

(270) Ma, J.; Wang, X.; Fu, Q.; Si, Y.; Yu, J.; Ding, B. Highly Carbonylated Cellulose Nanofibrous Membranes Utilizing Maleic Anhydride Grafting for Efficient Lysozyme Adsorption. *ACS Appl. Mater. Interfaces* **2015**, *7* (28), 15658–15666. https://doi.org/10.1021/acsami.5b04741.

(271) Sehaqui, H.; Kulasinski, K.; Pfenninger, N.; Zimmermann, T.; Tingaut, P. Highly Carboxylated Cellulose Nanofibers via Succinic Anhydride Esterification of Wheat Fibers and Facile Mechanical Disintegration. *Biomacromolecules* **2017**, *18* (1), 242–248. https://doi.org/10.1021/acs.biomac.6b01548.

(272) Tang, L.; Huang, B.; Yang, N.; Li, T.; Lu, Q.; Lin, W.; Chen, X. Organic Solvent-Free and

Efficient Manufacture of Functionalized Cellulose Nanocrystals via One-Pot Tandem Reactions. *Green Chem.* **2013**, *15* (9), 2369–2373. https://doi.org/10.1039/c3gc40965a.

(273) Quellmalz, A.; Mihranyan, A. Citric Acid Cross-Linked Nanocellulose-Based Paper for Size-Exclusion Nanofiltration. *ACS Biomater. Sci. Eng.* **2015**, *1* (4), 271–276. https://doi.org/10.1021/ab500161x.

(274) Mariano, M.; Hantao, L. W.; da Silva Bernardes, J.; Strauss, M. Microstructural Characterization of Nanocellulose Foams Prepared in the Presence of Cationic Surfactants. *Carbohydr. Polym.* **2018**, *195* (January), 153–162. https://doi.org/10.1016/j.carbpol.2018.04.075.

(275) Chu, G.; Qu, D.; Zussman, E.; Xu, Y. Ice-Assisted Assembly of Liquid Crystalline Cellulose Nanocrystals for Preparing Anisotropic Aerogels with Ordered Structures. *Chem. Mater.* **2017**, *29* (9), 3980–3988. https://doi.org/10.1021/acs.chemmater.7b00361.

(276) Munier, P.; Gordeyeva, K.; Bergström, L.; Fall, A. B. Directional Freezing of Nanocellulose Dispersions Aligns the Rod-Like Particles and Produces Low-Density and Robust Particle Networks. *Biomacromolecules* **2016**, *17* (5), 1875–1881. https://doi.org/10.1021/acs.biomac.6b00304.

(277) Wang, J.; Liu, M.; Duan, C.; Sun, J.; Xu, Y. Preparation and Characterization of Cellulose-Based Adsorbent and Its Application in Heavy Metal Ions Removal. *Carbohydr. Polym.* **2019**, *206*, 837–843. https://doi.org/10.1016/j.carbpol.2018.11.059.

(278) Zhu, C.; Liu, P.; Mathew, A. P. Self-Assembled TEMPO Cellulose Nanofibers: Graphene Oxide-Based Biohybrids for Water Purification. *ACS Appl. Mater. Interfaces* **2017**, *9* (24), 21048–21058. https://doi.org/10.1021/acsami.7b06358.

(279) Zhao, B.; Jiang, H.; Lin, Z.; Xu, S.; Xie, J.; Zhang, A. Preparation of Acrylamide/Acrylic Acid Cellulose Hydrogels for the Adsorption of Heavy Metal Ions. *Carbohydr. Polym.* **2019**, *224* (June), 115022. https://doi.org/10.1016/j.carbpol.2019.115022.

(280) Feng, L.; Zhang, Z.; Mai, Z.; Ma, Y.; Liu, B.; Jiang, L.; Zhu, D. A Super-Hydrophobic and Super-Oleophilic Coating Mesh Film for the Separation of Oil and Water. *Angew. Chemie - Int. Ed.* **2004**, *43* (15), 2012–2014. https://doi.org/10.1002/anie.200353381.

(281) Xue, Z.; Wang, S.; Lin, L.; Chen, L.; Liu, M.; Feng, L.; Jiang, L. A Novel Superhydrophilic and Underwater Superoleophobic Hydrogel-Coated Mesh for Oil/Water Separation. *Adv. Mater.* **2011**, *23* (37), 4270–4273. https://doi.org/10.1002/adma.201102616.

(282) Xiao, J.; Lv, W.; Song, Y.; Zheng, Q. Graphene/Nanofiber Aerogels: Performance Regulation towards Multiple Applications in Dye Adsorption and Oil/Water Separation. *Chem. Eng. J.* **2018**, *338*, 202–210. https://doi.org/10.1016/j.cej.2017.12.156.

(283) Peng, H.; Wu, J.; Wang, Y.; Wang, H.; Liu, Z.; Shi, Y.; Guo, X. A Facile Approach for Preparation of Underwater Superoleophobicity Cellulose/Chitosan Composite Aerogel for Oil/Water Separation. *Appl. Phys. A* **2016**, *122* (5), 516. https://doi.org/10.1007/s00339-016-0049-0.

(284) Bai, Y.; Peng, J.; Li, J.; Lai, G. Use of Carboxylated Polyethylene Glycol as Promoter for Platinum-Catalyzed Hydrosilylation of Alkenes. *Appl. Organomet. Chem.* **2011**, *25* (5), 400–405. https://doi.org/10.1002/aoc.1776.

(285) Parray, Z. A.; Hassan, M. I.; Ahmad, F.; Islam, A. Amphiphilic Nature of Polyethylene Glycols and Their Role in Medical Research. *Polymer Testing*. Elsevier Ltd February 1, 2020, p 106316. https://doi.org/10.1016/j.polymertesting.2019.106316.

(286) Ding, G.; Jiao, W.; Wang, R.; Niu, Y.; Chen, L.; Hao, L. Ultrafast, Reversible Transition of Superwettability of Graphene Network and Controllable Underwater Oil Adhesion for Oil Microdroplet Transportation. *Adv. Funct. Mater.* **2018**, *28* (18), 1–11. https://doi.org/10.1002/adfm.201706686.

(287) Wang, S.; Liu, K.; Yao, X.; Jiang, L. Bioinspired Surfaces with Superwettability: New Insight on Theory, Design, and Applications. *Chem. Rev.* **2015**, *115* (16), 8230–8293. https://doi.org/10.1021/cr400083y.

(288) Calcagnile, P.; Sibillano, T.; Giannini, C.; Sannino, A.; Demitri, C. Biodegradable Poly(Lactic Acid)/Cellulose-Based Superabsorbent Hydrogel Composite Material as Water and Fertilizer Reservoir in Agricultural Applications. *J. Appl. Polym. Sci.* **2019**, *136* (21), 1–9. https://doi.org/10.1002/app.47546.

(289) Senna, A. M.; Botaro, V. R. Biodegradable Hydrogel Derived from Cellulose Acetate and EDTA as a Reduction Substrate of Leaching NPK Compound Fertilizer and Water Retention in Soil. *J. Control. Release* **2017**, *260* (May), 194–201. https://doi.org/10.1016/j.jconrel.2017.06.009.